

# **A Comprehensive Mechanical Engineering Perspective on the Implementation of an Organic Rankine Cycle for Data Center Waste Heat Recovery**

May 4th, 2021

Submitted by:

Yu Him Au, [ymau@wpi.edu](mailto:y mau@wpi.edu)

Olivia Lattanzi, [ollattanzi@wpi.edu](mailto:ollattanzi@wpi.edu)

Dan Seeley, [drseeley@wpi.edu](mailto:drseeley@wpi.edu)

Claire Victor, [cavictor@wpi.edu](mailto:cavictor@wpi.edu)

Advisor:

Professor Fiona Levey, [fclevey@wpi.edu](mailto:fclevey@wpi.edu)



**Worcester Polytechnic Institute**

Worcester, MA

*This report represents the work of one or more WPI undergraduate students submitted to the faculty as evidence of completion of a degree requirement. WPI routinely publishes these reports on the web without editorial or peer review.*

# Table of Contents

<b>Nomenclature</b>	<b>3</b>
<b>Abstract</b>	<b>5</b>
<b>1.0 Introduction</b>	<b>6</b>
<b>2.0 Background</b>	<b>7</b>
2.1 Data Centers	7
2.2 Low-Grade Heat Recovery Systems	9
2.3 Organic Rankine Cycles	15
2.3.1 ORC Breakdown By Components	16
2.3.2 ORC Working Fluids	16
2.3.3 ORC Operating Conditions	18
2.4 Data Center Cooling Technologies	22
2.4.1 Air Cooling	23
2.4.2 Liquid Cooling	25
2.4.3 Two-Phase Cooling Systems	29
<b>3.0 Preliminary Design</b>	<b>33</b>
3.1 Insight from Prior Research Efforts	33
3.2 Extending Prior Research Efforts	36
3.3 Design Overview	37
3.3.1 Design Constraints	38
3.3.2 Design Criteria	39
3.4 ORC Component	39
3.4.1 Thermodynamic Analysis	39
3.4.2 Fluid Mechanics Analysis	44
3.4.3 Heat Loss Through ORC Pipes and Insulation	47
3.5 SHEC Component	51
<b>4.0 Development of Microchannel Heat Sink Simulations</b>	<b>54</b>
4.1 Development of Liquid Cooling MCHS Simulation	54
4.1.1 Stage One: 2D Simulations with Laminar Flow	57
4.1.2 Stage Two: 3D Simulations with Laminar Flow	66
4.1.3 Stage Three: 3D Simulations with Turbulent Flow	71
4.2 Development of Two-Phase Cooling MCHS Simulation	75
<b>5.0 Simulated Experiments</b>	<b>78</b>
5.1 Experiments	80
5.2 Experiment Results	83
5.3 Selected Model & Final Remarks	85

<b>6.0 Final Design</b>	<b>93</b>
6.1 Liquid Cooling Heat Sink	94
6.2 Integrated Analysis	97
6.2.1 ORC Heat Exchanger - Evaporator	99
6.2.2 ORC Heat Exchanger - Condenser	112
6.2.3 ORC Thermodynamic Analysis	119
6.2.4 ORC Fluid Mechanics Analysis	122
6.2.5 SHEC Piping & Fluids Analysis	122
6.3 Final Results	128
6.3.1 ORC Heat Exchanger Results	129
6.3.2 ORC Thermodynamics & Fluid Mechanics Results	133
6.3.3 SHEC Piping & Fluid Mechanics Results	135
<b>7.0 Economic Analysis</b>	<b>137</b>
7.1 Calculation of Cost Parameters	137
7.1.1 General Cost Parameters	137
7.1.2 ORC/SHEC System Cost Parameters	138
7.1.3 Conventional Air Cooling Cost Parameters	139
7.2 Annual Cost Analysis	140
7.3 Payback Period	141
<b>8.0 Conclusions &amp; Recommendations</b>	<b>143</b>
<b>9.0 References</b>	<b>145</b>
<b>Appendices</b>	<b>153</b>
Appendix A: MATLAB Code for Initial Thermodynamics Calculations	153
Appendix B: Thermodynamic Analysis Results from MATLAB Code	154
Appendix C: Fluid Mechanics of Each ORC Connecting Pipe	155
Appendix D: Pre-Simulation Report (single-phase laminar flow through a single microchannel)	157
Appendix E: Example 5.2 from Kandlikar et al.	164
Appendix F: Discounted Payback Period (cont.)	171
Appendix G: MATLAB Code for Final Design of ORC/SHEC System	173

## Nomenclature

A	area (m <sup>2</sup> ), annual capital flow
a	width of channel (m)
AIO	all in one (referring to a liquid cooling unit)
b	height of channel (m)
c	specific heat capacity (kJ/kg-K)
CAD	computer aided design
CDU	coolant distribution unit
CF	counterflow
CFM	cubic feet per minute
CHF	critical heat flux
CHP	combined heat and power
CRAC	computer room air conditioning
COP	coefficient of performance
CPU	central processing unit
DIMM	dual in-line memory module
EAC	equivalent annual cost
f	friction factor
F	correction factor
FCF	fin correction factor
GWP	global warming potential
h	heat transfer coefficient (W/m <sup>2</sup> -K), specific enthalpy (kJ/kg)
HCPV	high concentration photovoltaic
HEX	heat exchanger
HF	heat flux
HPC	high performance computing
HTC	heat transfer coefficient
i	interest rate
IHS	integrated heat spreader
ID	inner diameter (m)
IT	information technology
K	loss constant

k	thermal conductivity (W/m-K)
l, L	length (m)
$\dot{m}$	mass flow rate (kg/s)
MCHS	microchannel (or minichannel) heat sink
MED	multiple effect desalination
$\eta$	isentropic efficiency
N	number of entities
Nu	Nusselt Number
NTU	number of transfer units
OD	outer diameter (m)
ORC	organic Rankine cycle
P	pressure (Pa), power (W), heat exchanger correction factor parameter, present value
Pr	Prandtl Number
PUE	power use effectiveness
Q	volumetric flow rate (m <sup>3</sup> /s)
$\dot{Q}$	heat transfer rate (W)
q	heat flux (W/m <sup>2</sup> )
R	thermal resistance (K/W), heat exchanger correction factor parameter
$\rho$	Fluid Density (kg/m <sup>3</sup> )
Re	Reynolds Number
s	specific entropy (kJ/kg-K), spacing between channels (m)
S&T	shell and tube
SHEC	server heat extraction cycle
T	Temperature (°C, K)
t	thickness (m)
TDP	thermal design power
TEC	thermoelectric cooling module
TIM	thermal interfacing material
$\mu$	Dynamic viscosity (kg/m-s)
v	specific volume (m <sup>3</sup> /kg), Fluid Viscosity (kg/m-s), kinematic viscosity (m <sup>2</sup> /s)
$\dot{W}$	Power (W)
WPI	Worcester Polytechnic Institute
x	quality, displacement (m)

## Abstract

Modern digitalization has led to massive growth in data center (DC) electricity consumption—half of which is dedicated to IT equipment cooling. This project investigated the viability of an organic Rankine cycle (ORC) for DC waste heat recovery in terms of mechanical practicality, sustainability, and economic feasibility. A liquid cooling system for capturing CPU waste heat with microchannel heat sinks was designed with COMSOL simulation software. An integrated thermodynamic, fluid, and heat exchanger analysis was developed in MATLAB to fully characterize the ORC heat recovery system. The payback period of the optimized design was under 5 years, thereby enabling the DC to reduce energy demands, as well as generate revenue from its cooling.

# 1.0 Introduction

The United States is experiencing a significant growth in the number and size of data centers, which are buildings that house a large collection of computer systems for data storage, processing, and distribution [1]. Data centers require large amounts of power, wherein the largest facilities (known as “hyperscale” data centers) can have power demands greater than 100 MW [2]. Already, data centers account for more than 2% of the total electricity consumed in the United States [3]. In addition, the power demand from data centers is predicted to increase by 15-20% annually [4]. Nearly all of the electrical power supplied to the servers within the data center is converted to heat, thus requiring large-scale cooling to ensure the computer equipment is maintained within safe operating conditions (usually less than 85°C) [1]. The enormous and ever-growing power usage from major data enterprises has increased the need for low-grade heat recovery systems to utilize waste heat and improve cooling system efficiencies. Thus far, literature has identified organic Rankine cycles (ORCs) and absorption chillers as the two most promising systems for data center waste heat recovery [1].

The purpose of this project was to develop a practical, economical, and sustainable ORC waste heat recovery system that could be implemented in data centers. The system design and optimization was based on a small server room with a High Performance Computing (HPC) Cluster at Worcester Polytechnic Institute (WPI). The project consisted of two primary, integrated aspects: (1) a theoretically modeled and optimized ORC specified for the application at the WPI data center, and (2) specification and design of a cooling system for capturing and dissipating waste heat from computer equipment.

Specific goals and outcomes of the project included:

- Investigate liquid cooling to determine the most effective method, design, and materials for extracting heat from the servers (to transfer to the ORC) while maintaining the computer equipment within a safe operating range.
- Test and optimize the heat transfer between the cooling system and the IT equipment at the CPU level using simulation software.
- Design and optimize the ORC data center waste heat recovery system with respect to the thermodynamic processes, overall system efficiency, capital/operating costs, and environmental impact.
- Perform an engineering economic analysis to determine the economic practicality of the ORC waste heat recovery system and to compare against conventional data center cooling systems.
- Propose future investigations of optimal data center cooling technologies and further efforts to specify, evaluate, and optimize components of the waste heat recovery system.

## 2.0 Background

This section covers a variety of topics relevant to the development of an effective waste heat recovery system for data centers. The section begins with an overview of data centers, followed by a descriptive list of a number of potential systems and technologies that may be used in data centers for waste heat recovery. Then, a discussion is dedicated specifically to organic Rankine cycles to explain how the system works and to explore different working fluids that may be utilized. The last subsection describes three primary types of data center cooling systems, including air-cooling, liquid-cooling, and two-phase cooling. In addition, numerous examples of technologies within each type of cooling are also provided.

### 2.1 Data Centers

When it comes to general topics of energy consumption and conservation, the impact of data centers often goes unnoticed. Daily use of personal electronic devices does not typically allude to the extensive and complicated systems involved in data processing and storage. However, modern electronic devices and services correspond with significant power demands. In 2014, US data centers consumed 226 TW of electric power, half of which was required for server cooling processes [5]. A major factor that contributes to the high electricity usage of data centers is storage drives—generally classified as any type of hardware that stores data. Disk storage is a type of hardware which involves recording data by making electronic, magnetic, optical, or mechanical changes to the surface of rotating disks. Running many electronic network devices, which communicate and interact with other devices on a computer network, also results in continual electricity consumption. As network devices mediate data transmission, their influence will only become more prominent as the data sector expands, further increasing energy consumption.

The rapidly growing number of internet users over past decades has raised concerns in terms of data center energy demand, in addition to the increasing demand for storage capacity and network communications. The advancement of computer technologies has resulted in a dramatic growth of the data center industry, and the predicted increase in annual power demands is as high as 15-20% [4]. Altogether, the rise in internet users will correlate with data consumption. As a result, data consumption will have a considerable impact on the future of sourcing energy and electricity.

Another facet of the 21<sup>st</sup> century that impacts the future of data centers is company consolidation. Company consolidation is the merging and acquisition of many smaller companies into a few larger ones. In response to the tech giants that have grown as a result of company consolidation, hyperscale data center growth has tripled since the beginning of 2013 [6]. The rapid growth is highlighted in the graph presented in **Figure 1**. Hyperscale data centers house tens of thousands of servers, a great leap from the hundreds that are typically supported in a traditional data center [7]. At a minimum, hyperscale facilities contain 5,000 servers connected over an ultra-high speed network.

A hyperscale data center is operated by the company it supports, and has become a necessity of cloud and big data storage. Companies such as Microsoft, Google, and Amazon contribute to the most frequent openings of these centers, with the latter two accounting for over half of all new data centers

constructed in the past year alone [8]. Synergy Research Group collected information on hyperscale data center growth by analyzing 20 of the world’s major cloud and internet service firms, which confirmed a large portion of firms are located primarily in the US [8].

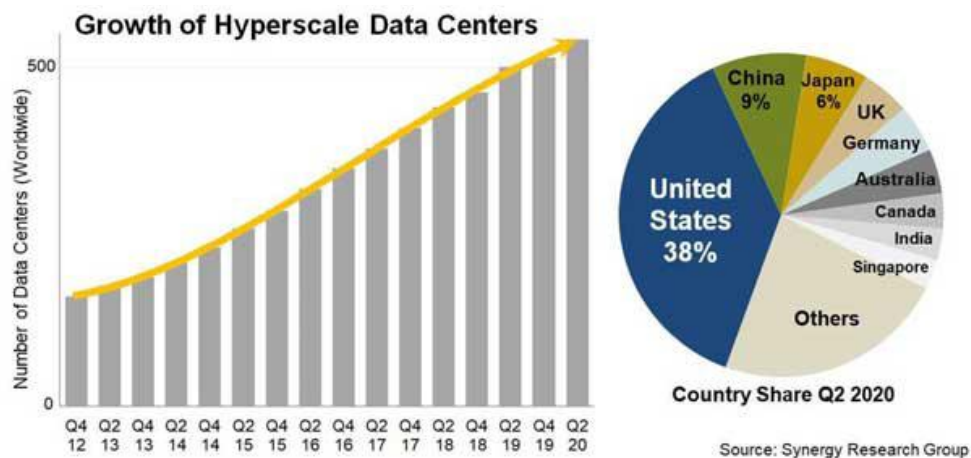


**Figure 1:** The Growth of Hyperscale Data Centers [8].

There is a smaller subset of data centers which includes (1) colocation, (2) enterprise, and (3) managed services data centers [9]. Colocation data centers consist of one data center owner who sells space to multiple enterprises and hyperscale companies in a specific location. Enterprise data centers are owned and operated by their respective companies. Likewise, managed services data centers are operated by a third party on the behalf of a company, who leases the equipment and services as opposed to buying it.

As data centers store, process, and secure data, they generate waste heat. The waste heat density is comparable to the power density of the system, as nearly all the power put into the system is given off as waste heat [1], [3]. Current projections for IT equipment anticipate that the power densities for advanced servers and communication devices may soon reach the range of 8-15 kW/m<sup>2</sup> [1]. The average power consumption for server racks in legacy (older) data centers is approximately 7 kW [1]. However, current high performance racks at full capacity typically consume 10-15 kW of power [1]. In the United States, the majority of data centers (approximately 2/3) utilize racks that consume 15 kW - 16 kW; some data centers average more than 20 kW per rack [10]. In a few specialized cases, a single rack may be filled with extreme density computer servers, resulting in a power consumption as high as 35 kW [1]. In all cases, higher rack powers are associated with the increased production of waste heat, which is more difficult to dissipate at higher densities.

Waste heat from servers has garnered increasing attention over the past couple decades, due to its potential to be recovered and repurposed. As predictions of data center power demand place the US consumption for 2020 at 73 billion kWh, advancements in waste heat recovery have the potential to change the trajectory of data center energy consumption [11].

## 2.2 Low-Grade Heat Recovery Systems

In response to the growth in the number and size of data centers in our technologically driven world, significant research has been conducted on various systems that may have potential in low-grade heat waste applications for data centers. Some show more promise than others, depending on the extent of technological development, scaling flexibility, as well as cultural practicality.

### *District Heating*

The waste heat produced by data centers can be used to provide district heating. However, it requires the replacement of large, centralized data centers with small-scale “micro-data centers,” wherein the heat produced by the localized data centers is utilized as a primary heating source for local residential and commercial buildings [1]. District heating is a well-established means for potential data center waste heat reutilization in Europe, but the practicality of such a system would face challenges in the United States, where district heating is not common [1]. While district heating reduces the cost of ownership for data center operators, the cost of electricity can be 10-50% higher than that of industrial areas. There is also a higher risk of maintenance issues, considering the geographical distribution of small-scale, local data centers, compared to conventional, centralized data centers [1].

### *Power Plant Co-Location*

Power plant co-location utilizes waste heat to reduce overall fossil fuel consumption. Used in conjunction with a two-phase data center cooling system, or even a standard liquid cooled system, power plant efficiency can be improved by upwards of 2.2% [1]. However, power plant co-location is most efficient with higher quality waste heat. Since data center waste heat is already low-grade, and due to the fact that the quality of heat degrades significantly as the heat transfer fluid travels over far distances, the data center would need to be located at the power plant site in order to make the process worthwhile [1].

### *Absorption Cooling*

Computer room air conditioning units (CRAC) are cooling units that utilize a vapor compression refrigeration cycle to keep computer rooms cool. By making some adjustments to the CRAC process, absorption cooling can become viable. Absorption cooling is similar to the vapor compression refrigeration cycle, except for that it most notably uses a liquid solution of an absorbent fluid and refrigerant, as opposed to a vapor [1]. Substantial power savings can be achieved with absorption cooling, as the liquid absorbent and refrigerant eliminate the need for a compressor, which consumes a significant amount of power in the vapor refrigeration process. The absorption cooling system also uses the data center waste heat directly as the absorption generator heat source [1]. Thus, absorption cooling lowers the energy (and costs) for running the CRAC in two ways: (1) through the capture and utilization of IT waste heat that otherwise would have been cooled by the CRAC unit and (2) through the reduced CRAC load enabled by the absorption cooling process. Furthermore, an absorption cooling system can be retrofitted in any existing liquid or two-phase cooled data center, as space allows. **Figure 2** shows a diagram of a simple absorption cooling process driven by data center waste heat [1].

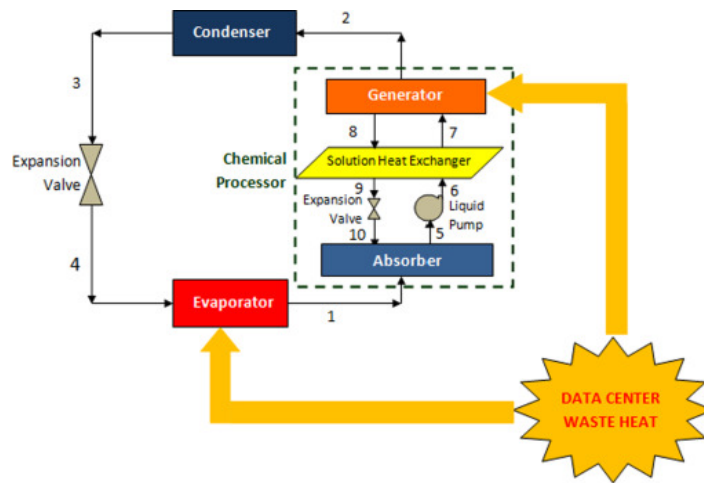


**Figure 2:** Absorption cooling process driven by data center waste heat [1].

Working fluids used in absorption cycles are a combination of a refrigerant and an absorbent. Absorption cycles can use a variety of working fluids, which are responsible for transferring force, motion, or various types of energy within the system. A working fluid transfers mechanical energy by the motion it undergoes during the cycle. Thermal energy, or heat, is also transferred to and from the fluid, making it a key component of the thermodynamic processes in a refrigeration cycle. Sun et al. divided absorption cycle working fluids into five groups based on the type of refrigerant used: (1)  $\text{NH}_3$ , (2)  $\text{H}_2\text{O}$ , (3) alcohol, (4) halogenated hydrocarbon, and (5) other [12]. To be considered viable in an absorption cycle, the working fluid needs to have low environmental impact, be non-corrosive, low-cost, and have a high heat of vaporization [12]. The  $\text{H}_2\text{O} + \text{NH}_3$  pair is common in absorption refrigeration since  $\text{H}_2\text{O}$  and  $\text{NH}_3$  are very stable across a wide range of operating temperatures. Furthermore, working fluids with  $\text{H}_2\text{O}$  as the refrigerant are favorable since  $\text{H}_2\text{O}$  has a high latent heat of vaporization. However, absorption cycles with  $\text{H}_2\text{O} + \text{LiBr}$  produce higher system efficiencies compared to cycles with  $\text{NH}_3$ . Working fluids with alcohol have a high thermal stability and high output temperature, but can have high toxicities and are more suitable at higher operating temperatures. Regarding HFCs, R21 shows a high Coefficient of Performance (COP) due to its high latent heat of vaporization, but it is corrosive to copper [12].

While the simple schematic in **Figure 2** depicts the general concept of absorption cooling, the actual system of interfacing loops is more intricate. In an example  $\text{H}_2\text{O} + \text{LiBr}$  system (illustrated in **Figure 3**), there are four primary loops that comprise the absorption chilling process:

- Cooling Tower: condenses the water and lithium bromide mixture in the absorber and condenses the water vapor in the condenser.
- Heat Exchanger: exchanges heat between the cooler weak concentration of LiBr (directed to the generator) and the heated strong concentration of LiBr (directed to the absorber).
- Chilled Water: supplies chilled water from air conditioning units containing waste heat to the evaporator, and returns the chilled water to the building at a lower temperature
- Hot Water/Steam: supplies heated water vapor or liquid (carrying IT waste heat) to the generator, which is transferred to the reservoir of the LiBr-water mix, whereby the water returns at a reduced temperature.

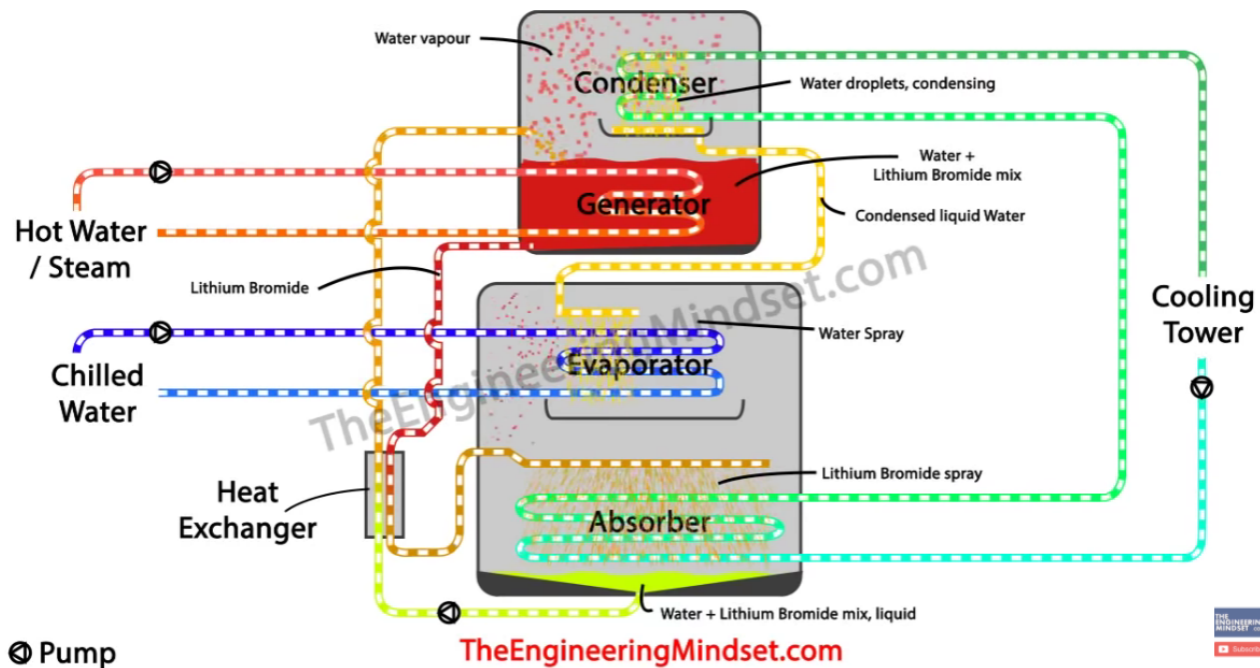


**Figure 3:** Absorption chiller schematic with various loops [13].

As depicted in **Figure 3**, absorption chillers consist of two main chambers and a heat exchanger (to efficiency of the system). The upper chamber consists of the condenser and the generator and the lower chamber consists of the evaporator and the absorber. From the bottom of the absorber, a LiBr-water mixture travels from the absorber, through a counterflow heat exchanger, to a generator via a weak solution line [13]. As the generator fills up with the mixture, a reservoir is created. A hot water line (typically containing the IT waste heat) provides heat to the generator, which causes the water and LiBr to separate. As the water particles evaporate and become steam, the heavy lithium bromide particles sink to the bottom of the reservoir and form a concentrated solution. This concentrated liquid flows back down along the weak solution line and passes through the heat exchanger [13]. Heat is transferred from the concentrated LiBr-water mix to the weak LiBr-water mix, cooling the concentrated mixture. The cooled LiBr mixture is then directed into the absorber, where it is sprayed into the chamber and mixed with the water, before being pumped back to the generator to repeat the loop.

Concurrently, water from a cooling tower is utilized to condense the evaporated water in the upper chamber, wherein the condensed droplets are caught in a collection tray. The condensed water is directed back to the lower chamber where it is sprayed into the evaporator. The evaporator, which is at a very low pressure (near vacuum conditions), causes the water to flash and drop to a very low temperature ( $\sim 4^{\circ}\text{C}$ ) [13]. A chilled water loop containing the heat from the air handling units, fan cooled units, or CRAC units then enters the evaporator in pipes and transfers all the unwanted heat from the building to the cold condensed water spray that forms a film on the pipes. Due to the low pressure of the lower chamber, the cold water spray evaporates upon gaining heat from the chilled water loop. The water vapor then combines with the LiBr spray in the absorber, whereby the strong chemical attraction between the two fluids causes the low pressure vacuum conditions in the chamber [13]. The cooling tower loop passes through the absorber to remove excess heat generated by the combination of water

and LiBr and to ensure that the LiBr-water mix condenses back into a liquid at the bottom of the absorber to repeat the entire cycle [13].

The potential for waste heat recovery in data centers through the use of absorption cooling has been explored in research studies. Haywood et al. modeled a 10-ton LiBr + H<sub>2</sub>O absorption refrigeration cycle that required a minimum heat input of 14.1 kW at 70°C from the data center [14]. It was estimated that if 85% of the heat dissipated from the central processing units (CPUs) was captured and efficiently transported to the chiller, the data center could have a Power Usage Effectiveness (PUE) of 1.16 [14]. (An ideal PUE is at or slightly above 1.0. At 1.0, every kW of energy used by the data center goes towards the IT equipment, and is indicative of a highly efficient system.) With the 14.1 kW at 70°C heat input from the data center, the maximum COP was 0.62 [1]. However, it was also found that if the generator temperature was set at 80°C, the COP of the system was capable of reaching a maximum value of 0.86 [1]. The primary challenge for viable absorption cooling systems is capturing high enough waste heat temperatures from the IT equipment, and subsequently transporting the heat effectively to the absorption cooler generator [1]. It was found that a liquid cooling system composed of water and cold plates was capable of capturing 85% of waste heat from the CPUs, and could provide a sufficient heat input to the generator [14]. Overall, the performance of the absorption cooling system depends significantly on the temperature of the waste heat, and therefore is not economically viable in data centers with lower quality waste heat (e.g. air cooled data centers) [1].

Chiriac et al. developed a model of a system to cool data centers with a combination of LiBr + H<sub>2</sub>O absorption chillers and thermal energy from renewable sources [15]. An alternative heat source, such as solar, supplemented the data center waste heat when the energy from the data center was not sufficient to activate the chiller. The system used liquid cooling and a refrigerant to extract the heat from the data center (shown in **Figure 4**). A heat exchanger was used to transfer the data center waste heat to water, which entered the absorption chiller at approximately 75°C [15]. The researchers estimated that the system could reach a coefficient of performance (COP) of 0.6. (COP is the ratio of the useful heating/cooling provided to the work/energy required, where higher COPs correspond to higher efficiencies, less energy consumption, and lower operating costs.)

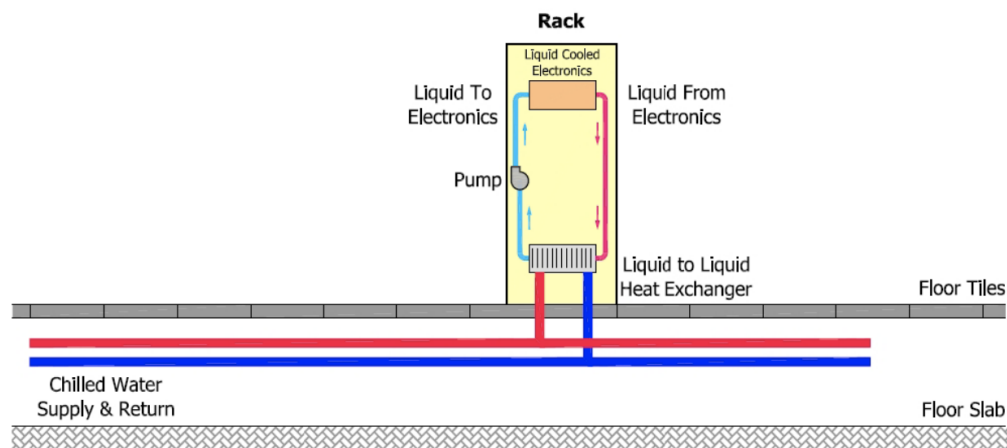


**Figure 4:** Internal liquid cooling of a server rack [15].

An alternative application of absorption cooling is the combined heat and power (CHP) process, in the cases where the data center has on-site power generation. CHP provides both electric power and cooling for the data center since the waste heat from the power cycle can be used in an absorption refrigeration cycle to chill water [1]. Thus, CHP systems can enable significant energy reductions to be made as no additional energy is required to provide data center cooling. Consequently, energy-related costs can be primarily limited to the electrical energy required to power the IT equipment.

### *Piezoelectrics*

Piezoelectric generation can convert turbulent oscillations into electricity, and can be utilized as a means for waste heat recovery for data center air cooling. The crystalline materials in piezoelectrics produce an electric charge when subjected to mechanical stress and/or strain, and are useful at waste heat streams of 100–150°C. Placement near CRAC air supply systems allows for a direct conversion of kinetic to electrical energy, as they capture the oscillating frequencies induced by turbulence in the CRAC air flow [1]. Although the power produced by piezoelectric would be small (mW), they may be useful for providing localized power to fans or lighting [1]. However, the location constraint makes piezoelectrics impractical in many data centers, and, in addition to long-term durability issues, low efficiencies (~1%) and significantly high costs (\$10,000/W), they were not recommended for future study in data center applications [1].

### *Thermoelectrics*

Thermoelectric cooling modules (TECs) operate by the Seebeck effect, which states that a voltage is induced when two materials with different conduction band energy levels are subjected to a temperature difference, and vice versa. For the purposes of waste heat recovery, if the TEC can be exposed to a significant temperature difference, it can be used to create a voltage, and subsequently, electricity. In such cases, the ‘hot side’ of the TEC is coupled to the waste heat source, wherein the energy absorbed at the junction induces an electrical flow [1]. Via thermoelectric generation, thermal energy can be converted directly into electrical energy. However, the technology does require that the thermoelectric device be closely coupled to the chip in order for sufficient energy capture to occur.

While thermoelectrics are applicable in advanced two-phase flow cooling systems, where waste heat temperatures can be in the range of 80–175°C, their high costs have hindered widespread use [1]. Thermoelectrics will need to reach \$5/Watt, as opposed to current estimates around \$30/Watt, in order for thermoelectric technology to compete with simply purchasing electricity. Cost, in addition to low efficiencies (2% to 5%), have made their implementation in data centers a challenge. Even with recent advances that have increased conversion efficiencies, defined as the ratio of the electrical energy produced to the waste heat energy absorbed, thermoelectrics likely require many years of development before their implementation in data centers is economically or technologically practical.

## Desalination/Clean Water Production

The desalination process allows data center waste heat to be repurposed for distillation, enabling clean water production from seawater – also known as multiple effect desalination (MED). **Figure 5** demonstrates a theoretical three stage desalination system, wherein heat from a steam boiler is used to drive the desalination stages.

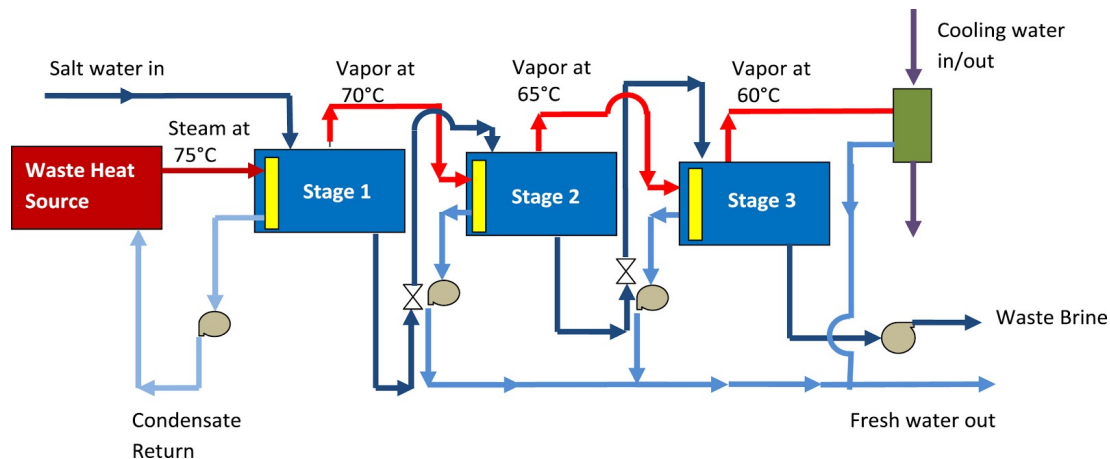


**Figure 5:** A three stage MED with the first stage energized by data center waste heat [1].

Waste heat from the data center is used to boil water, creating steam, which is used as the heat source to boil salt water. Waste heat temperatures must be 75°C or higher for the process to be worthwhile, which makes it a potential option for data centers with two-phase flow cooling systems and some water cooling systems [1]. The quality of waste heat is important since outlet steam from each stage is used as the heat source for the next stage (at incrementally lower temperatures as a result of heat transfer from the steam to the salt water during each stage) [1]. Iterations of heat exchange from the steam to boil salt water continue over each stage until the quality of heat of the steam is too low for use [1]. Increasing the number of stages does reduce overall energy consumption, but capital and operating costs also increase as a consequence. The number of stages in typical MED systems may range from 4 to 21 stages. The primary obstacles that face the deployment of MED systems for data center waste heat recovery are (1) the lack of application for air cooled centers, and (2) the fact that most data centers do not have a particular need for producing masses of clean water on-site.

## Biomass Co-Location

Data centers located at a biomass production site have the potential for on-site power and revenue streams since its waste heat can be used in numerous ways within the processes for generating energy or renewable fuels from organic plant or animal material [1]. The burning of dried-out plant materials can be used as the heat source to generate steam in a power cycle, thereby producing electricity for the data center on-site [1]. The waste heat from the data center is useful for a biomass-steam power cycle since the temperatures required to dry out the plant material can be as low as 45°C, and the best efficiencies for biomass drying occur above 60°C [1]. Alternatively, data center waste heat can be used in anaerobic digestion processes, which consist of breaking down organic matter in an oxygen-free environment to produce biogas containing 60-70% methane [1]. Data center waste heat above 60°C can be utilized to

either limit moisture in the biowaste before anaerobic digestion or to maintain the elevated temperatures within the anaerobic digestion reactor [1]. The product methane can subsequently be used for heating, cooling, or power production [1].

Thus, biomass co-location can enable the production of on-site renewable energy/fuels which can reduce energy costs or provide revenue streams for the data center [1]. However, air cooled data centers cannot be used for this application and it is difficult to retrofit biomass systems into most existing liquid cooled data centers [1]. Additionally, the data centers must be located very close to the biomass power plant to minimize degradation of the waste heat degradation through transportation [1].

### *Organic Rankine Cycle*

One of the systems that has shown the most promise for data center waste heat recovery is the organic Rankine cycle (ORC). An ORC fundamentally consists of an evaporator, turbine, condenser, and pump, whereby a working fluid is used to transfer energy throughout the cycle to ultimately produce an electrical output. ORCs use refrigerants or volatile organic liquids as the working fluid, instead of water as in steam Rankine cycles. Since organic working fluids have lower boiling points, they can enable energy recovery from low temperature waste heat sources [16]. The slope of the vapor-saturation curve in the temperature-entropy (T-s) diagram of the selected organic fluid is indicative of how efficiently the ORC will perform. (Organic fluid types are discussed further in section 2.3.2.) The thermal efficiency of an ORC depends both on the thermodynamic properties of the working fluid and operating conditions of the cycle. ORCs operate most successfully with waste heat temperatures that are 65°C or higher, though optimal conditions are dependent on the precise organic working fluid used. As a low-temperature cycle, the operating efficiencies are inherently lower than that of a higher temperature system, typically in the range of 5% to 20% [1]. Despite lower efficiencies, it is important to note that the actual observed ORC efficiency is often very close to the theoretical maximum Carnot efficiency for the same temperature range, indicating that ORCs are a promising solution for recovering data center waste heat.

Over the past thirty years, ORCs have been adopted and developed in a growing number of low-grade waste heat applications to generate power. Recent studies have demonstrated that an ORC can be considered a viable, effective solution for the recovery of low-quality waste heat from data centers due to its versatility, high margins of safety, minimal maintenance, and potential for good thermal performance [16]. ORCs enable both the possibility for on-site electricity generation and significant reductions to costs related to cooling, without additional conditions or constraints which are present in other potential heat recovery systems (e.g. division into localized “micro data centers,” site-specific requirements, proximity to other production facilities, etc). For the reasons listed above, the ORC is a particular system of interest for future study in data center waste heat recovery applications.

## **2.3 Organic Rankine Cycles**

Organic Rankine cycles have been identified as a promising system for recovering low-grade waste heat from data centers. In this section, the ORC system and its components are investigated in more detail. In

addition, the available research regarding the performance of different organic fluids and the effects of different ORC operating conditions are also discussed.

### 2.3.1 ORC Breakdown By Components

The simple organic Rankine cycle is composed of four main components: an evaporator, a turbine, a condenser, and a pump, which are connected by pipes in a closed loop. Point 1 in **Figure 6** indicates the evaporator (also referred to as the boiler), where the working fluid evaporates due to the transfer of thermal energy from the heat source [17]. The evaporated working fluid (i.e. vapor) flows through the turbine at Point 3, causing the blades of the turbine to spin as the pressure and temperature of the fluid drop. The turbine shaft is coupled to a generator (Point 4), which produces electricity. At Point 5, the vapor condenses to a liquid in the condenser. The pump at Point 7 pressurizes the system to drive the working fluid throughout the ORC, ultimately back to the evaporator. An ORC may also include a superheater after the evaporator (theoretically at Point 2) to ensure a higher quality vapor at the turbine inlet (which is often necessary when the working fluid is a wet organic fluid) [1].

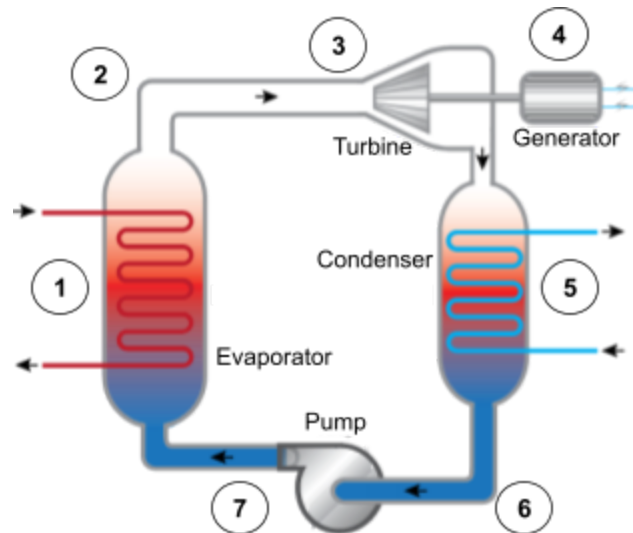


**Figure 6:** A simplified schematic of an organic Rankine cycle [17].

ORCs can be used in a variety of applications at the industrial scale, as well as the microscale, where power outputs typically range from 1 kW to 5 kW [1], [18]. For example, Zhang and Wang developed a microscale ORC that used the waste heat from High Concentration Photovoltaic (HCPV) [19]. The microscale ORC replaced the HCPV's liquid cooling system and was able to produce an 8.8% increase in power generation efficiency. A similarly small-scale ORC design can be applied to data center cooling whereby the scale can be tailored to the thermal and fluid characteristics of the waste heat stream. The size and capabilities of the ORC can be manipulated as they mainly depend on the selection of the four main components as shown in **Figure 6**.

### 2.3.2 ORC Working Fluids

The most significant challenge associated with the utilization of ORCs for low-grade waste heat recovery is the inherently low thermal efficiency (modeling in research has produced efficiencies

between 2% and 8%) [20]. There are two primary factors that affect the thermal efficiency of the ORC: (1) the working fluid and (2) the ORC operating conditions. To start, there are three different classes of working fluids: wet, isentropic, and dry. These fluids are characterized by the slope of their curve in the saturation region of a T-s diagram (see **Figure 7**) [3]. Wet fluids have a positive saturation vapor curve and are prone to condensation during the expansion process in the turbine [3]. To avoid damaging the turbine when using wet fluids, superheaters are often utilized to ensure the fluid is fully vaporized [3]. Isentropic fluids have near-vertical slopes in the saturation region and dry fluids have negative saturation curves [3].

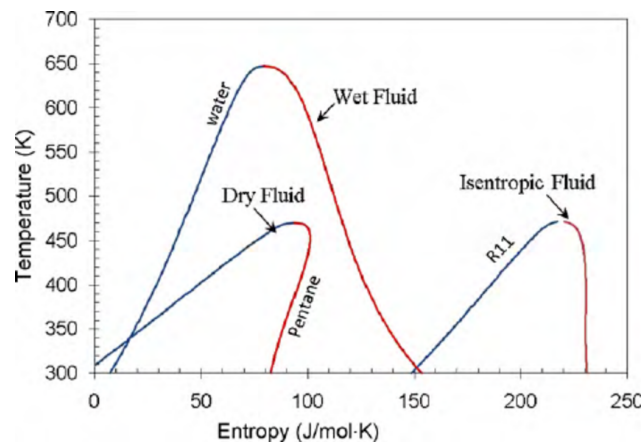


**Figure 7:** T-s Diagram with wet, isentropic, and dry working fluids [21].

Neither isentropic nor dry fluids produce fluid condensation during expansion through the turbine and thus do not require the addition of a superheating process. From an overall-system perspective, superheaters are in fact disadvantageous because of their power draw. Therefore, isentropic and dry fluids are typically preferred for ORC applications.

The thermodynamic properties of the working fluid in an ORC have strong effects on the overall efficiency and performance of the system [3]. Working fluid choice in ORCs has been investigated in a number of studies. In a study that explored the application of ORCs for recovering heat from engine exhaust gas, a computational model was utilized to evaluate the thermodynamic performance of nine different fluids [22]. R11, R141b, R113 and R123 produced the best results, and R245fa and R245ca were identified as the most promising for low environmental impact [22]. A study by Sadeghi et al. explored the use of zeotropic fluid mixtures in ORCs and determined that careful selection of the zeotropic composition can result in improved ORC performance [23].

Finally, Ebrahimi et al. developed a thermodynamic model using MATLAB and the REFPROP subroutine program to analyze the effect of four different working fluids on the performance of a dual loop ORC for data center applications [3]. The researchers determined that the optimum fluid choices for the server coolant loop and ORC were R134a and R245fa [3]. However, the researchers also noted that R134a and R245fa are moderate greenhouse gases with Global Warming Potentials (GWP) of 1300 and 950, respectively [3]. Presently, R134a and R245fa are considered environmentally friendly alternatives to R12, which was phased out because of its high ozone depletion potential [3]. Ebrahimi et

al. considered the environmental factors for working fluid selection and investigated the potential of R1234ze, which has a GWP of 1 [3]. In their analyses, the use of R1234ze only produced slight drops in efficiency (4.7% to 4.1%) and thus was suggested that it may be a viable swap-out for R134a and/or R245fa [3].

### 2.3.3 ORC Operating Conditions

In addition to the working fluid, the performance and thermal efficiency of the ORC is significantly affected by the operating conditions. In their 2017 study, Ebrahimi et al. utilized a steady-state thermodynamic model to examine a series of operating conditions and their effects on the overall performance of the ORC system [3]. Their model of a dual loop system consisted of an ORC loop and a two-phase chip cooling loop, which supplied waste heat to the ORC via the intermediate heat exchanger. A schematic of the system is shown in **Figure 8** [3].

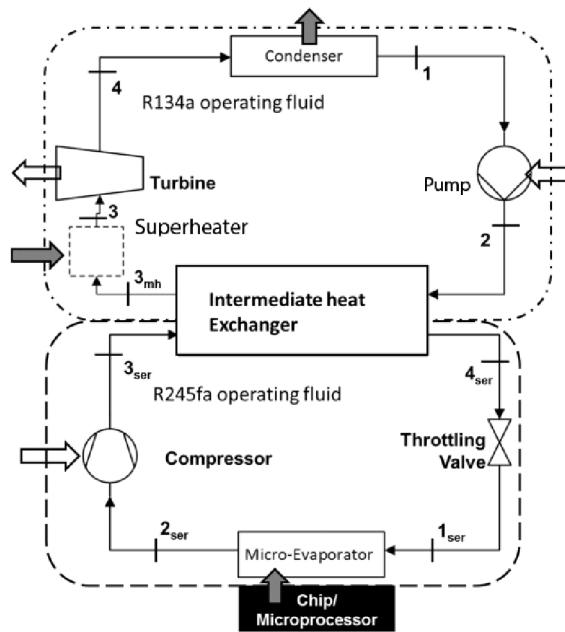


**Figure 8:** Dual-loop data center ORC system schematic [3].

The user-defined inputs to the thermodynamic model included: working fluids, waste heat input, evaporator pressure, turbine inlet temperature, pump efficiency, and turbine efficiency [3]. The thermodynamic model subsequently calculated outputs that included: mass flowrate of the working fluids, power generated by expander/turbine, pump power, heat transfer rate at the superheater (if used), heat transfer rate at the condenser, first and second law thermal efficiencies, and exergy destruction in the cycle [3]. In the study, the effects of four major aspects of the operating conditions were evaluated in terms of the overall system performance: (1) the effect of superheating, (2) the effect of the micro-evaporator temperature, (3) the effect of temperature in the intermediate heat exchanger, and (4) the effect of the condenser temperature.

The analyses provided by Ebrahimi et al. were derived from an operating situation wherein R134a and R245fa were designated as the ORC working fluid and chip loop coolant, respectively. Furthermore, the operating conditions for their parametric analysis assumed a heat load of 162.5 W (heat flux of 65 W/cm<sup>2</sup>) at the micro-evaporator, a micro-evaporator temperature of 60°C, a server coolant temperature of 90°C at the inlet of the intermediate heat exchanger, an ORC fluid temperature of 20°C at the outlet of the condenser, and a pump and turbine efficiency of 85% and 80%, respectively. The researchers also assumed the chip could operate at its maximum allowable temperature of 85°C and the minimum temperature difference between the micro-evaporator and the chip was 5°C.

Superheating in the ORC had a negative effect on the overall system COP. However, superheating is required if the vapor quality at the outlet of the heat exchanger is less than 1 to avoid damaging the turbine during expansion [3]. If the quality dropped to less than 0.93, the superheater consumed 35% of the total power consumption of the system, which subsequently reduced the first law efficiency from 4.5% to 0%, the 2nd law efficiency from 21.1% to 1.8%, and the COP from 1.48 to 1.0 (for the operating situation described above) [3]. Superheating may also be used to increase the output from the turbine due to the enthalpy increase, but the total power consumption of the system also increases, which decreases the COP [3]. In any case, introducing a superheater negatively affected the overall performance of the system [3]. Rather, the optimal performance of the system can be achieved in cases where the working fluid exits the intermediate heat exchanger as a saturated vapor, which does not require the subsequent use of a superheater [3].

The micro-evaporator temperature has a significant effect on the thermodynamic performance of the system. Using two-phase cooling, the temperature of the coolant at the outlet of the micro-evaporator could be as high as 80°C [3]. The effect of micro-evaporator temperature on the overall performance is shown in **Figure 9**, (while the temperature of the R245fa coolant at the inlet of the intermediate heat exchanger and the ORC fluid at the outlet of the condenser was kept constant, at 90°C and 20°C respectively) [3].

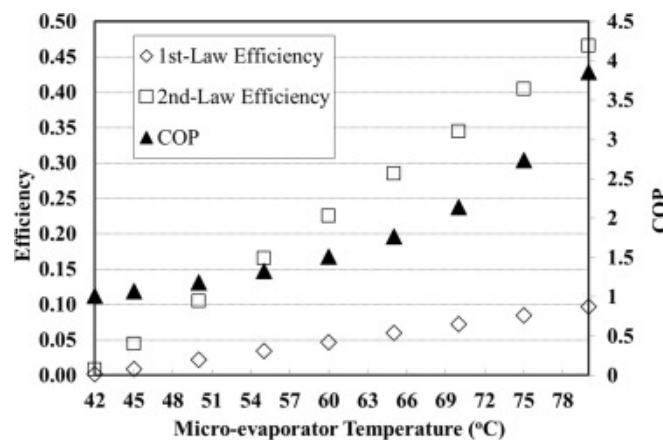


**Figure 9:** Effect of micro-evaporator temperature on system performance [3].

Over the increase of the micro-evaporator temperature from 42°C to 80°C, as indicated by the bottom horizontal axis, first law efficiency, second law efficiency, and COP all experienced a significant

increase. COP, as indicated by the right vertical axis, increased by a factor of 2.8 [3]. First law efficiency increased from about zero to 10%, while second law increased from zero to nearly 50% [3]. Therefore, it can be concluded that it is advisable to operate the chip cooling system at elevated temperatures (near 80°C) as long as it does not compromise the operability of the computing equipment.

The temperature of the waste heat affects the heat transfer in the intermediate heat exchanger, which has a profound impact on the thermodynamic performance of the system. The coolant (R245fa) in the chip cooling loop was initially specified at boiling temperature [3]. Within the micro-evaporator, the two-phase fluid was responsible for dissipating the heat generated by the chip, followed by additional heating of the fluid via a compressor placed after the micro-evaporator (see **Figure 8**) [3]. The performance of the system depended on both the micro-evaporator temperature and compressor heat upgrade [3]. Ebrahimi et al. determined the range of upgrade temperatures (90°C - 100°C) using a second law analysis and the critical temperature of the coolant. Four different micro-evaporator temperatures (60°C, 65°C, 70°C, and 75°C) over the range of upgrade temperatures were evaluated in terms of first law efficiency, as shown by **Figure 10** [3].

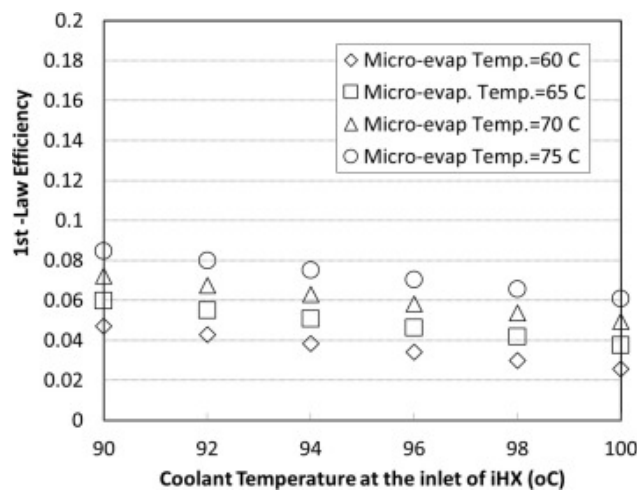


**Figure 10:** Effect of waste heat quality on system performance [3].

Because the compressor consumed significant amounts of additional power, upgrading the heat quality via the compressor reduced the overall system efficiency [3]. Therefore, it can be concluded that the chip cooling system should be operated at a temperature as high as possible (without causing damage to the electronics), and the additional heat provided to the fluid via a compressor should be limited due to the associated power draws [3].

Lastly, the temperature of the ORC working fluid at the outlet of the condenser also has a considerable impact on the overall system performance. By lowering the condenser exit temperature, the efficiency of the system can be increased [3]. The effect of adjusting the condenser exit temperature (from 5°C to 25°C) is shown in **Figure 11** in terms of the first and second law efficiencies. In addition to the efficiencies, the performance of the system was also put in terms of the number of servers (or racks) that were needed to provide enough waste heat to the ORC to generate the amount of power needed to

operate another server (or rack) of the same type [3]. This metric is presented along the right vertical axis in **Figure 11**. The analysis held the temperatures of the coolant at the micro-evaporator and the inlet of the intermediate heat exchanger constant at 75°C and 90°C, respectively [3]. Additionally, the turbine inlet pressure was specified at 1006 kPa [3].

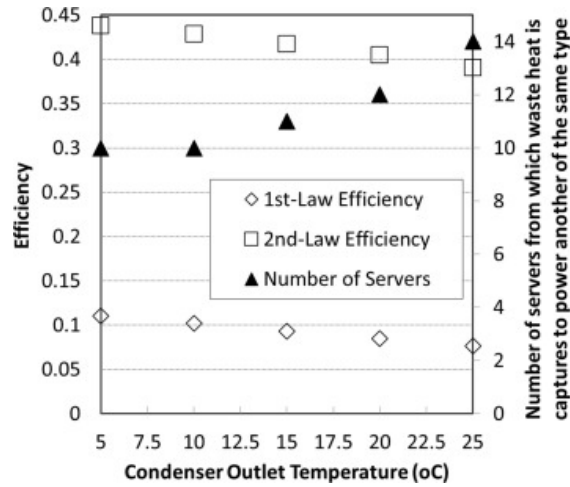


**Figure 11:** Effect of condenser outlet temperature on system performance [3].

When the condenser outlet temperature was lowered to approximately 5°C the first and second law efficiencies could reach 11% and 44%, respectively [3]. In such a case, only 10 servers (or racks) were required to generate enough waste heat to power another of the same type [3].

In addition, the results produced by a 2018 experimental ORC prototype from Araya et al. both confirmed and expanded upon the model-based results from Ebrahimi et al. [3], [20]. Concurrently, Araya et al. determined that higher waste heat temperatures resulted in greater electrical outputs from the ORC [20]. As the server waste heat temperature was elevated from 60°C to 85°C, the Carnot efficiency increased 8.11% and the expander mechanical power increased by 11.94% [20].

The experimental study from Araya et al. also explored other operating conditions that affected the performance of the ORC and its components. In the ORC prototype, an A/C scroll compressor was operated in reverse as the volumetric expander by removing the internal check valve in the discharge compartment. Generally, an expander performs best when the pressure ratio of the system is the same as the expander's manufactured internal pressure ratio [20]. At higher pressure ratios ( $P_r = P_{\text{suction}} / P_{\text{discharge}}$ ), the expander isentropic efficiency decreases due to under-expansion in the expander when the internal pressure ratio of the expander is lower than that of the system [20]. The researchers found that by increasing the temperature of the chilled water at the condenser exit, the saturation temperature of the condensing refrigerant increased, which also decreased the pressure ratio in the expander, thereby increasing the isentropic efficiency of the expander [20]. Alternatively, an expander with a greater built-in pressure ratio can be utilized to achieve better agreement with the system pressure ratio. As a result, the thermal efficiency of the overall system can be improved [20].

## 2.4 Data Center Cooling Technologies

As with any powerful piece of computer hardware, the computer components in a server generate heat while under operation. The Central Processing Unit (CPU)—the principal component of computing systems—requires cooling (i.e. effective heat transfer) to ensure the component is maintained at safe operating temperatures between 60°C and 85°C [24]. Although CPU sizes can vary depending on the model and manufacturer, a typical CPU will have dimensions of approximately 3.75 cm × 3.75 cm and a thickness between 0.5 cm and 1.5 cm [25]. The term CPU actually references “a package” containing a combination of multiple components.

The most important component of the CPU package is the silicon wafer (of approximately 99.999999% purity) that is made into the CPU die [26]. A CPU die is manufactured with the circuitry that performs all of the tasks of a CPU in a computer (e.g. processing inputs, storing data, and outputting results from other computer components) [27]. Although new generations of CPUs can have multiple CPU dies, the silicon wafers are connected to an integrated circuit and take up approximately 20% of the surface area of the CPU [28]. Since high heat can damage electronic components, the remaining 80% of the surface area is often devoted to a heat-spreader denoted as an Integrated Heat Spreader (IHS) [28]. The IHS dissipates the heat generated by the CPU while under operation [28]. Since the purpose of the IHS is to dissipate heat, IHS materials have high thermal conductivities. The industry standard is often a copper alloy or a copper alloy plated in nickel [28].

When installed, the IHS always faces away from the motherboard (primary circuit board of a computer), and the input and output pins on the bottom of the CPU connect to the circuitry of the motherboard [28]. Thermal Interfacing material (TIM) is also integrated inside the CPU package (bottom of the IHS) to help dissipate heat. In addition to the CPU, other components of the computer also need to be properly cooled to ensure optimal performance. Although each server system will vary, it is typical for the Dual in-Line Memory Module (DIMM)—additional computer memory mounted onto the motherboard, also referred to as RAM—to be maintained at temperatures no higher than 85°C [1]. Different motherboards will have various DIMM slots, but they typically range in number from 4-8 [29]. Lastly, there is another temperature limit for disk drives (due to operation), which must be maintained at temperatures below 45°C [1]. The main components of a CPU are illustrated in **Figure 12**.

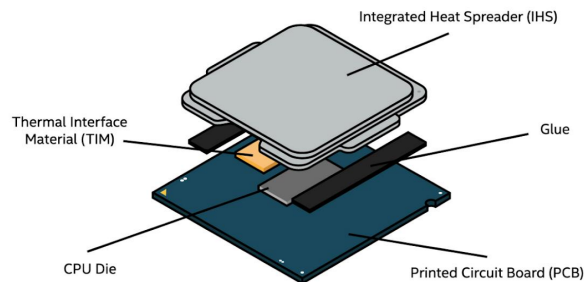


**Figure 12:** Exploded view of the components that make up a CPU package [24].

Ultimately, optimal computing systems require the optimal cooling of components. Furthermore, cooling systems emphasize heat transfer from the CPU which is the primary heat generator inside a computer. Air and liquid cooling are governed by the same operating principles: heat is absorbed via the IHS and is transferred from the hardware directly underneath it [24]. The essential difference between air and liquid cooling is the medium through which the heat from the CPU is dissipated. As the need for higher power and higher density data centers increase, so will the demand for optimized data center cooling methods.

### 2.4.1 Air Cooling

Traditional cooling of hardware in data centers consisted of air cooling, which included localized air cooling of the heat generating server components (e.g. CPU) as well as broader air cooling of the rows of server racks within the data center. At the CPU level, an air-cooler (i.e. heat sink) mounted on the CPU typically consists of many thin, rectangular heat fins that are cooled by forced convection of air induced by a fan. **Figure 13** illustrates the heat sink, consisting of many thin, vertically aligned fins, positioned on top of the CPU. A layer of thermal paste (also known as a thermal interface material, or TIM) is applied on top of the CPU IHS where it makes contact with the baseplate of the CPU heatsink. The material of the heat sink is often made of aluminum or copper, which are both powerful conductors of heat [24]. Also shown near the top left corner in **Figure 13** are four small black fans, responsible for forcing air into the server tray and through the heat sink to dissipate heat from the fins.

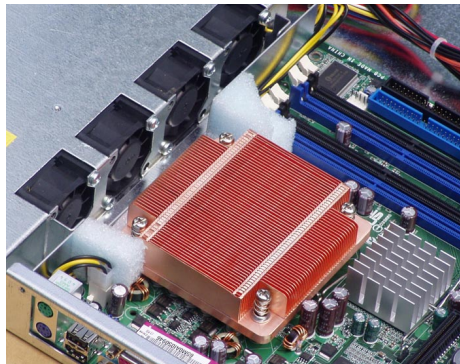


**Figure 13:** CPU air-cooler inside a server with fans [30].

During operation, heat generated by the CPU is transferred to the baseplate of the heat sink and up through the fins. Cool air flowing through the fins (due to fans) dissipates the collected heat within the fins via forced convection. A depiction of air flowing through a server tray (from left to right) is presented in **Figure 14**. Blue arrows on the left indicate the cool air at the inlet, which increases in temperature over the length of the server tray as a result of convective heat transfer between the air and the heat generating components. At the outlet (right end of the server), the air is at a much higher temperature, indicated by the red arrows.

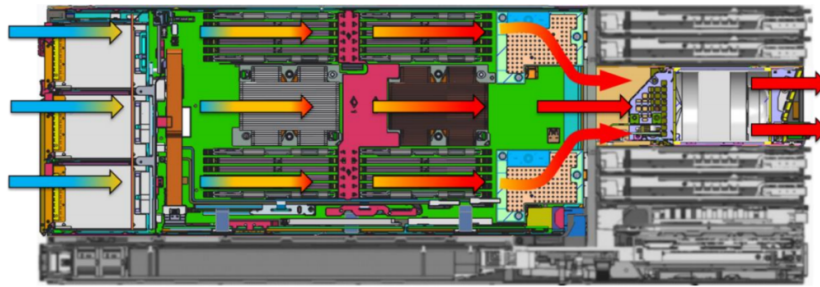


**Figure 14:** Dell MX7000 airflow [31].

For rack level cooling, Khalaj et al. described that current state-of-the-art data centers utilize housing racks for their servers which are arranged into rows and partitioned by aisles of either cold air intake or hot exhaust air (colloquially known as “hot aisle/cold aisle”) [32]. The cold air intake cools the heated components inside the server via forced convection and the hot air at the outlet of the server is expelled into the hot exhaust aisle. It is common for air cooled data centers to redirect the hot exhaust into a ventilation system where the exhaust is cooled via cooling coils connected to a water and air cooled chiller—commonly denoted as a “Chilled Water System” [33]. Alternatively, computer room air conditioning (CRAC) units may utilize a vapor compression refrigeration cycle to cool the hot exhaust air from the servers.

The hot aisle/cold aisle arrangement is typically utilized in a long-distance air cooling system [34]. Long-distance cooling systems are composed of CRAC units and air delivery ducts in the server room, in which a raised floor configuration is typically used, as shown in **Figure 15** [34]. The perforated floor tiles, combined with an overhead air supply system, are utilized to move chilled air toward the computer racks from CRAC units [34]. The chilled air enters the cold aisles from the floor or ceiling, and then flows into the server racks [34]. The outflows of heated air from the server racks are directed to the hot aisles, which circulate back to the CRAC, and the cycle continues [34]. Short-distance cooling circulates air within a closer proximity to the computer racks [34]. In such cases, the CRAC unit is placed nearby or even inside the server racks to force air circulation [34]. Recent research efforts have aimed to address overall data center airflow management, and how data center layouts can be optimized for these processes [34].

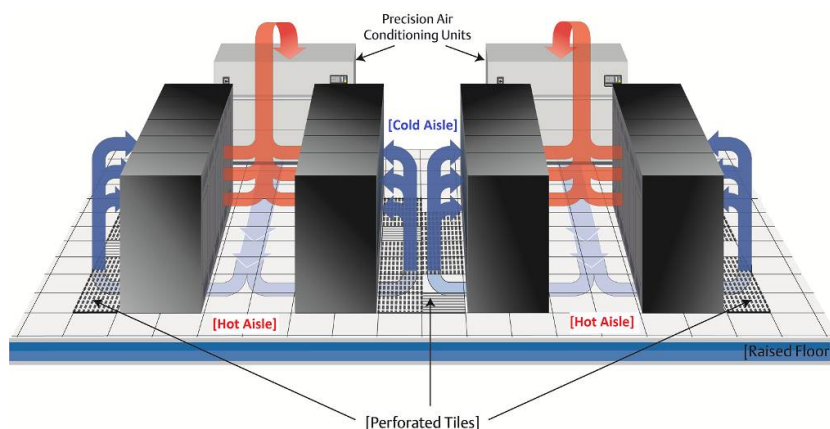


**Figure 15:** Hot aisle/cold aisle airway configuration [34].

Khalaj et al. further discussed the inefficiencies of rack level air cooling, which are primarily due to the low heat transfer coefficient of air [32]. Furthermore, the dissipated heat from operating server components can “intermingle with the supplied cold air causing localized hot spots around and inside the [server] racks” when data centers lack appropriate airflow control systems [32]. Hot-spots are problematic because they are combated by over-cooling the data center, and even so, some servers may still not receive sufficient cooling [32]. Additionally, the equipment required to ventilate the heated air consumes a large sum of power, which is an inefficient use of energy as the data center must keep the CRAC refrigeration cycle active at all times of operation [32]. As a potential solution, Khalaj et al. suggested that, since CPUs are made with a benchmarked voltage and frequency, controlling the frequency of the CPUs could effectively maintain core temperatures, thereby enabling energy savings while minimizing the timing penalties of CPU operations [32]. Although air cooling technology continues to improve, the effectiveness of the process is still limited by fundamental problems, as it is characterized by high energy usage and costly air-conditioning systems. Hot aisle/cold aisle systems typically produce PUEs varying from 1.7 to 2.1, which are high compared to other methods of cooling, such as liquid cooling, discussed below [35].

## 2.4.2 Liquid Cooling

In liquid cooling, a layer of thermal paste (i.e. TIM) is applied on top of the Integrated Heat Spreader (IHS) where contact is made with the baseplate of a liquid plate heat exchanger (also called a cold plate or waterblock). The waterblock is designed to allow cooled coolant to flow in, whereby the transfer of heat from the CPU to the coolant heats the coolant, which is then directed out. The coolant circulated through the waterblock can vary. Certain liquid cooling systems use distilled water, which is recommended over undistilled water which can contain contaminants that may cloud the water and cause clogs within the tubing/piping of the system. Anti-microbial and anti-corrosion additives are sometimes mixed with the water to prevent bacterial growth or corrosion inside piping [36]. Refrigerants and dielectric fluids are also recommended coolants since they may have some thermophysical properties, such as low boiling points, which may be favorable in some applications [35]. The hardware in a liquid cooling process can vary by design, but each employs the same principles of heat transfer. A widely available liquid cooling option is called “All-in-One” cooling (AIO). An AIO cooler is shown in **Figure 16**.

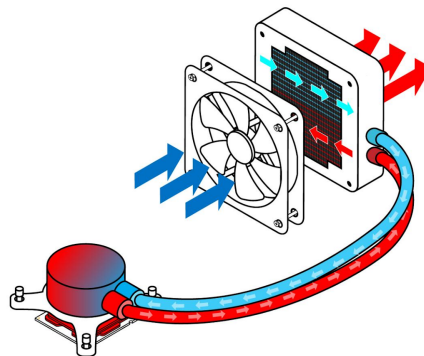


**Figure 16:** AIO cooler [24].

In an AIO cooler, heat from the CPU is transferred into the baseplate of the waterblock and into the coolant. The coolant is pumped into a radiator where it is subjected to forced convection by a fan. As the coolant travels through the radiator, heat from the coolant is dissipated by the air, providing a cooling effect. The cooled coolant at the exit of the radiator is circulated back to the CPU and waterblock where the cooling cycle repeats. At the data center scale, a similar process for a liquid cooling system is evoked. However, rather than an AIO design, the coolant from a series of waterblocks (from multiple servers trays or racks) may be joined and collectively cooled by a large radiator, as opposed to small, localized radiators within each server tray. A detailed diagram of an actual liquid cooled server is shown in **Figure 17**. The DIMM and CPU are the most relevant heat-generating components to consider for liquid cooling, as alluded to in section 2.4. (Additional extraneous labels of the server IT equipment are provided in the figure for context.)

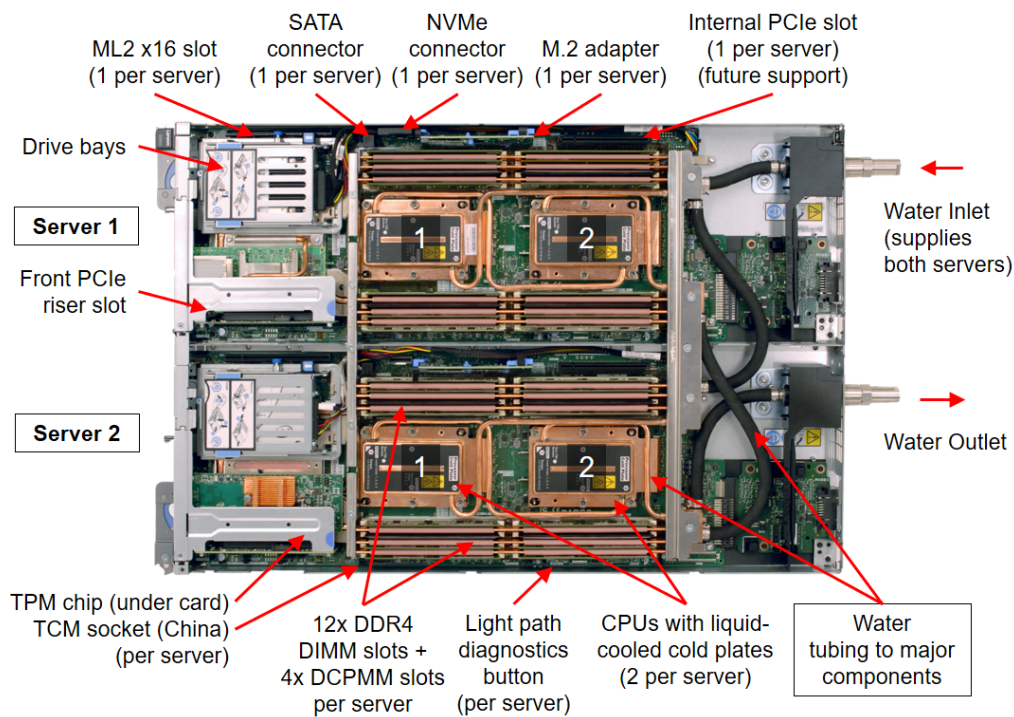


**Figure 17:** Inside view of two servers in a liquid (water) cooled tray [37].

Early incarnations of liquid cooling were expensive, complicated, and leakage posed a potential hazard to valuable computer components. However, the cooling power demand for data centers has increased, especially as data centers accommodate higher power densities [33]. High-density data centers require high thermal fluxes ( $100 \text{ W/cm}^2$ ) to dissipate heat, but air has a much lower heat removal capacity ( $\sim 37 \text{ W/cm}^2$ ) [1]. As a result, air cooling alone is no longer sufficient for newer generations of high density data centers [38]. Conversely, liquid cooling systems require less space and perform more effectively. Liquid cooling has become more prevalent, which has increased demand and driven the development of more reliable liquid cooling technologies [33]. Compared to air, liquid cooling does not require as much energy for air-conditioning, and as a result, produces a smaller carbon footprint [33]. Due to the

effectiveness and energy efficiency of liquid cooling, the utilization of liquid cooling is predicted to continue to increase as the technology advances and improves further [33].

There are three types of liquid cooling for data centers—indirect, direct, and rack-level—which are discussed in more detail below.

### *Indirect Liquid Cooling*

Indirect liquid cooling is a popular method of cooling CPUs, in which cold plates are installed as close to the heat-generating computing equipment as possible, but without direct contact between the electric components and the liquid coolant [3], [32]. Water, among various refrigerants and dielectric fluids, is most commonly used for the coolant due to its desirable thermophysical properties and high boiling point [32]. Typically, the cold plates are affixed to the IHS of the CPU, while the other heat-generating components in the server are cooled with chilled air in a hybrid air-liquid cooling system [32], [35]. In the indirect liquid cooling process, a chilled coolant travels over the CPU through channels of a cold plate (shown in **Figure 18**), capturing and dissipating the heat generated by the CPU. The heated coolant at the outlet of the cold plate is directed to a heat exchanger to remove the additional heat from the coolant and lower the temperature before it is returned to the CPU cold plate to repeat the cycle.

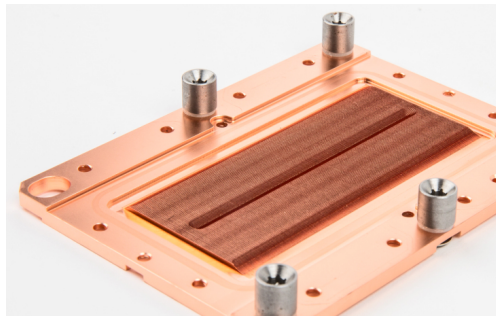


**Figure 18:** Copper SplitFlow Coldplate (2.4mm in height) [39].

Current research efforts are exploring the use of microchannel heat sinks since they have been shown to have enhanced heat transfer performance compared to traditional indirect liquid cooling methods, such as cold plates and water-blocks [32]. (Microchannel heat sinks are discussed in more detail in Section 2.4.3) **Figure 19** illustrates the layout of a typical indirect liquid cooling system within a data center. A coolant distribution unit (CDU) supplies chilled coolant to the electronics within the server trays, which is circulated back as heated coolant. A chiller expels the heat from the coolant to the atmosphere, and returns the chilled coolant to the CDU to be recirculated through the data center servers. One of the drawbacks to liquid cooled data centers is the lack of versatility. The piping system must be tailored specifically to the data center facility layout and unique server configurations [32].

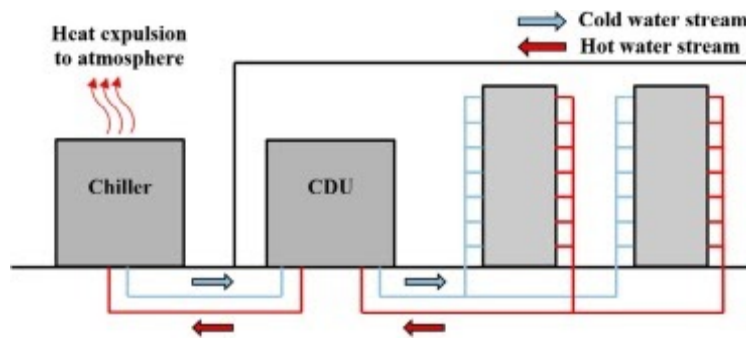


**Figure 19:** Typical diagram for indirect liquid cooling [32].

Since indirect liquid cooling systems are in close contact with the CPU, the thermal resistance can be less than 20% of the thermal resistance in air cooling systems [1]. As a result, indirect liquid cooling enables better energy capture, higher quality waste heat, and can increase the performance of the processor by up to 33% (compared to air cooling) [1]. In a study that installed cold plate heat exchangers on every server component generating more than 3 W of heat, the resulting PUE was as low as 1.15.

### *Direct Liquid Cooling*

With direct liquid cooling, the liquid coolant is in direct contact with electronic components. The liquid used for heat transfer is often a dielectric fluid to provide electrical insulation [32]. One of the most prevalent types of direct liquid cooling is pool boiling, wherein entire electronic boards are submerged in a dielectric fluid [32]. Pool boiling is also known as “two-phase passive immersion cooling” since the surface temperatures of the heat generating components exceed the saturation temperature of the dielectric fluid, resulting in nucleate boiling within the fluid bath, creating a two-phase mixture of liquid and vapor [32]. This method of direct, two-phase cooling is discussed further in Section 2.4.3.

### *Rack-Level Liquid Cooling*

Rack-level liquid cooling is a form of hybrid air-liquid cooling that consists of liquid cooled doors installed on the backs of server racks [35]. Cold air enters the front of the rack, dissipates heat from the computer components via convection, and exits the rack as hot exhaust air [35]. The hot air then encounters the door, which is an air-to-liquid heat exchanger, and thus transfers heat from the hot air, reducing its temperature. A rack-level cooling schematic is presented in **Figure 20** [35]. A major benefit of rack-level liquid cooling is that it eliminates the need to sector the hot and cold air flows between the server racks into hot and cold aisles [35]. Thus, data center managers can have more flexibility over the layout of the data center while still ensuring effective cooling of the IT equipment. Studies have shown that the implementation of rack-level air-to-liquid heat exchanger doors can enable data centers to reach a PUE of 1.3 [35].

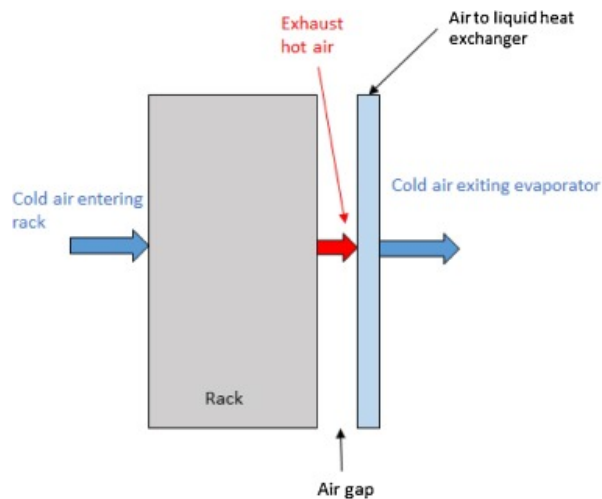


**Figure 20:** Schematic of rack-level liquid cooling [35].

There are a number of emerging liquid cooling technologies for data centers. Liquid cooling is highly effective and often produces PUEs much closer to 1 compared to air-cooling. Additionally, liquid cooling is more environmentally-conscious because it requires significantly less energy to operate.

### 2.4.3 Two-Phase Cooling Systems

#### *Two-phase cooling*

Two-phase cooling utilizes a dielectric fluid or refrigerant with a low boiling temperature as a working fluid [32]. In general, two-phase cooling involves the latent heating of a fluid to produce a liquid to vapor phase change [32]. Two-phase cooling is of interest for many next-generation data centers due to the enhanced heat transfer rates and reduced temperature gradients across IT surfaces which are enabled by latent heating of the fluid [32].

In one type of two-phase cooling, cold plate heat exchangers (i.e. evaporators or micro-evaporators) are installed on the heat generating components (e.g. CPUs) [39]. As the fluid absorbs heat from the electronics, the liquid begins to evaporate, as displayed in **Figure 21**. The two-phase liquid-vapor mix then flows to a condenser where the removal of heat condenses the working fluid back into the liquid phase before it is redirected back to the cold plate.

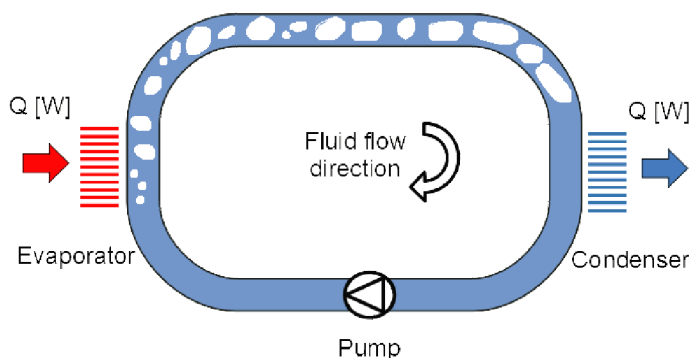


**Figure 21:** Simplified Model of Two-Phase Cooling [39].

Two-phase cooling systems typically utilize lower flow rates and thus do not require as high of pumping powers compared to many water cooling systems [1]. Additionally, two-phase cooling does not produce large temperature gradients over the computer hardware, which can sometimes occur in water-cooled systems and may cause damage to the equipment [1]. Furthermore, two-phase cooling takes advantage of higher heat transfer coefficients that result from nucleate boiling of working fluids through micro-evaporators (e.g. microchannel heat sinks) [1], [32]. Depending on the system, two-phase cooling is capable of removing heat fluxes between  $790 \text{ W/cm}^2$  and  $27,000 \text{ W/cm}^2$  (whereas the heat removal capacity of air is only about  $37 \text{ W/cm}^2$ ) [1].

### *Microchannel Heat Sinks*

Data center cooling via microchannel heat sinks has been gaining attention in recent years, especially as the cooling needs of modern processing chips demand the dissipation of heat fluxes upwards of  $300 \text{ W/cm}^2$  (while operating at  $85^\circ\text{C}$  maximum) [40]. Thus far, single-phase water cooling has often been favored for data center cooling due to its simplicity, low operating pressures, and high heat capacity of water [40]. However, water cooling can introduce significant temperature distributions along the processors. Additionally, water has a high freezing point that can be problematic for shipping, and if the cooling hardware is not sealed properly, water can cause damage to the electrical connections [40].

In the area of microchannel cooling of processing chips, recent publications indicate the emergence of four contending technologies: microchannel single-phase (water) flow, porous media flow, jet impingement cooling, and microchannel two-phase flow [41]. However, the pumping powers required in water flow, porous media flow, and impingement cooling must be elevated to ensure that the temperature differential at the inlet and outlet remains within the allowable limits [41]. And although microchannel two-phase flow is more complex, there are still a number of promising advantages that have contributed to the recent rise in its development and potential as a long term solution for new generation data center cooling [41].

Two-phase flow boiling takes advantage of latent heat utilized for the evaporation of the dielectric refrigerant flowing through the microchannel heat sink [40]. Because the phase change of the fluid occurs at a near constant temperature, there is no risk of creating large temperature gradients along the processing chips that may result in efficiency losses or damage [40]. Microchannel two-phase flow is also favored for its ability to manage hotspots, since the heat transfer coefficient increases with heat flux and decreases only slightly with vapor quality [40]. However, there is an important phenomena in flow boiling known as the critical heat flux (CHF) which limits two-phase cooling. “The nucleate boiling heat flux cannot be increased indefinitely” because the production of vapor creates an insulating layer over the surface of the microchannel walls, which consequently reduces the heat transfer coefficient [42]. Recent studies have shown that it is possible to increase the CHF by utilizing higher mass fluxes ( $\text{kg/m}^2\text{s}$ ), wherein the dryout phenomena (i.e. the formation of a vapor layer on the wall surface) is delayed [40].

There have also been studies on the beneficial effects of split flow microchannel heat sink designs, wherein there is one inlet and two outlets [1]. Split flow designs can produce higher CHF's (by up to 80%) and reduce the pressure drops relative to the standard configurations of one centered opening at the inlet and outlet [1]. Furthermore, high aspect ratio microchannel designs can produce extremely high heat transfer coefficients [41]. Essentially, the much higher effectiveness of microchannel two-phase flow enables the required pumping power to be reduced drastically (as low as 1/10 of the pumping power needed for water cooling systems) [41].

Although two-phase microchannel heat sinks pose a promising potential solution for modern data center cooling needs, there are a number of drawbacks resulting from unstable two-phase flows. Flow instabilities can lead to variability in pressures and temperatures, flow reversal, and other thermo-fluid phenomena that can cause superheating or burnout of the heated surfaces [32]. Due to these operational challenges, two-phase cooling through microchannel heat sinks has scarcely been developed in industry [32]. Additionally, the predictive techniques for determining performance parameters (such as local heat transfer coefficients, CHF, and pressure drop in the two-phase region) are still largely under development [41]. There is a significant number of published papers concerning two-phase microchannel heat sinks, but the existing databases are not sufficient for developing robust models and correlations [43]. The databases neither encompass broad enough ranges of operational/geometric parameters and thermophysical fluid properties, nor do they clearly distinguish two-phase flow regimes in subcooled versus saturated conditions to enable a more careful assessment of heat loss [43]. Overall, there is a lack of correlations in literature that properly utilize dimensionless groups to represent the dominant fluid and physical interactions to characterize individual flow regions [43].

The potential of two-phase microchannel heat sinks has excited the heat transfer community in recent years. However, the tools for characterizing and modeling two-phase flow are unfinished as this scientific area is still largely under development.

#### *Two-phase submersion cooling*

Two-phase submersion cooling (a form of direct liquid cooling), illustrated in **Figure 22**, is an emerging technology for cooling data center components [44]. In two-phase submersion cooling, the physical computer components are submerged in a tank of dielectric liquid that can enable a more effective heat transfer [44]. Dielectric liquids are better conductors of heat than air or water and have low boiling points near 56°C (compared to 100°C with water) [44]. Examples of dielectric fluids used in submersion cooling include Fluorinert™ FC-72, Novec™ 7100, Novec™ 649, and PF-5060 [32]. With increasing consideration for the environment, global warming potential has become a key factor in dielectric liquid development. For example, Novec™ 7100 and similar products are preferable for their lower global warming potentials [45].

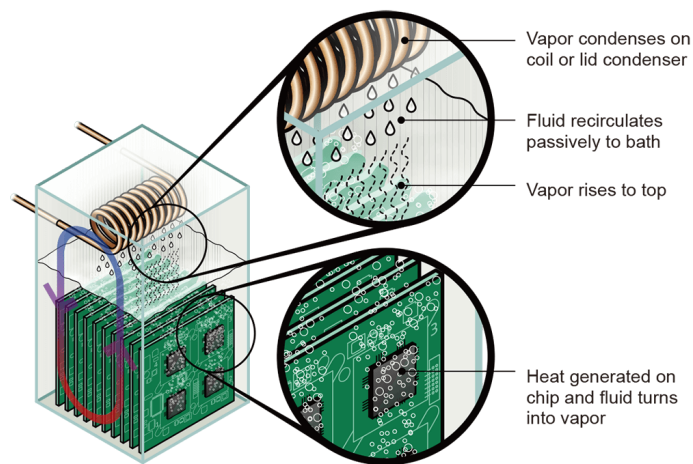


**Figure 22:** Illustration of two-phase submersion cooling [44].

As shown in **Figure 22**, the heat generated from the components of the computer causes the dielectric fluid to evaporate due to its low boiling point. The dielectric vapor rises to the top of the tank where heat from the vapor is transferred to a condenser coil. The condenser coil is often placed above the open tank, where the vapor condenses, falls back down into the tank, and the cycle repeats. Two-phase immersion cooling has higher efficiency and energy savings (eliminates the need to power a pump), improved reliability compared to air and liquid cooling, and allows for higher data center densities [32], [44]. Data centers with submersion cooling systems have reported PUEs as low as 1.05 [38]. However, two-phase submersion is prone to information technology (IT) equipment failures and high up-front costs [46]. Nonetheless, the use of immersion cooling in the data center industry has been rising, and further development of the technology will strengthen its case as a high-performance alternative to air cooling systems, especially for high density data centers [32].

Ultimately, there are a number of viable technologies for cooling data centers. However, the most suitable option often depends on the specific cooling needs of the data center.

## 3.0 Preliminary Design

In this section, the major features of the project are defined, described, and justified. The preliminary design section begins with a summary of the important findings from the background research that led to key design decisions. The following subsection explains how this project intended to expand and improve upon the efforts made in previous studies. An overview of the design, including the design constraints and design criteria, is also described. A focused discussion about each component of the design, which included a modeled ORC and server heat extraction cycle (SHEC), concludes the preliminary design section. Schematics and provisional calculations are presented to help characterize the components of the preliminary design.

### 3.1 Insight from Prior Research Efforts

The background research and literature review provided insight that informed several initial design decisions for the project. Initially, the review of data center cooling and waste heat technology published by Ebrahimi et al. in 2014 indicated that organic Rankine cycles (ORCs) and absorption cooling were the two most promising systems for low-grade waste heat recovery in data centers [1]. They examined a multitude of other systems, including district heating (i.e. hot water production), power plant co-location, piezoelectrics, thermoelectrics, biomass co-location, and desalination/clean water production [1]. However, ORCs and absorption cooling were favored for their potential to (1) dramatically reduce energy requirements and costs related to cooling and (2) utilize the data center waste heat as the heat source for the system without additional site-specific constraints or necessitating significant alterations to the data center [1]. The selection of an ORC system as the means for data waste heat recovery was primarily due to its capacity to generate electrical energy from waste heat, while simultaneously reducing cooling demands for the data center. Thus, the ORC system presented the unique capacity to convert what was initially waste, and a significant source of cost for the data center, into the means for producing a product—electricity; a source of income for the data center. Furthermore, ORCs are regarded as a highly developed, reliable, and versatile technology, and are considered the premier technology for converting low-grade waste heat into power [1]. While an absorption cooling system can provide sufficient cooling to the electronic components while dramatically cutting costs, the additional benefit of electricity generation from the ORC made it more favorable. With an ORC, there was potential for the system to become a revenue stream for the data center, once the initial capital costs were paid off. Additionally, the development of environmentally-conscious refrigerants for ORCs in recent years has made its application in waste heat recovery an even more valuable and exciting endeavor, particularly with the suggested potential of R1234ze [3].

A later study conducted by Ebrahimi et al. in 2017 explored the viability of ORCs for data center waste heat recovery using a computational model [3]. The thermodynamic model evaluated the performance of a myriad of organic fluids (R12, R134a, R245fa, and R1234ze in 16 unique combinations) in a two-phase cooling, dual loop ORC system under different ranges of operating conditions for many of the components (micro-evaporator, compressor, condenser, superheater, etc.) [3]. The key results from the study included: (1) R134a and R245fa were optimal working fluids, but R1234ze could be

substituted as a more sustainable alternative. (2) Using a superheater reduced the COP of the overall system. (3) Increasing the waste heat recovery temperature greatly improved system performance. (4) An economic analysis predicted a payback period of 4-8 years for ORCs in data center applications [3]. The overall significance of the 2017 Ebrahimi et al. study was that it demonstrated the viability of ORCs as a means for data center heat waste recovery. Under their initial set of operating conditions, their thermodynamic model predicted a range of first law efficiencies between 2.5% and 4.7%, depending on the combination of working fluids used [3]. Assuming an ORC could produce  $1.5 \text{ kW}_{\text{el}}$  from a  $30 \text{ kW}_{\text{th}}$  input (i.e., a typical ORC module from *Orcan Energy*), the payback period for the system was only about 5.5 years [3]. While the servers and storage drives themselves are replaced every few years, a data center facility can last upwards of 20 years [47]. Thus, a 5.5 year payback period for a waste heat recovery ORC system is economically feasible and a practical investment for data centers. Based on the compelling findings regarding the potential for ORCs to be implemented in data centers, ORC systems were pursued as the technological solution for low-grade waste heat recovery in this project.

After the method of waste heat recovery was determined, it was crucial to identify which type of data center cooling system would be the most suitable. The research regarding data center cooling technologies strongly indicated that direct liquid cooling could be the most advantageous for ORC integration. Liquid cooling systems are becoming more prevalent (as air cooling becomes obsolete) due to the growing number of high density data centers [38]. More importantly, however, is the fact that direct liquid cooling achieves better energy capture and higher quality waste heat due to close contact with the CPU [3]. The thermodynamic performance of ORC systems is heavily dependent upon the waste heat recovery temperature [1]. Higher recovery temperatures resulted in significant improvements in ORC performance and efficiency, as demonstrated by the model-based study from Ebrahimi et al. and experimental-based study from Araya et al. [3], [20]. Furthermore, liquid cooling systems provide an efficient means of transporting the extracted thermal energy from the servers to the ORC. Whereas a number of issues occur with air cooling, such as low heat transfer coefficient of air and hot/cold air intermixing, liquid cooling enables better energy capture and delivery with a lower power demand and cost [32], [33]. Therefore, a liquid cooling system was investigated for the server heat extraction cycle (SHEC).

Another type of data center cooling system that demonstrated high potential for supporting an ORC heat recovery system was two-phase cooling. Unlike liquid cooling, two-phase cooling takes advantage of a high convection heat transfer coefficient associated with nucleate boiling—evaporation that occurs when a surface temperature is hotter than the saturated fluid temperature [1]. When nucleate boiling occurs, steam bubbles form at the heat transfer surface, break away, and are carried into the main stream of the fluid [48]. Movement of steam bubbles enhances heat transfer as the surface heat is carried into the fluid stream [48]. Ebrahimi et al. further explained that two-phase cooling has been shown to remove high heat fluxes, ranging from  $790 \text{ W/cm}^2$  to  $27,000 \text{ W/cm}^2$  [1]. Due to the higher capacity for cooling, two-phase systems can maintain the temperature of an operating CPU  $13^\circ\text{C}$  lower than a liquid (water) cooling system with the same pumping power [1]. The nucleate boiling phenomenon can be desirable for cooling computer components (such as CPUs) since the heat in the surface of the

component can be efficiently dissipated into the fluid. Subsequently, that thermal energy can be transported and utilized as the heat source in a proposed ORC. Although two-phase cooling was emphasized as the preeminent means for data center waste heat recovery according to Ebrahimi et al. [1], [3], persisting issues associated with flow instability have prevented the technology from being widely adopted in industry [32]. Thus, an investigation regarding the optimal cooling system for interfacing with an ORC was warranted.

Concurrently, it was important to consider the major findings from research about how certain operating parameters of the ORC can improve performance and increase thermal efficiencies. (Both liquid and two-phase cooling methods had to be examined to determine which system may facilitate or hinder the conditions which optimize ORC performance.) The model-based study from Ebrahimi et al. in 2017 provided a number of findings regarding optimized conditions for a dual loop ORC in a data center environment. The results from the study indicated that the use of a superheater in any case produced a negative effect on the overall system COP [3]. Therefore, the possibility of integrating a superheater in the data center ORC was not investigated in this project. Ebrahimi et al. also determined that increasing the micro-evaporator temperature at the chip greatly improved the thermodynamic performance of the ORC [3]. Thus, it was essential to maximize the temperature of the coolant fluid following the heat exchange with the IT equipment, in both the liquid and two-phase cooling systems. Furthermore, Ebrahimi et al. utilized a compressor in the two-phase cooling loop to increase the temperature of the fluid entering the heat exchanger of the ORC [3]. However, greater temperature upgrades through the compressor consequently required more power and led to reduced thermal efficiencies [3]. A liquid cooling system uses a pump rather than a compressor, wherein the power draw may be considerably less (depending on the working pressures), but does not typically produce a significant temperature increase in the coolant fluid. Overall, the temperature of the waste heat has a profound effect on the performance of the ORC, and should be maximized through the heat exchange with the computing components. Additional heat upgrades from other components (e.g. compressor) must be optimized with regards to their corresponding power draws.

Lastly, Ebrahimi et al. determined that lowering the temperature of the ORC working fluid at the outlet of the condenser improved the thermal efficiency of the system [3]. Therefore, in both liquid and two-phase systems, ORC condenser exit temperatures should be as low as possible, within the constraints of the available chilled water supply and required conditions for the ORC operability. Additionally, the results from the experimental study from Araya et al. determined that the performance of the ORC expander (turbine) is affected by the difference in pressure ratios between that of the system and the expander's built-in pressure ratio [20]. The expander performs better (higher isentropic efficiency) when the difference between the pressure ratios is limited [20]. The pressure ratio can be reduced by increasing the chilled water exit temperature (which could potentially decrease the thermal efficiency of the system.) Instead, it would be more advisable to select a turbine with a similar built-in pressure ratio to that of the system to avoid compromising the optimal operating conditions of the ORC.

### 3.2 Extending Prior Research Efforts

Thus far, the investigation of ORC waste recovery systems for data centers has been primarily limited to theoretical modeling and optimization-focused studies. The only physical ORC system that has been designed, constructed, and tested, specifically for the application in data centers, was a 2018 experimental ORC prototype from Villanova University [20]. The researchers designed their 20 kW lab-scale prototype to represent two server racks operating at full capacity [20]. They utilized a hot water cycle to simulate the waste heat conditions of the servers and developed a MATLAB thermodynamic model to estimate the sizes of the main components of the ORC [20]. The researchers used R245fa as their working fluid for the ORC and ran several experimental tests at varying temperatures and mass flow rates to characterize the ORC thermodynamic performance [20]. The experimental setup is shown in **Figure 23**. Additionally, the MATLAB program was utilized to evaluate the performance of the ORC system under different conditions [20].

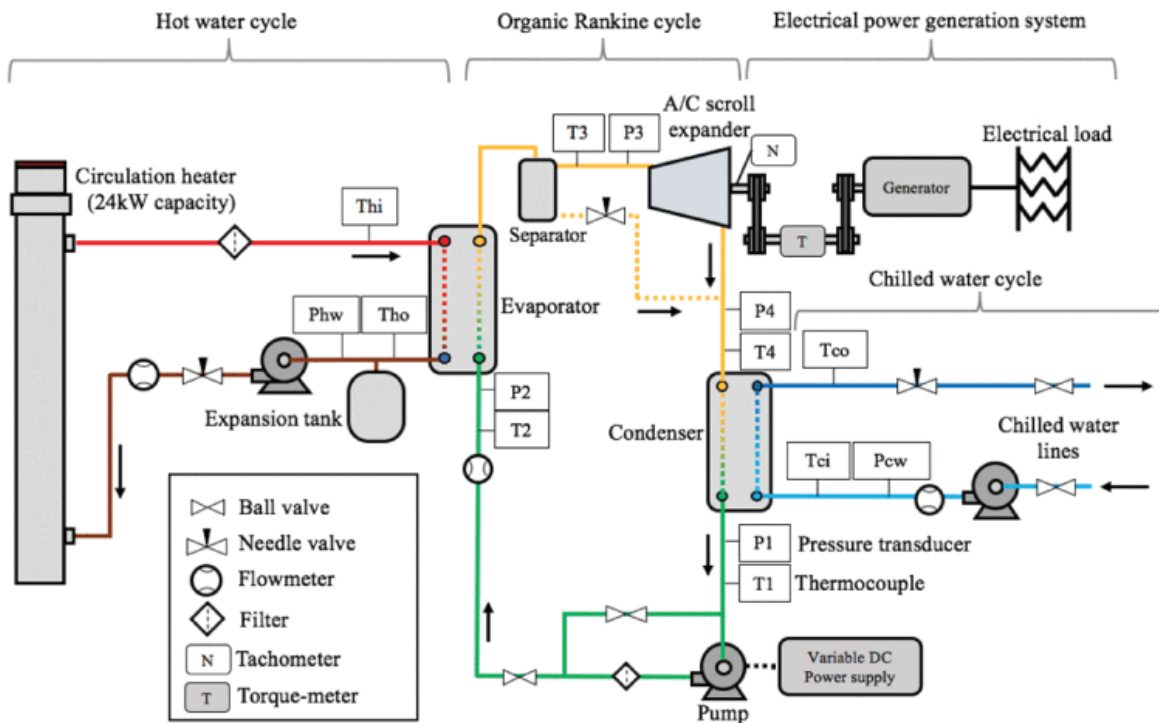


**Figure 23:** Schematic of the experimental ORC prototype from Araya et al [20].

The researchers determined that there was greater heat recovery at higher operating temperatures. The results from the experimental tests showed that the turbine power output increased by 56.9% when the waste heat temperature was increased by 20°C (from 60°C to 80°C), corresponding to a 40% increase in waste heat [20]. Overall, the thermodynamic model of the system predicted a thermal efficiency between 2% and 8%, and the maximum efficiency reached with the experimental ORC prototype was 3.33% [20].

The work by Araya et al. made exceptional strides in validating ORC waste heat recovery systems for data centers at the experimental level. Their findings on optimal waste heat temperatures (80°C)

informed the preliminary theoretical model for the ORC system in this project. However, there were some weaknesses and omissions in their study that this project attempted to improve and expand upon. First, the experimental ORC prototype omitted the physical system responsible for extracting the heat from the servers. Instead, Araya et al. utilized a Watlow circulation heater (24 kW capacity) to represent the server waste heat. The adjustability of the circulation heater enabled the research group to run the prototype at varying temperatures for their thermodynamic analyses. However, if an ORC waste heat recovery system was implemented in an actual data center, then the specification of the server heat extraction system would be essential. Therefore, this project aimed to expand on the experimental research from Araya et al. by directly addressing the data center cooling system/waste heat extraction system. In this project, essential aspects of the physical server heat extraction cycle (SHEC) were researched, designed, evaluated, and optimized, all of which had been simply replaced by a circulation heater in the experiments performed by Araya et al. This project sought to provide a complement to the ORC prototype from Araya et al. by virtually simulating the heat exchange between the heat-generating IT components and the fluid in the SHEC/data center cooling system. Thus, it was not assumed that a given amount of waste heat would be extracted from the servers and transported to the ORC system. Ultimately, careful consideration and investigation of the SHEC served as the next step for verifying the utilization of ORCs in data centers for waste heat recovery.

Additionally, this project sought to further consider the sustainability of ORC systems. The thermodynamic model and prototype from Araya et al. utilized R245fa as the working fluid [20]. However, Ebrahimi et al. cautioned that R245fa may not always be available because of its moderate Global Warming Potential (GWP) of 900 [3]. Rather, it has been suggested that R1234ze can be used as a replacement with only minor drops in efficiency [3]. Thus, this project aimed to improve upon the sustainability of proposed ORC heat waste recovery systems for data centers by conducting the ORC thermodynamic analysis and optimization with R1234ze. Furthermore, the components of the ORC were sized and evaluated under the conditions that they were operating with R1234ze. Thus, the practical use and performance of R1234ze in data center-ORC applications was verified.

### 3.3 Design Overview

The data center low-grade waste heat recovery system pursued in this project consisted of two fundamental systems, the organic Rankine cycle (ORC) and server heat extraction cycle (SHEC). There were two leading computer cooling systems that demonstrated strong potential for use in the SHEC, either liquid cooling or two-phase cooling. The SHEC may be considered conceptually similar to the primary component in a data center cooling system which distributes/circulates coolant to the IT equipment—the coolant distribution unit (CDU). However, since the purpose of the system is not only to maintain the computing equipment within safe operating temperatures, but to deliver the heat generated by the equipment to an ORC evaporator, the system has been renamed ‘server heat extraction cycle.’ In other words, the SHEC extracts heat from the computing equipment, thereby providing cooling, and supplies the extracted heat to the ORC. The recovered waste heat from the SHEC is then converted into electrical energy as a result of the thermodynamic processes in the ORC. A simplified graphic of the overall system is shown in **Figure 24**.

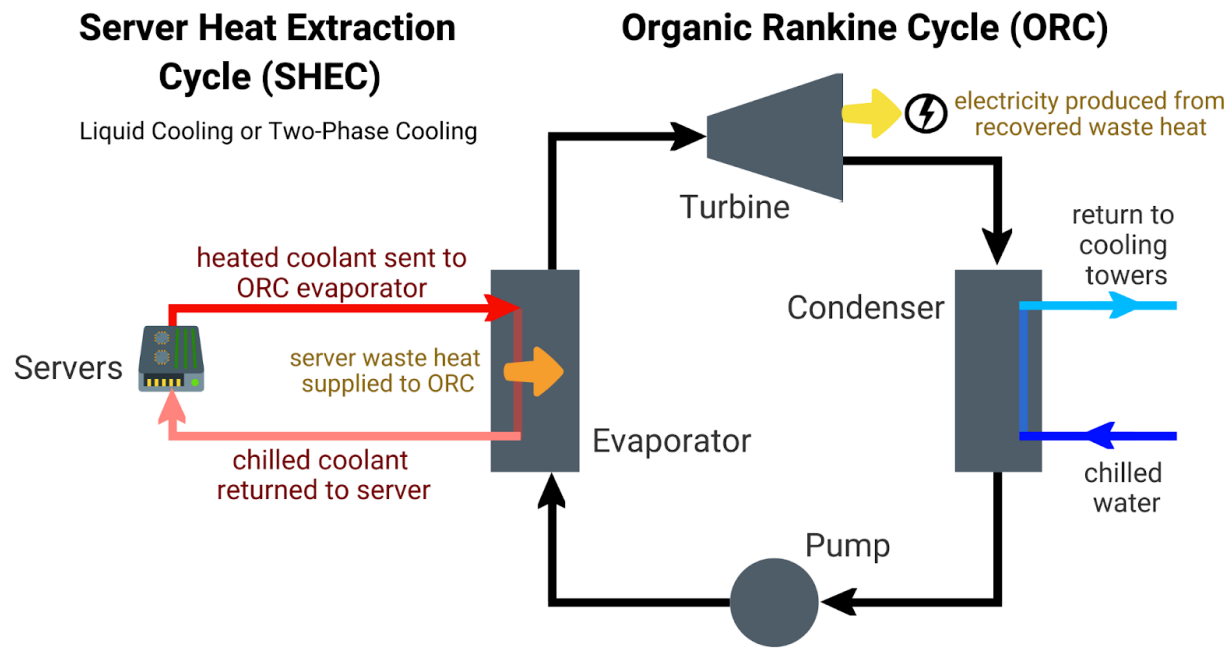


**Figure 24:** Simplified schematic of overall data center heat waste recovery system.

The main investigative aspect of the project was to determine which computer cooling system, liquid cooling or two-phase cooling, would be the superior choice for interfacing with the ORC. A wide array of factors, such as availability, economic feasibility, practicality, reliability, and sustainability were considered for both cooling systems employed in the SHEC. After much consideration, it was concluded that the scope of this project could not encapsulate a full scale analysis of both systems. Thus, the project included an intensive analysis and optimization of a liquid cooling system using the simulation software, COMSOL. The two-phase analysis was only taken to the preliminary stages of development, as it was found that comprehensive research on two-phase flow phenomena and heat transfer correlations was warranted for the design and assessment of adequate two-phase simulation models. However, for the liquid cooling system selected, further modeling of the SHEC fluid mechanics was conducted via the development of a program in MATLAB. Similarly, the ORC was represented by a thermodynamic model in MATLAB, which also included heat exchanger and fluid mechanics analyses. The operating limitations and simulated outputs of the SHEC served as the inputs to the ORC system to ensure a cohesive system. The development of the two fundamental systems (ORC and SHEC) consisted of dynamic design iterations as each subsystem was refined to reflect the results of the other until a complete optimized system was reached. The overall design constraints and criteria are listed in sections 3.3.1 and 3.3.2, respectively, followed by a more detailed breakdown of the preliminary design of the ORC and SHEC in sections 3.4 and 3.5, respectively.

### 3.3.1 Design Constraints

The project adhered to the following design constraints:

- The total cost of the project was less than \$1000, the amount allotted by WPI to a four-person Mechanical Engineering MQP group.

- The condenser used chilled facilities water at 45°F and returned the water back to facilities.
- In consideration of the 10 kW server room located in the Atwater Kent Laboratories at WPI (AK120b), the output of data center heat waste was specified at 10 kW.
- The SHEC was designed to maintain computing equipment within safe operating temperatures (<85°C).
- The liquid cooling system for the SHEC was compatible with the standard rack unit U sizing (1U is 1.75” tall) to fit inside a server rack in AK120b (approx. 17.75” wide and 24-30” long).

### 3.3.2 Design Criteria

The project adhered to the following criteria:

- The theoretical model of the ORC accommodated a 10 kW heat load from the computer servers in AK120b.
- Both ORC heat exchangers were less than 1 m in overall length to exhibit size practicality for a 10 kW heat load.
- The ORC had a thermal efficiency between 2% and 8% to indicate effectiveness.
- The ORC system had an estimated payback-period between 4 and 8 years to demonstrate economic practicality.
- The ORC and SHEC utilized environmentally-conscious working fluids.
- The SHEC extracted heat from the CPUs using a liquid cooling system or a two-phase cooling system.
- The thermal performance of the cooling system for the SHEC was characterized via simulation.

## 3.4 ORC Component

Various theoretical analyses were conducted to provisionally characterize the ORC system operations. In this section, the calculations processes for thermodynamic, fluid, and heat transfer analysis are defined and described, wherein numerical variable changes were subsequently made over the course of developing the system via further modeling and simulation.

### 3.4.1 Thermodynamic Analysis

This section details the method for characterizing the thermodynamic processes and performance parameters of the ORC. A simple schematic of the ORC is shown in **Figure 25**, which designates the four state points referenced in the preliminary thermodynamic analysis (1 = turbine inlet, 2 = condenser inlet, 3 = pump inlet, 4 = evaporator inlet). Server waste heat is supplied to the ORC via the SHEC, which is used to drive the ORC thermodynamic processes in each ORC component and ultimately produce electricity. The working fluid of the ORC is R1234ze, a sustainable refrigerant alternative. Honeywell’s *Genetron Refrigerants Modeling Software* was used in analyzing the implementation of their Solstice® ze Refrigerant (R1234ze) in the ORC waste heat recovery system [49].

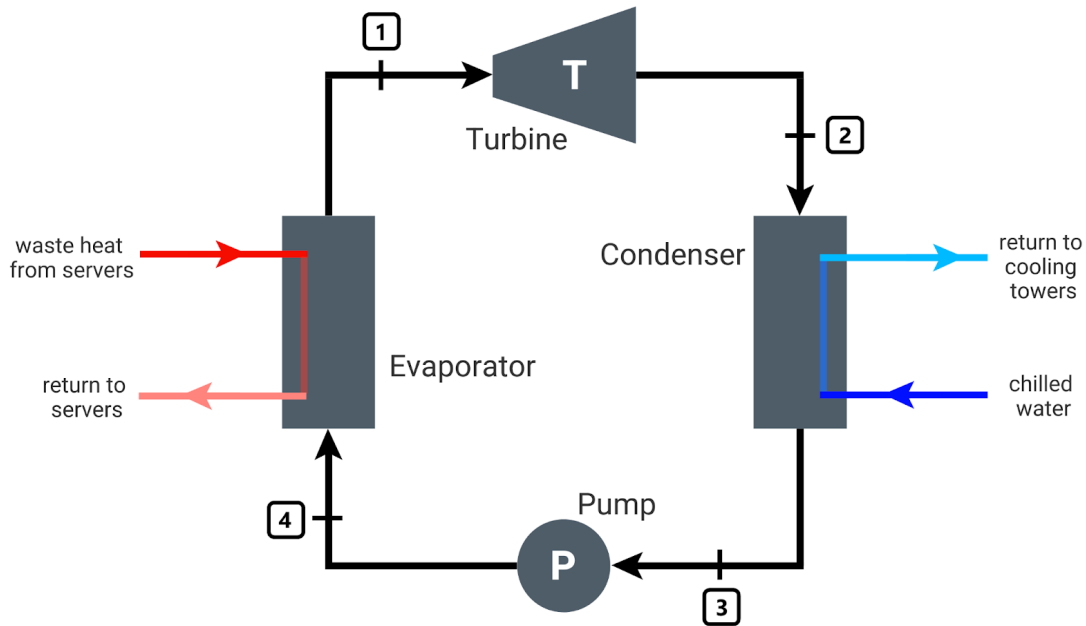


**Figure 25:** ORC Schematic.

The ORC was initially considered ideal, wherein turbine and pump efficiencies were considered in subsequent calculations. In an ideal Rankine cycle, the specific entropy across the turbine and pump is constant ( $s_1 = s_2$  and  $s_3 = s_4$ ). Additionally, the pressure across the condenser and evaporator is constant ( $P_2 = P_3$  and  $P_1 = P_4$ ). Lastly, the temperature across the condenser of an ideal Rankine cycle is constant ( $T_2 = T_3$ ) wherein the heat energy removed is just enough to change the phase of the working fluid from a saturated vapor ( $x_2 = 1$ ) to a saturated liquid ( $x_3 = 0$ ). Initially, it was assumed that the low temperature ( $T_L$ ) of the working fluid was 40°C and the high temperature ( $T_H$ ) was near 80°C. A state-strategy table was used to determine the pressure (bar), temperature (°C), specific entropy (kJ/kg-K), specific enthalpy (kJ/kg), specific volume (m<sup>3</sup>/kg), and phase/quality at each stage of the Rankine cycle. To complete each row of the table, at least two properties needed to be known. The thermodynamic properties were found in the saturation tables provided in the *Genetron Refrigerants Modeling Software* from Honeywell [49]. The completed state-strategy table is shown in **Table 1**, and the method used to complete the table is listed and described below. In the table, given or assumed values are shown in black text, values determined from the saturation tables are shown in red text, and calculated values are shown in blue text.

**Table 1:** ORC state-strategy table for R1234ze.

State	P (bar)	T (°C)	Specific entropy (s, kJ/kg-K)	Specific enthalpy (h, kJ/kg)	Specific volume (v, m <sup>3</sup> /kg)	Phase / quality
1	20.73	81.5	1.6805	427.7	0.008	Saturated vapor (x=1)
2	7.665	40	1.6805 ( $s_{2s}$ )	$h_{2s} = 409.8$ $h_2 = 413.4$	0.0246	Saturated vapor (x=1)

3	7.665	40	1.1861	255.0	0.0009	Saturated liquid (x=0)
4	20.73	40.85*	1.1861 (s <sub>4s</sub> )	h <sub>4s</sub> = 256.2 h <sub>4</sub> = 256.4	0.0009*	Compressed/ subcooled liquid

\*indicates that the values were determined with the MATLAB program, not from the Honeywell software which did not provide the tools for determining T<sub>4</sub> and v<sub>4</sub> under the State 4 conditions

*Method:*

1. The given and/or assumed values were filled-in first:  $T_2 = T_L = 40^\circ\text{C}$ ,  $x_2 = 1$ ,  $x_3 = 0$ , ( $s_1 = s_2$ ), ( $s_3 = s_4$ ), ( $P_2 = P_3$ ), ( $P_1 = P_4$ ), and ( $T_2 = T_3$ )
2. *State 2* was characterized first, as the saturation pressure at 40°C is 7.665 bar. At a saturated vapor, the specific entropy is 1.6805 kJ/kg-K, the ideal specific enthalpy is 409.8 kJ/kg-K, and the specific volume is 0.0246 m<sup>3</sup>/kg.
3. *State 1* was defined next, since  $s_1 = s_2$ , then  $s_1 = 1.6805$  kJ/kg-K. For an enthalpy value of 1.6805 kJ/kg-K near 80°C, the working fluid is a saturated vapor with a precise temperature and pressure of 81.5°C and 20.75 bar, respectively. The corresponding specific entropy and specific volume values are 427.7 kJ/kg and 0.008 m<sup>3</sup>/kg, respectively.
4. *State 3* was characterized next; since  $P_2 = P_3$  and  $T_2 = T_3$ , then  $P_3 = 7.665$  bar and  $T_3 = 40^\circ\text{C}$ . At a saturated liquid ( $x_3 = 0$ ), the specific entropy is 1.1861 kJ/kg-K, the specific enthalpy is 255.0 kJ/kg-K, and the specific volume is 0.0009 m<sup>3</sup>/kg.
5. *State 4* conditions were defined based on the assumptions that  $P_1 = P_4$  and  $s_3 = s_4$ . Thus,  $P_4 = 20.75$  bar and  $s_4 = 1.1861$  kJ/kg-K.

*State-Strategy Table Calculations*

6. The actual specific enthalpy at *State 2* ( $h_2$ ), was determined using the turbine efficiency formula (equation 3.4.1.1). The isentropic efficiency of the turbine ( $\eta_t$ ) was assigned a typical value of 80% [50]. The other variables in the formula included: the specific enthalpy at *State 1* ( $h_1$ ), the ideal specific enthalpy at *State 2* ( $h_{2s}$ ), and the actual specific enthalpy at *State 2* ( $h_2$ ). Equation 3.4.1.1 was rearranged to solve for  $h_2$ .

$$\eta_t = \frac{h_1 - h_2}{h_1 - h_{2s}} \quad (\text{equation 3.4.1.1})$$

$$h_2 = h_1 - \eta_t(h_1 - h_{2s}) \quad (\text{equation 3.4.1.2})$$

Using the corresponding numerical values from the state-strategy table in equation 3.4.1.2,  $h_2$  is 413.4 kJ/kg.

7. The ideal specific enthalpy at *State 4*, assuming an incompressible fluid, is given by equation 3.4.1.3.

$$h_{4s} = h_3 + v_3(P_4 - P_3) \quad (\text{equation 3.4.1.3})$$

Using the corresponding numerical values from the state-strategy table in equation 3.4.1.3,  $h_{4s}$  is 256.2 kJ/kg.

8. The actual specific enthalpy at *State 4* was determined using the pump efficiency formula (equation 3.4.1.4), wherein  $\eta_p$  is the isentropic efficiency of the pump, which was assigned a typical value of 85% [51],  $h_3$  is the specific enthalpy at *State 3*,  $h_{4s}$  is the ideal specific enthalpy at *State 4*, and  $h_4$  is the actual specific enthalpy at *State 4*. Equation 3.4.1.4 was rearranged to solve for  $h_4$ , given by equation 3.4.1.5.

$$\eta_p = \frac{h_{4s} - h_3}{h_4 - h_3} \quad (\text{equation 3.4.1.4})$$

$$h_4 = h_3 + \frac{h_{4s} - h_3}{\eta_p} \quad (\text{equation 3.4.1.5})$$

Using the corresponding numerical values from the state-strategy table in equation 3.4.1.5,  $h_4$  is 256.4 kJ/kg.

Once the State-Strategy table was completed, additional calculations were performed in order to determine important parameters and characteristics of the ORC.

#### *Mass Flow Rate of the Working Fluid (R1234ze)*

The mass flow rate of the working fluid (R1234ze) was determined by utilizing the enthalpy change across the evaporator. It was assumed that 10 kW from the WPI servers in AK120b was transferred to the ORC working fluid, ie. Heat-Out from servers ( $\dot{Q}_{\text{servers}}$ ) = Heat-In to working fluid ( $\dot{Q}_{\text{working fluid}}$ ). Additionally, heat transferred to the working fluid ( $\dot{Q}_{\text{working fluid}}$ ) can be represented by the enthalpy change of the working fluid across the evaporator,  $\dot{m}_R(h_1 - h_4)$ . Thus, the mass flow rate of the working fluid ( $\dot{m}_R$ ) was given by equation 3.4.1.6.

$$\dot{m}_R = \frac{\dot{Q}_{\text{servers}}}{(h_1 - h_4)} \quad (\text{equation 3.4.1.6})$$

Using the corresponding numerical values from the state-strategy table in equation 3.2.1.6,  $\dot{m}_R$  is 0.0584 kg/s.

#### *Turbine Power Output*

The turbine power output ( $\dot{W}_t$ ) was determined by utilizing the enthalpy change across the turbine and the mass flow rate of the working fluid. The solution is given by equation 3.4.1.7.

$$\dot{W}_t = \dot{m}_R(h_1 - h_2) \quad (\text{equation 3.4.1.7})$$

Using the corresponding numerical values from the state-strategy table and the previously calculated mass flow rate of the working fluid,  $\dot{W}_t$  is 0.836 kW.

#### *Pump Power*

The pump power draw ( $\dot{W}_p$ ) was determined by utilizing the enthalpy change across the pump and the mass flow rate of the working fluid. The solution is given by equation 3.4.1.8.

$$\dot{W}_p = \dot{m}_R(h_4 - h_3) \quad (\text{equation 3.4.1.8})$$

Using the corresponding value for  $h_3$  from the state-strategy table and the previously calculated actual specific enthalpy at state 4 ( $h_4$ ) and mass flow rate of the working fluid,  $\dot{W}_p$  is 0.0809 kW. However, it must also be noted that the pump must overcome the pressure drops throughout the system, which

requires additional pumping power. The pressure drop for each section of ORC piping (and associated pump power) are further explored in Section 3.4.2.

### *Heat Transfer Rate in Condenser*

The heat transfer rate in the condenser was determined by utilizing the enthalpy change of the working fluid across the condenser. It was assumed that all the heat leaving the ORC fluid ( $\dot{Q}_{\text{working fluid}}$ ) to change its state from a saturated vapor to a saturated liquid was transferred to the coolant ( $\dot{Q}_{\text{coolant}}$ ) inside the condenser (i.e. chilled water in **Figure 25**). The heat transfer rate in the condenser is given by equation 3.4.1.9.

$$\dot{Q}_{\text{coolant}} = \dot{Q}_{\text{working fluid}} = \dot{m}_R(h_2 - h_3) \quad (\text{equation 3.4.1.9})$$

Using the corresponding numerical values from the state-strategy table and the previously calculated mass flow rate of the working fluid,  $\dot{Q}_{\text{coolant}}$  is 9.245 kW.

### *Carnot (Maximum) Efficiency*

The Carnot efficiency ( $\eta_{\text{carnot}}$ ) is the ideal maximum efficiency of power cycle operating between two thermal reservoirs, and is characterized by the relationship between the high temperature ( $T_H = T_1$ ) and low temperature ( $T_C = T_2$ ) of the cycle. The Carnot efficiency is given by equation 3.4.1.10

$$\eta_{\text{carnot}} = 1 - \frac{T_C}{T_H} \quad (\text{equation 3.4.1.10})$$

Using the corresponding numerical values from the state-strategy table in equation 3.4.1.10,  $\eta_{\text{carnot}}$  is 11.7%.

### *Thermal Efficiency*

The thermal efficiency ( $\eta_{\text{th}}$ ) is the ratio of the net work of the Rankine cycle ( $\dot{W}_{\text{net}}$ ) to the heat supplied to the cycle ( $\dot{Q}_{\text{in}}$ ). The net work is given by the difference between the turbine power output and power supplied to the pump ( $\dot{W}_{\text{net}} = \dot{W}_t - \dot{W}_p$ ). The heat supplied to the cycle is equivalent to the server waste heat  $\dot{Q}_{\text{in}} = \dot{Q}_{\text{servers}}$ . The final equation for thermal efficiency is given by equation 3.4.1.11.

$$\eta_{\text{th}} = \frac{\dot{W}_{\text{net}}}{\dot{Q}_{\text{in}}} = \frac{\dot{W}_t - \dot{W}_p}{\dot{Q}_{\text{servers}}} \quad (\text{equation 3.4.1.11})$$

Using the previously calculated turbine power output, pump power, and server waste heat (10 kW),  $\eta_{\text{th}}$  is 7.55%.

### *Second Law Efficiency*

The second law efficiency ( $\eta_{II}$ ) is the ratio between the thermal efficiency and Carnot efficiency. The second law efficiency is given by equation 3.4.1.12.

$$\eta_{II} = \frac{\eta_{\text{th}}}{\eta_{\text{c}}} \quad (\text{equation 3.4.1.12})$$

Using the previously calculated thermal and Carnot efficiency in equation 3.4.1.12,  $\eta_{II}$  is 64.5%.

## Thermodynamic Model

The preliminary calculations shown above were determined using the R1234ze saturation tables provided by Honeywell in their *Genetron Refrigerants Modeling Software* [49]. Additionally, the thermodynamic analysis was implemented in MATLAB using a thermodynamic properties package for the fluid properties. The results from the program were nearly identical to the results determined from the Honeywell reference. The MATLAB code and results can be found in **Appendix A** and **Appendix B**, respectively.

### 3.4.2 Fluid Mechanics Analysis

A fluid mechanics analysis was used to characterize the pressure drops over the four sections of pipe within the ORC system and subsequently determine the additional pumping power required. The length of piping between the components of the ORC was approximated at 1.5 feet (~0.5 m)—a rough estimation made based on the expected size of the overall system, but without provided dimensions of an existing ORC system (which was not publicly available). The analysis began with the mass flow rate equation, wherein  $D$  is the inner pipe diameter (m),  $V$  is the fluid velocity (m/s),  $\rho$  is the fluid density ( $\text{kg/m}^3$ ), and  $\dot{m}$  is the mass flow rate of the working fluid (kg/s). The mass flow rate was given by equation 3.4.1.6 from the thermodynamics analysis and the diameter was specified as a manual (and mutable) input. The density was determined based on the fluid state of the R1234ze, as the fluid property varies with temperature and pressure.

$$\dot{m} = \rho V A = \rho V \frac{\pi}{4} D^2 \quad (\text{equation 3.4.2.1})$$

Rearranging equation 3.4.2.1 to solve for velocity produces equation 3.4.2.2.

$$V = \frac{\dot{m}}{\rho \frac{\pi}{4} D^2} \quad (\text{equation 3.4.2.2})$$

With the velocity of R1234ze known, the Reynolds number was calculated, wherein  $\mu$  is the dynamic viscosity of R1234ze (Pa-s), which varies with temperature and pressure.

$$Re = \frac{\rho V D}{\mu} \quad (\text{equation 3.4.2.3})$$

With the Reynolds number known, the friction factor was calculated using Haaland's equation, wherein  $\epsilon$  is the roughness of copper piping, a value of  $1.5 \mu\text{m}$  [52].

$$\frac{1}{\sqrt{f}} = -1.8 \log \left[ \left( \frac{6.9}{Re} \right) + \left( \frac{\epsilon/D}{3.7} \right)^{1.11} \right] \quad (\text{equation 3.4.2.4})$$

Where  $f$  can be re-written as:

$$f = \left( -1.8 \log \left[ \left( \frac{6.9}{Re} \right) + \left( \frac{\epsilon/D}{3.7} \right)^{1.11} \right] \right)^{-2} \quad (\text{equation 3.4.2.5})$$

With  $f$  known, the head loss ( $h_L$ ) for each section of pipe in the ORC system could be found, while assuming a constant pipe diameter. The  $K_L$  term is a loss coefficient (dimensionless number), that accounts for the minor losses associated with changes in velocity due to pipe roughness, fittings, valves, bends, expansion, contraction, etc. For the preliminary fluids analysis of the ORC system, it was assumed that there were  $90^\circ$  bends in the pipes connecting the components so that they were arranged in

a consolidated rectangular formation. A value of 0.9 is used for  $K_L$  to represent a 90° bend with threads inside the piping.

$$h_L = \left( f \frac{L}{D} + \sum K_L \right) \times \frac{v^2}{2g} \quad (\text{equation 3.4.2.7})$$

The pressure drop across each section of pipe could be determined using equation 3.4.2.8, as all the variables had been determined from equations 3.4.2.1 - 3.4.2.7. Note that the  $f \frac{L}{D}$  term represents the friction loss in a straight pipe, and the  $\sum K_L$  term represents the local losses within the piping system.

$$\Delta P_L = h_L \times \rho \times g = \left( f \frac{L}{D} + \sum K_L \right) \times \frac{\rho V^2}{2} \quad (\text{equation 3.4.2.8})$$

Once the pressure drops through each ORC pipe were calculated, the associated power required to pump the R1234ze could be determined, given the velocity and diameter of the pipe. For each pipe section of the ORC, the power required to pump the fluid was given by equation 3.4.2.9.

$$P_{power} = \Delta P_L Q = h_L \times \dot{m} \times g \quad (\text{equation 3.4.2.9})$$

Where volumetric flow rate  $Q$  ( $\text{m}^3/\text{s}$ ) is given by:

$$Q = V_{avg} \times A = V_{avg} \left( \frac{\pi}{4} D^2 \right) \quad (\text{equation 3.4.2.10})$$

As shown in **Table 2**, the R1234ze has four distinct states as it flows throughout the ORC (see **Figure 25**). Each state corresponded to distinct fluid properties for viscosity and density, which were ultimately used to calculate the pressure drops and the power requirements of the ORC pump.

**Table 2:** Fluid properties of R1234ze at all states within the ORC.

State of R1234ze	Temperature (°C)	Pressure (kPa)	Density ( $\text{kg}/\text{m}^3$ )	Viscosity ( $\mu\text{Pa}\cdot\text{s}$ )
1 (Saturated Vapor)	81.5	2073.1	125.39	16.005
2 (Saturated Vapor)	40	766.5	40.64	12.93
3 (Saturated Liquid)	40	766.5	1111.51	167
4 (Subcooled Liquid)	40.85	2073.1	1117.4	159.86

An important aspect of the fluid mechanics analysis was examining the effect of varying the pipe diameter. Different pipe sizes correspond to changes in velocity, pressure drop, and pump power. Since the purpose of the ORC system is to generate electricity, the power required to pump the R1234ze through the ORC should be minimized, thus enabling a greater net output of electricity. To evaluate the effect of different pipe sizes, numerous iterations of the analytical process presented in equations 3.4.2.1-3.4.2.10 were conducted for a range of pipe sizes for each of the four pipe sections in the ORC.

The results for each pipe section (corresponding with each of the four ORC fluid states) are included in **Appendix C**.

The most notable result from the fluid mechanics analysis was the total power required to pump R1234ze through the ORC. Since the pipe sections within the ORC were in series, the total pressure drop of the system was represented by the sum of the pressure drops from each pipe section. Similarly, the total pump power required to overcome the pressure losses within the ORC was represented by the sum of the pump powers from each pipe section. To examine the effect of pipe size on the total pump power, the inner diameter of the pipe varied from 0.305 inches to 2.907 inches (0.008 meters to 0.074 meters), based on available copper pipes from *Lakeside Supply Company* [53]. The results from the fluid mechanics analysis are presented in **Table 3**.

**Table 3:** Preliminary pump power results with varying inner diameter [53].

Outer Diameter (in)	Outer Diameter (m)	Inner Diameter (in)	Inner Diameter (m)	Wall Thickness (in)	Wall Thickness (m)	Total Pump Power (W)
0.375	0.010	0.305	0.008	0.035	0.0009	53.35
0.500	0.013	0.402	0.010	0.049	0.0012	15.50
0.625	0.017	0.527	0.013	0.049	0.0012	4.73
0.750	0.019	0.652	0.017	0.049	0.0012	1.89
0.875	0.022	0.745	0.019	0.065	0.0017	1.07
1.125	0.029	0.995	0.025	0.065	0.0017	0.31
1.375	0.035	1.245	0.032	0.065	0.0017	0.12
1.625	0.041	1.481	0.038	0.075	0.0018	0.06
2.125	0.054	1.959	0.050	0.083	0.0021	0.02
2.625	0.067	2.435	0.062	0.095	0.0024	0.01
3.125	0.079	2.907	0.074	0.109	0.0028	0.00371

Considering the results from **Table 3**, the recommended pipe size was determined to have an inner diameter of 0.010 meters (0.402 inches) [53]. The 0.010 meter inner diameter pipe was selected for a few reasons. First, the pipe diameter ensured an economical liquid velocity of approximately 0.6 m/s [54] (the velocity of the vapor R1234ze ranged from 5 m/s - 18 m/s in the other sections of pipe). Second, the pipe size selected could withstand the working pressures of the system. For a temperature of 200°F (93°C), the pipe with an inner diameter of 0.010 m and a wall thickness of 0.0012 m (0.049 inches) has a rated pressure of 904 psig (6232.86 kPa) [53]. The highest pressure in the ORC is only 2073 kPa (see **Table 2**), which is well below the rated pressure. Lastly, the 0.010 m inner diameter pipe had a lower associated pump power than the 0.008 m pipe, which is why it was selected for the ideal pipe. Further increasing the inner pipe diameter to reduce the required pump power decreased the velocities of the R1234ze to impractical rates.

The recommended pipe size for the ORC connecting pipes both minimized the required pumping power and ensured an economical fluid velocity, based on the fluid conditions corresponding to the preliminary thermodynamic analysis. Ultimately, the chosen pipe diameter was 0.010 meters (0.402 inches), which required a pumping power of 15.50 W.

### 3.4.3 Heat Loss Through ORC Pipes and Insulation

A heat transfer analysis of the four sections of insulated connecting pipe within the ORC was conducted in order to characterize the heat exchange through the pipes, and to verify that there was negligible heat loss throughout the ORC system. **Figure 26** shows a cross-section of the ORC connecting pipe and insulation, where R1, R2, and R3 represent the inside radius of the pipe, outside radius of the pipe, and the radius of the insulation, respectively.

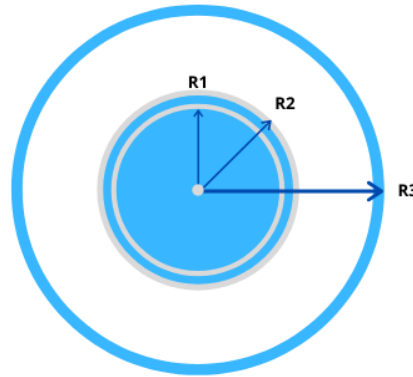


**Figure 26:** Cross-section of copper pipe and insulation.

Using the known thermal properties of given copper piping and fiberglass insulation for the ORC system, the heat loss through the pipe was found. The values for these materials were determined based on experimental results from Thermtest Instruments ( $k_{insulation} = 0.0430 \text{ W/m-K}$ ) [55]. Materials from *Grainger Industrial Supply* were also used for the purposes of these calculations ( $t_{insulation} = 0.0381 \text{ m}$ ) [56], [57]. Based on the results from section 3.4.2,  $D_1 = 0.0102 \text{ m}$ , and  $D_2 = 0.0127 \text{ m}$ .  $D_1$  represents the inner diameter of the ORC system pipe, while  $D_2$  represents the outer (a summation of the recommended inner diameter and wall thickness). For each section of pipe, it was assumed that  $L = 1.5 \text{ ft}$  ( $\sim 0.5 \text{ m}$ ).

Next, the contact areas of the pipe that would be contributing to the heat transfer were calculated with the following equations.

$$A_{D1} = \pi D_1 L \quad (\text{equation 2.4.3.1})$$

$$A_{D2} = \pi D_2 L \quad (\text{equation 2.4.3.2})$$

$$A_{tot} = \pi (D_2 + 2t_{insulation})L \quad (\text{equation 2.4.3.3})$$

The Honeywell *Genetron Refrigerants Modeling Software* provided fluid properties for R1234ze at each state throughout the ORC, illustrated in **Table 4**.

**Table 4:** Fluid properties of R1234ze at relevant states.

State of R1234ze	Temperature (°C)	Fluid Viscosity ( $\mu\text{Pa}\cdot\text{s}$ )	Prandtl Number	Thermal Conductivity (mW/m-K)
1 - Saturated vapor	81.5	16.00	1.175045	21.642
2 - Saturated vapor	40	12.93	0.90862	14.952
3 - Saturated Liquid	40	167	3.48347	69.187
4 - Subcooled liquid	40.85	159.86	3.47456	70.015

The fluid property values in **Table 4** correspond to the R1234ze vapor in its saturated state at a high temperature, followed by a saturated vapor at a lower temperature, then saturated liquid, and finally a subcooled liquid.

In order to determine the heat loss, the heat transfer coefficient  $h$  in each unique pipe section of the ORC was calculated. The first step of this process was finding the Reynolds number ( $Re$ ) for each section of the pipe. The Reynolds number is the ratio of inertial forces to viscous forces within the working fluid and is useful for predicting flow regimes. For this analysis, turbulent flow (corresponding to a high Reynolds number  $>2300$ ), was assumed. The formula used to determine the Reynolds number in each ORC pipe section is presented in equation 2.4.3.4.

$$Re = \frac{\dot{m} \times D_h}{\mu \times A_s} \quad (\text{equation 2.4.3.4})$$

Mass flow rate was calculated in Section 3.4.1, and was found to be 0.058 kg/s. However, fluid viscosity is a property and function of temperature. In a circular tube, which was assumed for the ORC connecting pipes, the hydraulic diameter  $D_h$  is simply the inner diameter of the pipe [58]. Subsequently,  $A_s$  is the cross-sectional area of this region.

$$A_s = \pi \left( \frac{D_i}{2} \right)^2 \quad (\text{equation 2.4.3.5})$$

The Reynolds number was found in order to determine the Nusselt number ( $Nu$ ), another dimensionless ratio that is used to analyze fluid flow. The Nusselt number describes the relative effect of convective to conductive heat transfer across a boundary, and varies if a hot fluid enters a cold-walled duct, or vice versa [59].

Given the turbulent flow assumption, the *Dittus-Boelter Equation* (equation 2.4.2.6 & equation 2.4.2.7) was utilized to calculate the Nusselt number. The equation is valid if the following conditions are met:

1.  $0.6 \leq Pr \leq 160$
2.  $ReD \geq 10,000$
3.  $L/D \geq 10$

The Dittus-Boelter equation, shown below, was analyzed in its two forms in understanding the relevant conditions for this system.  $Pr$  refers to the *Prandtl number*, the final non-dimensional ratio used in this analysis. Prandtl number describes the quantity of momentum diffusivity, or kinematic viscosity, to

thermal diffusivity. The Prandtl number relates the viscosity of a fluid to its thermal conductivity, and can therefore be utilized to simultaneously examine the momentum transport and thermal transport capacity of a fluid [60]. The exponent of the Prandtl number changes based on whether the fluid is hotter or colder than the pipe in the following equations.

$$Nu = \frac{hD_h}{k} = 0.023Re^{0.8} + Pr^{0.3}, T_{pipe} < T_{fluid} \quad (\text{equation 2.4.3.6})$$

$$Nu = \frac{hD_h}{k} = 0.023Re^{0.8} + Pr^{0.4}, T_{pipe} > T_{fluid} \quad (\text{equation 2.4.3.7})$$

For a cooling fluid, that is losing heat to the pipe,  $n = 0.3$ . For a heating fluid,  $n = 0.4$  [61]. For the purposes of this cycle, as R1234ze was never colder than the assumed  $T_{air}$  of 20 °C,  $n = 0.3$  was used for all sections of the system.

For the analysis, the variables for  $\dot{m}$ ,  $\mu$ ,  $Pr$ ,  $D_h$ , and  $k$  are fluid properties either obtained from the *Honeywell* software or previously calculated. Reynolds number ( $Re$ ) was calculated with equation 2.4.2.4 for each state, as presented in **Table 5**. Additionally, the heat transfer coefficient of the R1234ze was calculated by rearranging equation 2.4.3.6 to solve for  $h$ . The results for the heat transfer coefficient throughout the four sections of connecting pipe in the ORC are also presented in **Table 5**.

**Table 5:** Resulting Reynolds number and heat transfer coefficient throughout ORC.

State of R1234ze	Reynolds number	Heat transfer coefficient (W/m <sup>2</sup> -K)
1 - Saturated vapor	453,900	1639 W/m <sup>2</sup> -K
2 - Saturated vapor	561,900	1343 W/m <sup>2</sup> -K
3 - Saturated Liquid	43,500	811.5 W/m <sup>2</sup> -K
4 - Subcooled Liquid	45,450	850.0 W/m <sup>2</sup> -K

With known heat transfer coefficients throughout the pipe, the thermal resistance could be calculated. Knowledge of the thermal resistances of the R1234ze fluid throughout the pipe sections could then be used to determine associated temperature gradients over the pipe and insulation in each pipe section. Equations 2.4.3.8 through 2.4.3.11 represent the thermal resistance corresponding to each region or boundary of the pipe configuration.  $R_i$  ( $R_{conv,1}$ ) represents the convective resistance of the R1234ze fluid inside the pipe;  $R_1$  ( $R_{pipe}$ ) represents the conductive resistance across the wall of the pipe;  $R_2$  ( $R_{ins}$ ) represents the convective resistance across the layer of insulation; and  $R_o$  ( $R_{conv,2}$ ) represents the convective resistance of the ambient air outside the pipe.

$$R_i = R_{conv,1} = \frac{1}{h_1 A_{D2}} \quad (\text{equation 2.4.3.8})$$

$$R_1 = R_{pipe} = \frac{\ln[(D_3/2)/(D_2/2)]}{2\pi k_{pipe} L} \quad (\text{equation 2.4.3.9})$$

$$R_2 = R_{ins} = \frac{\ln[(D_4/2)/(D_3/2)]}{2\pi k_{ins} L} \quad (\text{equation 2.4.3.10})$$

$$R_0 = R_{conv,2} = R_{air} = \frac{1}{h_{air} \cdot A_{tot}} \quad (\text{equation 2.4.3.11})$$

Together, the thermal resistances represent the physical set up of the pipe configuration, from the fluid inside the copper pipe to the exterior of the insulation. For each section of pipe, it was assumed that  $L = 1.5$  ft ( $\sim 0.5$  m). It was also assumed that  $R_{pipe}$  and  $R_{ins}$  were the same in each section of pipe regardless of the fluid's state, as the thermal properties of the pipe and insulation remain essentially constant (although there would be slight changes due to the changing R1234ze temperature throughout the ORC). Additionally, it was assumed that  $R_{air}$  was the same in all sections of pipe since the outside air temperature was not changing. The heat transfer coefficient of air ( $h_{air}$ ) was estimated between a range of  $2.5$  W/m<sup>2</sup>-K to  $25$  W/m<sup>2</sup>-K [62]. A final value of  $10$  W/m<sup>2</sup>-K was decided upon, which is typically associated with free/natural convection [63].

$R_{conv,1}$  was calculated for each state, since the heat transfer coefficient of the working fluid was different for each section of the connecting pipe. The individual resistances ( $R_{conv,1}$ ,  $R_{pipe}$ ,  $R_{ins}$ , and  $R_{conv,2}$ ) were added together to find  $R_{total}$  for each section of the pipe, as summarized in **Table 6**.

**Table 6:** Thermal resistances and temperature gradients in ORC connecting pipe sections.

State of R1234ze	$R_{conv,1}$ (K/W)	$R_{total} = R_{conv,1} + R_{pipe} + R_{ins} + R_{conv,2}$ (K/W)	$\Delta T_{pipe}$ (°C)	$\Delta T_{insulation}$ (°C)
1 - Saturated vapor	0.04164	5.627	0.002166	52.48
2 - Saturated vapor	0.05083	5.636	0.0007034	17.04
3 - Saturated liquid	0.0841	5.669	0.0006993	16.94
4 - Subcooled liquid	0.0803	5.665	0.0007295	17.67

Subsequently, the rate of heat loss in the pipe was found, as well as the temperature difference exhibited in both the pipe and insulation (not the fluid).  $T$  refers to the fluid temperature, while  $T_{\infty}$  refers to the outer air temperature (also known as  $T_{air}$ ). **Table 7** summarizes the total heat loss for each pipe section.

$$\dot{Q} = \frac{T - T_{\infty}}{R_{total}} \quad (\text{equation 2.4.3.12})$$

$$\Delta T_{pipe} = \dot{Q} \cdot R_{pipe} \quad (\text{equation 2.4.3.13})$$

$$\Delta T_{ins} = \dot{Q} \cdot R_{ins} \quad (\text{equation 2.4.3.14})$$

$$\Delta T_{fluid} = \dot{Q} \cdot R_{conv,1} \quad (\text{equation 2.4.3.15})$$

**Table 7:** Heat loss exhibited in ORC connecting pipes with R1234ze working fluid.

State of R1234ze	$\dot{Q}$ (W)	$\Delta T_{fluid}$ (°C)
1 - Saturated vapor	23.64	0.9844
2 - Saturated vapor	7.573	0.3849

3 - Saturated liquid	7.223	0.6075
4 - Subcooled liquid	7.527	0.6044

Based on these results, it was observed that the most significant changes occur in the first pipe section of the ORC system, wherein the fluid is a saturated vapor at a high temperature exiting the evaporator and traveling to the turbine. Since the fluid is at its highest temperature across the first section of pipe, the greatest heat losses were correspondingly experienced over that region. It is important to note that the rate of heat loss was determined within each region of the system in order to confirm that the losses were not significant. Since the heat input to the ORC was 10 kW, the sum of the losses across the pipes only accounted for a difference of approximately 0.5%. Furthermore, the drops in fluid temperature across the pipes ( $\Delta T_{fluid}$ ) as a result of heat loss were also very small. For the worst case (the first pipe section where the temperature of R1234ze is greatest), there was less than 1°C difference. Therefore, the analysis presented in this section for the heat loss through the insulated ORC connecting pipes showed that the heat losses could be considered negligible.

### 3.5 SHEC Component

For the server heat extraction cycle (SHEC), there were two leading data center cooling systems that presented strong potential. Liquid cooling technology has advanced over recent years and is now emerging as the dominant means of cooling computing equipment in modern, high density data centers. Due to its higher heat removal capacity, liquid cooling enables better energy capture and can increase the performance of the processor by up to 33% (compared to air cooling) [3]. Thus, direct liquid cooling was a strong candidate for the SHEC as a developed, reliable, and effective means of server heat extraction. However, the exciting potential of two-phase cooling, which has been explored in research over the last decade, could not be ignored. By utilizing microchannel heat sinks, significant increases in convection heat transfer coefficients can be achieved via the process of nucleate boiling [1]. Furthermore, two-phase cooling can provide better uniformity of heat transfer across the micro-evaporator, compared to liquid cooling systems with water [1]. Nonetheless, two-phase cooling with microchannel heat sinks is in the early stages of technological development, and a consensus on how to model and characterize these systems has yet to be reached in the scientific community [43]. Both liquid cooling and two-phase cooling demonstrated a potential for application in the SHEC, yet each is associated with various advantages, conditions, and limitations. Most notably, the current gaps in research in regards to two-phase cooling made a fully developed analysis not possible at this time. Therefore, the performance of a liquid cooling system was selected for the robust investigation, design, evaluation, and optimization for the SHEC. A simplified schematic of the liquid cooling system is shown in **Figure 27**. As shown in the diagram, waste heat from the CPU(s) is transferred to a coolant (liquid), thus increasing the temperature of the coolant. The heated liquid coolant is directed to the ORC evaporator heat exchanger, where it transfers the waste heat to the ORC working fluid. The waste heat from the CPUs is used to raise the temperature of the chilled ORC working fluid (liquid) to the saturation temperature, and also to change the phase of the fluid to a saturated vapor. Thus, at the outlet of the evaporator, the ORC fluid is a heated vapor. After transferring the CPU waste heat to the ORC fluid, the coolant exits the ORC evaporator at a lower temperature, and is pumped as a cooled liquid

back to the CPUs to repeat the cycle. The coolant effectively provides cooling to the CPUs while also acting as a means of capturing and transferring heat to the ORC.

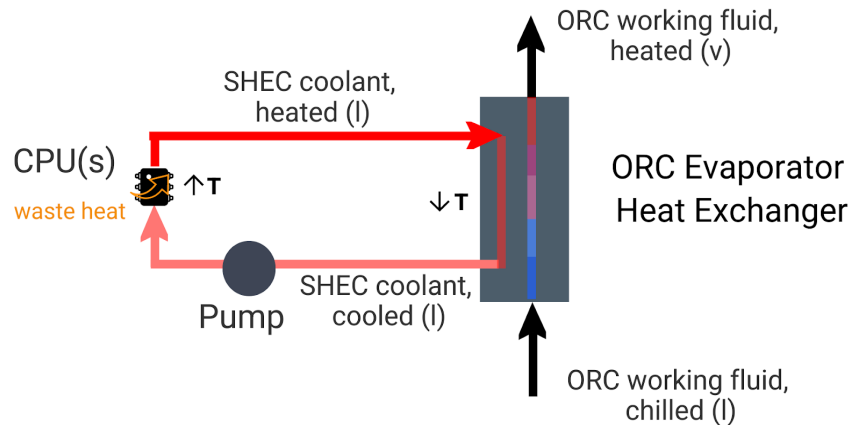


**Figure 27:** Simplified schematic of the SHEC with liquid cooling.

**Figure 28** presents a potential schematic for two-phase cooling, should this system be taken beyond the preliminary stages as proposed by this project. Due to the thermal-physical differences between liquid cooling and two-phase cooling, the mechanical designs of the SHEC would be different. The liquid cooling SHEC required a pump to move the coolant through the system. However, a compressor should be used in the two-phase cooling SHEC to move the coolant, since it is in the vapor phase. Additionally, the compressor can provide a temperature upgrade to the vapor coolant, thus increasing the quality of heat entering the ORC evaporator heat exchanger. It is recommended that the two-phase SHEC includes a separator following the heat transfer over the CPU(s) to ensure that only a saturated vapor enters the compressor. In the ORC evaporator, the heated SHEC coolant (vapor) transfers its heat to the ORC working fluid, heating and evaporating it. As a result of losing thermal energy, the SHEC vapor condenses and cools. The SHEC coolant then exits the heat exchanger as a chilled liquid, and recombines with the slightly heated excess liquid from the separator.

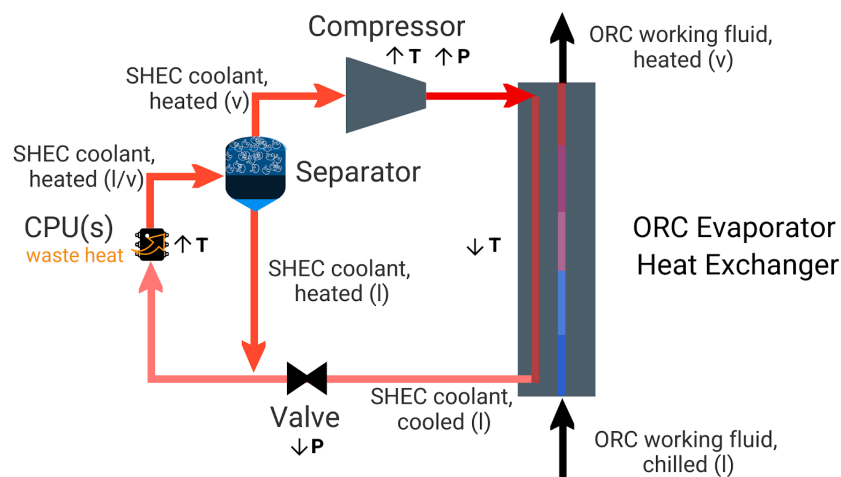


**Figure 28:** Simplified schematic of the SHEC with two-phase cooling.

Though both mechanical systems present a strong potential for SHEC application, a comprehensive analysis of the liquid cooling system was completed using simulation software. Ultimately, a comparison of both systems is encouraged in determining the superior SHEC design. Discussed in the following sections are heat and fluid flow simulations for a liquid cooling system, wherein the microchannel heat sink and corresponding coolant flow are considered from a 2D and 3D perspective.

## 4.0 Development of Microchannel Heat Sink Simulations

A thorough and detailed process was required to simulate the fluid flows through a microchannel heat sink mounted on a CPU for data center cooling. Two different flow conditions were considered for simulation, including single-phase liquid fluid flow (associated with the ‘liquid cooling’ SHEC) and two-phase liquid and vapor fluid flow (associated with the ‘two-phase cooling’ SHEC). However, only single-phase liquid flow scenarios were pursued with the simulation software due to complications later discovered with characterizing two-phase flows. The finite element analysis program COMSOL was utilized to create the simulation. However, prior to beginning the COMSOL simulations, it was critical to explore and understand the theory that characterizes heat transfer and fluid flow through microchannels. The textbook from Kandlikar et al., *Heat Transfer and Fluid Flow in Minichannels and Microchannels* [64] was consulted to create a pre-simulation report of the problem setup and expected outcomes. Then, two 2D slices of the 3D liquid cooling microchannel problem were developed in COMSOL to understand the basics of simulation and facilitate the debugging process. Once the 2D simulations were completed, working 3D simulations were developed.

The 3D simulations consisted of both laminar and turbulent models to observe potential effects of different flow conditions. Additionally, the 3D simulations included additional design considerations for the microchannel heat sink (MCHS) to more accurately represent the physical system. Lastly, a similar set of pre-simulation steps were followed for the setup of the two-phase MCHS simulation, which started with a review of relevant theory and examples from Kandlikar et al. [64]. However, it was found that the complexity of two-phase flow through MCHSs warranted a far deeper investigation and thus exceeded the scope of the project. The development of two-phase MCHS simulations in COMSOL was not pursued, but is recommended for future project endeavors.

### 4.1 Development of Liquid Cooling MCHS Simulation

Prior to beginning the COMSOL simulations, a proper understanding of the theoretical heat transfer and fluid mechanics principles was required. The textbook from Kandlikar et al. was consulted to determine the relevant parameters for setting up the heat transfer and flow problem [64]. The following initial assumptions could be reasonably made:

- 1.) The system is under steady-state conditions with a constant heat flux of  $65 \text{ W/cm}^2$  (or alternatively a constant maximum temperature of  $85^\circ\text{C}$ ) from the CPU.
- 2.) All walls of the microchannels of the heat sink are smooth.
- 3.) The liquid coolant is an incompressible fluid.
- 4.) The flow through the microchannels is fully developed and laminar, or turbulent.
- 5.) The channels are completely filled by the fluid (i.e. no capillary effects associated with open channels).

The heat flux for the simulated model was selected based on a table from Ebrahimi et al. that summarized typical heat load and dimensions of microprocessors/cores in recent literature [1]. One of

the mid-range examples listed in the table was from Marcinichen et al, which had a heat load of 162.5 W applied over a 2.5 cm<sup>2</sup> area, for a heat flux of 65 W/cm<sup>2</sup> [1].

Due to the recommendations from Ebrahimi et al., R1234ze was initially chosen as the working fluid for both the single-phase and two-phase MCHS simulations [3]. Kandlikar et al. provided equations and tabulated values for fully developed, laminar conditions for flow through a microchannel and included a helpful worked example that demonstrated how to determine the geometry of the heat sink and how to calculate the flowrate of the fluid, heat transfer coefficient of the fluid, and the pressure drop throughout the microchannel (as well as several other parameters) [64]. The geometry of the heat sink and flow rate influence the effectiveness of heat transfer from the heat sink to the working fluid. The pressure drop is also a crucial parameter, as it affects the power required to pump the working fluid throughout the cooling system.

Example 3.1 from Kandlikar et al. was studied and replicated for the case of R1234ze liquid fluid flow through a MCHS over a CPU [64]. The complete pre-simulation report with theoretical calculations can be found in **Appendix D**. The outcomes based on the calculation process in example 3.1 from Kandlikar et al. served as a basis for validating whether the results of the COMSOL simulations were reasonable [64]. To reduce the computational load in COMSOL, the fluid flow through only a single microchannel was simulated, as opposed to an analysis of the entire MCHS. Therefore, it is also assumed that each channel of the MCHS exhibits the same thermal and fluid behavior. However, studies with robust experimental testing resources have shown that flows through each channel vary across the heat sink, notably at the peripheries of the MCHS [64]. Although beyond the scope of this investigation, it is recommended that future research groups undergo a closer examination of the fluid flows over the entire MCHS. A schematic of the simulated microchannel section in COMSOL is shown in **Figure 29**, which includes the approximated mass flow rate of R1234ze ( $5 \times 10^{-5} \text{ kg/s}$ ) from the theoretical calculations in **Appendix D** (based on the example from Kandlikar et al.).

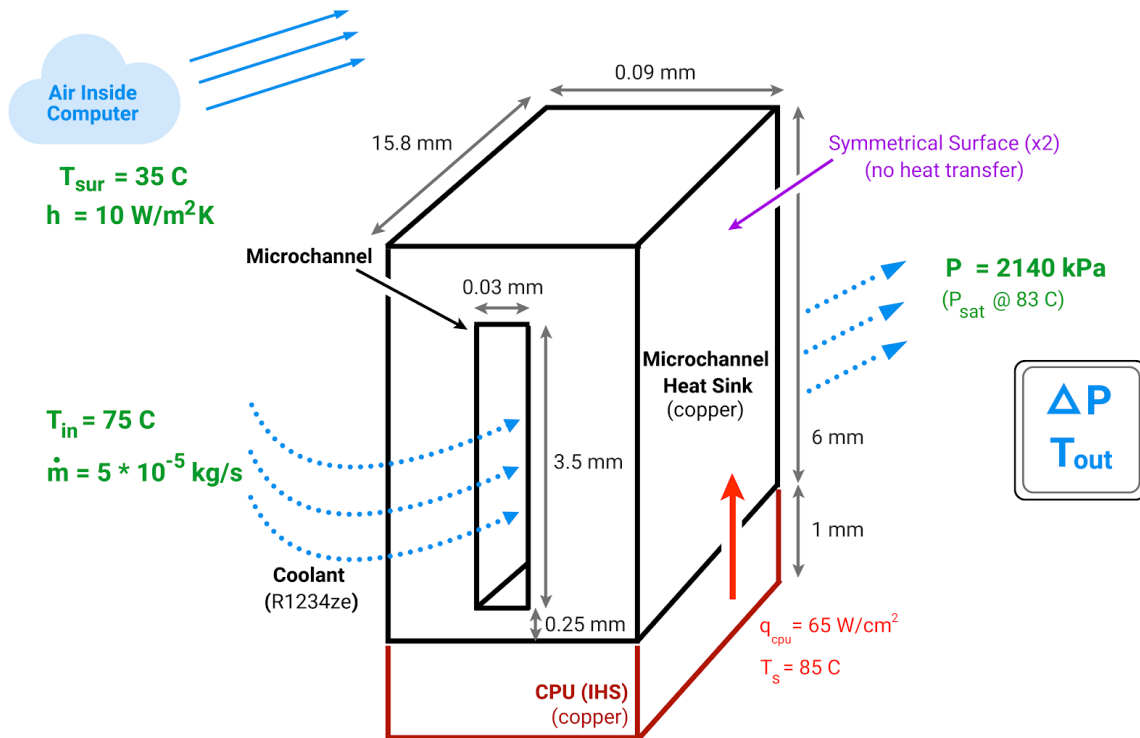


**Figure 29:** Model of isolated microchannel for initial liquid cooling MCHS simulation.

Additional assumptions were identified to fully define the problem:

- 6.) The air surrounding the MCHS inside the computer is approximately 35°C (free convection,  $h = 10 \text{ W/m}^2\text{K}$ ).
- 7.) No heat transfer occurs at the outer left and right surfaces of the MCHS which are internally contained within the MCHS for each microchannel (symmetry boundary condition).

An inlet fluid temperature was initially set at 75°C, which is the typical maximum for liquid cooling systems as summarized by Ebrahimi et al. [1]. The absolute system pressure (2140 kPa) was set at the liquid saturation pressure of R1234ze at 83°C to ensure that the fluid would not begin to vaporize as a result of the heat transfer through the microchannel. In other words, the increase in temperature of the R1234ze over the CPU was not expected to reach or exceed 83°C, so the R1234ze would therefore remain in the liquid state if the system pressure was set to the saturation pressure of 83°C. The dimensions of the microchannel were selected through a process of several iterations of theoretical calculations to produce the conditions for laminar flow (Reynolds Number < 2300). The results from the theoretical calculations approximated the pressure drop (including major and minor losses) to be approximately 11 kPa. Ebrahimi et al. indicates that a typical temperature increase of 2-5°C over the CPU can be expected [1].

After the pre-simulation report and calculations were compiled for single-phase, laminar flow through the MCHS (see **Appendix D**), the two different slices of the 3D problem were examined using 2D simulations in COMSOL. The 2D simulations are described in detail in section 4.1.1. The 2D simulations helped to initially simplify the complicated 3D model to ensure the proper setup of the

problem in COMSOL. The comparison of the results from the 2D simulations and the pre-simulation calculations served as an empirical check before the 3D simulation was created for single-phase, laminar flow through the MCHS.

One of the most important things to note is the integrity of 2D laminar flow simulations as a starting point, as it was the first step towards a theoretical understanding of fluid flow through a single microchannel over the CPU. Due to the limitations of the 2D simulations, the creation of 3D simulations was essential for accurately characterizing the thermal and fluid behavior through the microchannels of the MCHS. The 3D simulations included both laminar and turbulent models to investigate whether certain flow conditions might enable optimal heat transfer across the MCHS since higher heat transfer coefficients are typically observed in turbulent and developing flows. Finally, the development of the 3D COMSOL simulations of the microchannel fluid flows led to additional design considerations in the final iterations of the MCHS simulation models.

#### 4.1.1 Stage One: 2D Simulations with Laminar Flow

The first 2D simulations developed in COMSOL were comprised of two distinct cross-sectional slices through the 3D geometry of a single microchannel in the MCHS. The orientation and dimensions of the slices are shown in **Figure 30**.

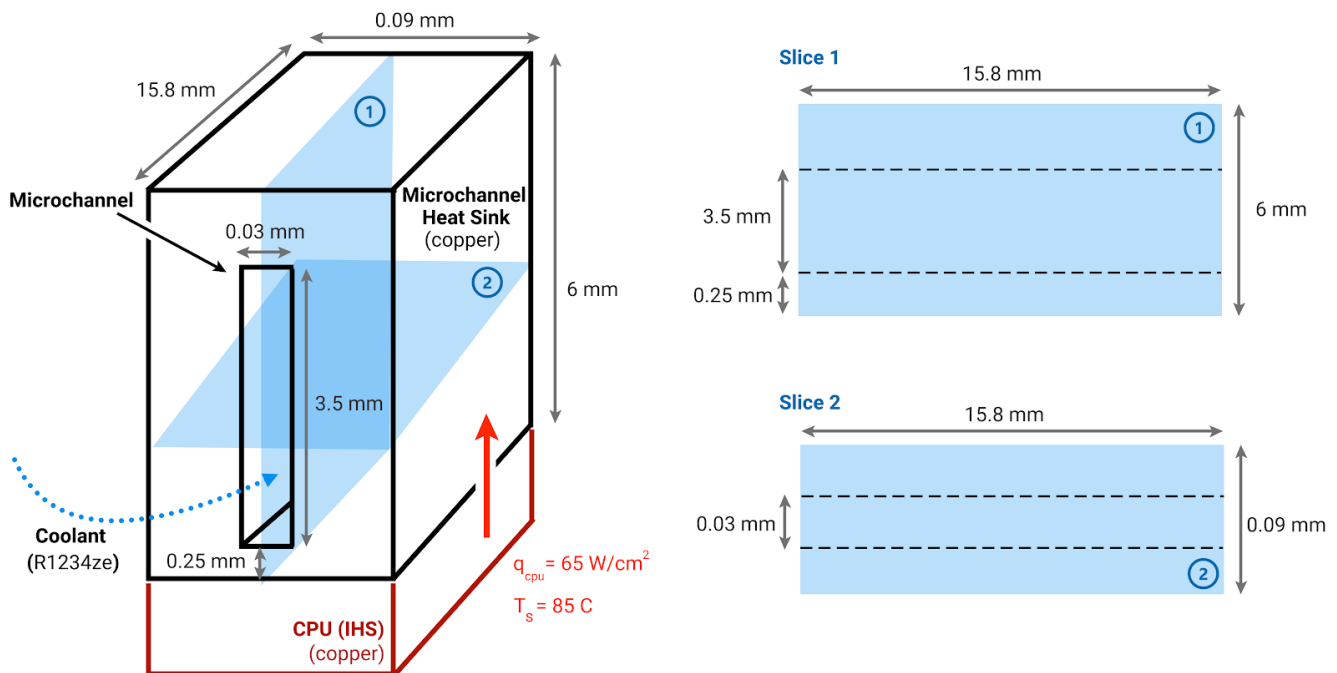


**Figure 30:** Visualization of 2D cross-sections from 3D microchannel over CPU.

The first cross-section, “Slice 1,” is a view of the microchannel from the side that was useful in analyzing the characteristics of fluid flow, as well as heat transfer along the surface that interfaces with the CPU. The geometry of Slice 1 in COMSOL is shown in **Figure 31** wherein the fluid flows from left to right. “Slice 2” is a view from the top down, parallel to the surface of the CPU. Since Slice 2 does not

include the interface with the heat producing element (CPU), only flow conditions such as velocity and pressure could be determined. The geometry of Slice 2 in COMSOL is shown in **Figure 32** wherein the fluid flows from bottom to top. Since the microchannel was very narrow, the x-axis in **Figure 32** was scaled by a factor of 20 to aid with visualization.

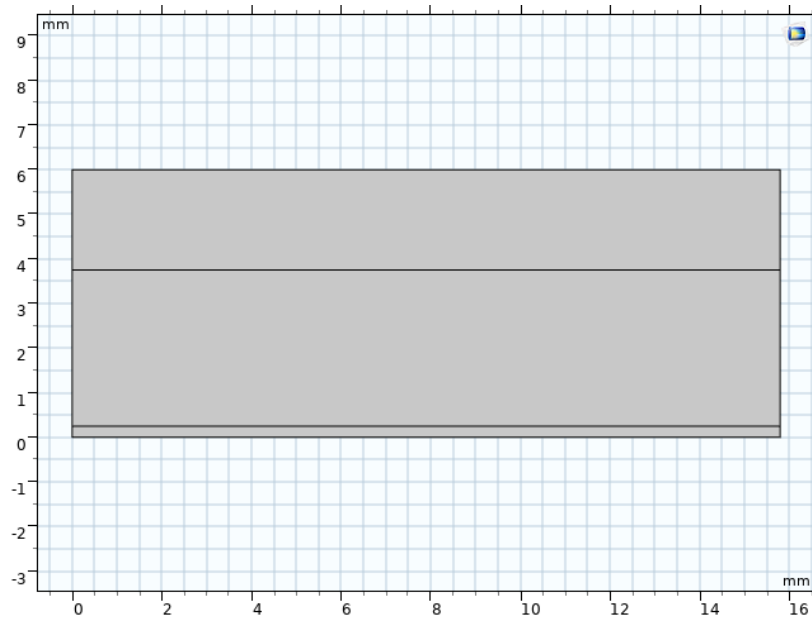


**Figure 31:** Geometry of slice 1 of the microchannel in COMSOL.

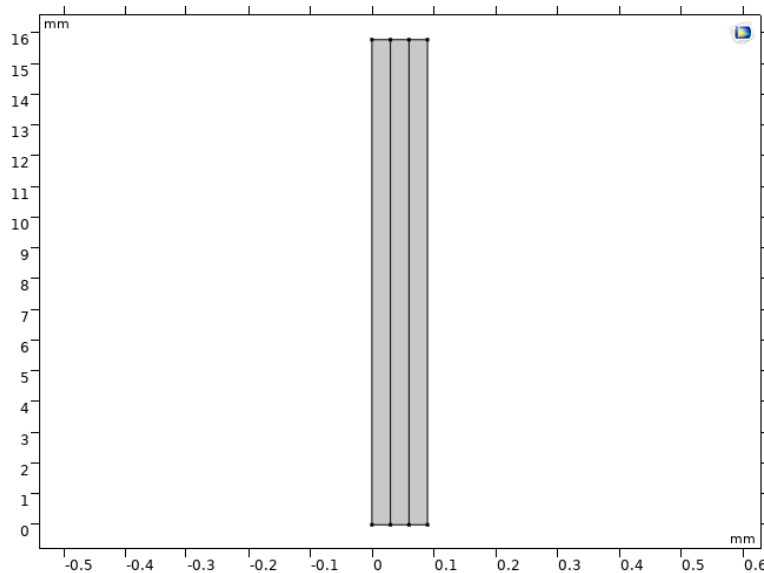


**Figure 32:** Geometry of slice 2 of the microchannel in COMSOL.

To compare the performance of different fluids, the two cross-sectional slices were analyzed with regard to four unique coolants: R1234ze, R134a, air, and water. Initially, it was anticipated that R1234ze would be the appropriate choice for both the single-phase liquid cooling SHEC and the two-phase SHEC. However, COMSOL only had the properties for R134a loaded in the material library. Thus, R134a was used as the fluid for the first simulation, instead of R1234ze. The system pressure (absolute) was

adjusted to the corresponding liquid saturation pressure of R134a at 83°C (~2800 kPa), as opposed to that for R1234ze (~2140 kPa). However, all other boundary conditions determined for R1234ze from the pre-simulation calculations were kept the same (e.g. flow rate, inlet temperature, etc.). Additionally, water and air were included as fluids for comparison, with an atmospheric (0 gauge) system pressure while all other boundary conditions remained the same. Lastly, the *Genetron Software* from Honeywell was utilized to create plots and curve fits of the relevant material properties of R1234ze (dynamic viscosity, specific heat capacity, density, thermal conductivity, and specific heat ratio:  $c_p/c_v$ ) in order to simulate the fluid behavior of R1234ze in the COMSOL simulations.

All the 2D simulations presented in this section were run with the constant heat flux boundary condition ( $65 \text{ W/cm}^2$ ). However, when initially troubleshooting the simulations in COMSOL, it was helpful to run the constant temperature boundary condition ( $85^\circ\text{C}$ ) as a comparison. The two different thermal boundary conditions were officially compared in section 4.1.2 in the 3D simulations.

Based on the results from the 2D simulations, water indicated a better performance than R1234ze for single-phase liquid flow through the microchannel. The following set of figures (**Figure 33 - Figure 38**) convey the results from the 2D simulations with water set as the working fluid. The overall trends (i.e. color patterns/distributions) of the resulting plots were very similar across the four fluids, thus only the plots for water are shown with further descriptions and comparisons to the resulting values from the 2D simulations for the other three fluids (R134a, R1234ze, and air).

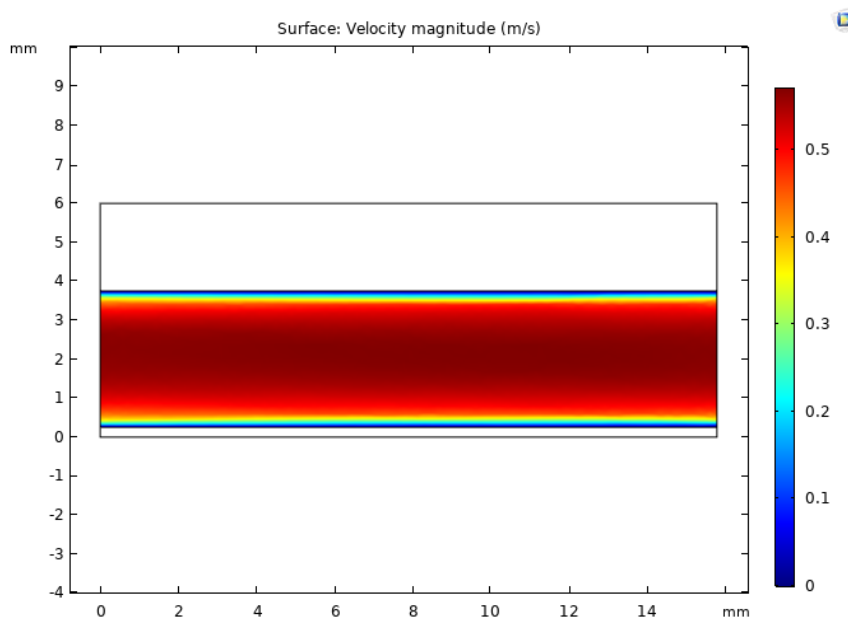


**Figure 33:** Surface plot of velocity for Slice 1 with water.

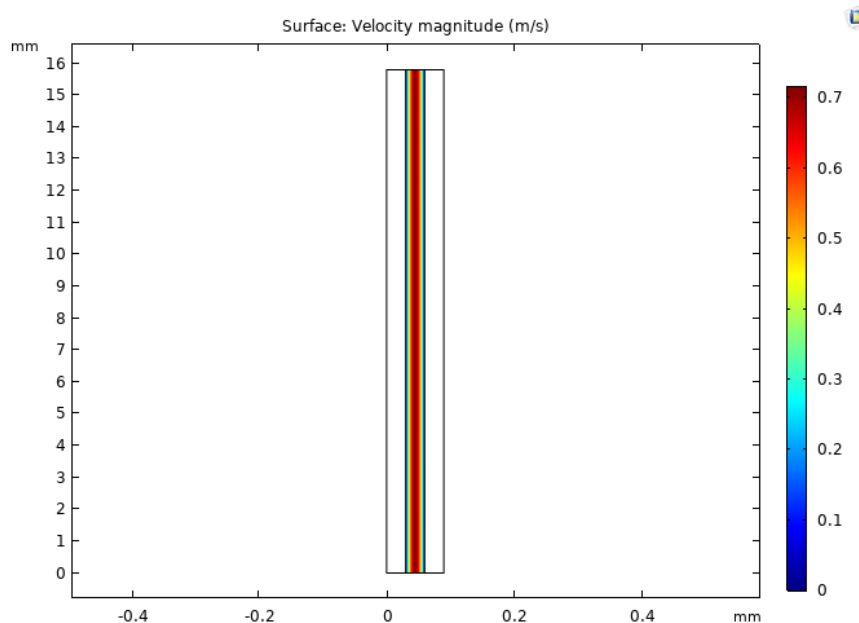


**Figure 34:** Surface plot of velocity for Slice 2 with water.

As shown in **Figure 33** and **Figure 34**, the fluid velocity profile is consistent across both cross-sections of the microchannel. The fluid velocity is zero at the walls of the microchannel and increases towards the center. For Slice 1 shown in **Figure 33**, the average velocity at the inlet and outlet of the microchannel for water, R134a, and R1234ze was 0.5 m/s  $\pm$  0.01 m/s, which is a reasonable fluid velocity and consistent with the velocity calculation (0.5 m/s) from the pre-simulation report (**Appendix D**). However the average velocity for air (using the same simulation inputs and boundary conditions) was approximately 472 m/s, due to the gaseous phase of air in contrast to the liquid phases of the other three fluids. The results from the 2D simulation of Slice 2 shown in **Figure 34** produced similar trends but with slightly different numerical results. The average velocity at the inlet and outlet of the microchannel for water, R134a, and R1234ze was 0.43 m/s  $\pm$  0.05 m/s. The average velocity for air was approximately 395 m/s.

The variation in the average fluid velocity through the microchannel between Slice 1 and Slice 2 was due to the limitations associated with only examining a 2D cross-section of a 3D geometry. Therefore, development of a 3D simulation was needed to more accurately characterize the flow of the various fluids.

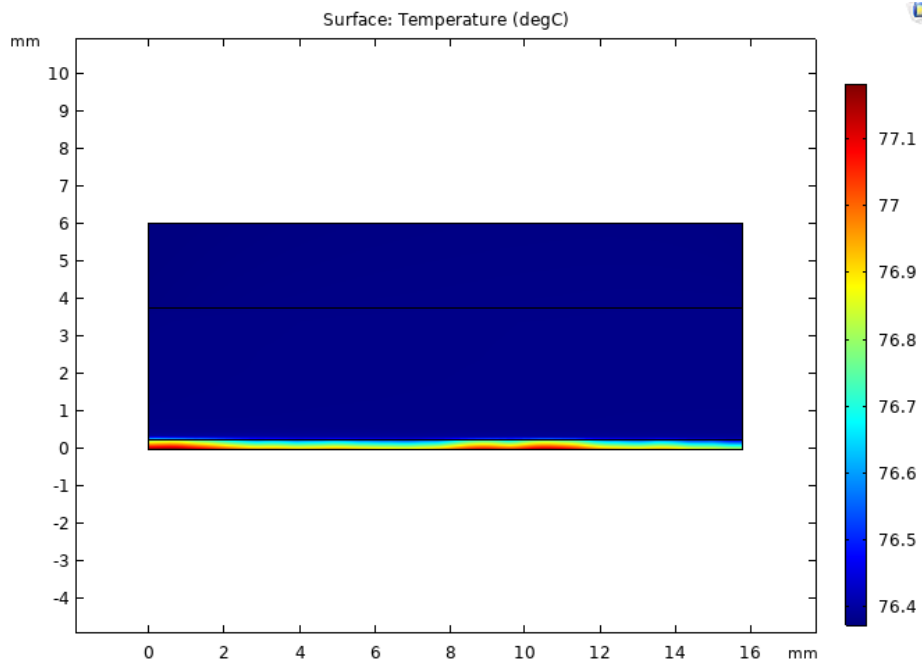


**Figure 35:** Surface temperature plot of Slice 1 with water.

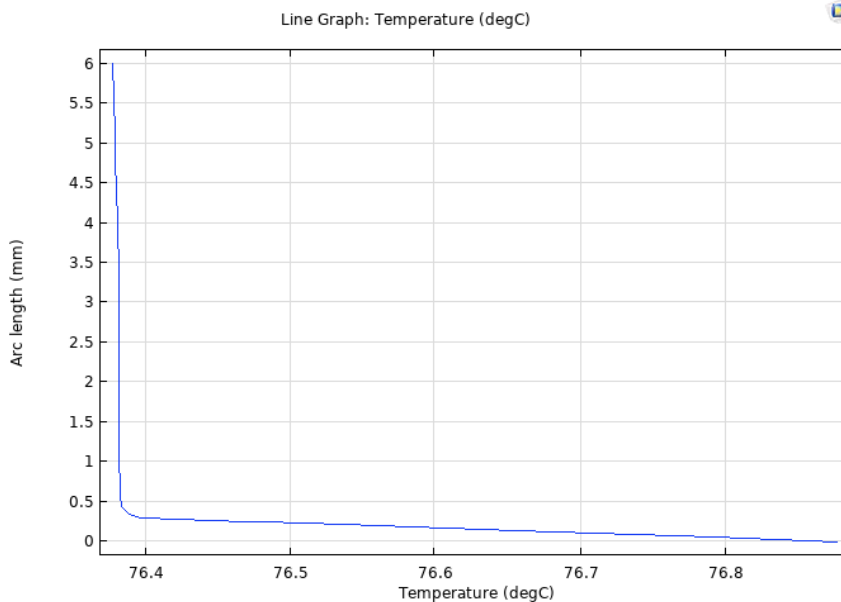


**Figure 36:** One-dimensional line plot of temperature near outlet ( $x=15\text{mm}$ ) with water.

As shown in **Figure 35** and **Figure 36**, the maximum temperature near the outlet, with water as the fluid, occurred at  $76.878^\circ\text{C}$  and was located at the bottom of the heat sink. In **Figure 36**, arc length is the distance along a vertical cut near the outlet of the heat sink. Since Slice 1 interfaces directly with the heat source (IHS/CPU), it was expected that the bottom of the microchannel heat sink would experience the highest temperatures. The fluid that resulted in the highest temperature at the bottom of the heat sink near the outlet was air, at  $77.446^\circ\text{C}$ , followed by R1234ze at  $77.121^\circ\text{C}$  and R134a at  $77.072^\circ\text{C}$ . Though

water experienced the lowest maximum temperature in comparison to R1234ze, R134a, and air, the maximum temperatures for the fluids were all within 0.9°C of each other.

Using a line average of the temperature at the exit edge of Slice 1, the average temperature of the fluid at the outlet could be determined. The fluid with the highest average outlet temperature was air, at 76.774°C, followed by R1234ze at 76.605°C, R134a at 76.432°C, and water at 76.383°C. Although water again experienced the lowest average outlet temperature in comparison to the other fluids, the average outlet temperatures for the fluids were all within 0.4°C of each other. Additionally, the temperature rise from the inlet temperature to the average outlet temperature of approximately 1.5°C is nearly within the typical temperature rise range (2-5°C) provided by Ebrahimi et al. [1].

Once again, it is important to consider that the 2D simulation of Slice 1 only represents a cross-section of the 3D geometry. Therefore, development of a 3D simulation was needed to accurately characterize the heat transfer and fluid mechanics through the microchannel to determine the maximum temperature and average outlet temperature of the fluid.

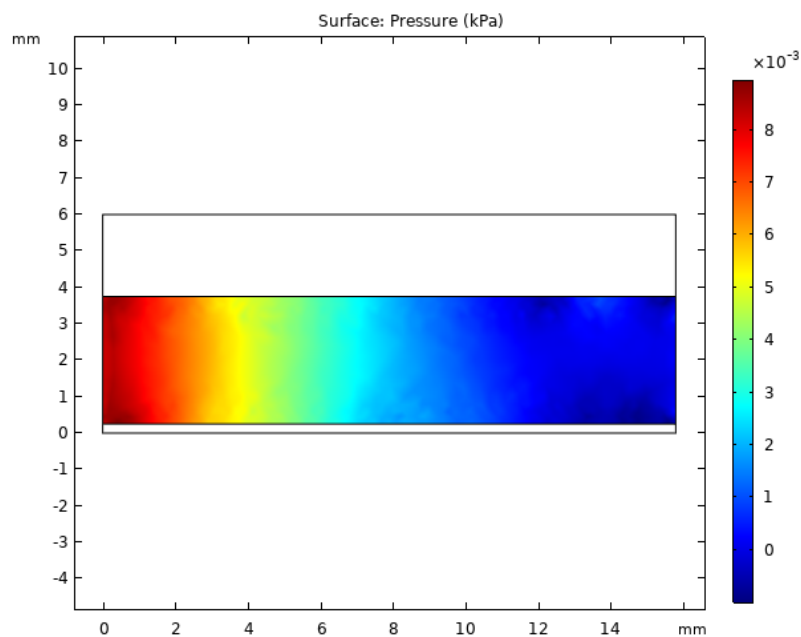


**Figure 37:** Surface plot of gauge pressure (kPa) for Slice 1 with water.

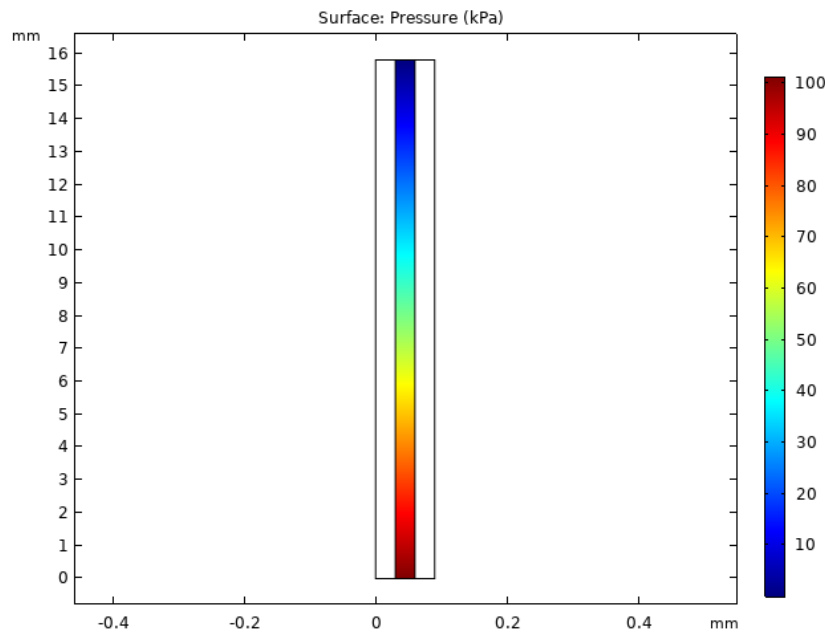


**Figure 38:** Surface plot of gauge pressure (kPa) for Slice 2 with water.

**Figure 37** and **Figure 38** depict the pressure gradient of the fluid (water) through the microchannel in each of the 2D cross-sections. The trends were comparable across each of the slices, as pressure dropped from the inlet to the outlet. However, there was a significant difference between the magnitudes of the pressure drops between each slice. For Slice 1, shown in **Figure 37**, the fluid flows with water, R134a, and R1234ze produced pressure drops less than 10 Pa, and air produced a pressure drop of 2914 Pa. However, for Slice 2, shown in **Figure 38**, the resulting pressure drops were as follows: 101.41 kPa for water, 16.9 kPa for R134a, 18 kPa for R1234ze, and 1510 kPa for air. The result of approximately 18 kPa for the R1234ze is consistent with the theoretically calculated pressure drop of 11 kPa from the pre-simulation report (see **Appendix D**)

Again, the differences in the resulting pressure drops between the 2D simulations for Slice 1 and Slice 2 were mostly due to the fact that they were determined from only a cross-section of the 3D geometry. To obtain a more accurate characterization of the pressure gradient of the fluid through the microchannel, the development of a 3D simulation was required.

All the numeric outputs from the 2D simulations of Slice 1 and Slice 2 are summarized in **Table 8**.

**Table 8:** Results from 2D simulations for laminar liquid flow through the microchannel

	<b>R1234ze</b>	<b>R134a</b>	<b>Air</b>	<b>Water</b>
<b>Slice 1 average temperature at outlet (°C)</b>	76.605	76.432	76.774	76.383
<b>Slice 1 temperature at the base of the heat sink at x=15mm (°C)</b>	77.121	77.072	77.446	76.878
<b>Slice 1 pressure drop (Pa)</b>	5.125	4.911	2914.0	8.2538

<b>Slice 1 average velocity at inlet (m/s)</b>	0.50995	0.51148	471.97	0.48890
<b>Slice 1 average velocity at outlet (m/s)</b>	0.50985	0.51139	471.98	0.48872
<b>Slice 2 pressure drop (kPa)</b>	18.0	16.9	1509.7	101.41
<b>Slice 2 average velocity at inlet (m/s)</b>	0.40523	0.38538	395.40	0.47705
<b>Slice 2 average velocity at outlet (m/s)</b>	0.40386	0.38408	394.37	0.47523

Overall, water produced the best performance in comparison to the other three fluids that were tested, contrary to the initial assumption that the refrigerants (specifically R1234ze) would result in the superior performance. Water performed more optimally since it resulted in the lowest temperature at the base of the heat sink at the outlet and did not require an elevated system pressure to keep the fluid in a liquid state (which would be required for the refrigerants R134a and R1234ze). To understand why water would produce better results in the MCHS, a brief investigation was performed to compare the heat transfer-related fluid properties of water and several common refrigerants.

To begin, the liquid thermal conductivities of various refrigerants, water, and air were plotted as a function of temperature to compare their performance in conduction heat transfer (shown in **Figure 39**).

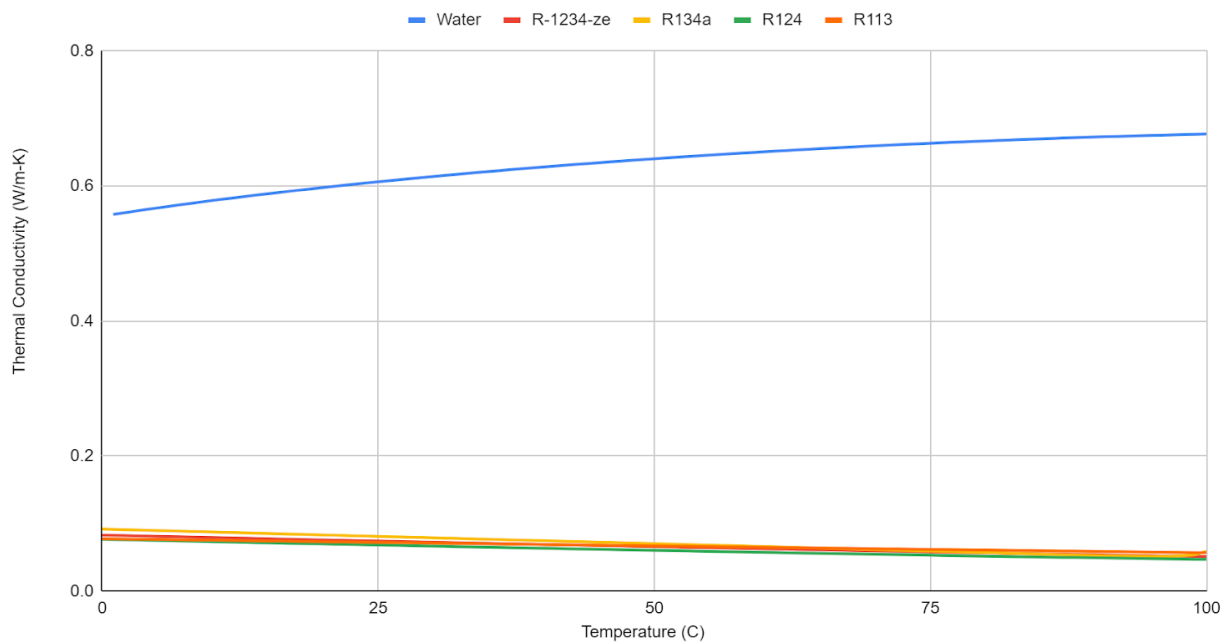


**Figure 39:** Liquid thermal conductivity as a function of temperature.

Water has a higher liquid thermal conductivity (by approximately six times) in comparison to the refrigerants throughout the temperature range utilized in the electronics cooling MCHS scenario. In other words, liquid water is capable of transferring more heat via conduction than a refrigerant in the liquid phase. Therefore, it was decided that for future COMSOL models, water would be used as the optimal fluid in the liquid cooling MCHS, which also affirmed literature on liquid cooling and industry practices [1].

Furthermore, since the scope of this project considered the potential of two-phase flow through a MCHS, wherein a heated vapor would be transported to the ORC evaporator to exchange heat, an additional investigation into the vapor thermal conductivities of the various fluids was also conducted. Comparing the vapor thermal conductivities also provided thermal context for the refrigerants involved in the ORC system, wherein Ebrahimi et al. had suggested R1234ze could be a viable candidate. A similar plot for *vapor* thermal conductivity as a function of temperature was created (shown in **Figure 40.**)

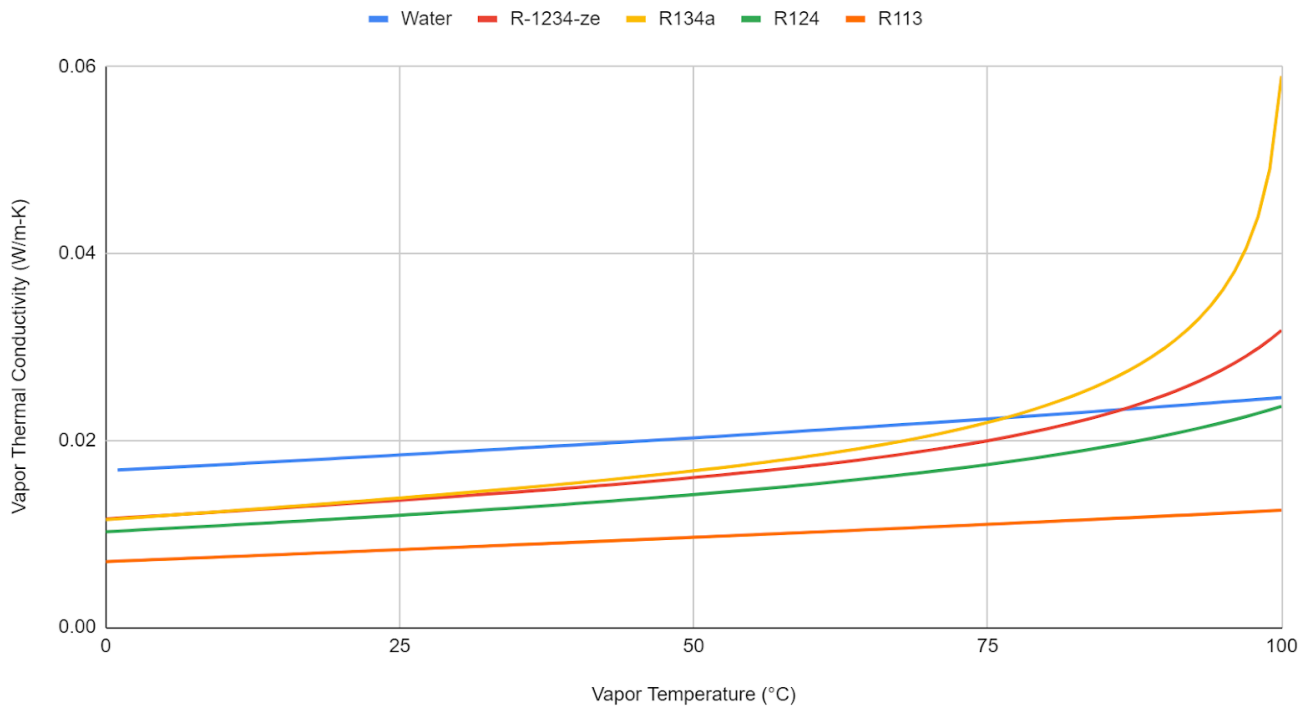


**Figure 40:** Vapor thermal conductivity as a function of temperature.

Unlike the liquid plot, the thermal conductivity of water vapor does not remain superior to the other vaporous fluids at the elevated temperatures of electronics cooling. At approximately 87°C, R1234ze vapor has a higher thermal conductivity than water vapor. R134a vapor surpasses water vapor thermal conductivity around 76°C. Vapor thermal performance is relevant for the heat waste recovery system since the fluids may be in the vapor phase in the MCHS or ORC evaporator, depending on which SHEC cooling system is used and the designated operating conditions. However, it is important to note that thermal conductivity only provides insight about a fluid’s performance in conduction, not convection. Future investigation of the Reynolds number and Nusselt number (and potentially the Rayleigh number) may provide further theoretical validation as to why certain fluids exhibit better heat transfer performance. Reynolds number is significant in forced convection as it indicates the relative importance of inertial and viscous effects for a moving fluid. The Nusselt number represents the relative importance of convection to conduction for a layer of fluid. For free or natural convection, the Rayleigh number represents the ratio of buoyant to viscous forces multiplied by the ratio of momentum and thermal diffusivities.

Ultimately, the design and testing of a 3D COMSOL simulation for fluid flow through the microchannel was required to determine whether water (or another fluid) had the superior thermal performance. (The prediction that water would exhibit optimal performance was officially tested in Section 5.0).

### 4.1.2 Stage Two: 3D Simulations with Laminar Flow

The results from the 2D laminar simulations of the cross-sections of the microchannel were encouraging. However, variations from the expected results and discrepancies between the two simulated 2D slices indicated that a 3D simulation had to be developed. A 3D simulation of the microchannel would fully characterize the heat transfer and fluid mechanics and would provide more accurate representations of the key output parameters of the MCHS. Furthermore, the 3D simulation would enable a comparative study between constant heat flux and constant temperature boundary conditions at the interface with the heat-generating CPU. As was concluded from the 2D simulations and fluid property investigation, water was the most appropriate fluid for the single-phase liquid flow. The same dimensions and problem setup that were utilized in the simulations for the 2D slices were also used for the 3D simulations.

For the first 3D simulation, as in the 2D simulations, a constant heat flux of  $65 \text{ W/cm}^2$  was specified at the bottom surface of the MCHS. The following plots (Figure 41- Figure 43) represent the results for the velocity, temperature, and pressure of liquid water flow through a single microchannel. The plots for the velocity, temperature, and pressure depict the conditions at an analytical slice taken at the center of the microchannel. Note that this results ‘slice’ can be seen as the same as “Slice 1” from the 2D simulations, since it is in the same location and orientation along the MCHS. However, in the 2D simulations, it was “Slice 1” itself that was modeled and simulated whereas in the 3D simulations, the entire microchannel (i.e. isolated section of the MCHS) was simulated, but the results are visually presented on a specified plane (i.e. slice). A centrally located plane provides the best visual depiction of the overall results.

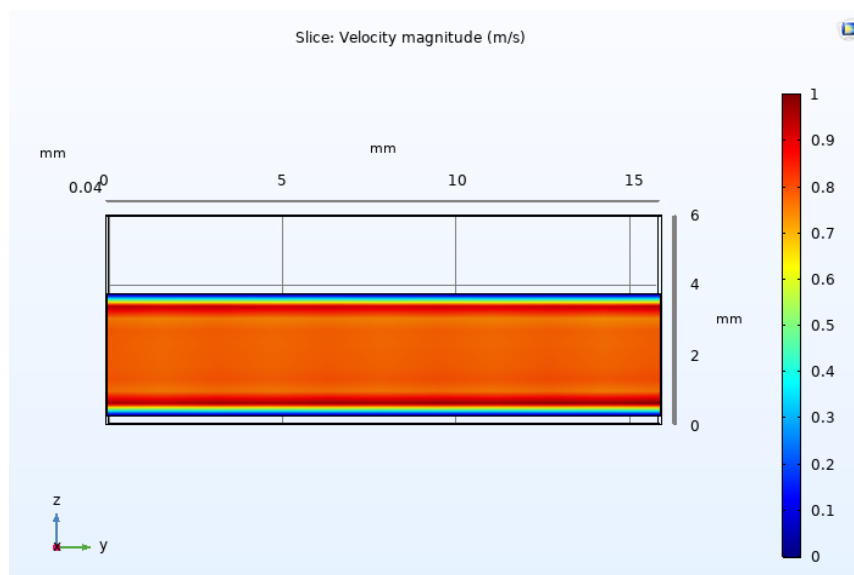


**Figure 41:** Plot of water velocity (m/s) at a mid-channel slice.

As shown in **Figure 41**, the velocity profile was very similar to that produced by the 2D simulations. The velocity ranged from 0 m/s (at the microchannel walls) to about 1 m/s, with an average inlet velocity of 0.48853 m/s and 0.48983 m/s at the outlet. Since the density, mass flow rate, and cross-sectional area of the microchannel were all constant, it was reasonable that the average velocity of the fluid remained essentially the same. Additionally, the average velocity of the water flow at the inlet and outlet of the microchannel was close to the velocity calculation (0.5 m/s) from the pre-simulation report (**Appendix D**). The variation is justified since the velocity calculation included in the pre-simulation report was based on R1234ze, not water, which has different material properties.

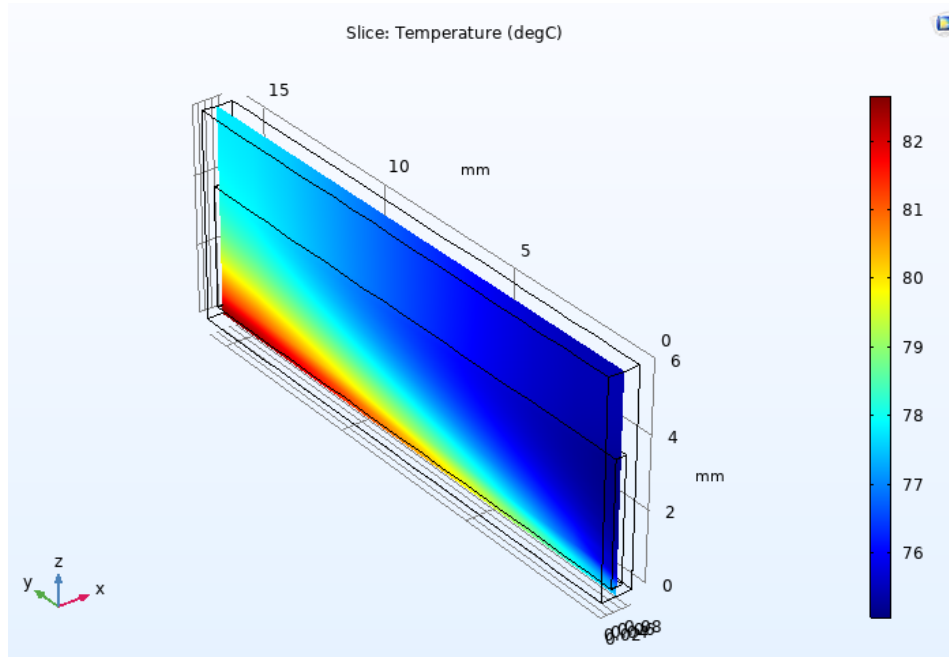


**Figure 42:** Plot of temperature ( $^{\circ}\text{C}$ ) at a mid-channel slice.

**Figure 42** illustrates the temperature distribution throughout the microchannel and fluid. The inlet was near  $75^{\circ}\text{C}$  with temperatures increasing towards the base of the MCHS where the  $65 \text{ W}/\text{cm}^2$  heat flux was applied. Increasing in the  $y$ -direction along the length of the MCHS, the temperature increases and the heat is transferred into the fluid in the microchannel. The average temperature of the water at the outlet of the microchannel was  $79.447^{\circ}\text{C}$  and the maximum temperature experienced in the MCHS was  $82.628^{\circ}\text{C}$ . Therefore, the water fluid temperature rose by approximately  $4.4^{\circ}\text{C}$  over the CPU, which was consistent with the typical temperature rise range ( $2\text{-}5^{\circ}\text{C}$ ) provided by Ebrahimi et al. [1].

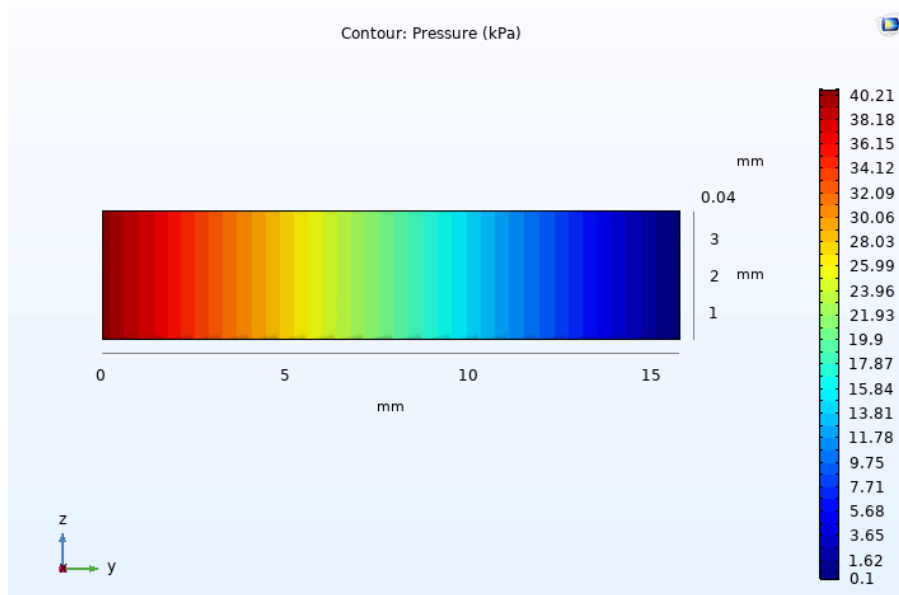


**Figure 43:** Plot of water gauge pressure (kPa) through the microchannel.

As shown in **Figure 43**, the pressure of the fluid dropped from the inlet to the outlet of the microchannel. Since water does not begin to vaporize until  $100^{\circ}\text{C}$ , the working pressure of the system can be at atmospheric conditions (specified at 0 gauge pressure in the simulation). The resulting pressure drop across the microchannel was 40.810 kPa. In terms of absolute pressure, the water would exit the microchannel at atmospheric pressure (101.325 kPa) and the pressure at the inlet would be the atmospheric pressure plus the pressure drop ( $101.325\text{kPa} + 40.810\text{ kPa} = 142.135\text{ kPa}$ ). The initial calculation for pressure drop from the pre-simulation report (**Appendix D**) was 11 kPa, however the theoretical approximation was made for R1234ze at a working pressure of 2140 kPa. Thus, it is reasonable that there was a numerical difference in the results, yet the orders of magnitude are the same.

For the second 3D simulation, a constant temperature of  $85^{\circ}\text{C}$  was specified at the bottom surface of the MCHS. The following plots (**Figure 44 - Figure 46**) represent the corresponding results for the velocity, temperature, and pressure, but with the constant temperature boundary condition, as opposed to the  $65\text{ W/cm}^2$  constant heat flux boundary condition. As shown in **Figure 44**, the velocity profile and magnitudes were very similar to those observed in the constant heat flux 3D simulation.

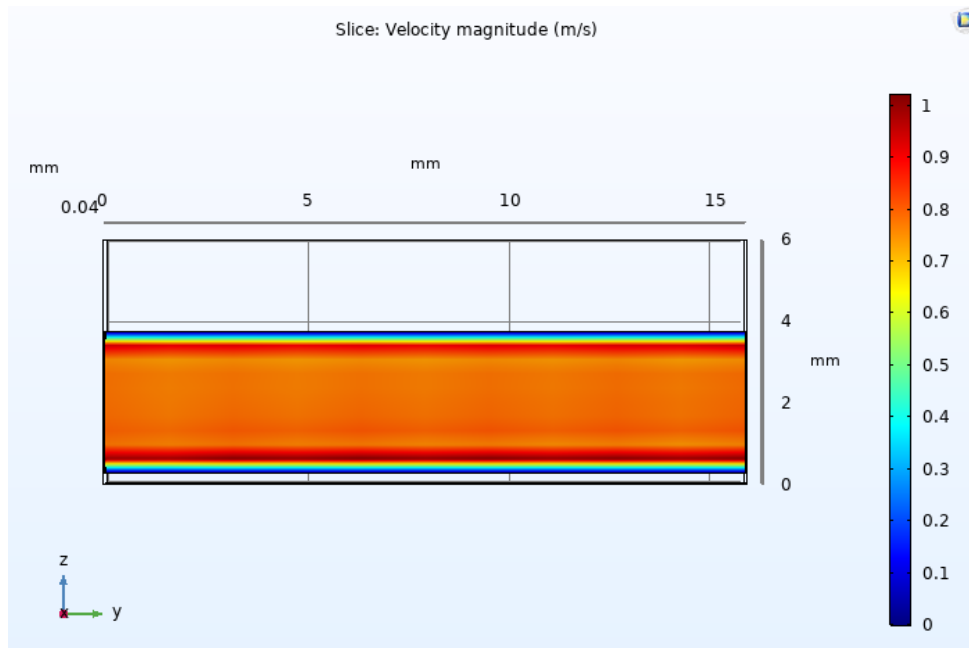


**Figure 44:** Plot of water velocity (m/s) at a mid-channel slice.

The velocity ranged from 0 m/s (at the microchannel walls) to about 1 m/s, with an average inlet velocity of 0.48867 m/s and 0.49071 m/s at the outlet. Once again, the average velocity of the water flow at the inlet and outlet of the microchannel was close to the velocity calculation from the pre-simulation report (**Appendix D**). **Figure 45** illustrates the temperature distribution throughout the microchannel and fluid, and depicts very similar results to the constant heat flux 3D simulation.

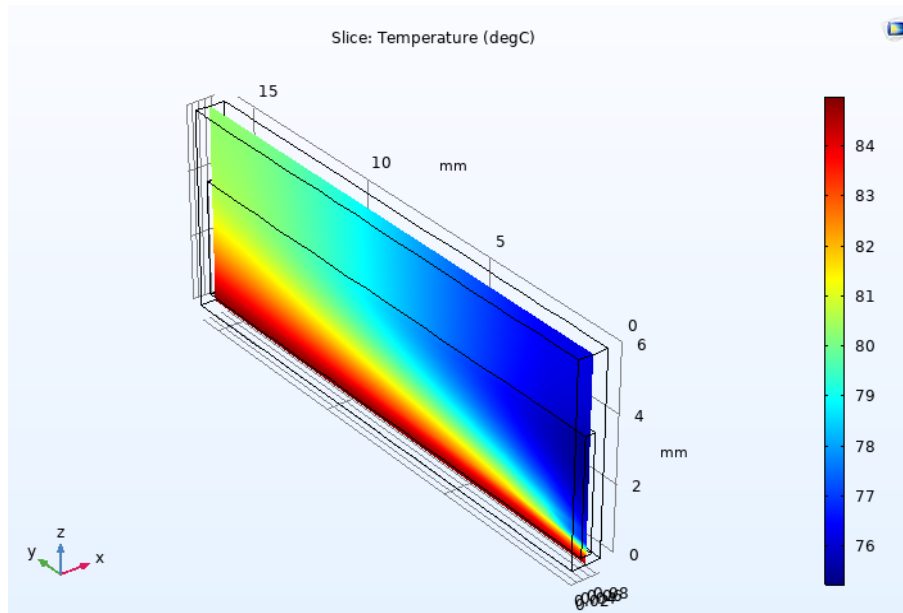


**Figure 45:** Plot of temperature (°C) at a mid-channel slice.

The inlet was near 75°C with temperatures increasing towards the base of the MCHS, where the 85°C surface temperature is defined. Increasing in the y-direction along the length of the MCHS, the

temperature increased as the heat was transferred to the fluid. The average temperature of the water at the outlet of the microchannel (82.190°C) was a few degrees higher than that of the water with the constant heat flux condition. The maximum temperature experienced in the MCHS was also higher than that observed in the constant heat flux 3D simulation, at 85°C (i.e. the boundary condition specified for the bottom surface of the MCHS). The water fluid temperature rose by approximately 7.2°C over the CPU, which is just outside the typical temperature rise range (2-5°C) provided by Ebrahimi et al. [1]. As shown in **Figure 46**, the pressure of the fluid dropped from approximately 39.558 kPa to 0 kPa (gauge), which was almost exactly the same as the pressure drop from the constant heat flux 3D simulation.

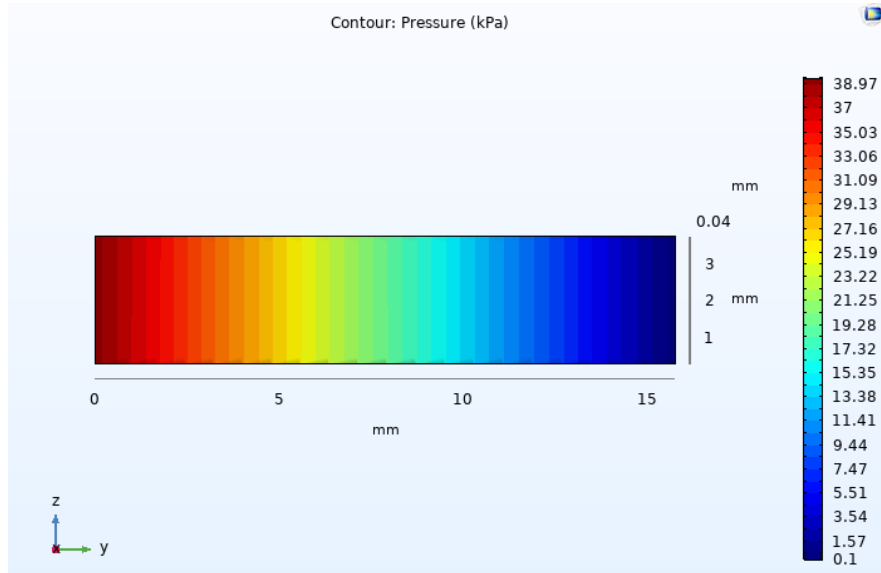


**Figure 46:** Plot of water gauge pressure (kPa) through the microchannel.

And once again, the simulated pressure drop was slightly higher, but the same order of magnitude as the initial calculation of the pressure drop from the pre-simulation report (**Appendix D**).

All the numeric outputs from the laminar 3D simulations for the constant heat flux (65 W/cm<sup>2</sup>) and constant temperature (85°C) boundary conditions are summarized in **Table 9**.

**Table 9:** Results of 3D simulations for laminar liquid flow through the microchannel

Boundary Condition	Average Inlet Velocity (m/s)	Average Outlet Velocity (m/s)	Average Fluid Temperature at Outlet (°C)	Maximum Temperature of MCHS (°C)	Pressure Drop (kPa)
<i>Constant heat flux</i>	0.48853	0.48983	79.447	82.628	40.810
<i>Constant Temperature</i>	0.48867	0.49071	82.190	85.0	39.558

Overall, the 3D simulation of laminar water flow through a single microchannel produced successful results that were consistent with the theory from the pre-simulation report (**Appendix D**) and documented values and ranges from existing literature [1]. Furthermore, the numerical outputs indicated that there was not a significant difference between the results from the different thermal boundary conditions, except for the observed temperatures. It can be concluded that the average fluid temperature and maximum temperature of the MCHS lies somewhere in between the results from each simulation. However, it should be noted that heat flux is a more appropriate means of characterizing the heat load from electronic components and likely provides a better representation of the MCHS thermal performance.

The next iteration of the 3D simulation for the single-phase liquid cooling scenario (Section 4.1.3) considered turbulent flow in order to investigate whether the heat transfer between the CPU and MCHS fluid may be enhanced, compared to the laminar flow model.

### 4.1.3 Stage Three: 3D Simulations with Turbulent Flow

COMSOL offers eight turbulence models for solving turbulent flow problems. The three models that were considered to evaluate the turbulent flow through the microchannel were Algebraic yPlus, k- $\epsilon$ , and low Reynolds number k- $\epsilon$ . Algebraic yPlus is the least accurate but most efficient model, providing adequate estimates for fluid flow, particularly in the case of electronics cooling [65]. The k- $\epsilon$  model is the most frequently used model, since it is relatively fast and allows coarser meshes to be used near the wall. [65]. However, the k- $\epsilon$  model is less accurate than other models, and is less suitable when there is an adverse pressure gradient [66]. The low Reynolds number k- $\epsilon$  model has advantages over k- $\epsilon$ , including accurate modeling of heat fluxes—but requires a denser mesh. Other options for turbulent models in COMSOL were either intended for aerodynamic applications or were too computationally intensive [65].

Turbulent flow simulations can be verified by checking the wall resolution viscous units, a non-dimensional unit of distance measured from the wall. The value of wall resolution indicates how far into the boundary layer of the fluid that the computational domain begins. Typically, the wall resolution value should not exceed a few hundred, and a value of 11.06 is considered ideal [65], [66].

To observe the differences in the three turbulence models considered for the 3D turbulent simulation of the MCHS, the 3D geometry (and boundary conditions) were simulated in each. A heat flux of 65 W/cm<sup>2</sup> was specified at the base of the heat sink, and the inlet water flow to the microchannel was assigned a mass flow rate of  $1.20 \times 10^{-4}$  kg/s and an initial temperature of 75°C. The results of the three simulations with each of the COMSOL turbulent models are shown in **Table 10**. The resulting wall resolution plots for each of the three turbulent models are presented in **Figure 47 - Figure 49**.

**Table 10:** Results of 3D simulations with different COMSOL turbulent models

	k-ε	Algebraic yPlus	Low Reynolds number k-ε
Average temperature at inlet (°C)	75.006	75.144	75.159
Average temperature at outlet (°C)	81.953	82.337	82.578
Maximum temperature at base of heat sink (°C)	86.816	86.672	87.627
Pressure drop (kPa)	116.92	159.70	127.75
Average inlet velocity (m/s)	7.0341	7.0342	7.0341
Average outlet velocity (m/s)	7.0639	7.0342	7.0653

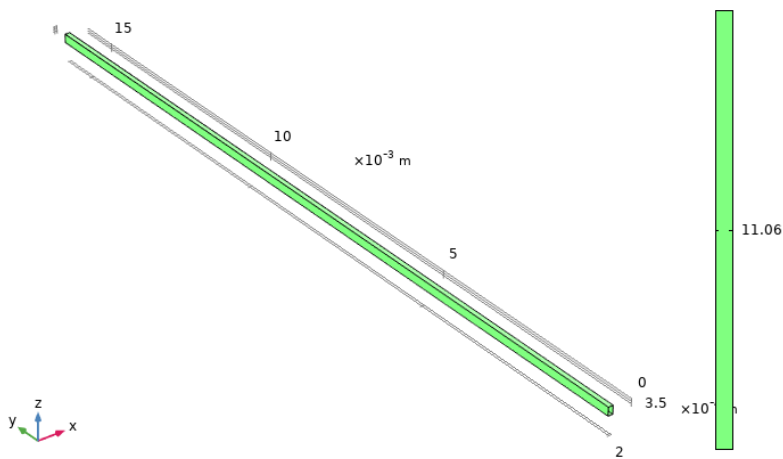


**Figure 47:** Wall resolution in viscous units using the k-ε turbulence model.

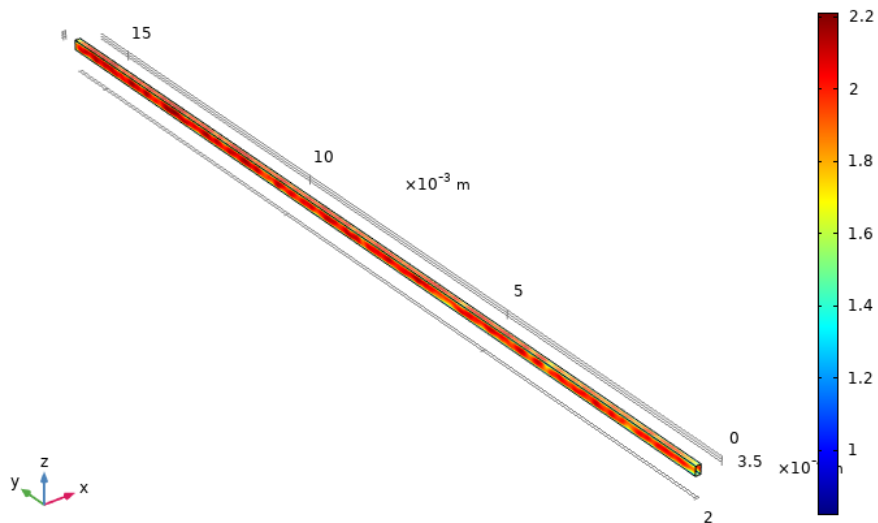


**Figure 48:** Wall resolution in viscous units using the algebraic yPlus turbulence model.

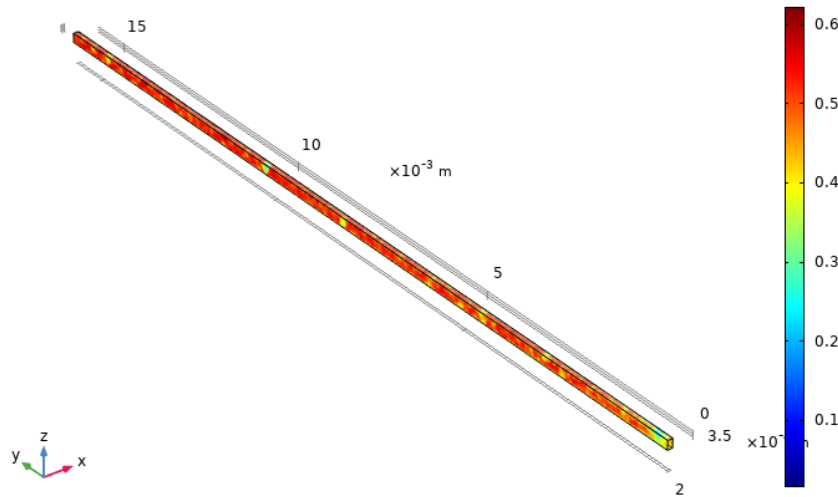


**Figure 49:** Wall resolution in viscous units using the low Reynolds number k- $\epsilon$  turbulence model.

The low Reynolds number k- $\epsilon$  model resulted in the highest average outlet and maximum temperatures at the heat sink. This was expected as the low Reynolds number k- $\epsilon$  model has a denser mesh and was the most computationally intensive. All models had similar pressure drops and velocities, as well as acceptable wall resolutions (either exactly at or below 11.06 viscous units). Therefore, the low Reynolds number k- $\epsilon$  model was chosen for the final turbulent simulations as listed in Section 5.0.

For the turbulent simulations, fluid reservoirs were added at the inlet and outlet of the channels. Previously, the top, front, and back surfaces of the heat sink were assigned contact with surrounding air (within the IT server). The air was specified at 35°C with a convection coefficient of 10  $W/m^2K$  (typical value for natural convection). Although the top surface of the heat sink remained in contact with air in the 3D turbulent simulations, the thermo-fluid interactions at the front and back face of the heat sink were modified. It was determined that in a realistic design of a MCHS, the front and back surfaces would be in contact with a reservoir of the fluid, not exposed to surrounding air. The fluid reservoirs would be contained in the MCHS apparatus, wherein the inflow of water would divide into the microchannels to travel over the heat sink and repool at the outlet of the channels. In other words, there would be one inlet and one outlet for the entire MCHS as opposed to N number of inlets and outlets for each of the channels. To simulate the fluid and thermal interactions due to the pooling effect of the liquid water at the front and back face of the MCHS, ‘floating’ blocks of the water were added to the 3D simulation model. The height of both fluid reservoirs was defined as the height of the heat sink. The width of both reservoirs was defined as the width of the isolated section of the MCHS. The extension (depth) of both of the reservoirs off the surface of the MCHS was designated as 1 mm. A depiction of the isolated MCHS section with the added fluid reservoirs (highlighted in blue) can be seen in **Figure 50**.

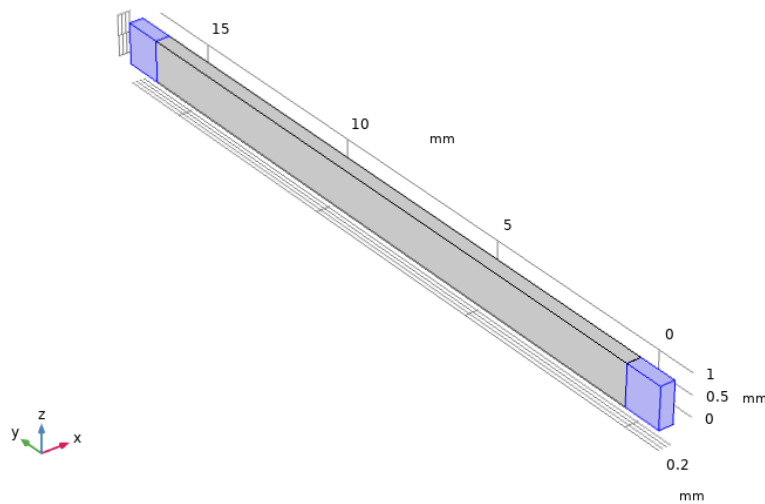


**Figure 50:** Fluid Reservoirs Added to Front and Back of the Heat Sink.

Then, to more accurately reflect the example in **Appendix D**, the geometry of the MCHS for turbulent conditions was updated to have a smaller width and higher depth. The calculations were based on Reynolds number calculations, following the analytical process presented in the pre-simulation report in **Appendix D**. To ensure the flow would be turbulent, the Reynolds number had to be approximately 2300 or greater. An initial geometry with a width of  $30\ \mu\text{m}$ , a height of  $250\ \mu\text{m}$ , and a spacing of  $300\ \mu\text{m}$  resulted in a Reynolds number of 2282. This geometry was associated with a mass flow rate per channel of  $1.15 \times 10^{-4}\ \text{kg/s}$ . The COMSOL simulation for this initial geometry resulted in a high pressure drop of 2893 kPa. To reduce the pressure drop, the geometry was altered to have a width of  $50\ \mu\text{m}$ , a height of  $230\ \mu\text{m}$ , and a spacing of  $300\ \mu\text{m}$ , which resulted in a Reynolds number of 2434. The new geometry had a per channel flow rate of  $1.23 \times 10^{-4}\ \text{kg/s}$ . Increasing the width and only slightly decreasing the depth increased the cross-sectional area of the microchannels, which resulted in a lower pressure drop. The second geometry produced a much lower pressure drop of 791.3 kPa. **Table 11** summarizes the results of the initial and final simulations, both of which had acceptable temperature changes. Since the Algebraic yPlus turbulence model was not as computationally intensive, it was utilized for both simulations. The final geometry was used for final turbulent simulations (Experiments 1 and 2 in Section 5.0).

**Table 11:** COMSOL simulation results for initial and final turbulent MCHS geometries

	<b>Initial geometry</b> ( $30\ \mu\text{m}$ width, $250\ \mu\text{m}$ height, $300\ \mu\text{m}$ spacing)	<b>Final geometry</b> ( $50\ \mu\text{m}$ width, $230\ \mu\text{m}$ height, $300\ \mu\text{m}$ spacing)
<b>Average temperature at inlet (°C)</b>	75.211	75.262
<b>Average temperature at outlet (°C)</b>	82.617	82.194
<b>Average temperature at reservoir inlet (°C)</b>	75.000	75.000
<b>Average temperature at reservoir outlet (°C)</b>	82.004	82.154

<b>Maximum temperature at base of heat sink (°C)</b>	84.217	84.576
<b>Pressure drop (kPa)</b>	2892.8	791.27
<b>Average inlet velocity (m/s)</b>	0.48066	0.48066
<b>Average outlet velocity (m/s)</b>	2.5241	2.0925

### *3D Laminar Simulation, Revisited*

It is important to note that the additional consideration of the pooling fluid at the front and back face of the MCHS was introduced during the process of developing the 3D turbulent simulations. Therefore, the geometry from the 3D laminar simulation was modified to include the fluid reservoirs. The width and height of the reservoirs was identical to the width and height of the laminar MCHS model and extended 1 mm from the surface of the MCHS. It was essential to modify the laminar model to reflect the same configuration and design considerations as the turbulent model before any comparative analysis between the two was conducted. All subsequent simulations with the laminar model (such as those listed in Section 5.0) included the fluid reservoirs in the geometry.

## **4.2 Development of Two-Phase Cooling MCHS Simulation**

The approach to developing the two-phase MCHS simulation in COMSOL was the same as the approach used for the single-phase liquid MCHS simulation. Before beginning the COMSOL simulation, the theoretical heat transfer and fluid mechanics principles were investigated to guide the design and specification of the model. The textbook from Kandlikar et al. was used again as a reference to understand the important conceptual background for two-phase flow through mini/microchannels, as well as for determining the relevant parameters for setting up the heat transfer and flow problem [64].

Upon review of the chapter on flow boiling through minichannels and microchannels, there were some important ideas worth noting [64]:

- Flow boiling has a high heat transfer coefficient and a higher heat removal capacity for a given mass flow rate (by an order of 10), compared to single-phase liquid cooling.
- Flow boiling is initiated by either two-phase entry ( $0 < x < 0.1$ ) following an expansion valve or subcooled liquid entry (generally used for electronics cooling applications).
- If the bubble growth rate of the vaporizing fluid is too high, it can cause instabilities such as reverse flow and severe pressure drop fluctuations.
- The critical (maximum) heat flux (CHF) that can be dissipated is limited by the two-phase flow (i.e., mass flux, tube diameter) and local wall interactions (e.g. nucleation sites).
- Unstable operation, caused by rapid growth of vapor bubbles and leading to flow reversal, remains a prominent concern for practical applications of flow boiling. Placing a constrictor (i.e., pressure drop element) at the inlet of the channel and adding artificial nucleation cavities on the walls of the channel to initiate nucleation before the liquid is superheated have shown to be the two most promising ways of reducing instabilities and reversed flow.

- It is difficult to predict heat transfer in microchannels because many researchers experience flow instability during their tests. Additionally, differences in the ranges of parameters (e.g., heat/mass flux) create an added difficulty when assessing available experimental data.
- The challenges involved with presenting a comprehensive analytical heat transfer model are due to the complexity of flow boiling in small diameter channels, which includes “liquid–vapor interactions, presence of expanding bubbles with thin evaporating film, nucleation of bubbles in the flow as well as in the thin film, etc.”
- High heat flux two-phase cooling systems have not developed as quickly as liquid cooled systems because of the following: (1) need for a refrigerant or low-pressure water with properties suitable for flow boiling under the operating conditions of electronics cooling, (2) flow instability from rapid bubble expansion and reversing flow, and (3) lack of CHF data and theoretical basis for flow boiling in microchannels.

Although two-phase flow boiling through microchannels enables much higher heat removal capacities, an exciting characteristic for cooling next-generation high density hyperscale data centers, the prevailing complications with achieving reliable, stable flow and absence of a fundamental understanding of the heat transfer within the channels are major hindrances to bringing two-phase MCHSs to the commercial world. Nonetheless, the design of a two-phase MCHS for application in the two-phase SHEC was pursued, using example 5.2 from Kandlikar et al. as a guide (a full copy of the example can be found in **Appendix E**) [64].

However, when attempting to utilize the theoretical calculation process presented in example 5.2, a number of complications were encountered. Although the example was based on an application for electronics cooling, some key input parameters in the example were quite different from the conditions explored in this project. For example, the dissipated heat flux, inlet temperature, and operating pressure of R123 in the textbook example were 13,000 W/m<sup>2</sup>, 20°C, and 101 kPa (1 atm), respectively. However, for this project, the heat flux from the CPU was much higher, at 650,000 W/m<sup>2</sup> (based on a 162.5 W, 2.5 cm<sup>2</sup> microprocessor [1]). Furthermore, in this project, R1234ze enters the microchannel at 75°C (to maximize the quality of the waste heat) and at a pressure much greater than 1 atm to ensure the refrigerant does not have a high vapor quality when entering the channel (since the operating temperature is significantly above its saturation temperature at atmospheric pressure). Due to the vast difference between the input parameters of the problem, it is questionable whether the analytical process presented in example 5.2 can be applied. However, as noted by Kandlikar et al., there is a lack of a fundamental understanding of two-phase flow and flow boiling through microchannels, so the resources for determining the proper design and evaluation of heat transfer and fluid flow through a proposed MCHS are severely limited.

Nonetheless, by using the equations presented in example 5.2, in addition to tabulated values for Nusselt number, a rough approximation of the geometry and operating conditions were defined. By adjusting the dimensions in the MCHS design, a channel width of 10 μm and height of 400 μm produced a heat transfer coefficient of 23.565 kW/m<sup>2</sup>-K, mass flow rate of 1.3\*10<sup>-6</sup> kg/s, and onset of nucleate boiling at 21 μm from the inlet (when the saturation pressure and temperature of the R1234ze

were set at 3210 kPa and 103°C). However, later calculations in example 5.2 no longer supported the electronics cooling scenario of this project. For example, the calculation for the quality of the fluid at the exit is equivalent to the difference between the enthalpy of the two-phase region and the inlet, divided by the latent heat of vaporization (see equation 9.1 from example 5.2 in **Appendix E**). However, the enthalpy in the two-phase region is based on the heat flux from the computer chip, which, in the example for this project, was 650,000 W/m<sup>2</sup> (50 times the heat flux in the example problem). Therefore, the enthalpy in the two-phase region (and the difference between the enthalpy in the two-phase region and the inlet) was much larger than that of the example, greatly increasing the result from the calculation for the quality of the fluid at the exit. The equation produced a result of 109 for the quality, which is a value that should always be between 0 and 1. At that point, the remainder of the calculations could not be completed because the quality was not in the appropriate range and was referenced in other equations. Likely, there was either an issue with (1) the proposed geometry or setup of the two-phase MCHS electronics cooling scenario for this project—as the channel dimensions and saturation pressure and temperature were somewhat dramatic to produce a sufficient heat transfer coefficient, or (2) a different sequence of equations, correlations, or tabulated values were needed to address the specific characteristics of flow boiling in microchannels for a much higher heat flux and a refrigerant at elevated pressures and temperatures.

Regardless, it became clear that the proper setup and design of a two-phase MCHS for evaluation in COMSOL simulations exceeded the scope of this project. The remainder of the project activities focused on the optimization of an ORC waste heat recovery system using a MCHS with single-phase, liquid (water) flow. However, as previously noted, flow boiling enables a much greater heat removal capacity and has exciting potential for the high cooling demands of new age data centers. The challenges that face the characterization, design, development, and stability of two-phase flow boiling through microchannels are worth addressing in future work on this project. An investigation of the optimal design of a two-phase MCHS with an interfacing ORC waste heat recovery system may lead to measurable improvements in the overall system performance, compared to optimized designs using single-phase liquid flow MCHSs.

## 5.0 Simulated Experiments

After the finalized versions of the 3D laminar and turbulent single-phase liquid flow simulations were developed in COMSOL, several relevant operating conditions and microchannel heat sink (MCHS) variables were tested. This occurred in a series of simulated experiments to investigate the effects on performance, of which the primary focus was to identify the optimal MCHS design and operating conditions. Two optimal designs were identified, one for laminar liquid water flow and one for turbulent liquid water flow. Additionally, 3D laminar simulations were completed with alternative fluids, including R1234ze, R134a, and air. The other fluids were tested in the 3D laminar simulation to ensure the previous conclusion (from the 2D laminar simulations in Section 4.1.1)—that water was the best performing fluid in the MCHS—was supported by 3D analysis.

**Figure 51** depicts a generalized model of the MCHS geometry and boundary conditions that represented the series of COMSOL experiments. The dimensions of the channel included the width of the channel ( $a$ ), the height of the channel ( $b$ ), and the spacing between channels ( $s$ ). The geometry of the MCHS section included the overall height, length, and depth of the block. The overall height included a 0.25 mm offset of the channel from the base, the height of the microchannel ( $b$ ), and another 0.5 mm offset from the top face (to represent a ‘cover plate’). The overall length included the channel width ( $a$ ) and the spacing ( $s$ ), wherein the channel was centered lengthwise with  $s/2$  on each side. The depth was 15.8 mm.

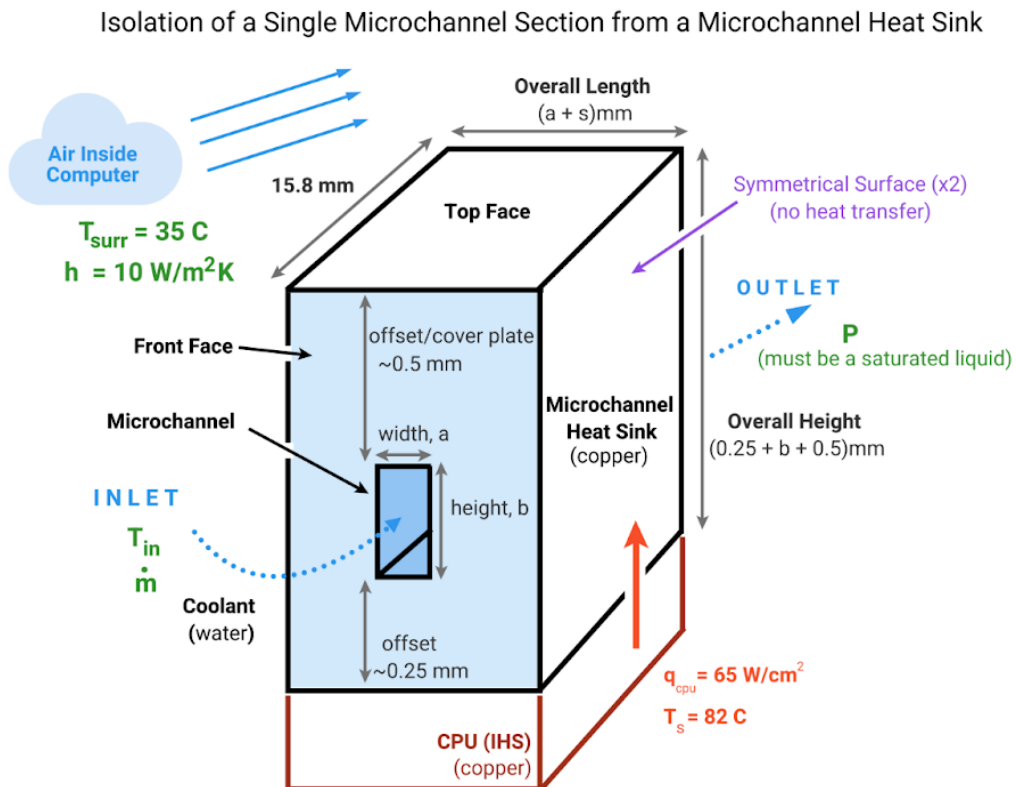


**Figure 51:** Model and boundary conditions for a single microchannel section, generalized for the COMSOL experiments.

The top face of the MCHS was exposed to convection from the air inside the server. The bottom face of the MCHS was subjected to either a constant heat flux or constant temperature thermal load from the CPU/IHS. The inflow temperature and flow rate of the liquid coolant was specified at the inlet. The system pressure was specified at the outlet, and approximately corresponded to the liquid saturation pressure of the fluid at the temperature leaving the microchannel. The left and right sides of the MCHS section were assigned thermal insulation, since the simulation was of a single microchannel wherein the ‘sides’ would not be exposed to the air. Rather, an array of microchannel sections comprise the MCHS, and it is assumed that the fluid and thermal performance within each is symmetrical. However, research has shown that fluid and heat interactions vary over the series of microchannels in the MCHS, which could be further investigated with more sophisticated and powerful simulation software [67].

In addition to the MCHS section, the COMSOL simulation included two ‘blocks’ that extended 1mm from the front and back face of the MCHS. The blocks represented the contained pooling of the coolant before and after dividing into all the microchannels along the length of the full MCHS (see **Figure 52**).

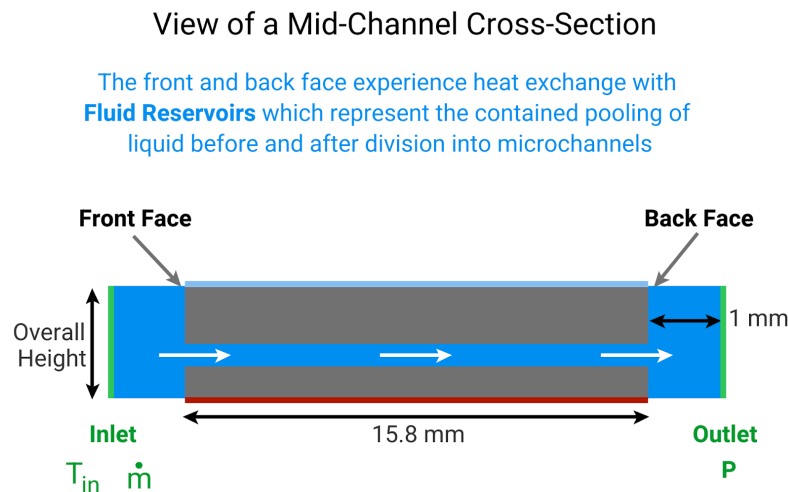


**Figure 52:** Elaboration on the ‘fluid reservoirs’ at the front and back face of the MCHS.

The inlet boundary conditions (inflow temperature and flow rate) were assigned to the front face of the front fluid reservoir block. The outlet boundary condition (pressure) was assigned to the back face of the back fluid reservoir block. Since the ‘fluid reservoirs’ are realistically contained in a fluid containment apparatus connected to the MCHS, they are not exposed to heat transfer with the computer air. Thus, the top, bottom, and side faces of the fluid reservoir blocks were assigned thermal insulation. All the assigned insulated surfaces in the model are depicted in **Figure 53**.

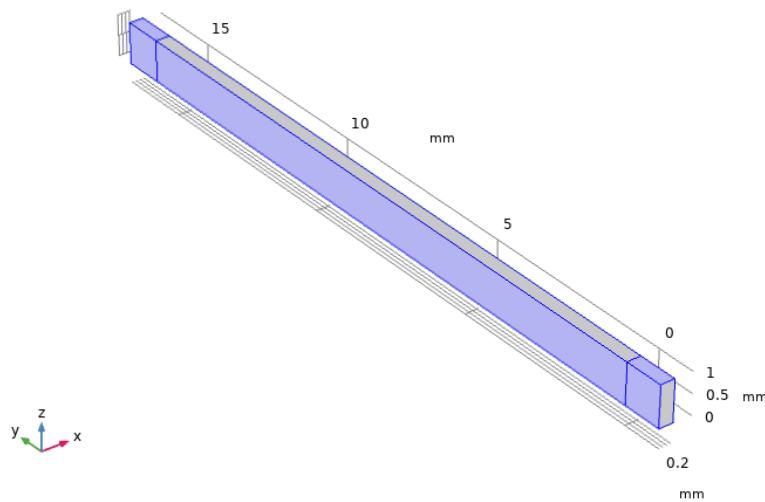


**Figure 53:** Surfaces modeled as thermal insulation.

## 5.1 Experiments

The simulated experiments in COMSOL aimed to accomplish three goals: (1) Identify the optimal MCHS geometry and operating conditions to maximize performance for turbulent flow of the coolant, (2) identify the optimal MCHS geometry and operating conditions to maximize performance for laminar flow of the coolant, and (3) verify the conclusion from the 2D laminar simulations that water was the optimal coolant fluid.

**Table 12** summarizes the experiments that were simulated in COMSOL. The first column designates the experiment number (for ease of referencing). The second column specifies the flow condition of the coolant as laminar or turbulent, and the third column specifies the fluid type. The fourth column contains important details regarding the geometry. In parentheses are the channel dimensions, which include the width, height, and spacing of the microchannel in micrometers. Following the parentheses are the total number of channels in the MCHS and the associated Reynolds number for the given geometry and fluid. The fifth and sixth columns designate the fluid inlet temperature ( $^{\circ}\text{C}$ ) and flow rate (kg/s). The system pressure (outlet boundary condition) is specified in the seventh column. The system pressure was, at minimum, the liquid saturation pressure corresponding to the estimated temperature at the outlet. For water (and air), an atmospheric pressure was assumed. For R1234ze and R134a, the saturation pressure at  $\sim 83^{\circ}\text{C}$  was assumed (2140 kPa and 2810 kPa, respectively). The eighth and final column specified which heat transfer boundary condition was applied to the bottom surface of the MCHS section in the simulation. The constant heat flux condition was set at  $65 \text{ W/cm}^2$  and the constant temperature condition was set at  $82^{\circ}\text{C}$ . During the development of the simulations (Section 4.0), the constant temperature boundary condition was initially set at  $85^{\circ}\text{C}$ , the maximum allowable operating temperature of the electronic equipment. However, for the final set of experiments, it was decided that the temperature should be lowered to  $82^{\circ}\text{C}$  to account for any thermal resistance that may occur between the CPU and the MCHS (wherein the actual temperature of the CPU is larger than what is experienced at the base of the MCHS). Additionally, the temperature was lowered to provide a small ‘safety buffer’ for the CPU. However, it should be noted that the constant heat flux boundary condition

is a better way to characterize the heat load from the CPU. The constant temperature boundary condition experiments were run primarily as a basis of comparison for the constant heat flux experiments to ensure reasonable results.

Experiments 1-10 were completed first. Experiments 1 and 2 tested a lowered inlet temperature for the turbulent MCHS model. Experiments 3 and 4 tested a new microchannel geometry for the laminar MCHS model. Experiments 5 and 6 tested a microchannel geometry and flow rate specifically suited for laminar flow of R1234ze. Experiments 7 and 8 tested a microchannel geometry and flow rate specifically suited for laminar flow of R134a. Experiments 9 and 10 tested a microchannel geometry and flow rate specifically suited for laminar flow of air.

Upon reviewing the results from the first round of simulated experiments (Ex. 1 - Ex. 10), Two additional experiments were run (with only the constant heat flux thermal boundary condition) to finalize the optimal design and operating conditions for the laminar and turbulent MCHS models. In Experiment 11, the inlet temperature of the water for the turbulent MCHS model was lowered further from 72°C to 70°C . In Experiment 12, the inlet temperature of the water for the laminar MCHS model was lowered from 75°C to 73.5°C.

**Table 12:** Key characteristics & boundary conditions for the 3D models in the simulated experiments

Ex. #	Flow Condition (lam/turb)	Fluid	Dimensions (width, height, spacing) $\mu\text{m}$ , # channels, Re	Fluid Inlet Temperature ( $^{\circ}\text{C}$ )	Fluid Flow Rate (kg/s)	System Pressure (kPa)	Heat Transfer Condition [const. heat flux (HF) / temp (T)]
1	Turb	water	(50, 230, 300) 45, 2434	72	1.23E-04	atm (0 gauge)	HF
2	Turb	water	(50, 230, 300) 45, 2434	72	1.23E-04	atm (0 gauge)	T
3	Lam	water	(40, 800, 40) 197, 185	75	2.81E-05	atm (0 gauge)	HF
4	Lam	water	(40, 800, 40) 197, 185	75	2.81E-05	atm (0 gauge)	T
5	Lam	R1234ze	(40, 1000, 40) 197, 1260	75	6.68E-05	2140	HF
6	Lam	R1234ze	(40, 1000, 40) 197, 1260	75	6.68E-05	2140	T
7	Lam	R134a	(40, 1000, 40) 197, 1218	75	5.90E-05	2810	HF
8	Lam	R134a	(40, 1000, 40) 197, 1218	75	5.90E-05	2810	T
9	Lam	air	(30, 4000, 30)	75	8.77E-05	atm (0 gauge)	HF

			263, 2094				
10	Lam	air	(30, 4000, 30) 263, 2094	75	8.77E-05	atm (0 gauge)	T
11	Turb	water	(50, 230, 300) 45, 2434	70	1.23E-04	atm (0 gauge)	HF
12	Lam	water	(40, 800, 40) 197, 185	73.5	2.81E-05	atm (0 gauge)	HF
13*	Lam (CPU)	water	(400, 800, 400) 70, 371	73.5	8.03E-05	atm (0 gauge)	HF= 3.768 W/cm <sup>2</sup> (165W, 43.8 cm <sup>2</sup> )
14*	Lam (CPU)	water	(400, 800, 400) 70, 371	74	8.03E-05	atm (0 gauge)	HF= 3.768 W/cm <sup>2</sup> (165W, 43.8 cm <sup>2</sup> )

Finally, the MCHS models, which were designed using the dimensions of a microprocessor (as often appears in simulations and experimental studies in literature), were scaled up to accommodate the greater sizes of commercial CPUs in data centers. A typical CPU was selected, the Intel® Xeon® Gold 6328H Processor (see **Figure 54**), which has a Thermal Design Power (TDP) of 165 W and a package size of 77.5 mm × 56.5 mm (43.8 cm<sup>2</sup>) [68]. TDP is the average power that a processor dissipates at base frequency [68]. Thus, the overall heat flux on the surface of the data center-scale CPU was approximately 3.768 W/cm<sup>2</sup> over the 43.8 cm<sup>2</sup> surface area, for a total load of 165 W. For comparison, the initial thermal load simulated in COMSOL was 65 W/cm<sup>2</sup> over a 2.5 cm<sup>2</sup> surface area, for a total load of 162.5 W.



**Figure 54:** Intel® Xeon® Gold 6328H Processor, part of the 3rd Generation Intel® Xeon® Scalable Processor Collection [68].

The laminar model was not difficult to scale since increasing the microchannel dimensions of the 2.5 cm<sup>2</sup> model by a factor of 10 produced a laminar Reynolds number of 371. However, the turbulent model did not scale as easily. The transition point from laminar to turbulent flow corresponds to a Reynolds number of approximately 2300. To increase Reynolds number ( $V \times D_h / \nu$ ), the velocity of the fluid or hydraulic diameter of the channel must be increased (since the kinematic viscosity property of water does not change). However, the total flow rate required to dissipate the 165 W thermal load is the same for both laminar and turbulent flow. Thus, the channel dimensions can be increased (to increase the hydraulic diameter) and the spacing between the channels increased (to reduce the number of channels

to produce a higher flow velocity per channel). Nonetheless, optimized channel geometries still required a significant degree of spacing (channel width  $\times$  12+) to produce turbulent flow conditions ( $Re > 2300$ ). However, large spacing between the microchannels may jeopardize the uniformity of heat removal from the CPU. Therefore, only the scaled-up laminar model was tested for the data center-scale CPU (165 W, 43.8 cm<sup>2</sup>) in Ex. 13\* and Ex. 14\*. The last modification to the COMSOL experimental model included the extension of the fluid reservoir blocks from 1 mm to 5 mm off the front and back face of the MCHS to better accommodate the larger MCHS geometry (77.5 mm heat sink/channel length, as opposed to the initial 15.8 mm).

## 5.2 Experiment Results

The results from the experiments are presented in **Table 13**. The first column designates the experiment number, which corresponds to the experiment setup listed in **Table 12**. The second column reports the average inlet velocity (m/s) at the front face of the front fluid reservoir. The third column reports the average outlet velocity (m/s) at the back face of the back fluid reservoir (for laminar flow, it should be nearly identical to the average inlet velocity; for turbulent flow, the total velocity magnitude increases because the turbulent flow picks up velocity in additional directions, besides just parallel to the channel). The fourth column reports the average outlet velocity (m/s) in the direction parallel to the channel (which, for both the laminar and turbulent flows, should be nearly equivalent to the average inlet velocity, which is directed only along the length of the channel). The fifth column reports the fluid temperature (°C) at the outlet (which was found by taking the average temperature at the back face of the back fluid reservoir). The sixth column reports the maximum temperature (°C) observed in the MCHS, which was found on the bottom surface of the simulated MCHS section. (Note: as detailed previously, the aim was to limit the maximum observed temperature in the MCHS to 82°C). The seventh column reports the temperature change (°C) of the fluid between the outlet and inlet. The eighth column reports the pressure drop (kPa) between the inlet and outlet, determined by subtracting the (set) outlet pressure from the average pressure observed at the inlet on the front face of the front fluid reservoir.

**Table 13:** Results from simulated experiments

Ex. #	Average Inlet Velocity (m/s)	Average Outlet Velocity (m/s)	Average Outlet Velocity - parallel to channel (m/s)	Average Fluid Temperature at Outlet (°C)	Maximum Temperature of MCHS (°C)	Temperature rise over CPU (°C)	Pressure Drop (kPa)
1	0.35206	1.6756	0.35206	77.667	83.584	5.667	536.57
2	0.35206	2.0453	0.35206	78.795	82.000	6.795	530.68
3	0.27117	0.27363	0.27069	82.021	83.509	7.021	40.726
4	0.27117	0.27359	0.27068	81.822	82.000	6.822	39.879
5	0.40609	0.49619	0.40604	81.960	86.093	6.960	19.0
6	0.40609	0.49597	0.40604	80.265	82.000	5.265	19.2

7	0.34106	0.44205	0.34106	81.874	84.995	6.874	18.9
8	0.34106	0.44187	0.34106	80.897	82.000	5.897	18.9
9	255.51	261.79	255.51	4914.1	4821.3	4839.1	7451.4
10	255.51	262.02	255.51	2549.4	82.000	2474.4	6872.9
11	0.35207	1.7321	0.35206	76.087	81.631	6.087	544.47
12	0.27115	0.27369	0.27067	80.520	82.020	7.02	42.005
13*	0.064875	0.091787	0.064876	80.483	81.278	6.983	0.99322
14*	0.064875	0.077743	0.064875	80.847	81.776	6.847	0.99447

As expected, the performance of the MCHS section was similar between the constant heat flux and constant temperature condition in Experiments 1 - 10, indicating that the heat flux simulations ran properly. Furthermore, the results from the 3D laminar simulations testing different fluids (water, R1234ze, R134a, and Air) supported the conclusion from the 2D laminar simulations in Section 4.4.1, that water would produce the best thermal performance. The 3D model was a better prediction of the performance of the fluids due to the fact that it more accurately replicates the conditions of a physical experimental prototype. Furthermore, the MCHS geometries and boundary conditions for the fluids in the 3D simulations were specific to those fluids (and their respective fluid properties), as opposed to applying the same geometry and boundary conditions across all four fluids (as was done in the 2D simulations). Thus, any factors pertaining to unsuitable MCHS design for each the fluids were mitigated in the 3D simulated experiments to more confidently discern the fluid with the best performance. For Experiments 3, 5, 7, and 9, the fluids all entered the MCHS with the same inlet temperature (75°C). The outlet temperature, temperature rise, and pressure drop of water, R1234ze, and R134a were all comparable, around 82°C, 6°C, and 30 kPa, respectively. However, the maximum temperature observed in the MCHS was 83.509°C for water, 86.093°C for R1234ze, and 84.995°C for R134a. In other words, the MCHS could be maintained at lower temperatures when water was used as the fluid, even though the refrigerants otherwise had very similar fluid temperature increases. Air was by far an exception, requiring extremely fast flow velocities and resulting in enormously high temperature increases and pressure drops, serving to show that MCHSs are not intended for pure gaseous flows. Therefore, water was clearly the optimum choice for single-phase liquid flow through the MCHS.

When comparing the turbulent simulations of water (Ex. 1, 2, 11) versus the laminar simulations (Ex. 3, 4, 12), there are a few important observations to note. First, as expected, the pressure drop is significantly higher (by about one order of magnitude) for the turbulent flow models, due to the flow condition and smaller microchannel dimensions. Second, the temperature rise of the fluid over the CPU was very consistent across both flow conditions (within ~1°C). However, the average inlet and outlet temperatures of the fluid for the turbulent flow models were lower than those for the laminar models to maintain approximately the same maximum temperature in the MCHS (compare Ex. 1 & 3 and Ex. 11 & 12). When comparing Ex. 1 and Ex. 3, the maximum temperature in the MCHS is about 83.5°C, but

the inlet/outlet temperatures of the fluid for the turbulent and laminar flow models are 72°C/77.7°C and 75°C/82.0°C, respectively. Similarly, when comparing Ex. 11 and Ex. 12, the refined turbulent and laminar models, the maximum temperature in the MCHS is about 81.8°C, but the inlet/outlet temperatures of the fluid for the turbulent and laminar flow models are 70°C/76.1°C and 73.5°C/80.5°C, respectively. However, turbulent flows typically result in better thermal performance because they are associated with higher heat transfer coefficients. Therefore, the resulting lower quality of heat from the turbulent model must be explained in other ways.

It was believed that the combined effects of the differences in velocity and surface area resulted in the suboptimal performance of the turbulent flow MCHS. For the turbulent model, the fluid velocity was higher (~0.35 m/s in Ex. 11 compared to ~0.27 m/s in Ex. 12); thus, there was less time for heat to transfer to the fluid as it traveled across the microchannel. Additionally, the surface area of the channel walls (channel perimeter × length of channel) for the turbulent and laminar models were 0.56 mm × 15.8 mm and 1.68 mm × 15.8 mm, respectively. Therefore, the turbulent model also had a smaller area over which the heat transfer could occur.

Experiments 11 and 12 represented the optimized MCHS models for turbulent and laminar flow conditions, respectively, and were the result of small adjustments to the inlet fluid temperature to maximize heat quality at the outlet and temperature rise while ensuring the MCHS did not experience temperatures much over 82°C. Between the two models, the laminar MCHS was favored for its higher quality heat (73.5°C/80.5°C at the inlet/outlet), slightly greater temperature rise (~7°C), and lower pressure drop (~42 kPa). Furthermore, when scaling up to the data center size CPU (165 W, 43.8 cm<sup>2</sup>), the laminar model could be adjusted with relative ease, whereas a turbulent geometry with a Reynolds number greater than 2300 was difficult to achieve under the constraints. Thus, a 3D laminar MCHS model was tested in Ex. 13\* with the updated MCHS section geometry, corresponding heat flux (3.768 W/cm<sup>2</sup>), flow rate ( $8.03 \times 10^{-5}$  kg/s), and inlet temperature of 73.5°C. The final iteration of the laminar MCHS model for the data center-scale CPU (Ex. 14\*) adjusted the size of the fluid reservoirs at the front and back face of the MCHS to extend 5 mm instead of 1 mm and increased the inlet temperature to 74°C to maximize the heat quality while remaining under the predefined maximum of 82°C in the MCHS. The results from Ex. 14\* are presented in Section 5.3.

### 5.3 Selected Model & Final Remarks

The results from Experiment 14\* indicated that the optimal design and operating conditions for a data center liquid cooling MCHS had been identified. Due to the increased size of the channels (as both the width and height were enlarged), the pressure drop was reduced to only ~1 kPa, compared to ~40 kPa in Ex. 3 and Ex. 4 with the smaller microprocessor (2.5 cm<sup>2</sup>, 65 W/cm<sup>2</sup>). With an inlet temperature of 74°C, the resulting outlet temperature of the water was about 80.85°C and the maximum temperature in the heat sink was 81.78°C.

The corresponding geometry for Ex. 14\* is shown in **Figure 55 - Figure 57**. **Figure 56** depicts the geometry with the y-axis scaled to 0.15, which was helpful for viewing many of the simulation result plots.

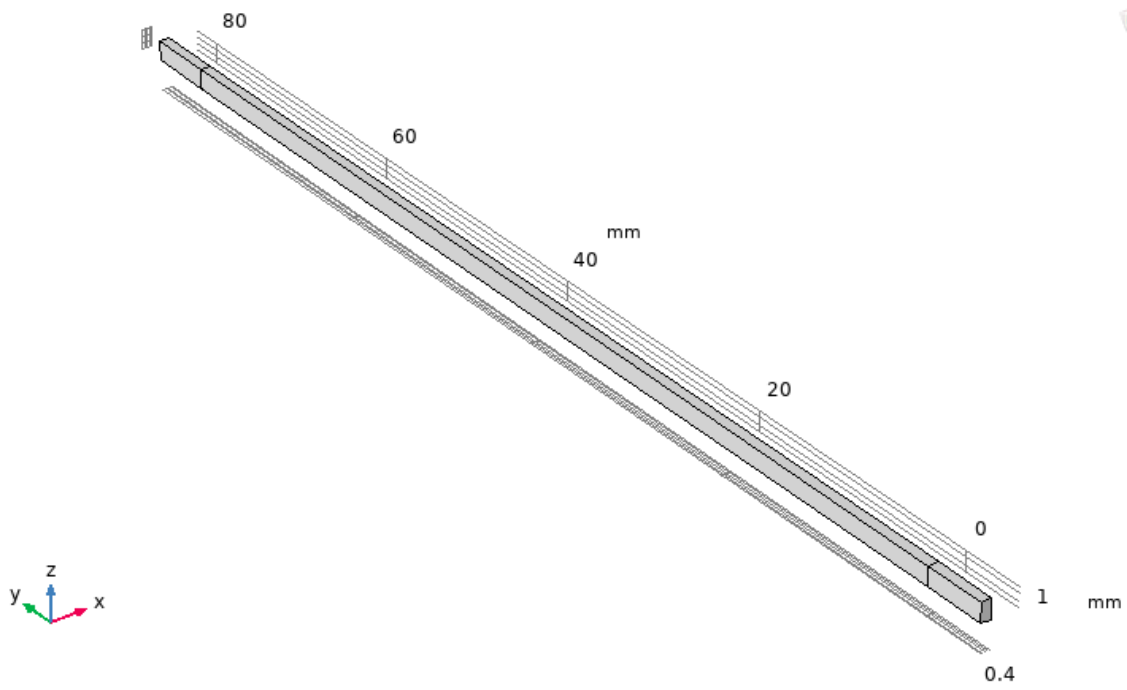


**Figure 55:** 3D geometry of the MCHS section in COMSOL, isometric view.

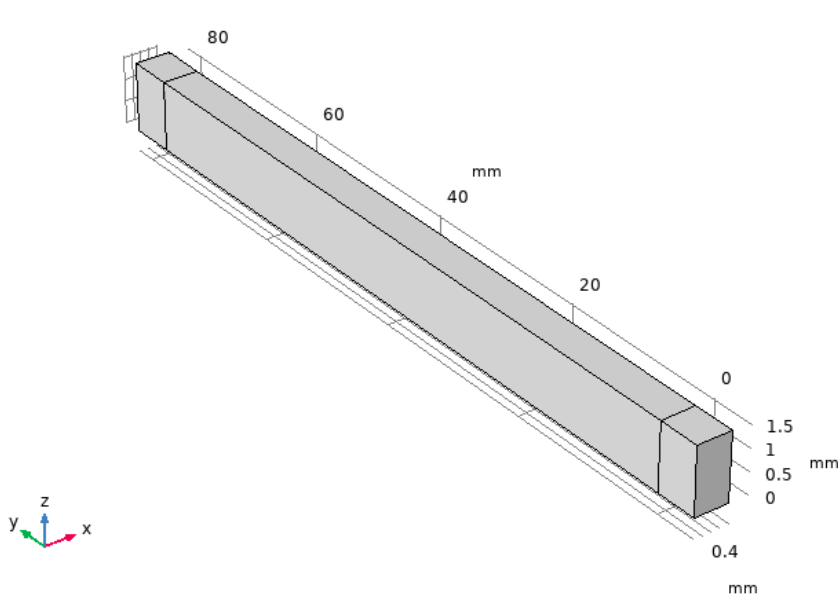


**Figure 56:** 3D Geometry of the MCHS section in COMSOL, isometric view (y-axis scaled 0.15).

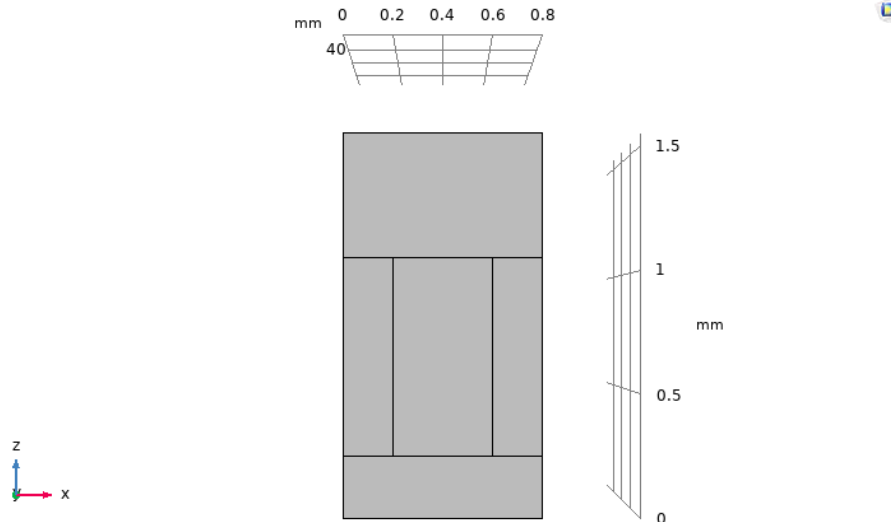


**Figure 57:** Geometry of the microchannel in COMSOL, front view.

**Figures 58 - 61** illustrate the velocity profiles of the fluid throughout the MCHS. All of the plots present the resulting velocity on a plane (or slice) that cuts through the center of the microchannel along the long edge of the MCHS. **Figure 58** depicts the velocity results with the y-axis scaled to 0.15, whereas the other velocity plots do not include a y-axis scaling factor.

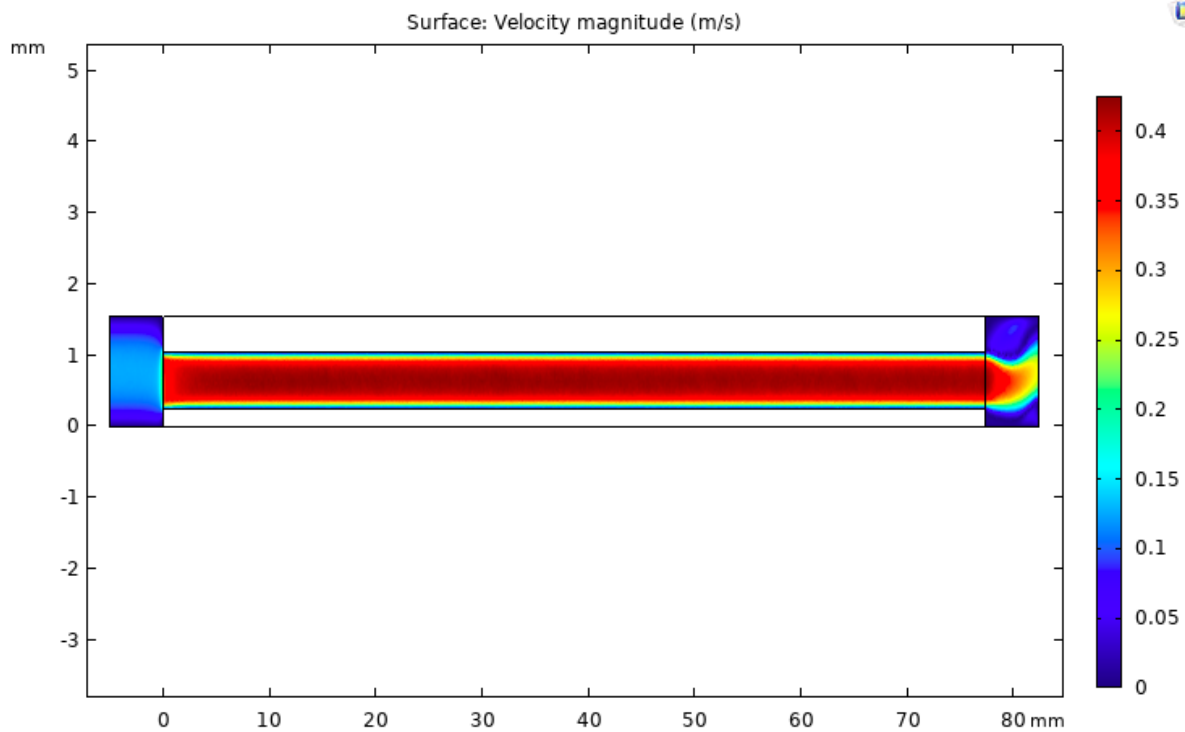


**Figure 58:** 3D velocity plot (m/s) along a mid-channel slice with water (y-axis scaled 0.15).

As shown in **Figure 58**, the velocity was uniform and slow through the inlet reservoir block. The liquid water displayed uniform, laminar flow through the channel, and exited the channel at a higher velocity

into the outlet reservoir block. The average inlet velocity (at the front face of front fluid reservoir) and outlet velocity (at the back face of the back fluid reservoir) parallel to the channel was 0.064875 m/s.

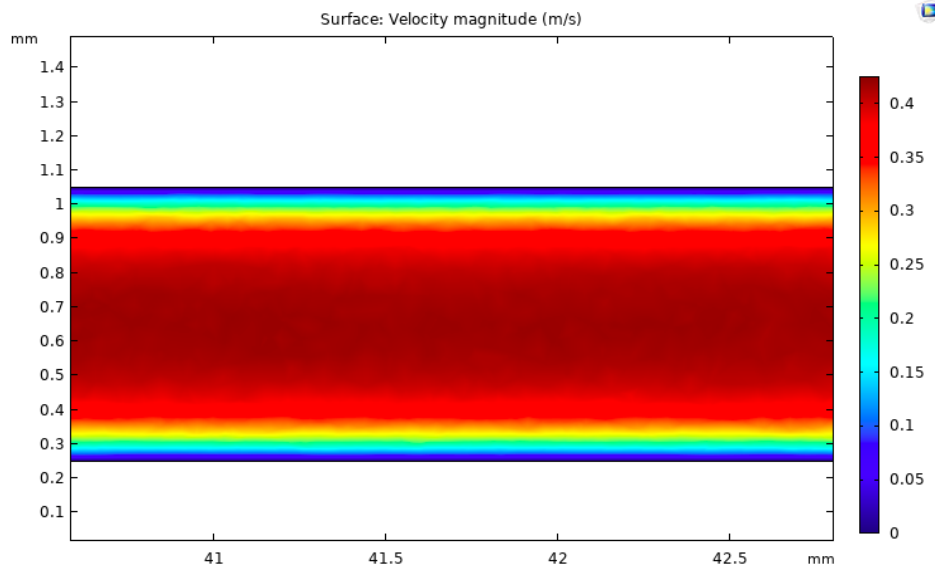


**Figure 59:** 3D velocity distribution at the center of a mid-channel slice with water.

**Figure 59** depicts the velocity profile mid-way through the microchannel. The velocity was highest in the center of the microchannel and decreased to 0 m/s at the walls.

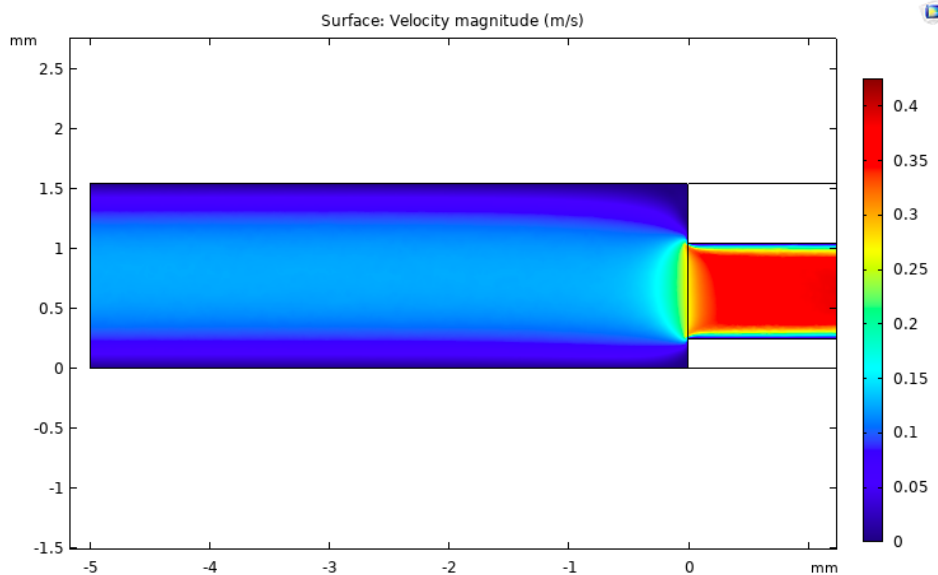


**Figure 60:** 3D velocity distribution at the inlet of a mid-channel slice with water.

**Figure 60** depicts a magnified view of the velocity distribution at the inlet. Since the flow rate and fluid density were constant, the larger cross-sectional area of the fluid reservoir resulted in slower fluid velocities. When the cross-sectional area decreased at the entrance of the channel, the velocity increased.

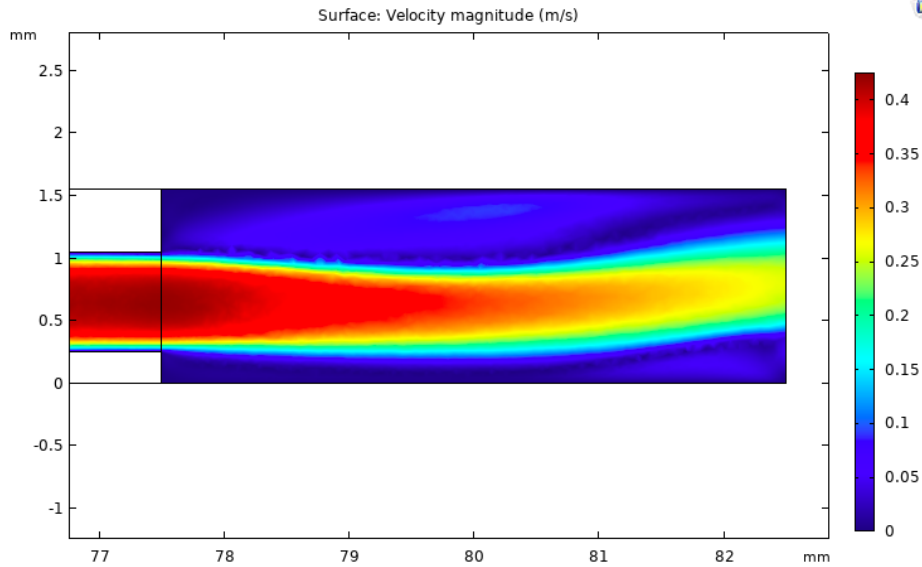


**Figure 61:** 3D velocity distribution at the outlet of a mid-channel slice with water.

**Figure 61** is a plot of the velocity distribution at the outlet. The fluid exits the channel as a small jet stream and meets the fluid reservoir at the back of the MCHS. The fluid interactions introduce velocity vectors in the x and z directions, resulting in a slight increase in the overall velocity magnitude at the outlet (0.077743 m/s).

**Figure 62** depicts the pressure drop along the microchannel (with the y-axis scaled). The pressure reported is gauge pressure (there is an added pressure of 1 atm for the ambient atmospheric pressure). The pressure drop over the microchannel was approximately 1 kPa (0.00987 atm).

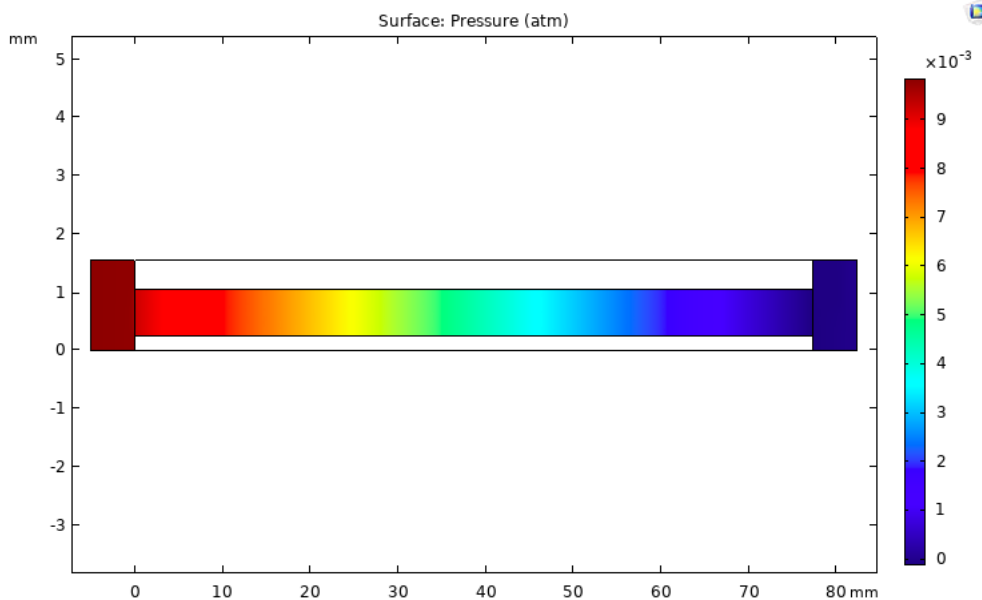


**Figure 62:** 3D pressure plot (atm) along a mid-channel slice with water (y-axis scaled 0.15).

**Figure 63** is a plot of the temperature over the whole MCHS slice geometry (with the y-axis scaled). The inlet fluid reservoir was the coldest, at the specified inflow temperature of 74°C and the exiting fluid at the back face of the back fluid reservoir was 80.85°C. The maximum temperature experienced in the heat sink (along the bottom face) was 81.78°C.

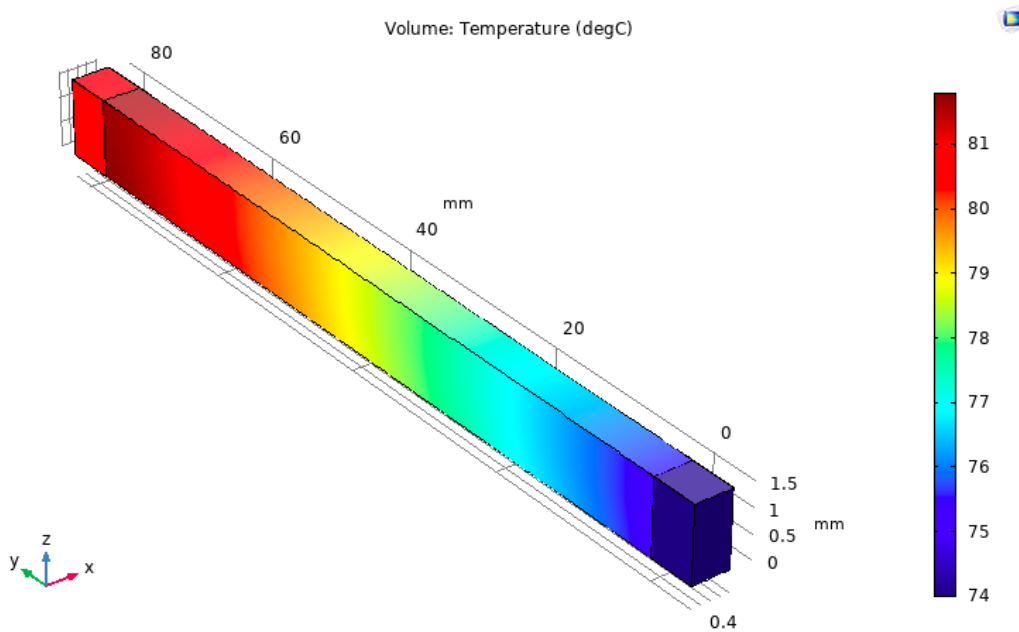


**Figure 63:** 3D temperature plot (°C) of the full geometry with water (y-axis scaled 0.15).

**Figure 64** depicts the temperature gradient along a mid-channel cross-section (with the y-axis scaled). The heat flux caused the temperature of the copper heat sink (which has a high thermal conductivity) to increase along its length. Then, the heat was dissipated into the fluid flowing through the microchannel.

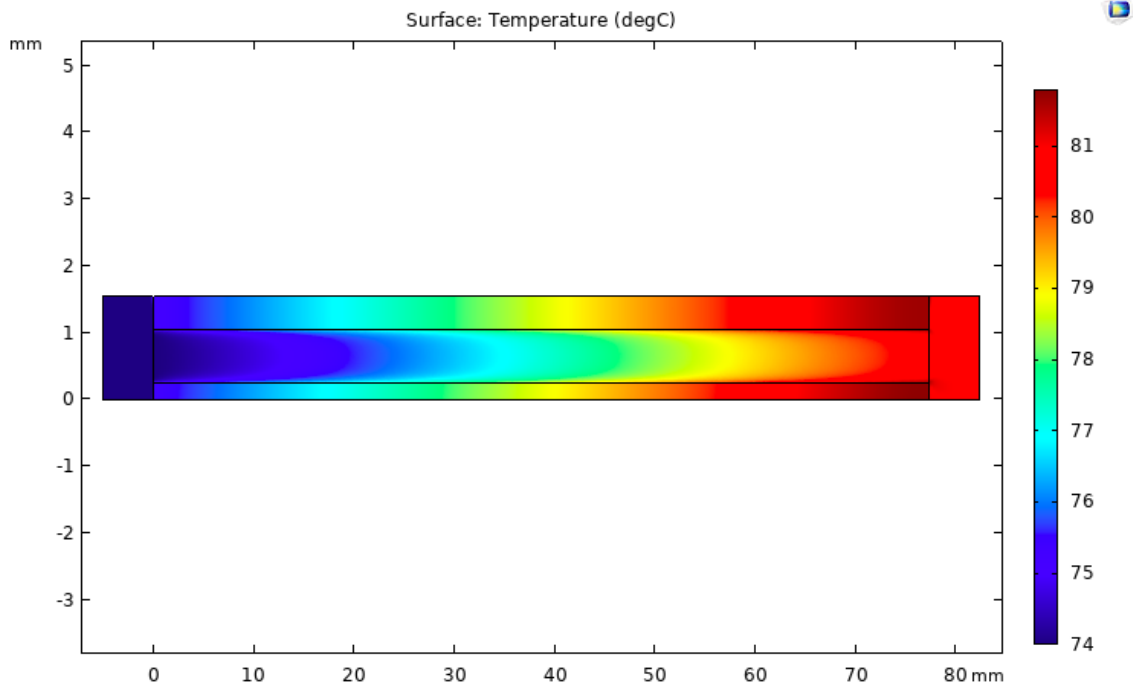


**Figure 64:** 3D temperature plot (°C) along a mid-channel slice with water (y-axis scaled 0.15).

The temperature plot in **Figure 65** illustrates how the heat is transferred from the MCHS and channel walls to the fluid flowing through the microchannel. The temperature plot was created from a cross-section of the microchannel, parallel to the front face of the heat sink, mid-way through the length of the microchannel ( $77.5 \text{ mm} \div 2$ ). As shown, heat was transferred to the fluid from all four walls of the microchannel. The fluid temperature is hottest near the walls and coldest at the center of the channel.

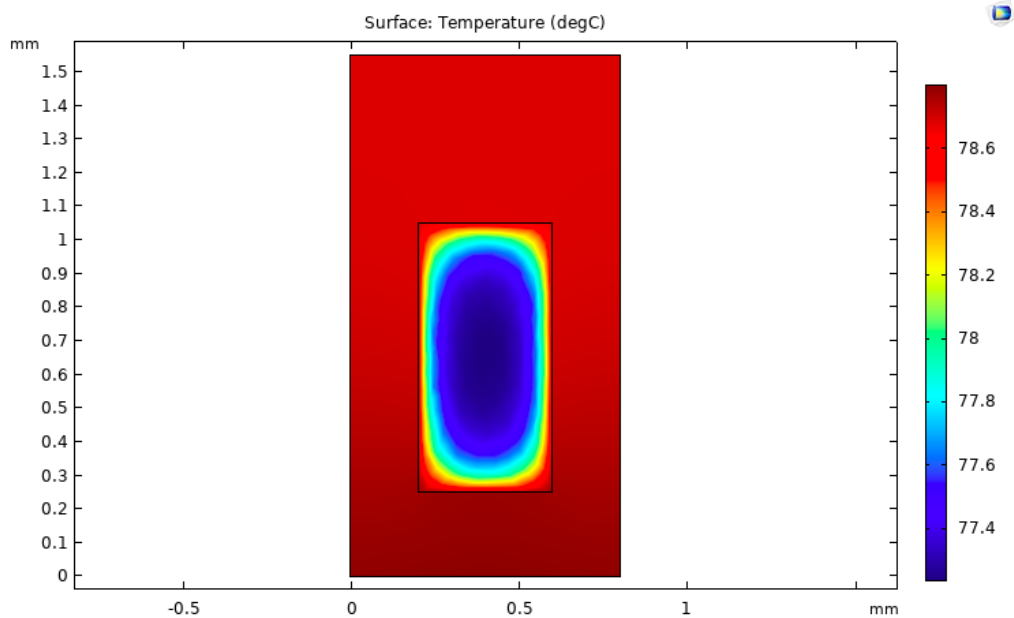


**Figure 65:** 3D temperature plot (°C) at a cross-section midway through the channel with water.

For the data center-scale CPU (Intel® Xeon® Gold 6328H Processor), Experiment 14\* demonstrated the successful achievement of numerous favorable characteristics, specifically pertaining to the quality of heat, temperature rise, and pressure drop. Throughout the process to identify the optimal design, a much smaller microprocessor (2.5 cm<sup>2</sup>) was initially utilized to explore the potential options of two-phase flow and turbulent single-phase liquid flow.

The investigation of two-phase flow revealed the complications with performing theoretical calculations and the experimental challenges with achieving stable flows. Thus, a far deeper exploration into literature and experimental studies of two-phase flow through MCHSs would be required to create and develop credible two-phase simulations for data center applications. Questions remain as to whether it is possible to use two-phase cooling at elevated temperatures (that necessitate significantly elevated pressures) to maximize waste heat quality for subsequent use by an ORC. Thus far, two-phase cooling has been used primarily to cool components with very high heat fluxes, with fluid flow temperatures closer to ambient conditions.

The development of turbulent flow MCHSs indicated that it was difficult to attain realistic geometries for the MCHS that ensured turbulent flow conditions through the microchannels under the given CPU heat load (3.768 W/cm<sup>2</sup>). It was found through theoretical calculations that lowering the temperature rise over the CPU (from ~7°C to only ~5°C) and increasing the CPU thermal design power (from 165 W to 250 W) allowed the spacing between the turbulent channels to be reduced (from over 12 times the channel width to approx. 4 times the channel width). Some modern processing chips do require the dissipation of much higher heat fluxes (such as the Intel® Xeon® Platinum 8380HL Processor) [69]. However, only one example of a typical data center-scale CPU (Intel® Xeon® Gold 6328H Processor; 165 W; 3.768 W/cm<sup>2</sup>) was investigated for the optimization in this project. Future work may include the identification of a variety of optimal MCHS designs/configurations for a range of CPUs with different thermal design powers (TDPs).



In typical data center applications that utilize liquid cooling (see **Figure 68**), the heated water transfers the heat it absorbs from the IT equipment to a water loop with a cooling tower [71]. Since the heat is removed from the servers, ultimately to be dissipated to the environment (via the cooling tower) and not utilized for any purpose, the heat is considered waste. However, by integrating an ORC with the data center cooling cycle, the heat generated by the IT equipment is captured (via the recirculating water in the liquid cooling system) and utilized as the heat input to drive the thermodynamic processes of the ORC. More specifically, server waste heat is transferred from the water in the SHEC to the ORC working fluid (R1234ze) in the ORC evaporator, which elevates the temperature of R1234ze and evaporates it. Energy is extracted from the working fluid as it flows through the ORC turbine, effectively recovering some of the (thermal) energy originally produced by the IT equipment. To complete the thermodynamic processes of the ORC, the working fluid exiting the turbine rejects some remaining heat to coolant water flowing through the ORC condenser, which cools and condenses the working fluid. The working fluid is then pumped back to the evaporator to repeat the cycle. When the water from the CPU liquid cooling system (SHEC) exits the ORC evaporator after transferring its heat to the ORC working fluid, it returns to be redistributed among the server racks. In other words, the SHEC provides the data center cooling functions that are typically attributed to a CDU. Lastly, the air temperature within the computer room is maintained via typical CRAC methods (e.g. refrigerant vapor compression cycle).

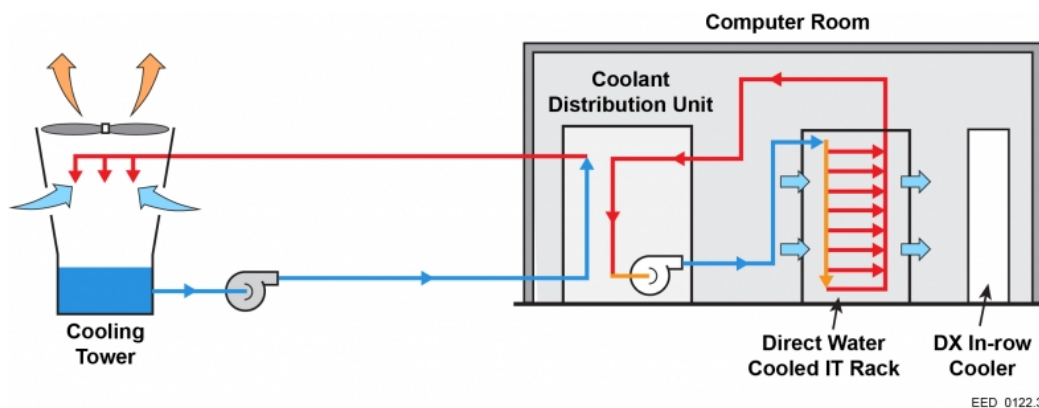


**Figure 68:** Simplified schematic of a liquid cooled data center [71].

In this section, all details regarding the final design of the ORC data center waste heat recovery system are presented. The section begins by summarizing the final design of the MCHS, which utilizes single-phase, laminar flow of liquid water. Next, all the calculations that were involved in the final design and integrated into the whole-system analysis are presented in detail. The calculations in the integrated analysis address the heat exchanger design of the ORC evaporator and condenser, ORC thermodynamics, ORC fluid mechanics, and SHEC piping and fluid mechanics. In the last section, the final numerical results of the calculations are presented.

## 6.1 Liquid Cooling Heat Sink

For the extraction and transport of the heat generated by the IT equipment (CPUs), it was found that single-phase, laminar flow of liquid water through a MCHS would be the optimal solution. However, it

should be noted that in this project, only the heat load from a CPU was considered, whereas in true data center applications, there are additional components within the servers that generate heat, such as DIMM. The series of simulated experiments conducted in COMSOL (see Section 5.0) enabled the testing of a variety of fluids, flow conditions, and microchannel geometries, and demonstrated that the configuration for Experiment 14\* produced the optimal desired results for the example CPU selected (Intel® Xeon® Gold 6328H Processor) [68]. The final design can be summarized as follows:

The heat sink is made from copper and has a width of 56.5 mm, a length of 77.5 mm, and a thickness of 1.55 mm (the length and width of the heat sink are the same as those of the CPU). The channels in the heat sink have a width of 0.4 mm, height of 0.8 mm, and span over the length of 77.5 mm. The channels are offset from the base of the heat sink (which interfaces with the CPU IHS) by 0.25 mm and are located 0.5 mm from the top surface of the heat sink. An array of 70 channels spans across the short edge of the heat sink (56.5 mm) with 0.4 mm of spacing between each channel.

The geometry of the final design is summarized in **Figure 69 (a)** and **(b)**, which depict the dimensions of the overall heat sink and channels, respectively.

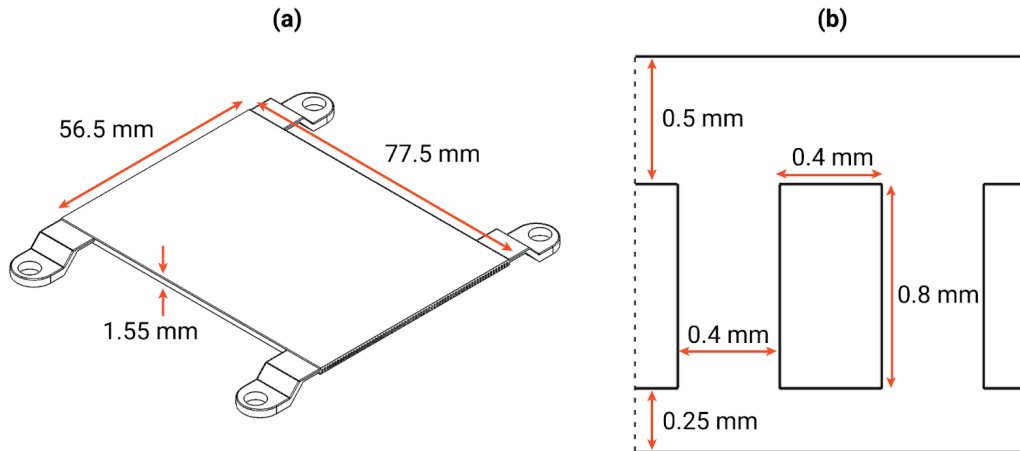


**Figure 69:** (a) Overall dimensions of liquid cooling heat sink. (b) Dimensions of heat sink channels.

It may be important to note that the final dimensions of the heat sink channels are classified as ‘minichannels’ as opposed to ‘microchannels.’ Microchannels are associated with hydraulic diameters between 10  $\mu\text{m}$  and 200  $\mu\text{m}$  whereas hydraulic diameters between 200  $\mu\text{m}$  and 3 mm are associated with minichannels [72]. The hydraulic diameter of the final channel design was 0.533 mm, designating the channels as *minichannels* in a *minichannel* heat sink (MCHS).

An isometric and exploded view of a SolidWorks model of the CPU heat sink assembly is shown in **Figure 70**. A closer view of the array of channels with the fluid distribution component hidden from view is depicted in **Figure 71**.

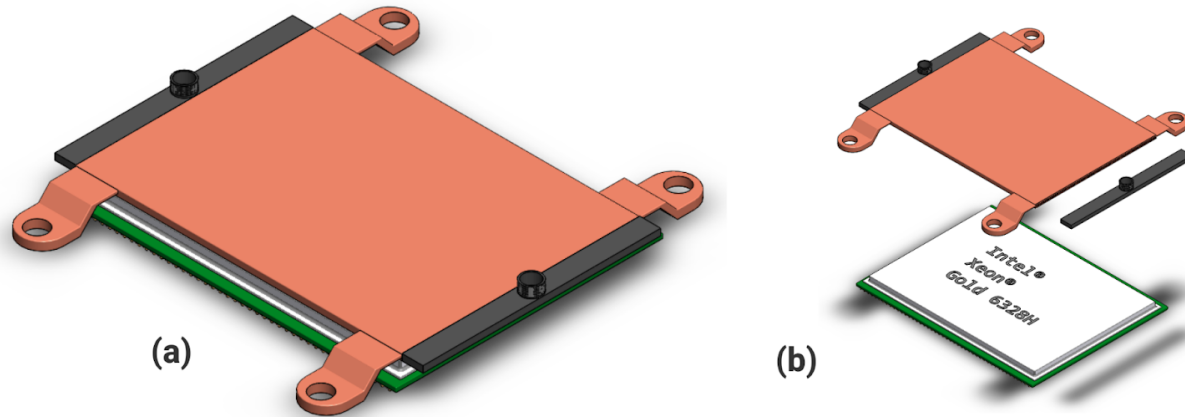


**Figure 70:** (a) Isometric and (b) exploded view of the MCHS mounted on the CPU.

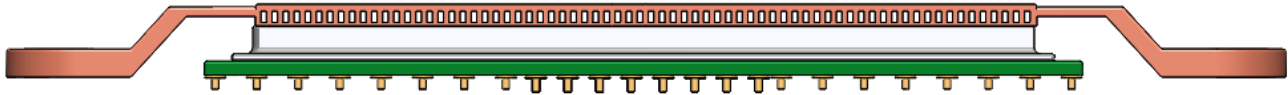


**Figure 71:** Array of channels at the front (inlet) of the heat sink.

The key input parameters and operating conditions of the final MCHS design are summarized in **Table 14**. The important output parameters and performance of the final MCHS design are summarized in **Table 15**.

**Table 14:** Summary of inputs for the final design of the MCHS.

<b>CPU Heat Load (W)</b>	165
<b>Heat Flux (W/cm<sup>2</sup>)</b>	3.768
<b>Mass Flow Rate of Water through Heat Sink (kg/s)</b>	$5.62 \times 10^{-3}$
<b>Mass Flow Rate of Water per Channel (kg/s)</b>	$8.03 \times 10^{-5}$
<b>Velocity of Water (m/s)</b>	0.0649
<b>Reynolds Number</b>	371
<b>Inlet Temperature of Water (°C)</b>	74.0
<b>Absolute Pressure at Heat Sink Outlet (kPa)</b>	101.325

**Table 15:** Summary of outputs for the final design of the MCHS.

<b>Outlet Temperature of Water (°C)</b>	80.85
<b>Maximum Temperature of MCHS (°C)</b>	81.78

<b>Temperature Rise of Water Across MCHS (°C)</b>	6.85
<b>Pressure Drop (kPa)</b>	0.994
<b>Absolute Pressure at Inlet (kPa)</b>	102.319

From the simulation of the MCHS final design, there were a few notable metrics that were needed for subsequent analyses in order to properly characterize the whole system. First, the temperature inputs and outputs were essential for the ORC evaporator calculations and overall ORC thermodynamic analysis. In prior research efforts, the data center waste heat temperatures were assumed in the ORC thermodynamic analyses [3], [20]. However, the heat transferred from the data center IT equipment (CPUs) to the ORC was not assumed in this project. Rather, the fluid and thermal interactions between a CPU and a heat transfer fluid were investigated and characterized via COMSOL simulations, which included the research and design of the optimal heat transfer process and mechanism (i.e. single-phase, laminar flow of liquid water through a MCHS). For the scenario explored in this project, the water exiting the MCHS had a temperature of 80.85°C, corresponding to the inlet temperature of the heating medium entering the ORC evaporator. The temperature of the water entering the MCHS had a temperature of 74.0°C, which corresponded to the temperature of the water exiting the ORC evaporator. Thus, the water experienced a temperature change of 6.85°C across both the MCHS and ORC evaporator.

Second, the pump power required for the SHEC could be determined since the pressure drop over the MCHS was identified via the COMSOL simulation. Rather than assuming a pump size or assuming a pressure drop over the heat sink, these values were precisely calculated in a fluid mechanics analysis of the SHEC piping, which included the pressure drop across the MCHS (based on the simulation). Lastly, the exact flow rate through each MCHS was identified from the COMSOL simulations, which enabled a precise estimation of the number of CPUs required to power the ORC for a given heat load.

In the following section, an integrated analysis is presented, wherein assumptions are limited to component-level particularities in order to provide a robust characterization of the entire system. The notable metrics from the COMSOL simulation of the MCHS final design are the foundation from which the subsequent analyses are carried out.

## 6.2 Integrated Analysis

Following a comprehensive investigation of ORC technologies, working fluids, data center cooling methods, as well as COMSOL simulations of fluid flow through a channel in a MCHS section, a consolidated analysis of the ORC system was warranted. In the following sections, the calculation processes developed for the essential system components (i.e. the evaporator, condenser, and SHEC piping) are presented in detail. Additionally, further development of the thermodynamic and fluid mechanics analyses is also described. However, the heat transfer analysis as previously described in Section 3.4.3 was not readdressed in the final design as it had simply served as verification that there was negligible heat loss from the ORC connecting pipes.

This section begins with the analytical processes used to characterize the two ORC heat exchangers, considering the configuration, materials, and additional features of the design. The evaporator calculations reference experimental data from the COMSOL simulations regarding temperature magnitudes and differentials. The evaporator was analyzed with regard to two stages, which included (1) heating the R1234ze to its saturation temperature, and (2) evaporating the saturated liquid at a constant temperature. The two stages of the evaporator were evaluated separately due to express differences in the thermo-fluid properties of the R1234ze through each stage, which warranted distinct calculation processes for determining the required pipe length. For the same reason, the condenser was also analyzed with regard to two stages, which included (1) cooling R1234ze vapor to its saturation temperature and (2) condensing the saturated vapor to a saturated liquid at a constant temperature. The required lengths of the heat exchangers were determined using the heat transfer coefficients of the fluids and piping material, wherein further research is recommended for precisely defining the thermo-fluid properties and heat transfer coefficient of R1234ze during its phase changes. The final heat exchanger designs of the evaporator and condenser consisted of the specification of the overall configuration as well as pipe design, dimensions, and length. Ultimately, the extensive heat exchanger calculations presented in this section were utilized to assess the feasibility of the data center conditions with operation of an ORC. Nonetheless, future work may include additional investigation of the design, mechanical integrity, safety factors, and pricing relevant to the ORC heat exchangers.

Since the evaporator and condenser are essential components of the ORC, the initial model for the ORC thermodynamic analysis (as presented in Section 3.4.1) was reassessed for the final design. Detailed analysis and specification of the ORC heat exchangers enabled a more accurate representation of the ORC to be generated, especially in relation to the fluid states and temperatures. The modifications to the ORC thermodynamic analysis subsequently led to adjustments to the fluid mechanics analysis of the ORC piping, specifically in regard to the revised fluid states of the R1234ze throughout the ORC. As a result, an updated optimization of pipe diameter was performed, and approximations for the pressure drop and pump power associated with each pipe section were determined for the final ORC design.

Finally, the physical configuration of the SHEC is identified and explained. After characterizing all other components and subsystems within the ORC data center heat waste recovery system, a proposed design for the SHEC piping manifold could be defined. The final design of the SHEC piping was evaluated with a fluid mechanics analysis, using the same fundamental fluid mechanics equations presented in the preliminary fluid mechanics section (Section 3.4.2). The diameters for the pipes in the SHEC were optimized, and approximations for pressure drop and pump power associated with each pipe section were determined. A final estimation of pump power required for the SHEC could be made based on the fluid mechanics analysis and the resulting pressure drop across the MCHS from the COMSOL simulation.

All the analyses for each aspect of the waste heat recovery system described in this section were implemented in a comprehensive, full-system integrated analysis in MATLAB. The program enabled efficient design iterations to be made, as the resulting effect of modifications to input variables or

calculation sequences could be observed instantaneously by re-running the program. The MATLAB code was essential to the refinement of the analyses and cohesivity between the interfacing systems, ultimately enabling an optimal design for the entire data center heat waste recovery system to be reached. Additionally, the MATLAB program developed for this project was designed with the intention that subsequent efforts in this field could utilize (or reference) the program to design and optimize waste heat recovery systems for a range of different applications, which may include different data center heat loads, piping diameters, CPU characteristics, temperature inputs, etc. Thus, the MATLAB program was designed for wider applicability, wherein its mutable characteristics may facilitate future efforts to specify a pilot ORC waste heat recovery system at a data center. Future efforts may also build upon the foundation of analyses presented in this section, further specifying components and physical system organization, which may lead to more effective and optimized system designs for an explicit application.

### 6.2.1 ORC Heat Exchanger - Evaporator

The heat supplied to the evaporator in the ORC drives the thermodynamic processes that enable the production of electrical energy. In prior research efforts, the heat supplied to the ORC evaporator and transferred to the ORC working fluid was assumed, wherein the high temperatures reached by the working fluid through the evaporator were simply assigned [3], [20]. However, in this project, neither the waste heat supplied to the ORC evaporator nor the high temperature of the ORC working fluid was assumed. From the COMSOL simulations, a liquid cooling heat sink was carefully designed for a typical data center scale CPU, wherein the resulting temperature magnitudes and differentials were used as the input parameters for the ORC evaporator calculations. To ensure a certain high temperature for the ORC working fluid at the outlet of the evaporator, an extensive design analysis of the heat exchanger was conducted. Furthermore, the ORC evaporator analysis investigated the feasibility of R1234ze as the ORC working fluid, which was suggested by Ebrahimi et al. as a viable, environmentally-conscious alternative to conventional refrigerants with high GWPs, such as R134a and R245fa [3].

#### *Basic Configuration*

The ORC evaporator was analyzed using a counterflow configuration, wherein the flows of the hot fluid and cold fluid are in opposite directions relative to one another. In other words, the hot fluid enters where the cold fluid exits and the cold fluid enters where the hot fluid exits. For the ORC evaporator, the hot fluid was the heated coolant water from the SHEC that had exited the MCHSs and contained the waste heat generated by the IT equipment in the data center. The cold fluid was the subcooled liquid R1234ze that had exited the condenser and then been pressurized by the pump. A T-x diagram of the fluids is shown in **Figure 72** (T is the relative temperature of the fluids and x is the relative length of the heat exchanger piping). It was assumed that the ORC evaporator consisted of two ‘stages’ that were combined in a single heat exchanger (as opposed to unique heat exchangers for each stage). The first stage of the evaporator consisted of heating the R1234ze subcooled liquid to its saturation temperature. The second stage of the evaporator consisted of evaporating the saturated liquid to a saturated vapor at a constant temperature.

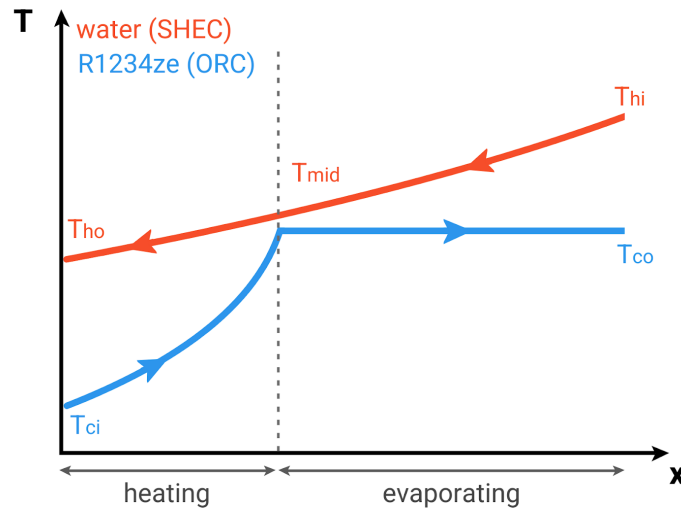


**Figure 72:** T-x diagram of the counterflow arrangement of the hot and cold fluids in ORC evaporator.

### *Temperatures, Heat Transfer Rates, & Flow Rates*

From the MCHS simulation,  $T_{hi}$  and  $T_{ho}$  were specified at 80.85°C and 74°C, respectively. However,  $T_{co}$  could be specified manually, as it should be as high as possible, to maximize the quality of heat of the R1234ze at the turbine inlet, while also being sufficiently below  $T_{hi}$  to allow for a realistically sized heat exchanger (not infinitely long). Thus,  $T_{co}$  was set as 6°C less than  $T_{hi}$ .

The temperature of the subcooled R1234ze liquid entering the evaporator ( $T_{ci}$ ) was determined based on the thermodynamics of an ideal Rankine cycle: The entropy of the fluid at the inlet of the condenser (state 2) equals the entropy at the inlet (state 1) and the temperature at the inlet of the evaporator (state 4) is the same temperature as the saturated liquid at the outlet of the condenser (state 3). At the inlet of the turbine, the R1234ze is a saturated vapor at the high temperature ( $T_1$ ) with specific entropy  $s_1$ . At the outlet of the turbine, the R1234ze is (ideally) a saturated vapor with the same entropy ( $s_2 = s_1$ ) at a lower temperature ( $T_2$ ). The vapor is condensed at a constant temperature through the condenser and then pumped to the evaporator inlet. Thus,  $T_{ci}$  is the temperature that corresponds to the low-temperature saturated vapor at the turbine outlet which has the same entropy as the high-temperature saturated vapor at the turbine inlet. It should be noted that there is a small temperature rise over the pump associated with the pump isentropic efficiency. However, the temperature rise is considered negligible for the purposes of designing the ORC evaporator, as designing with a slightly lower cold fluid inlet temperature ensures that sufficient heat would be transferred to the fluid in the actual system.

The temperature of the water at the intersection between the heating and evaporation stages ( $T_{mid}$ ) was dependent upon the mass flow rates of each of the fluids and the heat transfer rate during the evaporation stage of the heat exchanger. The mass flow rates were therefore calculated first, based on the rate of heat transfer to or from the fluid through the evaporator. The equations used to calculate mass flow rate for the R1234ze and water are represented by equations 6.2.1.1 through 6.2.1.4.

$$\dot{Q}_{total} = [\dot{m}_r \times c_p (T_{co} - T_{ci})] + (\dot{m}_r \times h_{fg}) \quad (\text{equation 6.2.1.1})$$

$$\dot{m}_r = \frac{\dot{Q}_{total}}{h_{fg} + c_p(T_{co} - T_{ci})} \quad (\text{equation 6.2.1.2})$$

where  $\dot{Q}_{total}$  is the total heat rate from the data center (10 kW),  $\dot{m}_r$  is the mass flow rate of the R1234ze (kg/s),  $h_{fg}$  is the latent heat of vaporization for R1234ze at the saturation temperature (kJ/kg),  $T_{co}$  is the temperature of the R1234ze at the outlet of the evaporator (°C),  $T_{ci}$  is the temperature of the R1234ze at the inlet of the evaporator (°C), and  $c_p$  is the specific heat capacity of R1234ze at the average temperature between  $T_{co}$  and  $T_{ci}$  (kJ/kg-K).

$$\dot{Q}_{total} = \dot{m}_w \times c_p (T_{hi} - T_{ho}) \quad (\text{equation 6.2.1.3})$$

$$\dot{m}_w = \frac{\dot{Q}_{total}}{c_p(T_{hi} - T_{ho})} \quad (\text{equation 6.2.1.4})$$

where  $\dot{m}_w$  is the mass flow rate of the water (kg/s),  $T_{hi}$  is the temperature of the water at the inlet of the evaporator (°C),  $T_{ho}$  is the temperature of the water at the outlet of the evaporator (°C), and  $c_p$  is the specific heat capacity of water at the average temperature between  $T_{hi}$  and  $T_{ho}$  (kJ/kg-K).

The heat transfer rate during the evaporation stage of the heat exchanger ( $\dot{Q}_{evap}$ ) is given by

$$\dot{Q}_{evap} = \dot{m}_r \times h_{fg} \quad (\text{equation 6.2.1.5})$$

Then,  $T_{mid}$  can be calculated based on the heat transfer rate during the evaporation stage of the heat exchanger, as shown by equation 6.2.1.6.

$$T_{mid} = T_{hi} - \frac{\dot{Q}_{evap}}{\dot{m}_w \times c_p} \quad (\text{equation 6.2.1.6})$$

where  $c_p$  is the specific heat capacity of water at the average temperature between  $T_{hi}$  and  $T_{mid}$  (kJ/kg-K).

And thus, the heat transfer rate during the heating stage of the heat exchanger ( $\dot{Q}_{heat}$ ) is given by

$$\dot{Q}_{heat} = \dot{m}_w \times c_p (T_{mid} - T_{ho}) \quad (\text{equation 6.2.1.7})$$

where  $c_p$  is the specific heat capacity of water at the average temperature between  $T_{mid}$  and  $T_{ho}$  (kJ/kg-K).

### Piping

As mentioned above, the ORC evaporator was analyzed in a counterflow configuration, which consisted of two concentric pipes. The R1234ze was directed through the inner pipe whereas the water was directed through the annulus between the inner and outer pipe. The R1234ze was chosen for the flow through the smaller inner pipe because the mass flow rate was an order of magnitude less than the flow rate of the water. The pipe configuration is summarized in **Figure 73**.

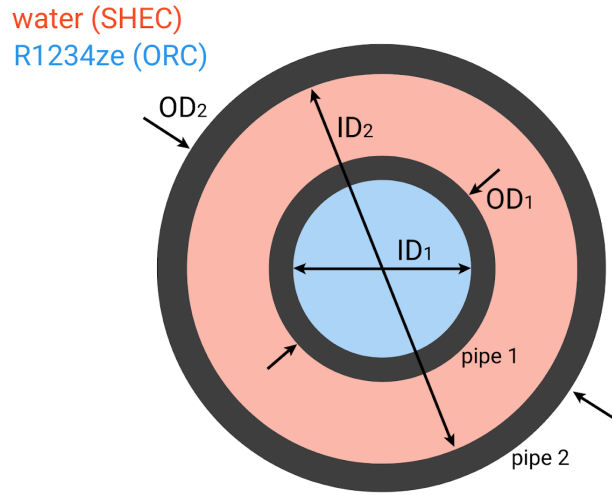


**Figure 73:** Evaporator counterflow concentric pipe configuration.

Copper pipes were selected for the piping material in the heat exchanger due to its high thermal conductivity and standard application in industry. However, it should be noted that R1234ze flows through the ORC at elevated temperatures and pressures, as high as  $\sim 75^{\circ}\text{C}$  and  $\sim 1800$  kPa. Thus, it was essential that the pipes chosen could withstand the operating conditions. For the inner tube, nominal pipe size of 3/8 inches was selected for K Type copper, which has a rated internal working pressure of 904 psig at  $200^{\circ}\text{F}$  ( $6232.86$  kPa at  $93.3^{\circ}\text{C}$ ) [53]. For the outer tube, a nominal pipe size of 1 inch was also selected for K Type copper, which has a rated internal working pressure of 557 psig at  $200^{\circ}\text{F}$  ( $3840.38$  kPa at  $93.3^{\circ}\text{C}$ ) [53]. Future work on this project could include an optimization of pipe diameter to ensure realistic flow rates of the fluids, reduce pipe costs, and specify a certain safety factor for the pipe working pressures.

For the design analysis of the heat exchanger, the hydraulic diameters and cross-sectional areas of the fluid flows were needed. For the R1234ze, the hydraulic diameter is equivalent to simply the inner diameter of the inner pipe ( $ID_1$ ) and the cross-sectional area ( $\text{m}^2$ ) is represented by

$$A_c = \pi \left( \frac{ID_1}{2} \right)^2 \quad (\text{equation 6.2.1.8})$$

For the water, the hydraulic diameter (m) and cross-sectional area ( $\text{m}^2$ ) of the annulus are represented by equations 6.2.1.9 and 6.2.1.10

$$D_h = \frac{4 \times A_c}{P_{\text{wetted}}} \quad (\text{equation 6.2.1.9})$$

$$A_c = \pi \left[ \left( \frac{ID_2}{2} \right)^2 - \left( \frac{OD_1}{2} \right)^2 \right] \quad (\text{equation 6.2.1.10})$$

where  $ID_2$  is the inner diameter of the outer pipe (m),  $OD_1$  is the outer diameter of the inner pipe (m), and  $P_{\text{wetted}}$  is the wetted perimeter of the water (m) (i.e. total perimeter of the surfaces touched by the water,  $\pi[ID_2 + OD_1]$ ). Thus, equation 6.2.1.9 can be simplified to

$$D_h = ID_2 - OD_1 \quad (\text{equation 6.2.1.11})$$

## HEX Design

The setup of the evaporator heat exchanger analysis was initially examined from a concentric pipe, counterflow perspective. However, most heat exchangers utilize various tube configurations to reduce the overall length of the HEX required to provide the desired rate of heat transfer. One prominent type of heat exchanger is the shell and tube (shown in **Figure 74**). In shell and tube heat exchangers, an array of small tubes are contained within a larger shell. In some designs, a large array of small tubes pass from one end of the shell to another. In other designs, less tubes may be included, but they may pass through the shell  $2n$  times. As shown in **Figure 74**, the U-tube passes twice along the length of the shell (i.e. two tube passes). Due to the flexibility of shell and tube designs and the many opportunities for optimization via additional features, such as baffles, fins, etc., a shell and tube HEX analysis was conducted in conjunction with the counterflow HEX analysis. (However, it should be noted that other HEX types, such as cross-flow, could potentially provide better performance. Therefore, it is recommended that further optimization efforts, with regard to the heat exchanger, should investigate other HEX types/tube configurations.)

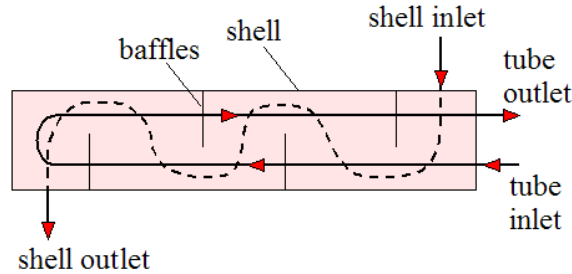


**Figure 74:** Diagram of shell and tube heat exchanger [73].

To account for the difference in effectiveness between the counterflow heat exchanger type (which is the ideal case, yet often physically impractical) and the shell and tube type, a correction factor was determined from the graph in **Figure 75**.

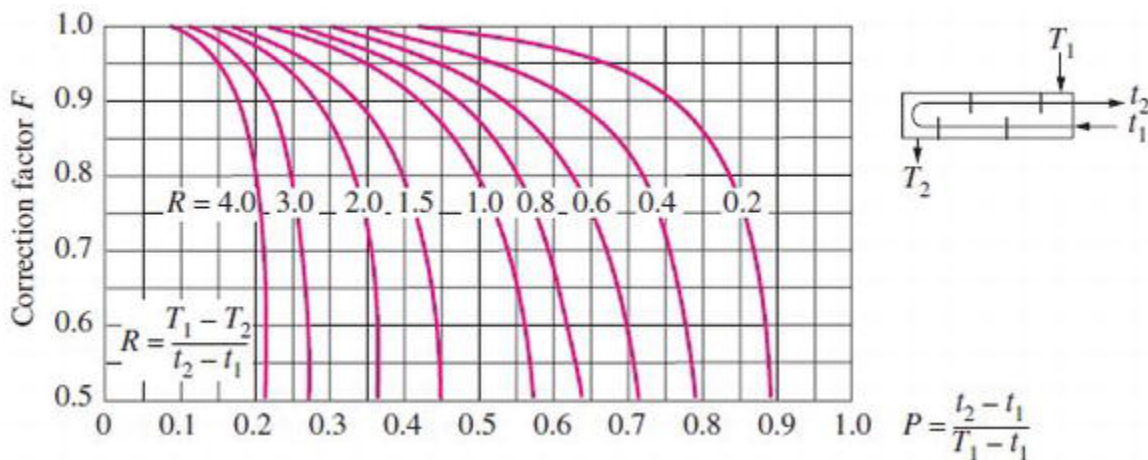


**Figure 75:** Correction factor graph for one shell pass and any multiple of two tube passes [74].

The shell and tube correction factor is determined based on the values of two parameters  $P$  and  $R$ , which are represented by the following equations,

$$P = \frac{t_2 - t_1}{T_1 - t_1} \quad (\text{equation 6.2.1.12})$$

$$R = \frac{T_1 - T_2}{t_2 - t_1} \quad (\text{equation 6.2.1.13})$$

where  $T_1$  and  $T_2$  are the temperatures of the shell fluid at the inlet and outlet, respectively, and  $t_1$  and  $t_2$  are the temperatures of the tube fluid at the inlet and outlet, respectively. For the ORC evaporator, the water was chosen as the shell fluid and the R1234ze was chosen for the tube fluid due to the differences in magnitude between the flow rates of the two fluids. Once the values of  $P$  and  $R$  were calculated, the corresponding correction factor for the shell and tube configuration was determined from the y-axis of the graph in **Figure 75**.

### *Fins (Part 1)*

Typically, fins are recommended for pipes when the heat transfer coefficient (HTC) of one fluid is significantly less (at least by a factor of  $\sim 10$ ) than the HTC of the other fluid. It was anticipated that the R1234ze would experience lower HTCs due to the much lower mass flow rate and generally lower thermal conductivities, compared to water. Thus, finned pipes were an additional feature of the heat exchanger that was considered in order to optimize the final design. Fins (i.e. extended surfaces) improve the effectiveness of heat exchangers by increasing the heat transfer area that the fluid is in contact with. A variety of different extended surfaces, including fins, are presented in **Figure 76**. The fin arrangement that was selected for the ORC evaporator was ‘internal axial fins’ (see (f) in **Figure 76**), wherein the fins were rectangular in shape. The fins were assigned to the pipe containing R1234ze.

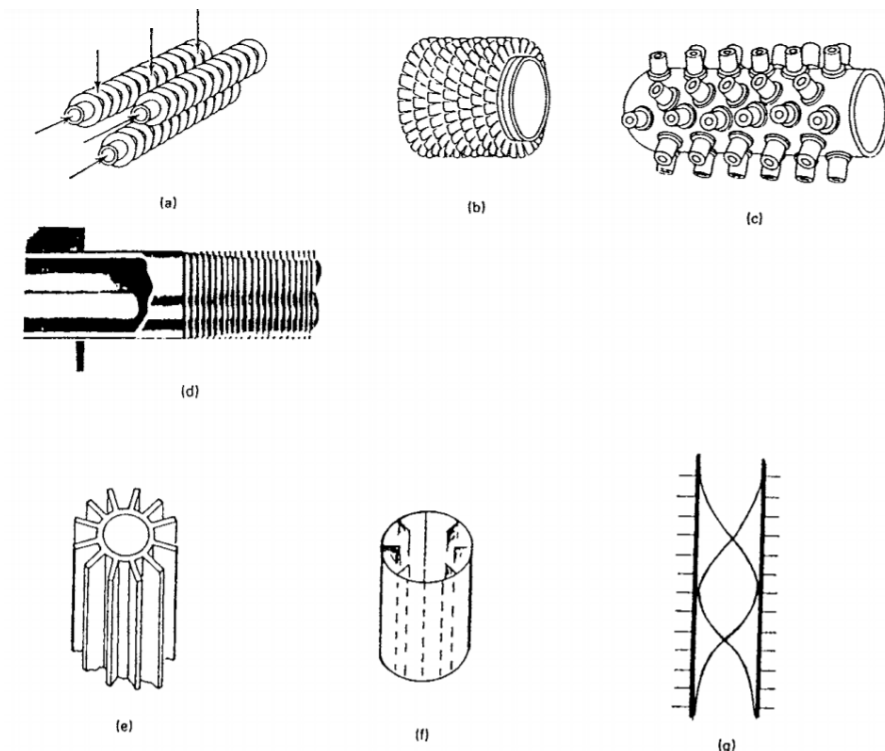


**Figure 76:** Examples of extended surfaces for heat exchanger pipes [75].

To maximize the additional surface area provided by the introduction of fins while also ensuring a realistic geometry, the following process was used to determine the thickness, extension, and number of fins on the interior surface of the inner pipe (i.e. tubes for the shell and tube HEX configuration).

1. Given the thickness of the pipe, a fin thickness was selected near one third the thickness of the inner pipe.
2. A “floating pipe” was designated in the center of the inner pipe to which the fins would extend, with a diameter of approximately 0.4 times the ID of the inner pipe (m). Subsequently, each fin extended 0.3 times the ID of the inner pipe (m).
3. A reasonable percentage of the circumference of the “floating pipe” which would be occupied by fins was specified at approximately 50%.
4. The number of axial fins within the inner pipe was represented by equation 6.2.1.14, rounded up to the next whole number.

$$N = \frac{ID_1 \times 0.4 \times 0.50}{t} \quad (\text{equation 6.2.1.14})$$

where  $ID_1$  is the inner diameter of the inner pipe and  $t$  is the thickness of the fins. The geometric fin parameters for the internal axial fins within the inner pipe are summarized in **Figure 77**.

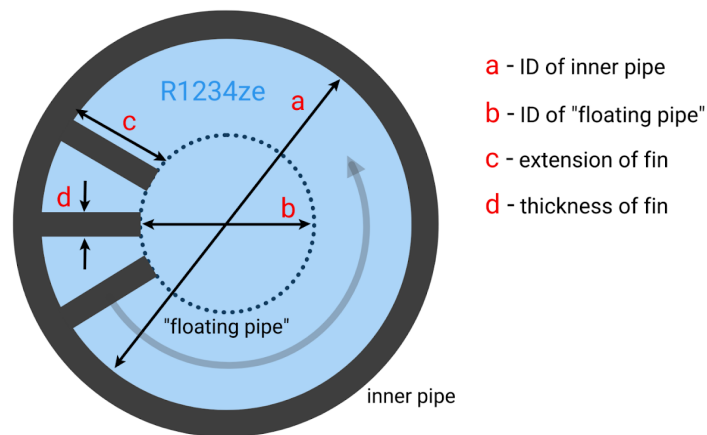


**Figure 77:** Diagram of fin geometry and parameters.

Lastly, it should be noted that there is a wide range of features and variations of HEX design that may optimize performance of the HEX, which could be investigated in a future project. Future work may also build on the fin design presented in this section, optimizing the geometry to minimize the required HEX pipe length to reduce costs while ensuring realistic flows conditions and feasible mechanical designs (e.g. must withstand elevated pressures of R1234ze). Parameters that may warrant closer attention in future work, in relation to fluid/mechanical feasibility, are the fin thickness and spacing between the fins.

#### *UA Using LMTD Method*

Since all of the temperatures of the water and R1234ze were known at the inlets and outlets of both the heating and evaporation stages of the heat exchanger, the Log Mean Temperature Difference (LMTD) Method was used for the design analysis. The analysis consisted of two sets of calculations since the

properties of the fluids were not constant over the heating and evaporation stages. During heating, the R1234ze is in a liquid phase. However, the R1234ze undergoes a phase change from liquid to vapor over the evaporation stage. Therefore, to precisely determine the HTC of each fluid in each stage (which is dependent on fluid properties) and calculate the required length of piping, each stage had to be treated as a separate heat exchanger. Ultimately, the resulting pipe lengths of each stage were summed up to determine the total required pipe length for the ORC evaporator, since it was assumed that both stages would occur in the same HEX (as opposed to two individual HEXs).

The governing equation for the LMTD method represents the heat transfer rate of the HEX as shown in equation 6.2.1.15. The equation was used as the starting point for each analysis of the heat exchanger stages, wherein all parameters pertained to the specific conditions of the individual stage, not the overall ORC evaporator.

$$\dot{Q} = U \times A \times \Delta T_{LMTD} \times F \quad (\text{equation 6.2.1.15})$$

where  $\dot{Q}$  is the heat transfer rate of the HEX (W),  $U$  is the overall heat transfer coefficient (W/m<sup>2</sup>-K),  $A$  is the HEX heat transfer area (m<sup>2</sup>),  $\Delta T_{LMTD}$  is the log mean temperature difference, and  $F$  is the correction factor for HEX types other than counterflow (e.g. shell and tube). When the particular HEX geometry is not predefined (as was the case for the evaporator design analysis), the overall heat transfer coefficient and area are combined into one term, represented by  $UA$ , which can be understood as the functional form of the overall heat transfer coefficient, with units W/K. The LMTD is given by the following expression:

$$\Delta T_{LMTD} = \frac{\Delta T_1 - \Delta T_2}{\ln\left(\frac{\Delta T_1}{\Delta T_2}\right)} \quad (\text{equation 6.2.1.16})$$

where  $\Delta T_1$  and  $\Delta T_2$  are the differences between the temperatures of the two fluids at each end of the heat exchanger. The fluid temperature differences which corresponded to  $\Delta T_1$  and  $\Delta T_2$  in the heating stage and evaporation stage are summarized in **Table 16**. The expressions correspond to the vertically aligned temperatures labeled on the T-x diagram in **Figure 72**.

**Table 16:** Expressions for  $\Delta T_1$  and  $\Delta T_2$  in the heating and evaporation stages.

	$\Delta T_1$	$\Delta T_2$
Heating Stage	$T_{ho} - T_{ci}$	$T_{mid} - T_{co}$
Evaporation Stage	$T_{hi} - T_{co}$	$T_{mid} - T_{co}$

It is important to note that the correction factor ( $F$ ) for the shell and tube heat exchanger was only relevant for the heating stage. For evaporating and condensing, the correction factor for different types/configurations of heat exchangers is 1. Correction factors for evaporation and condensing in HEXs are not needed due to the fact that the temperature of the fluid undergoing phase change remains fixed over the HEX, and thus effectiveness of the HEX does not depend on the specific interactions or layouts of the temperature differentials between the two fluids. Alternatively, in the  $\epsilon$ -NTU heat exchanger analysis method, the value for the number of transfer units (NTU) for all evaporators and

condensers is always represented by  $-\ln(1 - \varepsilon)$ , regardless of whether the HEX consists of counterflow concentric pipes, shell and tube, cross-flow, etc.

By rearranging equation 6.2.1.15, the expression for  $UA$  (evaluated separately for the heating and evaporation stages) is given by,

$$UA = \frac{\dot{Q}}{\Delta T_{LMTD} \times F} \quad (\text{equation 6.2.1.17})$$

#### Determining Heat Transfer Coefficient

The HTC of each fluid through each stage of the ORC evaporator was calculated using the Nusselt number, which is represented by the following two expressions:

$$Nu = \frac{h \times D_h}{k} \quad (\text{equation 6.2.1.18})$$

$$Nu = 0.023 \times Re^{0.8} \times Pr^n \quad (\text{equation 6.2.1.19})$$

where  $h$  is the HTC of the fluid ( $W/m^2-K$ ),  $D_h$  is the hydraulic diameter of the pipe (m),  $k$  is the thermal conductivity of the fluid ( $W/m-K$ ),  $Re$  is the Reynolds number,  $Pr$  is the Prandtl number, and  $n$  is the exponent of the Prandtl number, which is 0.3 when the fluid is hotter than the pipe surface ( $T_m > T_s$ ) and 0.4 when the fluid is colder than the pipe surface ( $T_m < T_s$ ). Equation 6.2.1.19 is a correlation for the Nusselt number of the fluid, and is valid for cases where the flow is turbulent and fully developed,  $0.6 \leq Pr \leq 160$ ,  $Re_D \geq 10,000$ , and  $L/D \geq 10$ . Calculations for the Reynolds number and Prandtl number were required for the evaluation of equation 6.2.1.19, and were given by the following expressions:

$$Re = \frac{\dot{m} \times D_h}{A_c \times \mu} \quad (\text{equation 6.2.1.20})$$

$$Pr = \frac{\mu \times c_p}{k} \quad (\text{equation 6.2.1.21})$$

where  $A_c$  is the cross-sectional area of the fluid through the pipe ( $m^2$ ),  $\mu$  is the dynamic viscosity (Pa-s), and  $c_p$  is the specific heat capacity ( $J/kg-K$ ). It is essential to note that all the fluid properties for the water and R1234ze in the heating and evaporation stages ( $k$ ,  $\mu$ ,  $c_p$ ) correspond to the properties at the average temperature of the fluid over each specific stage.

Once  $Re$ ,  $Pr$ , and  $Nu$  had been calculated, equation 6.2.1.18 was rearranged to solve for the HTC of the fluid as follows,

$$h = \frac{Nu \times k}{D_h} \quad (\text{equation 6.2.1.22})$$

During both the heating and evaporation stages, the water remains in the liquid phase, and thus the properties can be assumed constant at the average temperature of the water through each stage. The same can be assumed for the liquid R1234ze as it is heated to the saturation temperature during the heating stage. However, during the evaporation stage, the R1234ze changes from the liquid to the vapor phase, wherein the fluid properties vary greatly, and constantly undergo change as the vapor quality of the fluid changes. Therefore, when the R1234ze was evaporating, constant properties at the saturation temperature could not be assumed. Instead, experimental results from literature were consulted to approximate the heat transfer coefficient of the R1234ze during evaporation. There have been numerous

studies that have investigated the heat transfer coefficient of R1234ze experimentally over a wide range of varying conditions, including tube size, tube type (smooth vs microfins), mass flux, heat flux, saturation temperature, pressure, etc. Based on the review of several papers [76], [77], [78], the results from the study conducted by Li and Hrnjak was selected to approximate the HTC of R1234ze in the ORC evaporator calculations due to the reporting of HTC values that were mid-range among the papers reviewed. The results from their HTC experiments using a multiport microchannel tube and variation of mass flux, heat flux, and saturation temperature are presented in **Figure 78**.

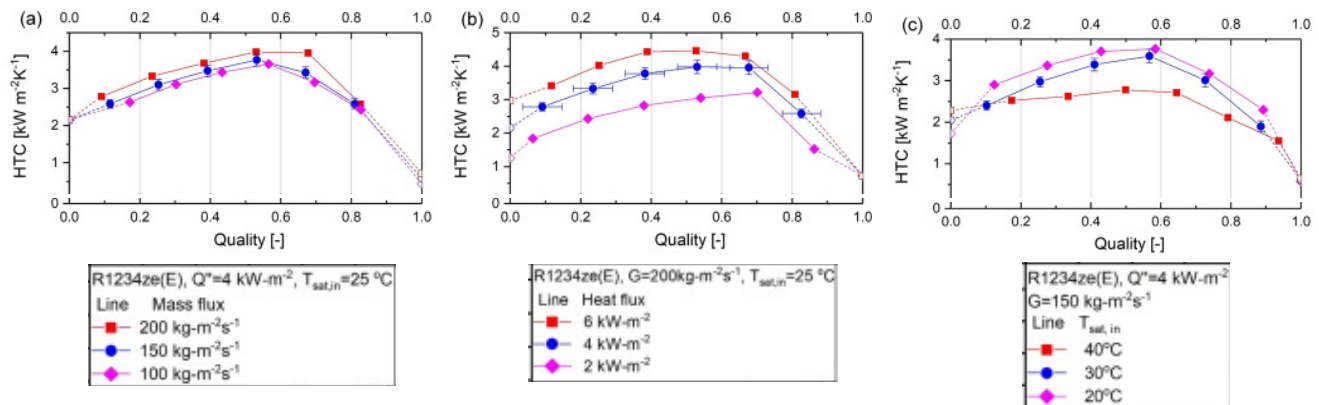


**Figure 78:** Heat transfer coefficients of R1234ze (boiling) versus vapor quality of R1234ze [78].

As can be seen from the graphs in **Figure 78**, the HTC of R1234ze varies greatly depending on the vapor quality ( $x$ ) of the fluid [78]. In other words, as the R1234ze changes phase from a saturated liquid to saturated vapor in the ORC evaporator, the HTC that corresponds with the liquid-vapor mix of the fluid also changes [78]. The general trend of the graphs shows that the HTC of R1234ze at a saturated liquid ( $x=0$ ) is around  $2 \text{ kW/m}^2\text{K}$ , which increases as the R1234ze begins to evaporate [78]. When the quality of R1234ze is approximately 0.5-0.6, the HTC reaches its highest value around  $4 \text{ kW/m}^2\text{K}$  [78]. As the fluid reaches higher fractions of vapor, the HTC decreases until about  $1 \text{ kW/m}^2\text{K}$  when it becomes a saturated vapor [78]. Other variations in HTC are shown as the result of varying the mass flux, heat flux, and saturation temperature: increasing the mass flux and heat flux increases the HTC, whereas increasing the saturation temperature decreases the HTC [78]. Due to the wide range of conditions that affect the HTC, and the fact that a precise characterization of the HTC is only obtainable through experiment, a range of R1234ze HTC values was used for the ORC evaporator analysis. Based on the experimental results from Li and Hrnjak, maximum, minimum, and average HTC values for R1234ze were specified at  $4200 \text{ W/m}^2\text{-K}$ ,  $1000 \text{ W/m}^2\text{-K}$ , and  $2600 \text{ W/m}^2\text{-K}$ , respectively. However, it should be noted that the HTCs for R1234ze through the evaporator were very roughly approximated based on existing experimental data. Future work on this project could pursue a more robust characterization of the flow conditions and fluid properties of the R1234ze through the pipes in the evaporator stage for a more precise specification of the heat exchanger design.

### Calculating Length of HEX

Once the HTC of the fluids were identified, the length of piping required for each heat exchanger stage was calculated. The expression for  $UA$  (summation of thermal resistances), as presented below, was utilized to determine the length.

$$\frac{1}{UA} = \frac{1}{h_i \times A_i} + \frac{\ln(OD/ID)}{2\pi kL} + \frac{1}{h_o \times A_o} \quad (\text{equation 6.2.1.23})$$

where  $h_i$  is the HTC of the inner fluid (R1234ze),  $h_o$  is the HTC of the outer fluid (water),  $ID$  and  $OD$  are the inner and outer diameters of the inner pipe, and  $k$  is the thermal conductivity of the inner pipe (at the average temperature of the pipe during each of the HEX stages). The thermal conductivity of the inner pipe was estimated based on tabulated values of thermal conductivity from *eFunda Engineering Fundamentals* [79]. The terms  $A_i$  and  $A_o$  are the heat transfer areas that correspond to the inner and outer surface of the pipe, respectively. The heat transfer area for the inner and outer fluid is represented by,

$$A = \pi \times D \times L \quad (\text{equation 6.2.1.24})$$

where  $D$  is the diameter (m)—which is the  $ID$  of the inner pipe for the inner fluid (R1234ze) and the  $OD$  of the inner pipe for the outer fluid (water). Thus, by substituting the expression for  $A_i$  and  $A_o$  (equation 6.2.1.24) into equation 6.2.1.23 and rearranging to solve for  $L$ , the required length of the HEX was given by,

$$L = UA \times \left[ \frac{1}{h_i \times \pi \times ID} + \frac{\ln(OD/ID)}{2\pi k} + \frac{1}{h_o \times \pi \times OD} \right] \quad (\text{equation 6.2.1.25})$$

For the heating stage, two results for length were recorded: (1) length of pipe for counterflow concentric tubes and (2) length of pipe for a shell and tube configuration. For the evaporation stage, no correction factor for the shell and tube calculation of  $UA$  was required, so the lengths were the same. However, there were three different values identified for the HTC of R1234ze during evaporation (maximum, minimum, and average), so three different length calculations were completed for the HEX analysis of the evaporation stage.

### Fins (Part 2)

The following set of steps describes the calculations that were used to account for the effect of adding axial fins to the internal surface of the inner pipe containing R1234ze. The derivation of a single metric, denoted as fin correction factor (FCF), was used to quantitatively represent the factor by which the heat transfer area was effectively increased by, due to the addition of fins. The 7th edition of *The Fundamentals of Heat and Mass Transfer* textbook from Bergman et al. was used as a reference to obtain the appropriate fin equations in the analysis [63].

To start, the effective thermal resistance of a fin array (accounting for parallel heat flow paths by conduction and convection in the fins and base surface) is given by,

$$R = \frac{1}{\eta_o \times h \times A_i} \quad (\text{equation 6.2.1.26})$$

where  $R$  is the effective resistance (K/W)—equivalent to  $(1/UA)$ ,  $\eta_o$  is the overall surface efficiency,  $h$  is the HTC of the fluid (W/m<sup>2</sup>-K), and  $A_i$  is the total surface area (m<sup>2</sup>). The total surface area includes the surface area of the fins and the exposed base surface on which the fins are attached, represented by,

$$A_t = NA_f + A_b \quad (\text{equation 6.2.1.27})$$

where  $N$  is the number of fins in the array,  $A_f$  is the area of one fin ( $\text{m}^2$ ), and  $A_b$  is the area of the exposed base surface ( $\text{m}^2$ ). The area of one fin can be determined via the following expressions,

$$A_f = 2 \times l_c \times L \quad (\text{equation 6.2.1.28})$$

$$l_c = l_e + (t/2) \quad (\text{equation 6.2.1.29})$$

where  $l_c$  is the corrected fin extension length (m),  $L$  is the length of the fin along the pipe (i.e. the length of the pipe),  $l_e$  is the fin extension length (m), and  $t$  is the thickness of the fin (m). The area of the exposed base is as follows,

$$A_b = L [\pi D - Nt] \quad (\text{equation 6.2.1.30})$$

where  $L$  is the length of the pipe (m) and  $D$  is the ID of the inner pipe.

The overall surface efficiency is represented by the following equation,

$$\eta_o = 1 - \frac{NA_f}{A_t} (1 - \eta_f) \quad (\text{equation 6.2.1.31})$$

where  $\eta_f$  is the efficiency of a single fin, and can be found using the following expressions,

$$\eta_f = \frac{\tanh(m \times l_c)}{m \times l_c} \quad (\text{equation 6.2.1.32})$$

$$m = \left[ \frac{2 \times h}{k \times t} \right]^{\frac{1}{2}} \quad (\text{equation 6.2.1.33})$$

where  $h$  is the HTC of the fluid (R1234ze) and  $k$  is the thermal conductivity of the pipe material (W/m-K).

By substituting equation 6.1.2.31 for  $\eta_o$  into 6.2.1.26 and simplifying, the thermal resistance term corresponding to R1234ze in the  $(1/UA)$  equation can be given by,

$$R = \frac{1}{h[A_t - (NA_f(1 - \eta_f))]} \quad (\text{equation 6.2.1.34})$$

where the bracketed term in the expression above represents the new “effective heat transfer area” as a result of the fins. The term can be presented in an alternative form, represented by the original heat transfer area (interior surface area of the inner pipe)  $A_i$ , multiplied by a fin correction factor (FCF).

$$\left[ A_t - (NA_f(1 - \eta_f)) \right] = A_i \times FCF \quad (\text{equation 6.2.1.35})$$

Thus, the thermal resistance term simplifies to

$$R = \frac{1}{h_i \times A_i \times FCF} \quad (\text{equation 6.2.1.36})$$

where FCF is represented by,

$$FCF = \frac{[A_t - (NA_f(1 - \eta_f))]}{A_i} \quad (\text{equation 6.2.1.37})$$

wherein the variable  $L$  for the length of the pipes and the fins (embedded in the expressions for  $A_t$ ,  $A_f$ , and  $A_i$ ) cancels, and thus is not required to compute the FCF.

Finally, the length of piping required for each heat exchanger stage—with *internal axial fins on the inside of the inner pipe*—is given by a simple modification to equation 6.2.1.25 as follows,

$$L = UA \times \left[ \frac{1}{h_i \times \pi \times ID \times FCF} + \frac{\ln(OD/ID)}{2\pi k} + \frac{1}{h_o \times \pi \times OD} \right] \quad (\text{equation 6.2.1.38})$$

From equation 6.2.1.38, five calculations of required HEX length (with finned pipes) were recorded for the ORC evaporator, listed as follows:

1. Heating stage, counterflow concentric pipe configuration
2. Heating stage, shell and tube configuration (correction factor  $F$  for UA calculation)
3. Evaporation stage, maximum HTC for R1234ze
4. Evaporation stage, minimum HTC for R1234ze
5. Evaporation stage, average HTC for R1234ze

For additional clarification, the prominent equations and parameters for the fin calculations are summarized in **Figure 79**.

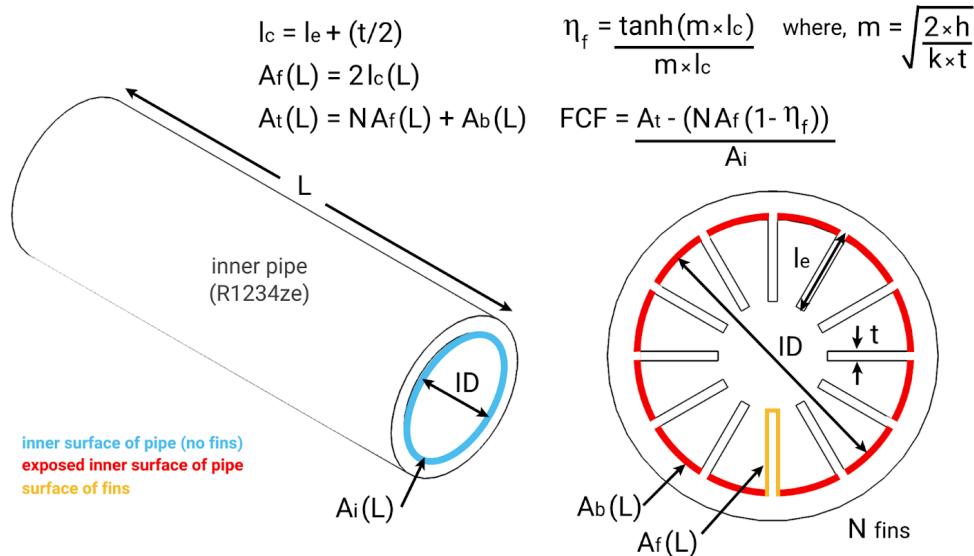


**Figure 79:** Diagrams, variables, and equations for internal axial fins analysis.

On the left side of **Figure 79** is a section of the pipe without fins, showing the diameter ( $ID$ ) and heat transfer area ( $A_i$ ), dependent on the unknown length of the pipe ( $L$ ), thus shown as  $A_i(L)$ . On the right side of **Figure 79** is the front view of the pipe with fins and the same diameter ( $ID$ ), but the graphic enlarged to aid in visualization. The front view shows the heat transfer area corresponding to the exposed section of the base, dependent on the length of the pipe  $A_b(L)$ , the heat transfer area corresponding to a single fin, dependent on the length of the pipe  $A_f(L)$ , number of fins ( $N$ ), fin thickness ( $t$ ), and fin extension length ( $l_e$ ). Above the diagrams, some essential equations and relations are summarized, where for the equation for FCF, the ( $L$ ) dependencies cancel.

The analytical process detailed in this section was implemented in the full-system MATLAB code (see **Appendix G**). The system-level integrated analysis enabled by the MATLAB program allowed for efficient design iterations to be made. The numerical results for the optimal ORC evaporator design are presented and discussed in Section 6.3.

## 6.2.2 ORC Heat Exchanger - Condenser

The overall process for designing the condenser in the ORC was the same as that described in Section 6.2.1 for the evaporator. In this section, the setup and calculations that were unique to the condenser are explained in detail whereas repeated processes and equations from the evaporator section are briefly summarized.

### *Basic Configuration*

The ORC condenser was also analyzed using a counterflow configuration, wherein the hot fluid was vapor R1234ze that had just exited the ORC turbine. The cold fluid was utility cooling water (not to be confused with the water used to cool the CPUs in the SHEC). A T-x diagram of the fluids is shown in **Figure 80**. Similar to the evaporator, it was assumed that the ORC condenser consisted of two ‘stages’ that were combined in a single heat exchanger (as opposed to a unique heat exchanger for each stage). The first stage of the condenser consisted of cooling the R1234ze vapor to the saturation temperature. The second stage of the condenser consisted of condensing the saturated vapor to a saturated liquid at a constant temperature.

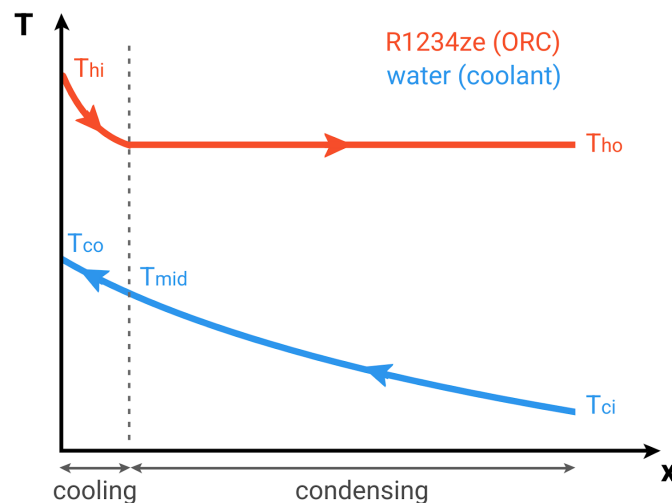


**Figure 80:** T-x diagram of the counterflow arrangement of the hot and cold fluids in the ORC condenser.

### *Temperatures, Heat Transfer Rates, & Flow Rates*

For the inlet temperature of the coolant water ( $T_{ci}$ ), a typical value of 45°F (7.22°C) was selected [80], and it was reasonably assumed that a change in coolant temperature of approximately 20°C over the condenser could be expected. Thus, the outlet temperature of the coolant water ( $T_{co}$ ) was set at 27.22°C.

The temperature of the R1234ze vapor entering the condenser ( $T_{hi}$ ) was determined based on the thermodynamics of an ideal Rankine cycle: The entropy of the fluid at the inlet of the condenser (state 2) equals the entropy at the inlet of the turbine (state 1). At the inlet of the turbine, the R1234ze is a

saturated vapor at the high temperature ( $T_1$ ) with specific entropy ( $s_1$ ). At the outlet of the turbine, the R1234ze is (ideally) a saturated vapor with the same entropy ( $s_2 = s_1$ ) at a lower temperature ( $T_2$ ). However, considering that the turbine is not ideal, with a typical isentropic efficiency of 80% [50], the actual specific enthalpy of the vapor exiting the turbine ( $h_2$ ) was calculated using equation 3.4.1.2 from the preliminary thermodynamics calculations (reproduced below).

$$h_2 = h_1 - \eta_t(h_1 - h_{2s}) \quad (\text{equation 3.4.1.2})$$

Since the outlet temperature ( $T_1$ ) of the saturated vapor ( $x_1 = 1$ ) from the ORC evaporator was known from the evaporator heat exchanger analysis in Section 6.2.1, and the state 2 ideal conditions were known based on the ideal rankine cycle assumptions ( $s_1 = s_2, T_2$ ), there was sufficient information to look up the fluid properties for equation 3.4.1.2. Once  $h_2$  was calculated, the temperature of the vapor at the outlet of the turbine (and inlet to the condenser,  $T_{hi}$ ) could be determined, based on the assumption that the pressure at the outlet of the turbine remained set at the saturation pressure of the (lower) vapor saturation temperature.

**Figure 81** below shows a Pressure-Enthalpy (P-h) graph of R1234ze [81], which is classified as a dry/isentropic working fluid [82]. Pressure (bar) is indicated by the y-axis, enthalpy (kJ/kg) is indicated by the x-axis, constant temperature ( $^{\circ}\text{C}$ ) is indicated by the red curves, constant entropy (kJ/kg-K) is indicated by the blue curves, and constant density is indicated by the green curves ( $\text{g}/\text{cm}^3$ ). The bolded black curve represents the liquid-vapor dome, to the left of which is the subcooled liquid region and to the right is the superheated vapor region.

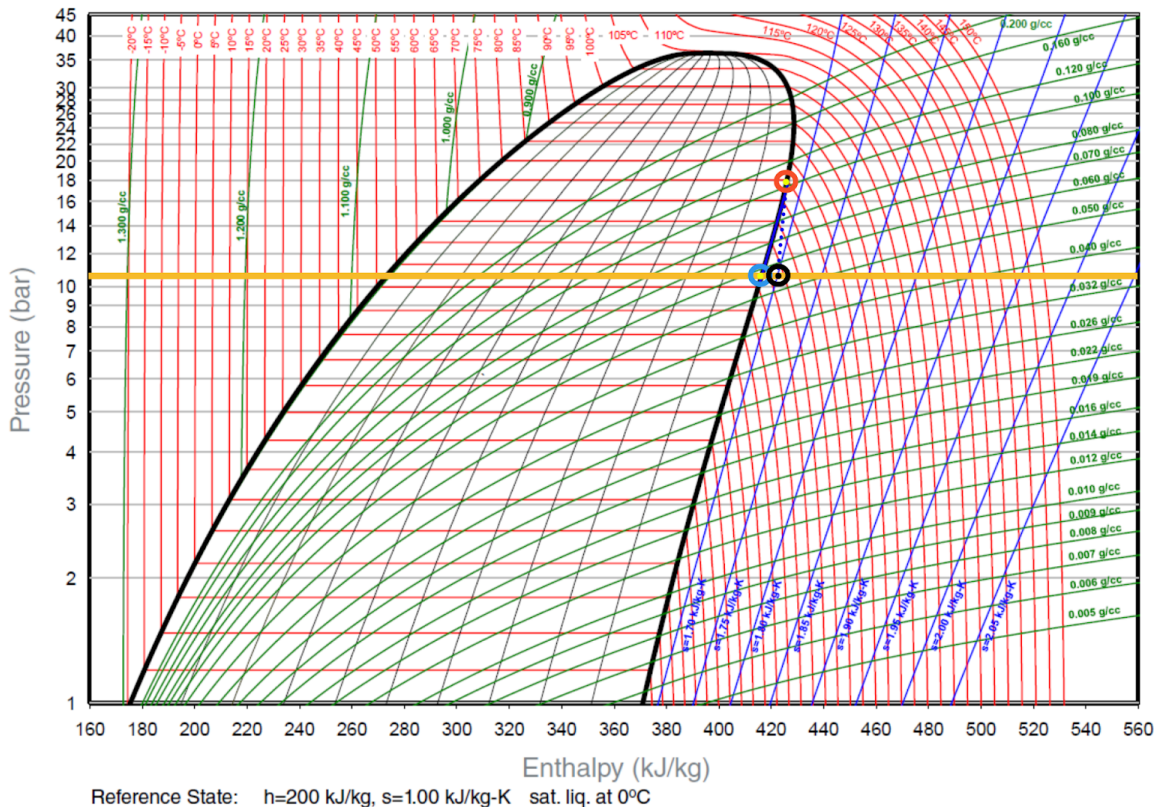


**Figure 81:** P-h diagram of R1234ze.

The fluid state of the R1234ze at the inlet of the turbine is marked by the red circle/yellow dot in **Figure 81**. At the turbine inlet, the R1234ze is a saturated vapor, near 75°C. In an ideal Rankine cycle, entropy is constant across the turbine. Due to the curvature of the liquid-vapor dome for R1234ze, a constant entropy process for a saturated vapor follows the curvature of the dome (which is parallel to the constant entropy curves), maintaining the quality ( $x=1$ ) of the vapor. However, in non-ideal systems, which was considered in the final design of the ORC heat exchangers, the turbine is not isentropic and the enthalpy of the fluid at the turbine outlet is greater. The closer view of the P-h diagram in **Figure 82** shows the difference between the ideal and non-ideal turbine process. In the ideal case, (red mark to blue mark on the saturated vapor curve of two-phase dome), the isentropic process is characterized by the blue constant entropy line along the dome, parallel to the entropy lines to the right. The fluid at the outlet of the turbine is a saturated vapor, between 50°C and 55°C at the corresponding saturation pressure near 10 bar (indicated by the blue circle/yellow dot). In the non-ideal case (red mark to black mark), where entropy is not conserved, the blue dotted entropy line deviates from the solid blue constant entropy line. The fluid at the turbine outlet has a slightly higher temperature (closer to 55°C) and greater enthalpy compared to the ideal case, at the same outlet pressure. In addition, the R1234ze actually exits the turbine as a superheated vapor (which is advantageous for the longevity of the turbine, since there is no concern that liquid droplets might form through the turbine process that damage the blades). The fluid state of the R1234ze at the turbine outlet is marked by the black circle/dot in the superheated region along the yellow constant pressure line.

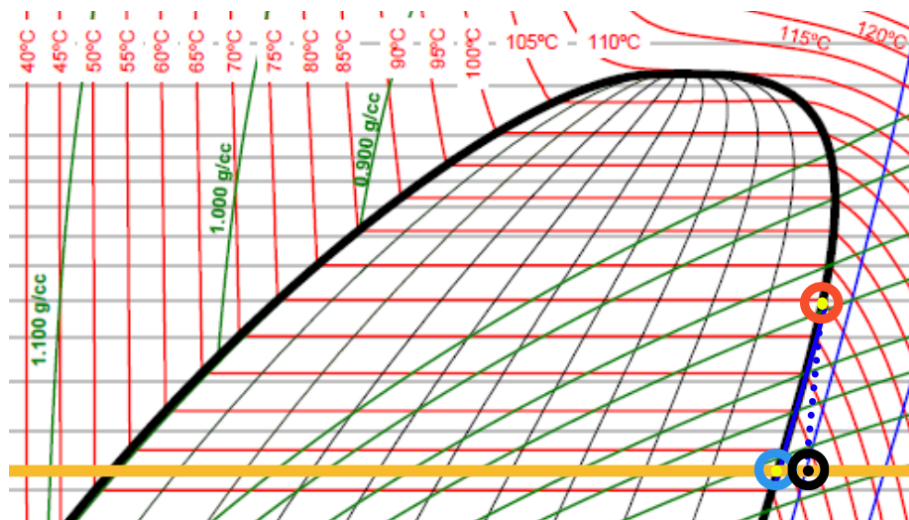


**Figure 82:** Ideal vs. non-ideal ORC turbine process.

In terms of the ORC condenser analysis, the R1234ze that enters the condenser ( $T_{hi}$ ) is superheated slightly above the saturation temperature. The first stage of the condenser cools the vapor to the saturation temperature and the second stage condenses the saturated vapor to a saturated liquid at a constant temperature and pressure. The temperature of the water at the intersection between the cooling and condensation stages ( $T_{mid}$ ) was dependent upon the mass flow rates of each of the fluids and the heat transfer rate during the condensation stage of the heat exchanger. The mass flow rate of the R1234ze was known from the prior analysis of the ORC evaporator, and was used to determine the heat

transfer rate through each of the cooling and condensing stages, as well as the overall HEX. Then, the flow rate of the coolant water was calculated, which was the last variable needed to solve for  $T_{mid}$ . The equations for the heat transfer rates, coolant water mass flow rate, and  $T_{mid}$  are represented by equations 6.2.2.1 through 6.2.2.5.

$$\dot{Q}_{cool} = \dot{m}_r \times c_p (T_{hi} - T_{ho}) \quad (\text{equation 6.2.2.1})$$

where  $\dot{Q}_{cool}$  is the total heat transfer rate through the cooling stage of the condenser (kW),  $\dot{m}_r$  is the mass flow rate of the R1234ze (kg/s),  $T_{hi}$  is the temperature of the R1234ze at the inlet of the condenser (°C),  $T_{ho}$  is the temperature of the R1234ze at the outlet of the condenser (°C), and  $c_p$  is the specific heat capacity of R1234ze at the average temperature between  $T_{hi}$  and  $T_{ho}$  (kJ/kg-K).

$$\dot{Q}_{cond} = \dot{m}_r \times h_{fg} \quad (\text{equation 6.2.2.2})$$

where  $\dot{Q}_{cond}$  is the heat transfer rate through the condensing stage of the condenser (kW) and  $h_{fg}$  is the latent heat of vaporization for R1234ze at the saturation temperature (kJ/kg).

$$\dot{Q}_{total} = \dot{Q}_{cool} + \dot{Q}_{cond} \quad (\text{equation 6.2.2.3})$$

where  $\dot{Q}_{total}$  is the total heat transfer rate through the condenser (kW), equivalent to the sum of the heat transfer rate through the cooling ( $\dot{Q}_{cool}$ ) and condensing ( $\dot{Q}_{cond}$ ) stages.

The mass flow rate of the coolant water ( $\dot{m}_c$ ), was thus found using

$$\dot{m}_c = \frac{\dot{Q}_{total}}{c_p(T_{co} - T_{ci})} \quad (\text{equation 6.2.2.4})$$

where  $T_{co}$  is the temperature of the coolant water at the outlet of the condenser (°C),  $T_{ci}$  is the temperature of the coolant water at the inlet of the condenser (°C), and  $c_p$  is the specific heat capacity of coolant water at the average temperature between  $T_{ci}$  and  $T_{co}$  (kJ/kg-K). The mass flow rate of the coolant water was then used to solve for  $T_{mid}$ , i.e. the temperature of the coolant water at the outlet of the condensing stage.

$$T_{mid} = T_{ci} + \frac{\dot{Q}_{cond}}{\dot{m}_c \times c_p} \quad (\text{equation 6.2.1.6})$$

where  $c_p$  is the specific heat capacity of water at the average temperature between  $T_{ci}$  and  $T_{mid}$  (kJ/kg-K).

### Piping

The same analytical method that was applied for the ORC evaporator was also applied to the ORC condenser. The analysis was based on a counterflow configuration of two concentric pipes, wherein the R1234ze was directed through the inner pipe and the coolant water was directed through the larger annulus between the inner and outer pipe due to its higher mass flow rate. The pipe configuration for the condenser is summarized in **Figure 83**.

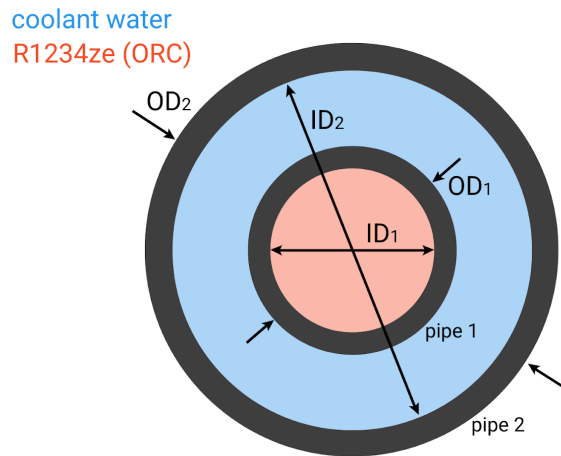


**Figure 83:** Condenser counterflow concentric pipe configuration.

Similar to the ORC evaporator analysis, nominal 3/8 inch and 1 inch size pipes made of Type K copper were utilized for the condenser tubes since they could withstand the high pressures at the elevated temperatures of R1234ze. All the equations that were presented in Section 6.2.1 for the cross-sectional area of the inner pipe as well as the hydraulic diameter and cross-sectional area of the annulus were the same for the condenser (see equations 6.2.1.8 - 6.2.1.11).

#### *HEX Design*

As stated above, the condenser heat exchanger analysis was initially examined from a concentric pipe, counterflow perspective. In the case of the ORC evaporator, a shell and tube HEX configuration was also investigated wherein a correction factor had to be determined for the heating stage. However, in the case of the condenser, the temperature change of the R1234ze from the slightly superheated vapor to the vapor saturation temperature in the cooling stage was so small that calculations of  $P$  and  $R$  (see equations 6.2.1.12 and 6.2.1.13) resulted in a shell and tube HEX correction factor that was approximately 1. Most of the heat transfer occurs across the condensing stage of the heat exchanger, where a correction factor for heat exchanger type is not required (i.e. correction factor is 1). Therefore, no additional calculations of  $UA$  to account for a shell and tube HEX correction factor were needed in the later stages of the condenser analysis.

#### *Fins (Part 1)*

The same fin configuration (internal axial fins) and geometry that was utilized in the ORC evaporator design was applied to the inner pipes containing R1234ze in the ORC condenser.

#### *UA Using LMTD Method*

Since all of the temperatures of the coolant water and R1234ze were known at the inlets and outlets of both the cooling and condensation stages of the heat exchanger, the LMTD method was used for the design analysis. The analysis consisted of two sets of calculations since the conditions and fluid properties in each of the stages were unique, and were thus treated as separate heat exchangers to calculate the required pipe length. The resulting pipe lengths for each stage were summed to determine

the total required pipe length for the ORC condenser, since it was assumed that both stages would occur in the same HEX.

All the equations for calculating  $UA$  can be found in the ORC evaporator section (equations 6.2.1.15 - 6.2.1.17), where the correction factor for the shell and tube HEX design ( $F$ ) was approximately 1 for both the cooling and condensing stages. The fluid temperature differences which corresponded to  $\Delta T_1$  and  $\Delta T_2$  in the cooling stage and condensation stage are summarized in **Table 17**. The expressions correspond to the vertically aligned temperatures labeled on the T-x diagram in **Figure 80**.

**Table 17:** Expressions for  $\Delta T_1$  and  $\Delta T_2$  in the Cooling and Condensation Stages.

	$\Delta T_1$	$\Delta T_2$
Cooling Stage	$T_{hi} - T_{co}$	$T_{ho} - T_{mid}$
Condensation Stage	$T_{ho} - T_{ci}$	$T_{ho} - T_{mid}$

#### *Determining Heat Transfer Coefficient*

The heat transfer coefficient (HTC) of each fluid through each stage of the ORC condenser was calculated using the Nusselt number and the same analytical process presented for the ORC evaporator in Section 6.2.1 (equations 6.2.1.18 through 6.2.1.22). Note, however, that the hot and cold fluid arrangement reversed for the condenser, wherein the hot R1234ze was directed through the inner pipe and the outer annulus contained the cold coolant water.

For the HTC of the R1234ze in the condensing stage, the fluid transitions from a saturated vapor to a saturated liquid, wherein the assumption for constant fluid properties at an average temperature is not valid. Similar to the strategy used in the evaporator analysis, another investigation into existing experimental data was conducted to identify a range of possible HTCs of condensing R1234ze to utilize for characterizing the HEX design of the ORC condenser. The International Journal of Heat and Mass Transfer was consulted, wherein the results from a study conducted by Li et al. were used to approximate the maximum, minimum, and average HTC of condensing R1234ze. In the experiments, multiport microchannels were used to investigate the HTCs of R447A, R1234ze, R134a, and R32 versus vapor quality ( $x$ ) at a constant temperature of 35°C, and varying mass flow rates at 100 kg/s, 200 kg/s, and 300 kg/s [83]. The experimental results for R1234ze are presented in **Figure 84**.

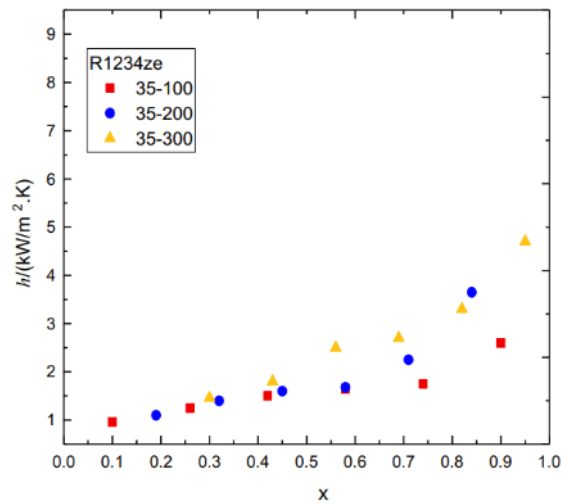


**Figure 84:** Heat transfer coefficients of R1234ze (condensing) versus quality of R1234ze [83].

Based on the experimental results from Li et al., maximum, minimum, and average HTC values for R1234z were specified at 4800 W/m<sup>2</sup>-K, 900 W/m<sup>2</sup>-K, and 2850 W/m<sup>2</sup>-K, respectively. However, it should be noted again that the HTCs for R1234ze through the condenser could only be roughly approximated based on the existing experimental data in literature. Future work on this project could pursue a more robust characterization of the flow conditions and fluid properties of the R1234ze through the pipes in the condenser stage for a more precise specification of the heat exchanger design.

### *Calculating Length of HEX*

Once the HTCs of the fluids were identified, the length of piping required for each heat exchanger stage was calculated. The same analytical process presented for the ORC evaporator in Section 6.2.1 was used for the condenser, with reference to equations 6.2.1.23 through 6.2.1.25.

For the cooling stage, one result for length was recorded: length of pipe for the counterflow concentric tubes (since the correction factor for shell and tube HEX was 1). For the condensation stage, three different length calculations were completed, each using one of the three values identified for the HTC of R1234ze during condensation (maximum, minimum, and average).

### *Fins (Part 2)*

The analytical process and set of equations used in the ORC evaporator section to derive the fin correction factor (FCF) for the addition of internal axial fins (within the inner pipe containing R1234ze) was subsequently applied for the condenser. Once FCF was found using equations 6.2.1.26 through 6.2.1.37, four calculations of required HEX length (with finned pipes) using equation 6.2.1.38 were recorded for the ORC condenser, listed as follows:

1. Cooling stage, counterflow concentric pipe configuration
2. Condensation stage, maximum HTC for R1234ze
3. Condensation stage, minimum HTC for R1234ze
4. Condensation stage, average HTC for R1234ze

### 6.2.3 ORC Thermodynamic Analysis

The preliminary thermodynamic analysis presented in Section 3.4.1 considered an ideal Rankine cycle, adjusted for turbine and pump isentropic efficiencies, with assumed values for temperatures based on the literature review conducted in Section 2.0. However, over the course of the project, the investigation and development of other systems, specifically the SHEC and heat exchangers, enabled a more robust thermodynamic analysis of the ORC. Initially, it was assumed that the 10 kW heat load from the servers would produce the desired temperature of the R1234ze vapor at the outlet of the evaporator. Similarly, it was assumed that the coolant loop would effectively extract heat from the R1234ze fluid over the condenser to change the phase of the R1234ze saturated vapor to a saturated liquid. However, in the final design, extensive heat exchanger design calculations were completed in order to assess whether the desired thermal operating conditions were actually feasible (i.e. reasonable lengths of HEX piping) and specify an optimal HEX design that would produce the desired results.

Most importantly, however, was the characterization of the thermal operating conditions of the SHEC, which determined the inlet/outlet temperatures to the ORC evaporator. Based on the simulations of a microchannel slice of a MCHS developed and tested in COMSOL, the optimal inlet and outlet temperatures of the water to the CPU via the single-phase liquid cooling cycle (i.e. SHEC) were identified. Once the key temperature parameters of the SHEC were known, the design analyses of the ORC evaporator and condenser could be completed. As a result of the HEX calculations, the previously assumed temperatures and operating conditions in the ORC were constrained and a more detailed specification of the fluid states of the R1234ze could be conducted. The original ORC schematic from Section 3.4.1 is reproduced in **Figure 85**. The associated state-strategy table, presented in variable form, is shown in **Table 18**. The numeric values for the initial assumptions for the operating conditions, corresponding fluid properties, and calculated results can be referenced in Section 3.4.1.

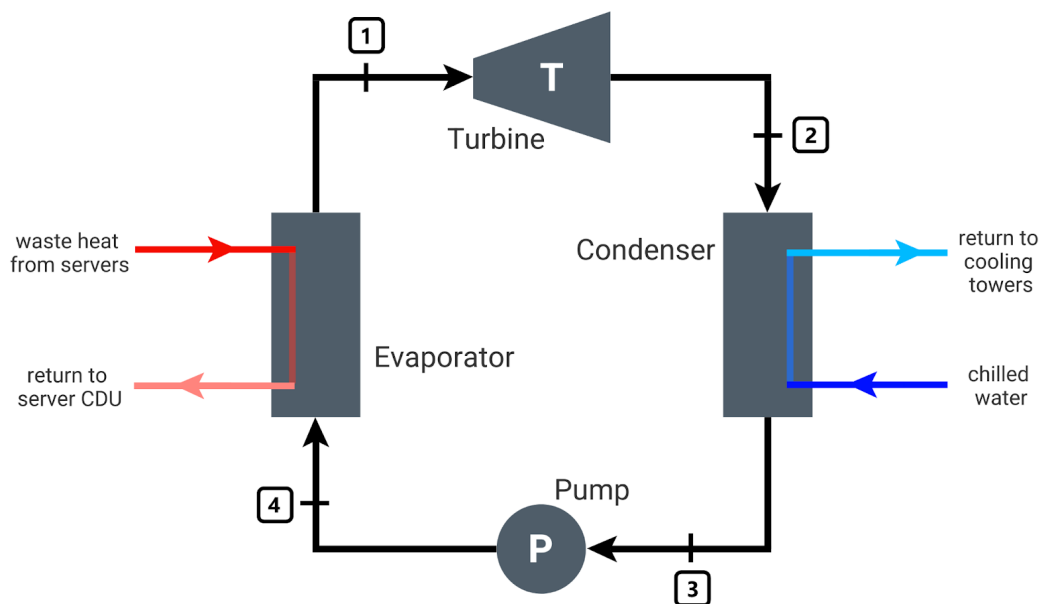


**Figure 85:** ORC schematic from preliminary thermodynamics analysis.

**Table 18:** Detailed state-strategy table corresponding to the preliminary ORC schematic.

State	Location	P (kPa)	T (°C)	Specific entropy (s, kJ/kg-K)	Specific enthalpy (h, kJ/kg)	Specific volume (v, m <sup>3</sup> /kg)	Phase / quality
1	Evaporator Outlet, Turbine Inlet	$P_1$	$T_1$	$s_1$	$h_1$	$v_1$	Saturated vapor (x=1)
2	Turbine Outlet, Condenser Inlet	$P_2$	$T_2$	$s_2 = s_1$	$h_{2s}$ $h_2$	$v_2$	Saturated vapor (x=1)
3	Condenser Outlet, Pump Inlet	$P_3 = P_2$	$T_3 = T_2$	$s_3$	$h_3$	$v_3$	Saturated liquid (x=0)
4	Pump Outlet, Evaporator Inlet	$P_4 = P_1$	$T_4$	$s_4 = s_3$	$h_{4s}$ $h_4$	$v_4$	Compressed / subcooled liquid

Note: input, calculation, thermodynamic property

After accounting for the thermal operating conditions of the SHEC (based on the COMSOL MCHS simulations), dual-stages of the evaporator and condenser (based on the heat exchanger design calculations), and additional fluid states, a more comprehensive schematic of the ORC is presented in **Figure 86**. The associated state-strategy table, presented in variable form, is shown in **Table 19**.

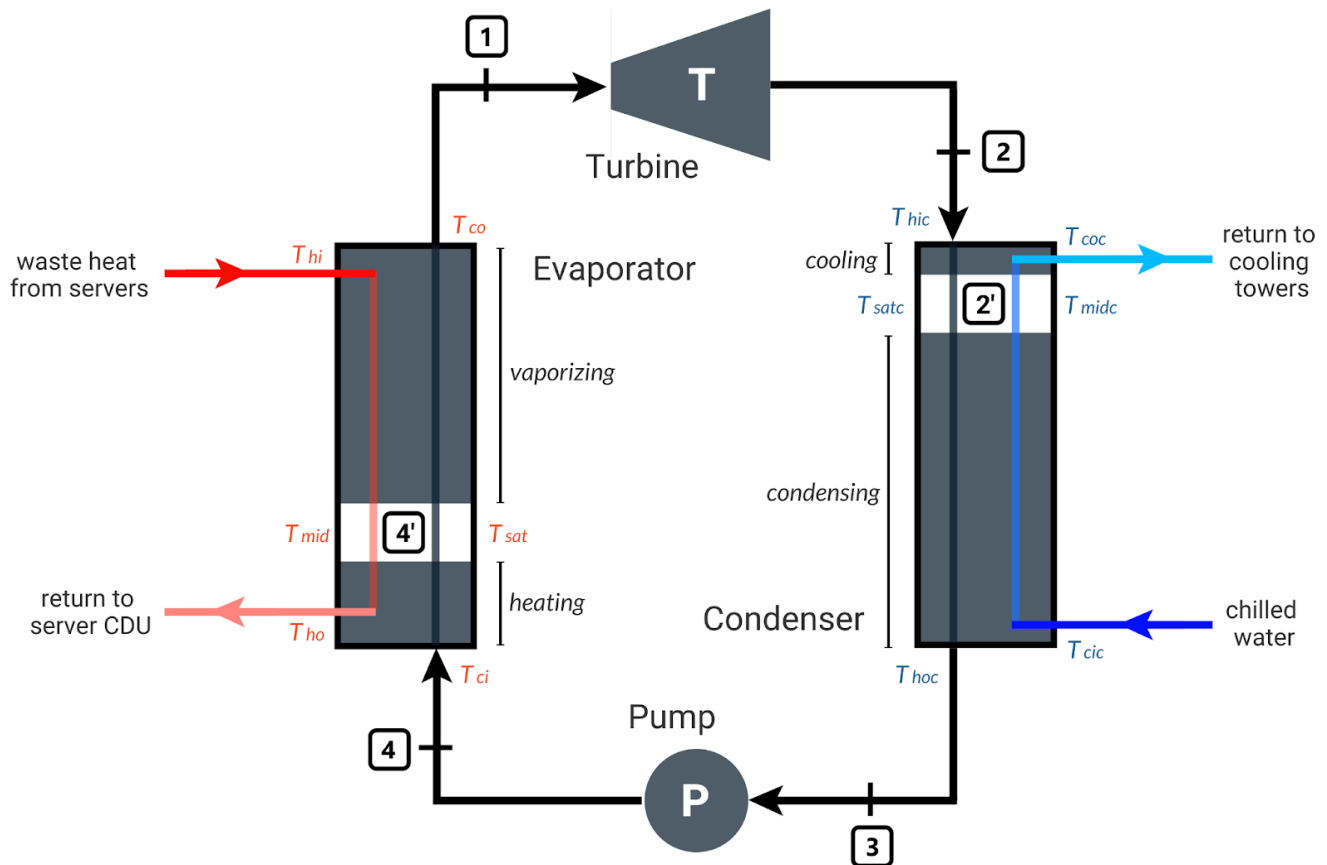


**Figure 86:** Comprehensive ORC schematic for final design.

**Table 19:** Detailed state-strategy table corresponding to the comprehensive ORC schematic.

State	Location	P (kPa)	T (°C)	Specific entropy (s, kJ/kg-K)	Specific enthalpy (h, kJ/kg)	Specific volume (v, m <sup>3</sup> /kg)	Phase / quality
1	<i>Evaporator Outlet, Turbine Inlet</i>	P <sub>1</sub>	T <sub>1</sub>	s <sub>1</sub>	h <sub>1</sub>	v <sub>1</sub>	Saturated vapor (x=1)
2	<i>Turbine Outlet, Condenser Inlet</i>	P <sub>2</sub>	T <sub>2SH</sub>	s <sub>2SH</sub>	h <sub>2</sub>	v <sub>2SH</sub>	Superheated vapor
2'	<i>Cooling Outlet, Condensing Inlet</i>	P <sub>2'</sub> = P <sub>2</sub>	T <sub>2</sub>	s <sub>2</sub> = s <sub>1</sub>	h <sub>2s</sub>	v <sub>2</sub>	Saturated vapor (x=1)
3	<i>Condenser Outlet, Pump Inlet</i>	P <sub>3</sub> = P <sub>2</sub>	T <sub>3</sub> = T <sub>2</sub>	s <sub>3</sub>	h <sub>3</sub>	v <sub>3</sub>	Saturated liquid (x=0)
4	<i>Pump Outlet, Evaporator Inlet</i>	P <sub>4</sub> = P <sub>1</sub>	T <sub>4SC</sub>	s <sub>4SC</sub>	h <sub>4</sub>	v <sub>4SC</sub>	Subcooled liquid
4'	<i>Heating Outlet, Vaporizing Inlet</i>	P <sub>4'</sub> = P <sub>4</sub>	T <sub>sat</sub>	s <sub>4sat</sub>	h <sub>4sat</sub>	v <sub>4sat</sub>	Saturated liquid (x=0)

Note: input / old calculation (from **Table 18**), **new thermodynamic property**

State 1 corresponds to the high temperature and pressure saturated vapor at the evaporator outlet and turbine inlet. It is the same referentially as State 1 in the preliminary state strategy table (**Table 18**). State 2 corresponds to the low temperature and pressure vapor at the turbine outlet and evaporator inlet. As a result of the ORC condenser analysis, it was found that the fluid at this state is actually a slightly superheated vapor, so it is not the same referentially as State 2 in **Table 18**, and the corresponding superheat (SH) properties were identified and added to the table. Rather, State 2 from **Table 18** corresponds to State 2' inside the condenser, at the cooling stage outlet and condensing stage inlet—when the low temperature vapor has been cooled to the saturation temperature. State 3 corresponds to the low temperature and pressure saturated liquid at the condenser outlet and pump inlet and is the same referentially as State 3 in **Table 18**. State 4 corresponds to the low temperature, high pressure subcooled liquid at the outlet of the pump and evaporator inlet. The pressure P<sub>4</sub> and enthalpy h<sub>4</sub> refer to the same values in State 4 as listed in **Table 18**, but the new subcooled (SC) liquid properties were identified and added to State 4 in **Table 19**. Finally, State 4' corresponds to the high temperature and pressure saturated liquid inside the evaporator, at the heating stage outlet and evaporating stage inlet. New saturated (sat) liquid properties for the fluid at State 4' were identified and added to the table as they were not the same referentially as State 4 in **Table 18**.

All the calculations presented in Section 3.4.1 remained the same, and the variable names in the equations also remained consistent and corresponded to those presented in **Table 19**. However, due the additional analyses completed in the final design for the ORC evaporator (Section 6.2.1) and ORC condenser (Section 6.2.2), equations 3.4.1.6 and 3.4.1.9 from the preliminary calculations for mass flow rate of R1234ze and heat transfer rate in the condenser were no longer relevant.

For the system-level analysis, the thermodynamics portion was updated in the MATLAB code to reflect the final design as detailed above and to enable efficient design iterations. The numerical results for the finalized thermodynamic analysis of the complete system are presented in Section 6.3.2.

#### 6.2.4 ORC Fluid Mechanics Analysis

The process utilized to analyze the fluid mechanics through the connecting pipes of the ORC reflected the calculation method presented in the preliminary fluid mechanics analysis in Section 3.4.2. However, the analysis was integrated into the full-system MATLAB code so that the updated fluid states of the R1234ze and corresponding fluid mechanics properties could be automatically implemented in subsequent iterations of the analysis. The final numerical results, corresponding to the fluid states and properties presented in **Figure 86** and **Table 19**, are presented in Section 6.3. However, it is important to acknowledge that the fluid mechanics analysis did not address the pressure drops corresponding to the pipes in the ORC evaporator and condenser. The liquid-vapor phase changes of the R1234ze in the evaporation and condensation stages of the heat exchangers are not associated with constant fluid properties that could be readily used to determine pressure drop. Thus, future work on this project could more precisely characterize the fluid properties (e.g. density and viscosity) of R1234ze during its phase changes to estimate pressure drop and pump power for ORC heat exchangers.

#### 6.2.5 SHEC Piping & Fluids Analysis

The server heat extraction cycle (SHEC) was responsible for circulating and distributing the liquid cooling water to the CPU heat sinks and ORC evaporator. In this project, a 10 kW data center waste heat load scenario was considered in the calculations. However, it is important to note that the 10 kW represents the heat load from a small server room (i.e. AK120b at WPI), whereas most existing centers are much larger. Thus, a generalized physical configuration for the ORC and SHEC was developed, wherein the physical lengths of the piping in different sections of the SHEC were approximated. If the SHEC were to be implemented at an existing data center, the SHEC layout and piping dimensions would be adjusted to reflect the specific spatial constraints and rack layout of the data center.

For the given heat load, the number of CPUs required to provide the heat output was determined based on the calculated flow rate of SHEC liquid cooling water through the ORC evaporator. The total flow rate was then divided by the flow rate through each MCHS (from the MCHS simulations) to determine the number of CPUs the system was composed of. For the 10 kW heat load, approximately 64 CPUs were required to provide the 10 kW heat input to the ORC evaporator. However, the number of CPUs was based on the specific thermal characteristics of the single example CPU chosen for the COMSOL simulation analysis, the Intel® Xeon® Gold 6328H Processor. The selected processor had a Thermal Design Power (TDP) of 165 W, corresponding to a  $3.768 \text{ W/cm}^2$  heat flux over its  $77.5 \text{ mm} \times 56.5 \text{ mm}$  surface. If a higher-power CPU was chosen with a greater TDP (such as the Intel® Xeon® Platinum 8380HL Processor with a TDP of 250 W [69]), then fewer CPUs may be required to produce the desired heat load. Additionally, it is also important to note that only the CPU was considered in the design and analysis of the ORC data center waste heat recovery system. Other heat-generating components, such as the DIMM and disk drive may be utilized as a source of waste heat to potentially

reduce the number of CPUs required. The integration of other heat-generating components in the liquid cooling system for the SHEC may be investigated in future efforts.

For the 64 CPUs required for the 10 kW system, it was assumed that they were equally divided among four server racks (industry standard 74 inches tall, 36 inches in depth, and 24 inches in length [84]). It was assumed that each rack contained eight blade servers, with two CPUs per blade (see **Figure 87**). Thus, each of the four racks housed sixteen CPUs in eight blade servers, equally spaced over the height of the server rack. However, racks in higher density data centers would be likely to contain more CPUs per blade server or more blades per rack. Thus, the SHEC configuration and analysis would be adjusted for the heat loads, CPUs, server blades, and server racks associated with a specific data center.

The overall physical layout of the data center server racks, ORC, and SHEC piping is depicted in **Figure 88**. (Note that the schematic of the data center, ORC, and SHEC shown prior in **Figure 66** is a visual representation of the interfacing systems and components, not the proposed physical layout.) Considering the limited space in the server rooms of data centers, which are densely packed with rows of server racks, the optimal physical location of the ORC was beneath the floor. As shown in **Figure 88**, the ORC (i.e. ORC heat exchanger) is located under the four server racks, although the diagram is not to scale. From the ORC heat exchanger (1), the cooled SHEC water is pumped up from beneath the floor of the server room to the top of the server racks (2). The main pipe is split into four pipes, each directed to one of the four server racks. At the server rack, the water is distributed to each of the sixteen MCHS on each CPU, in each of the eight blade servers. The water containing the CPU waste heat then recollects at the base of the server rack (3). The heated water from each server rack is redirected to a main pipe, which transports the water back down to the ORC (4).

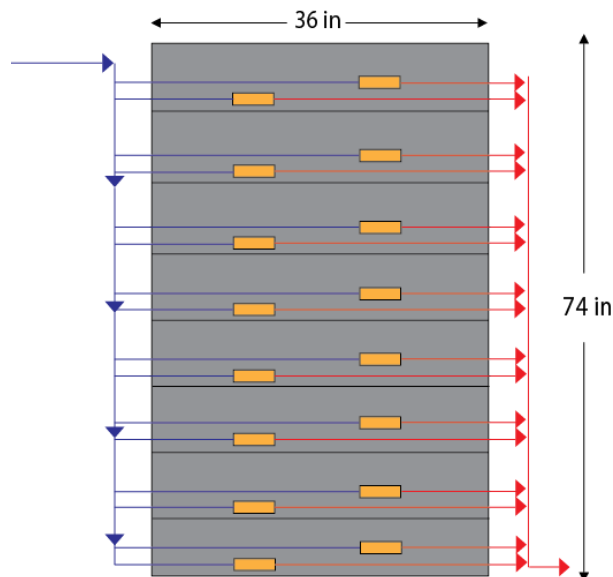


**Figure 87:** Fluid flow schematic through a server rack (with 8 blade servers, two heat sinks per blade).

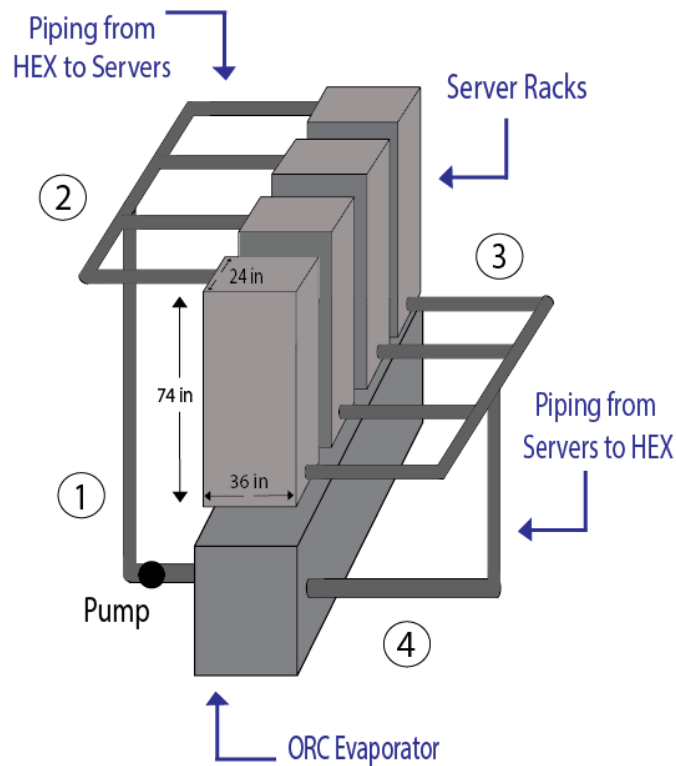


**Figure 88:** 3D diagram of SHEC piping system, with a pump placement along pipe section 1.

Additionally, it is important to note that the junction between the main pipe (1) and the four pipes that go to the servers (2) is a flow splitter (see example in **Figure 89**). To facilitate conceptual understanding, the graphic in **Figure 88** spaces out the four pipes along what appears as a horizontally oriented pipe. However, the actual system would include a flow splitter at the top of the main pipe (at the top of the server racks), which would divide the fluid between the pipes that lead to each of the server racks. Similarly, another flow splitter would be utilized to recombine the water at the junction between the pipes at the base of the servers (3) and the main pipe that directs the heated water back down to the ORC heat exchanger (4).



**Figure 89:** Example of a four-way flow splitter valve [85].

The dimensions chosen for the lengths of each pipe section in the SHEC piping manifold were estimated based on the general assumptions that were made for the overall layout of the system components. Additionally, the pipe length estimates were overestimated to ensure a conservative estimate of the required pump power. As shown in the piping manifold in **Figure 87**, many sections of pipe were vertically oriented. Therefore, the fluid mechanics analysis of each pipe section needed to

account for gravitational effects. (However, since the pipes are arranged in a vertical loop, the overall change in height of the fluid in the SHEC system is zero, and thus does not require additional pumping power.) It was assumed that the pipe from the ORC heat exchanger (1) to the top of the server racks (2) traveled a vertical height of ~5 meters, which included the 1.88 m (74 in) height of the server racks. The 5 m assumption was made based on the consideration that the ORC was below the floor of the server room, potentially on a separate floor (which is associated with an elevation change of approximately 10 ft or 3.05 m). Over the servers, the height decreases by 1.88 m, and from the servers (3) to the ORC heat exchanger (4), the height decreases by another 3.12 m (for a total of 5 m). With an increasing demand for data centers [44], the proposed generalized SHEC design assumes that data center proprietors will dedicate whole buildings and floors for their servers.

Each section of pipe in the SHEC piping manifold was analyzed using Bernoulli's equation, which is an expression for the conservation of energy for fluid flows. Bernoulli's equation (represented by equation 6.2.5.1) was used to solve for the pressure drop over each section of pipe to subsequently calculate the required pump power for the SHEC. The flow of water was assumed to be steady and incompressible.

$$\frac{P_i}{\rho g} + \frac{V_i^2}{2g} + z_i + h_{pump} = \frac{P_j}{\rho g} + \frac{V_j^2}{2g} + z_j + f \frac{L_{total}}{D} \frac{V_j^2}{2} + \sum K_L \rho \frac{v_j^2}{2} \quad (\text{equation 6.2.5.1})$$

where  $P$  is the pressure at given state,  $V$  is the average velocity of the fluid,  $z$  is the elevation (relative to the ORC heat exchanger),  $h_{pump}$  is the head loss from the pump,  $f$  is the friction factor of the pipe section, and  $K_L$  is the term that represents the loss constants for minor losses present in a pipe section. The subscripts  $i$  and  $j$  correspond to the states of the fluid at the entrance and exit of the pipe section. The friction factor can be calculated using Haaland's equation (equation 6.2.5.2) and the expression for Reynolds number (6.2.5.3). The pump power over each section of pipe is given by equation 6.2.5.4.

$$f = (-1.8 \log[ (\frac{6.9}{Re}) + (\frac{\epsilon/D}{3.7})^{1.11} ])^{-2} \quad (\text{equation 6.2.5.2})$$

$$Re = \frac{\rho_i V_i D_i}{\mu_i} \quad (\text{equation 6.2.5.3})$$

$$Power = \Delta P \times Q = \Delta P \times V_{avg} (\frac{\pi}{4} D^2) \quad (\text{equation 6.2.5.4})$$

where  $\epsilon$  is the roughness of copper piping (1.5  $\mu\text{m}$  [52]),  $\rho$  is the fluid density,  $\mu$  is the dynamic viscosity of R1234ze, and  $Q$  is the volumetric flow rate. The velocity was found using equation 6.2.5.5, given the mass flow rate of the water ( $m_{dot}$ —determined from the heat exchanger analysis), fluid density, and the diameter of the pipe.

$$V = \frac{m_{dot}}{\rho \frac{\pi}{4} D^2} \quad (\text{equation 6.2.5.5})$$

For each section of pipe, equation 6.2.5.1 was balanced with all known inputs and rearranged to solve for the pressure difference (between  $P_i$  and  $P_j$ ). It is important to note that the loss constants were neglected in the final design analysis (since the SHEC piping manifold was an approximation of a general layout, and the minor losses are attributed to very specific features of the piping). To verify whether the minor losses could be neglected, the relative impact of minor losses was evaluated in one of the iterations of the analyses. Various pipe features were assumed, assigned the appropriate loss constant values (according to **Figure 90** and **Figure 91**), and the entire system was evaluated. The

additional consideration of minor losses produced a combined effect of only 1% on the overall pressure drop in the SHEC. Therefore, the detailed specification of minor losses (and pump head) was neglected in the final analysis of the generalized SHEC manifold. However, it is recommended that the minor losses due to various pipe features are identified and considered if the SHEC were to be implemented at an existing data center, where the piping system could be entirely specified.

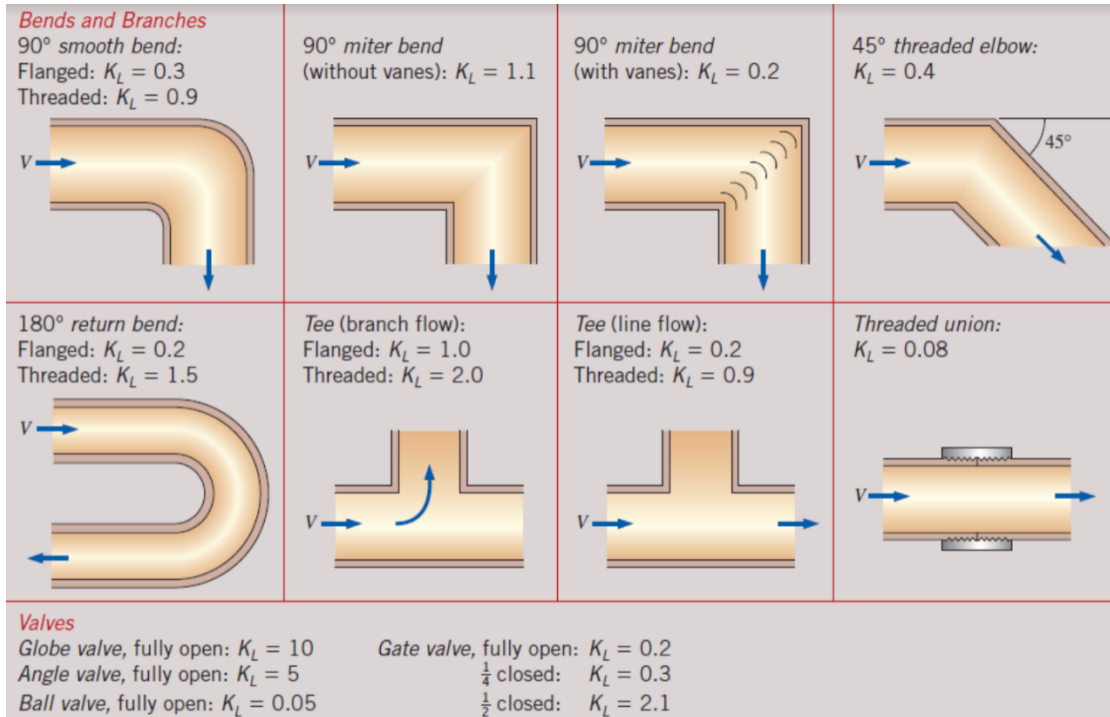


Figure 90: Loss constants for varying bends and branches within pipes [63].

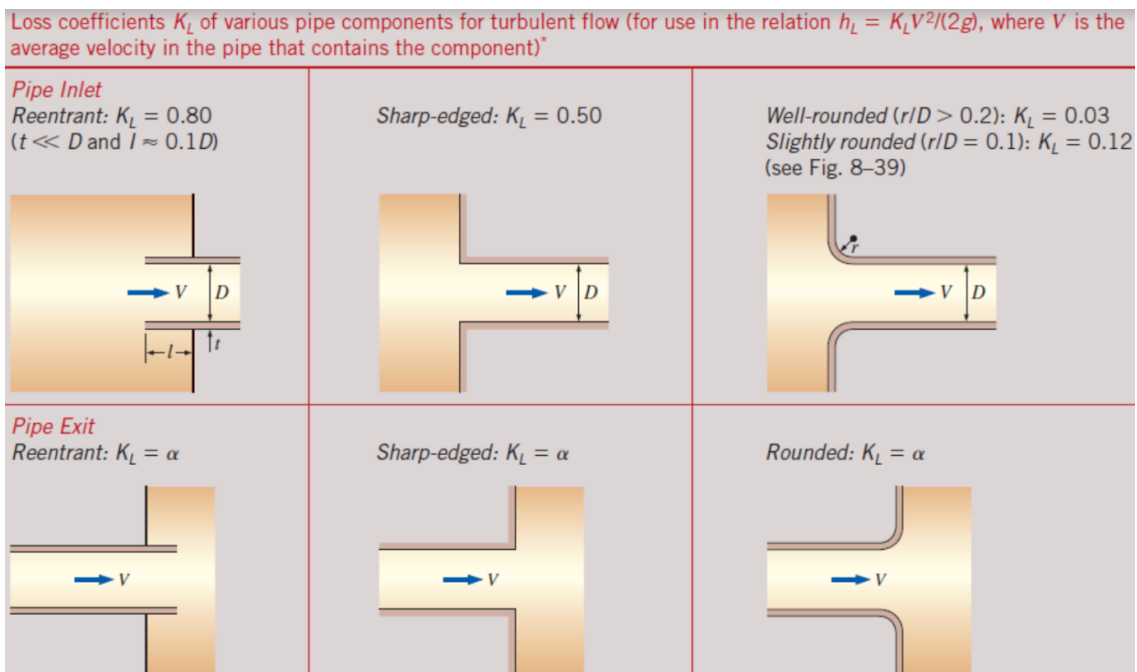


Figure 91: Loss constants for entry and exits within pipes [63].

Since pipe sections 1 & 2 are placed before the server racks, the fluid state of the water corresponds to the lower temperature, chilled water directed to the CPUs and MCHSs. The results from the COMSOL simulations indicated that the temperature of the water entering the MCHS is 74°C at approximately atmospheric pressure. Following the server racks (pipe sections 3 & 4) after the water has absorbed the heat from the IT equipment, the water is at an elevated temperature—approximately 81°C based on the results of the COMSOL simulation. The fluid properties of the water in the SHEC piping is summarized in **Table 20**.

**Table 20:** Fluid properties of the water through the SHEC pipe sections.

Pipe Sections	Temperature, T (°C)	Density of Water, $\rho$ (kg/m <sup>3</sup> )	Dynamic Viscosity, $\mu$ ( $\mu$ Pa*s)
1 & 2	74	975.41	382
3 & 4	81	971.14	350

For determining the total pressure drop of the SHEC piping manifold, it is important to note that the pressure drops were summed over the sections of the pipe that were in series, and single value of pressure drop corresponded to the sections of the pipe that were in parallel. The parallel sections of the pipe included the division of the fluid into four pipes into and out of the server racks, as well as the division of fluid to the sixteen MCHSs in each server rack. In other words the pressure drop across one of the four pipes was not multiplied by four, nor was the pressure drop for the MCHS multiplied by sixteen to obtain the total pressure drop for the system. Therefore, the total pressure drop could be represented by:

$$\Delta P_{total} = \Delta P_1 + \Delta P_2 + \Delta P_{server} + \Delta P_3 + \Delta P_4 \quad (\text{equation 6.2.5.6})$$

where  $\Delta P_1$  corresponds to the pressure drop over the main pipe from the ORC to the top of the servers,  $\Delta P_2$  corresponds to the pressure drop over one of the four pipes *to* the server racks,  $\Delta P_3$  corresponds to the pressure drop over one of the four pipes *from* the server racks, and  $\Delta P_4$  corresponds to the pressure drop over the main pipe from the base of the servers to the ORC.  $\Delta P_{server}$  is equivalent to the pressure drop over one MCHS (based on the results from the COMSOL simulation), and includes the corresponding pressure drop due to the change in height from the top of the server to the bottom. The pump powers that corresponded to the pressure drops in each section of piping (as listed in equation 6.2.5.6) were also summed to determine the total pump power required for the SHEC piping system. However, it is important to note that the fluid mechanics analysis did not extend to include the frictional losses associated with the numerous small tubes that direct the water to each of the sixteen MCHs in the server rack. It is recommended that future efforts include a more robust investigation of the optimal means of distributing the water to each CPU within the blade servers (and potentially other heat-generating IT equipment). Subsequently, a more accurate estimate of the SHEC pressure drop and pump power could be determined.

In initial iterations of the fluid mechanics analysis through the SHEC pipes, velocity was manually specified to determine appropriate inner diameters of the pipes by rearranging equation 6.2.5.5 to solve for diameter. For water, a fluid velocity of 1 m/s is considered an economical velocity which minimizes the annual cost (e.g. maintenance, replacement costs) of the piping system [54]. The resulting diameters from the 1 m/s velocity specification across the various sections of SHEC pipes were then matched to the closest nominal pipe sizes of K type copper [53]. The fluid mechanic analysis of the SHEC pipes was then repeated, but the diameter was specified to calculate the velocity, as represented by equation 6.2.5.5. The final numerical results for fluid mechanics analysis of the SHEC piping system are presented in Section 6.3.

The SHEC piping system detailed in this section represents a generalized configuration that may be adapted for a specific application at an existing data center. The system was based on a 10 kW heat load, corresponding to the AK120b server room at WPI. However, the physical configuration is suitable for data centers with far greater scales, and the efficiency of the SHEC is likely to improve with greater heat loads from more server racks (with higher power densities). There are many factors that impact the design of the SHEC piping system, several of which were mentioned throughout the discussion. Future work on this project may consider higher power CPUs (with greater TDPs), extending the liquid cooling system to other heat-generating components, varying the number of CPUs and blade servers in the racks, specifying all the pipe features and corresponding minor losses for a selected data center, etc. Lastly, the pressure drop across the ORC evaporator was not included in the fluid mechanics analysis. The ORC evaporator was represented by a shell and tube configuration, wherein the water passed through the shell. Due to the interference between the tubes, baffles, or other design features, the pressure drop could not be readily determined. However, future work could include the development of a COMSOL simulation of the shell and tube evaporator to more precisely determine the pressure drop of the water across the shell. Subsequently, a more accurate pump power for the full SHEC piping system could be determined.

## 6.3 Final Results

This section presents the numeric results for the optimized final design of the ORC data center waste heat recovery system. The values were determined via the methodologies and calculations presented in Section 6.2. The heat exchanger designs for the ORC evaporator and condenser are presented first, including results for the intermediary calculations of mass flow rates,  $UA$  values, heat transfer coefficients, fin correction factors, etc. The heat exchanger results are followed by the presentation of the final values corresponding to the state-strategy table of the final ORC design, overall results for the ORC thermodynamic performance, and the required pump power from the fluid mechanics analysis. Lastly, the numeric results for the SHEC piping manifold are presented, in addition to the corresponding pump power required to distribute the coolant water through the system.

### 6.3.1 ORC Heat Exchanger Results

In this section, the numeric results for the final, optimized designs of the ORC evaporator and ORC condenser are presented. The methodology applied to arrive at the numeric results can be found in Section 6.2.1 and Section 6.2.2.

The inlet and outlet temperatures corresponding to the heating and evaporating stages of the ORC evaporator and to the cooling and condensing stages of the ORC condenser are presented in **Table 21**. For reference, the hot and cold fluids in the ORC evaporator were the SHEC water and R1234ze, respectively; the hot and cold fluids in the ORC condenser were the R1234ze and coolant water, respectively. The HEX stage in the first column of the table is indicated by the heat exchanger [Evaporator/Condenser] followed by the stage indicating the transformation of the R1234ze (heating/evaporating, cooling/condensing).

**Table 21:** Summary of HEX temperatures (°C).

HEX Stage	Hot Fluid, Inlet Temperature (°C)	Hot Fluid, Outlet Temperature (°C)	Cold Fluid, Inlet Temperature (°C)	Cold Fluid, Outlet Temperature (°C)
Evaporator (heating)	75.59	74.00	52.50	74.85
Evaporator (evaporating)	80.85	75.59	74.85	74.85
Condenser (cooling)	54.16	52.50	26.96	27.22
Condenser (condensing)	52.5	52.5	7.22	26.96

The mass flow rates of the SHEC water, R1234ze, and coolant water are presented in **Table 22**.

**Table 22:** Summary of mass flow rates (kg/s).

Variable	Mass Flow Rate of SHEC Water	Mass Flow Rate of R1234ze	Mass Flow Rate of Coolant Water
Result (kg/s)	0.348	0.0654	0.113

The inputs for calculating the Reynolds number of the three fluids through the four different ORC heat exchanger stages (heating & evaporating in the ORC evaporator and cooling & condensing in the ORC condenser) for the counterflow concentric pipe configuration are presented in **Table 23**, in addition to the final results of the Reynolds numbers.

**Table 23:** Summary of Reynolds number calculations.

HEX stage	Fluid	Mass Flow Rate (kg/s)	Hydraulic Diameter (m)	Cross-Sectional Area (m <sup>2</sup> )	Dynamic Viscosity (Pa-s)	Reynolds Number
Evaporator (heating)	R1234ze	0.0654	0.0102	0.0000819	0.000116	70,235
Evaporator (heating)	Water (SHEC)	0.348	0.0126	0.000375	0.000378	30,835
Evaporator (evaporating)	Water (SHEC)				0.000362	32,228
Condenser (cooling)	R1234ze	0.0654	0.0102	0.0000819	0.0000139	585,920*
Condenser (cooling)	Water (coolant)	0.113	0.0126	0.000375	0.000849	4,473
Condenser (condensing)	Water (coolant)				0.00108	3,526

\*Note: the Reynolds number for the R1234ze in the cooling stage was very high since the fluid was in the vapor phase

The inputs for calculating the heat transfer coefficients (HTCs) of the three fluids through the four heat exchanger stages are presented in **Table 24**, in addition to the final results of the HTCs.

**Table 24:** Summary of HTC calculations.

HEX stage	Fluid	Reynolds Number	Specific Heat Capacity (J/kg-K)	Thermal Conductivity (W/m-K)	Prandtl Number	Nusselt Number	HTC (W/m <sup>2</sup> -K)
Evaporator (heating)	R1234ze	70,235	1588	0.0617	2.98	268	1,623
Evaporator (heating)	Water (SHEC)	30,835	4193	0.663	2.39	117	6,151
Evaporator (evaporating)	Water (SHEC)	32,228	4196	0.666	2.28	119	6,305
Condenser (cooling)	R1234ze	585,920*	1142	0.0164	0.968	934	1,500
Condenser (cooling)	Water (coolant)	4,473	4181	0.610	5.82	38.7	1,879
Condenser (condensing)	Water (coolant)	3,526	4187	0.593	7.61	35.7	1,681

The researched HTC values for the R1234ze in the evaporating and condensing stages of the heat exchangers are reproduced in **Table 25**. A range of HTCs were considered, represented by approximated maximum, minimum, and average values.

**Table 25:** Summary of HTCs ( $\text{W/m}^2\text{-K}$ ) for R1234ze during evaporation and condensation.

HTC ( $\text{W/m}^2\text{-K}$ )	Evaporation of R1234ze [78]	Condensation of R1234ze [83]
Maximum	4200	4800
Minimum	1000	900
Average	2600	2850

The piping dimensions (corresponding to 3/8 inch and 1 inch nominal size pipes [53]) and fin geometry of the heat exchangers are summarized in **Table 26**. Additionally, the heat transfer rates and corresponding  $UA$  values (for counterflow) for each of the four heat exchanger stages are also presented in **Table 26**.

**Table 26:** Summary of piping dimensions, fins, heat transfer rates, and  $UA$  values.

HEX stage	Inner Pipe (m)	Fin Thickness (m)	Number of Fins	Outer Pipe (m)	Heat Transfer Rate (kW)	$UA$ ( $\text{W/K}$ )
Evaporator (heating)	ID = 0.0102 OD = 0.0127	0.0003	22	ID = 0.0253 OD = 0.0286	2319.1	376.47
Evaporator (evaporating)					7680.9	3057.1
Condenser (cooling)					123.88	4.7222
Condenser (condensing)					9361.8	272.83

The resulting lengths of the four heat exchanger stages are presented in **Table 27**, in addition to the fin efficiencies and fin correction factors (FCFs). For the heating stage of the evaporator, the resulting P and R parameters were 0.7884 and 0.2967, respectively, corresponding to a correction factor (F) of approximately 0.80 for the shell and tube HEX type. Therefore, four calculations for HEX length are reported for the heating stage of the ORC evaporator, for a counterflow (CF) and shell and tube (S&T) HEX configuration without fins, and with fins. For all the other stages of the heat exchangers, the S&T correction factor was either approximately 1 or equal to 1, due to the near constant or constant temperature of the R1234ze. Thus, for all the other stages of the heat exchangers, two calculations for HEX length are reported, for a CF HEX without fins and with fins, since the S&T length calculations would be the same. For the evaporating and condensing stages, the maximum, minimum, and average HTC values for R1234ze from literature were used to calculate the required pipe length for a CF HEX, without fins and with fins.

**Table 27:** Summary of HEX lengths and effect of fins.

HEX stage	CF Length (m)	S&T Length (m)	Fin Efficiency	FCF	CF + Fins Length (m)	S&T + Fins Length (m)
Evaporator (heating)	8.80	11.0	0.916	4.83	2.52	3.83
Evaporator (evaporating, max HTC)	35.11		0.812	4.37	17.61	
Evaporator (evaporating, min HTC)	107.72		0.946	4.96	31.62	
Evaporator (evaporating, avg HTC)	49.08		0.872	4.64	20.32	
Condenser (cooling)	0.16		0.922	4.86	0.10	
Condenser (condensing, max HTC)	5.86		0.793	4.29	4.51	
Condenser (condensing, min HTC)	13.54		0.952	4.99	5.99	
Condenser (condensing, avg HTC)	7.08		0.864	4.60	4.74	

The evaporation stage in the ORC evaporator required the longest length of piping, due to the closeness of the temperature magnitudes and small temperature differentials. Adding internal axial fins to the inner pipe containing R1234ze was essential for reducing the HEX pipe length to a reasonable amount. Considering the worst case scenarios (minimum HTCs of R1234ze), the final designs of the ORC heat exchangers were as follows:

Both heat exchangers consist of a shell and tube configuration with nominal 3/8 inch Type K Copper tubes containing 22 evenly spaced rectangular axial fins with a thickness of 0.0003 m and extension length of 0.0031 m. The total length of piping required for the evaporator and condenser are 34.68 m and 6.09 m, respectively. Assuming a shell length of 30 inches (0.762 m) for the ORC evaporator and 12 inches (0.3048 m) for the ORC condenser, the heat exchangers consist of approximately 50 tube passes and 20 tube passes, respectively.

### 6.3.2 ORC Thermodynamics & Fluid Mechanics Results

#### ORC Thermodynamics Results

Based on the final design and results of the MCHS simulation and ORC heat exchangers, the resultant fluid states and properties corresponding to **Table 19** (state-strategy table of the final ORC design) from Section 6.2.3, are presented below in **Table 28**.

**Table 28:** Fluid states and properties for the final design of the ORC.

State	Pressure (kPa)	Temperature (°C)	Specific entropy (kJ/kg-K)	Specific enthalpy (kJ/kg)	Specific volume (m <sup>3</sup> /kg)
1	1795	74.85	1.6827	426.03	0.00958
2	1062	54.16	1.6885	418.51	0.0177
2'	1062	52.5	1.6827	416.63	0.0175
3	1062	52.5	1.2428	273.37	0.000940
4	1795	53.17	1.2432	274.19	0.000937
4'	1795	74.85	1.3449	308.49	0.00104

Notable resultant characteristics of the final design of the ORC are presented in **Table 29** and **Table 30**.

**Table 29:** Turbine, pump, and net powers (kW).

Output	Turbine Power	Pump Power	ORC Net Power
Result (kW)	0.4912	0.0450	0.4462

**Table 30:** Thermal, Carnot, and Second Law Efficiencies (%).

Output	Thermal Efficiency	Carnot Efficiency	Second Law Efficiency
Result (%)	4.46	6.42	69.48

The resultant outputs of the ORC performance were consistent with those found in literature. Araya et al. constructed an experimental prototype to test the feasibility of an ORC for data center waste heat recovery application and reported model-based thermal efficiencies between 2% and 8%, and a maximum experimental thermal efficiency of 3.33% [20]. Ebrahimi et al. conducted a model-based data center-ORC study with two-phase cooling of CPUs and reported first law efficiencies (i.e. thermal efficiencies) as high as 8.5%, provided that: (1) the temperature of the two-phase fluid leaving the micro-evaporator on the CPUs is was 75°C, (2) fluid temperature entering the ORC evaporator was boosted by a compressor to 90°C, (3) working fluid temperature at the outlet of the condenser is fixed at 20°C, and (4) the working fluids of the ORC loop and micro-evaporator loop are R134a and R245fa, respectively [3]. As shown by **Figure 92**, Ebrahimi et al. produced a range of thermal efficiencies

(3%-8.5%) by varying the micro-evaporator temperature (60°C-75°C) and the temperature at the inlet of the ORC evaporator (after boosting the heat through a compressor) (90°C-100°C) [3]. The resulting thermal efficiency of the final ORC design for this project was 4.46% and therefore consistent with existing research investigations.

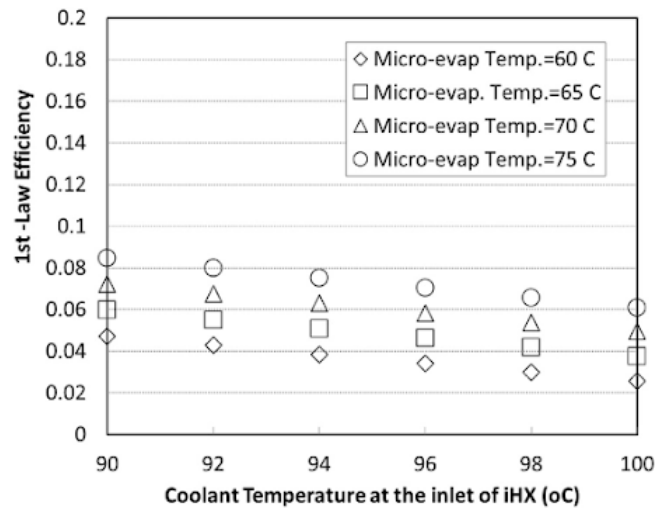


**Figure 92:** Effect of waste heat quality on ORC performance [3].

It is also important to note that the study conducted by Ebrahimi et al. utilized two-phase cooling in the CPU heat sink (i.e. micro-evaporator), and with the best-performing conventional refrigerants (R134a and R245fa). However, the final design of the SHEC-ORC in this project utilized single-phase liquid cooling of the CPUs, water, and environmentally-conscious R1234ze and nonetheless provided a comparable thermal efficiency. Thus, the extensive analyses and strategic design decisions that comprised the final system design demonstrated that a more sustainable version of the dual-loop ORC for data center waste heat recovery could remain competitive with other systems that use conventional (yet, environmentally harmful) refrigerants.

### *ORC Fluid Mechanics Results*

The fluid mechanics calculations were computed using the approach presented in Section 3.4.2. Based on the preliminary analysis, the ideal inner pipe diameter was 0.010 meters (0.402 inches) with a wall thickness of 0.0012 meters (0.049 inches). The selection of the optimum pipe considered (1) the pressure rating of the pipe (6232.86 kPa [53]), to ensure it was far greater than the highest pressure in the ORC, and (2) the minimization of required pump power. In the final design of the ORC waste heat recovery system, the fluid states and properties differed from those initially utilized in the preliminary fluid mechanics calculations. The velocity, Reynolds number, friction factor, pressure drop, and pump power corresponding to the final fluid states and properties in each of the four sections of the ORC connecting pipe (see **Table 28**) are summarized in **Table 31**.

**Table 31:** Summary of ORC pressure drop and pump power calculations.

State	Velocity (m/s)	Reynolds Number	Friction Factor	Pressure Drop (Pa)	Pump Power (W)
1	7.66	525,620	0.0220	5786	3.623
2	14.1	586,210	0.0220	10,655	6.673
3	0.752	60,958	0.0245	600	0.0369
4	0.749	60,103	0.0245	599	0.0366

Therefore, the resulting total pressure drop and associated total pump power for the four connecting pipes in the SHEC was 17.64 kPa and 10.37 W, respectively. The ORC fluid mechanics results indicate that the final design required a very small power input for the pump. However, it is important to note that the pressure losses across the heat exchangers in the ORC were not included in the analysis due to the non-uniform fluid properties of R1234ze during evaporation or condensation. Future efforts could investigate the characterization of pressure drop in the ORC heat exchanger tubes for a more accurate representation of the pressure drop over the entire ORC system. Furthermore, future endeavors could include a stress analysis of the piping system. Although the highest pressure in the ORC (1795 kPa) was well below the rated pressure of the pipes, a stress analysis could provide further insight about the practicality and durability of the selected ORC piping. Additional investigation into the fatigue and failure rates of the various sections of the ORC piping (which experience different fluid phases, temperatures, and pressures), could indicate when the pipes should be serviced or replaced to avoid system failure.

### 6.3.3 SHEC Piping & Fluid Mechanics Results

Using the methodology presented in section 6.2.5, the results for the pressure drop and corresponding pump power for each pipe section of the SHEC were computed via the MATLAB program. The final input parameters and results from the SHEC piping and fluid mechanics are summarized in **Table 32**. The column headers in the table correspond to the labels in **Figure 88** and terms in equation 6.2.5.6.

**Table 32:** Summary of SHEC pressure drop and pump power calculations.

	Pipe Section 1	Pipe Section 2	Servers*	Pipe Section 3	Pipe Section 4
<b>Inner Diameter (m)</b>	0.0253	0.0102		0.0102	0.0253
<b>Flow Rate (kg/s)</b>	0.360	0.0899	0.0056	0.0899	0.360
<b>Velocity (m/s)</b>	0.733	1.13		1.13	0.737
<b>Reynolds Number</b>	47,327	29,347		32,035	51,661
<b>Change in elevation (m)</b>	5	0	-1.8796	0	-3.1204

<b>Total Pipe Length (m)</b>	6	2		2	4
<b>Friction Factor</b>	0.0227	0.0268		0.0264	0.0224
<b>Pressure Drop (Pa)</b>	49,240	3,259	-16,985	3,231	-28,785
<b>Pump Power (W)</b>	18.154	0.30037	-0.0980	0.2991	-10.658

\*Note: the “Servers” section has an additional 997 kPa of pressure drop associated with the MCHS, determined from the COMSOL simulation results.

The total pressure drop over the SHEC was thus 9,960 Pa (9.960 kPa), which was associated with a required pump power of 7.9971 W. However, only piping to four server racks was included in the SHEC for the 10 kW heat load scenario. If implemented in a mid-size data center, the provided heat load and number of server racks would increase. Subsequently, the length of piping required to distribute and circulate the water would increase, producing greater pressure drops and required pump power. Future efforts could experiment with variations to the SHEC design and inputs for a specific data center. Alternatively, the SHEC piping system could be implemented in COMSOL for a robust characterization of the pressure drop over the SHEC.

## 7.0 Economic Analysis

Although the resulting thermal efficiency of the final design (4.46%) appeared low, the thermal performance of the system very closely approached the maximum efficiency possible predicted by the Carnot efficiency (6.42%). It is also important to recall that the ORC is powered entirely by the waste heat from the data center, thereby producing electricity from an unreserved source of energy. The electricity generated by the thermodynamic processes in the ORC can then provide a source of revenue for the data center in the form of offsetting electricity costs.

In this section, the economic feasibility of the proposed ORC system was evaluated to understand whether the system was commercially viable. Two data center applications were evaluated: (1) 10 kW thermal load from a data center, resembling the server room in AK120b at WPI, and (2) 1000 kW (1 MW) thermal load from a typical mid-size data center. In addition, the ORC waste heat recovery system was compared against conventional data center cooling technology—specifically, rack level air cooling in a hot aisle-cold aisle layout. An annual cost analysis was performed to compare the two options in the two different data center applications. An annual cost analysis, also known as equivalent annual cost (EAC), is a computation of “the annual cost of owning, operating, and maintaining an asset over its entire life” and accounts for the time value of money [86]. An EAC analysis is often used to make budgeting decisions as it enables the cost-effectiveness of assets with different lifetimes to be compared [86]. In addition, both the simple payback period and discounted payback period (which accounts for the time value of money) were calculated. The payback period was used to determine whether the ORC would pay itself back and produce electricity (essentially for free) before the system had to be retired or replaced.

### 7.1 Calculation of Cost Parameters

Listed in this section are all the variables and preliminary calculations necessary for evaluating the EAC of the two systems in each data center scenario. General parameters are listed first, followed by the cost parameters for the ORC/SHEC and air cooling scenarios.

#### 7.1.1 General Cost Parameters

The long term average for the US Long-Term Investment Rate is 4.52% [87], thus the discount rate (i.e. investment rate) was approximated at 5%. For the cost of electricity, a few different values were considered, as shown in **Table 33**:

**Table 33:** Electricity Prices (\$/kWh).

US Residential	0.1269
US Commercial	0.1031
MA Residential	0.2232
MA Commercial	0.1627

\*data sourced from [88].

Since the WPI server room is located in Massachusetts and the ORC system is designed for commercial data center applications, the MA commercial rate of electricity (\$0.1627 per kWh as of January 2021 [88]) was selected for the EAC analysis. Two data centers with different thermal loads (10 kW and 1000 kW) were considered, wherein the lifetime of the data centers were approximated at 20 years [47]. It was assumed that the data centers would operate at full capacity year round (8760 hours/year).

### 7.1.2 ORC/SHEC System Cost Parameters

The lifespans of modern ORCs can exceed 20 years [89], wherein the turbine can last up to 30 years when the fluid is dry/isentropic (which was the case for R1234ze in the proposed ORC) [90]. Thus, the lifetime of the ORC system was set at the same value as that of the data center, 20 years.

From the results of the final design, it was determined that the ORC had a net power of 446.2 W. In addition, it was found that the SHEC required a pump power of 8.00 Watts. Thus, the whole-system net power ( $\dot{W}_{net}$ ) was 0.438 kW for a 10 kW thermal load. With the price of electricity and operation of 8760 hrs/yr, the annual revenue from the production of electricity was determined using the following equation,

$$\text{Annual Revenue} = \dot{W}_{net} \times 8760 \frac{h}{yr} \times 0.1627 \frac{\$}{kWh} \quad (\text{equation 7.1.2.1})$$

Since costing data for various sized ORC systems is not typically made public, the cost parameters for the ORC were primarily sourced from the first-order economic analysis presented by Ebrahimi et al. in their model-based study on the viability of a dual loop ORC system with two-phase cooling in data center applications [3]. Ebrahimi et al. obtained pricing data based on cost estimates for 30kW thermal load ORC modules, provided by *Orcan Energy*, which designs ORC systems for low power and temperature applications [3]. For the purposes of the economic analysis, it was assumed that the data center would contain the least number of modules that would satisfy its heat load [3]. Each module is capable of producing 1.5 kW of electricity from a 30 kW thermal input [3].

*Orcan Energy* (a German company) provided estimates for the capital, installation, and maintenance costs of the ORC [3]. However, the cost estimates were provided in May 2017 and in Euros [3]. Therefore, the rates were converted first from Euros to USD, using the 2017 exchange rate of 1 Euro = 1.1304 USD [91]. Then, the USD price was converted to the present value by adjusting for inflation using an inflation calculator [92]. As of May 2017, the capital cost of the ORC modules was 3333€ per kW of electricity produced (based on the 30 kW<sub>th</sub> module), the installation cost was 15% of the capital cost, and the annual maintenance cost was 200€ per module [3]. After adjusting for the conversion from Euros to USD and inflation, the capital cost was \$4,126/kW<sub>e</sub> and the annual maintenance cost was \$247/module.

The number of modules ( $N$ ) required for each data center application was determined by dividing the heat load of the data center by the 30 kW<sub>th</sub> module load, rounding up to the nearest whole number. The cost of the ORC modules for each data center application was determined by multiplying the output

power of the whole-system net output power ( $Wdot_{net}$ ) by the cost per  $kW_e$ . The following equations were used to determine the capital, installation, and maintenance costs for each data center application:

$$Capital\ Cost = Wdot_{net} \times 4,136 \frac{USD}{kW_e} \quad (equation\ 7.1.2.2)$$

$$Installation\ Cost = Capital\ Cost \times 0.15 \quad (equation\ 7.1.2.3)$$

$$Maintenance\ Cost = N \times 247 \frac{USD}{module} \quad (equation\ 7.1.2.4)$$

Then, the total capital cost and annual net revenue were given by,

$$Total\ Capital\ Cost = Capital\ Cost + Installation\ Cost \quad (equation\ 7.1.2.5)$$

$$Annual\ Net\ Revenue = Revenue - Maintenance\ Cost \quad (equation\ 7.1.2.6)$$

The results from the calculations for each data center application are summarized in **Table 34**.

**Table 34:** Summary of ORC data center preliminary calculations.

	10 kW <sub>th</sub> Data Center	1000 kW <sub>th</sub> Data Center
Whole-system net power (kW <sub>e</sub> )	0.4382	43.82
Number of 30 kW <sub>th</sub> modules	1	34
Capital Cost	\$1,808.03	\$180,802.52
Installation Cost	\$271.20	\$27,120.38
Annual Revenue	\$624.55	\$62,454.96
Annual Maintenance Cost	\$247.00	\$8,398.00
<b>Total Capital Cost</b>	<b>\$2,079.23</b>	<b>\$207,922.89</b>
<b>Annual Net Revenue</b>	<b>\$377.55</b>	<b>\$54,056.96</b>

(Note that cost of the CPU heat sinks was not included in the analysis. Future efforts could investigate the cost of manufacturing the optimal MCHS design presented in Section 6.1. and account for the additional costs in the EAC analysis)

### 7.1.3 Conventional Air Cooling Cost Parameters

To understand the cost of cooling the same size data centers with conventional technology, cost parameters for an air cooled data center were also determined. It was assumed that the data center would use hot-aisle cold-aisle cooling with fans installed on the server racks. The required cooling airflow was determined based on the general air flow requirement through an enclosure (regardless of delivery method), represented by the following expression [93]:

$$Required\ Air\ Flow = kW_{per\ enclosure} \times 125\ CFM \quad (equation\ 7.1.3.1)$$

A variable speed fan panel from *Server Racks Online, LLC* was selected for the rack fan (see **Figure 93**). The fan panel consisted of 9 fans with a total cooling capacity of 972 CFM and power requirement of 60 W [94]. The cost of the fan panel was \$733, with the average time before failure of 50,000 hours (5.7 years) [94].



**Figure 93:** MRF-33.9A vertical door mount 33U master fan panel [94].

The number of fan panels ( $N$ ) required for each data center application was determined by dividing the required air flow of the data center by the cooling air flow rate of each fan panel, rounding up to the nearest whole number. The capital cost of the air cooling system was found by multiplying the cost of a single fan panel by the number of fan panels required by the data center. With the fan panel power ( $W_{fan\ panel}$ ), number of fan panels ( $N$ ), price of electricity, and operation of 8760 hrs/yr, the annual cost of powering the fan panels for the air cooling system was determined using the following equation,

$$Annual\ Cost = W_{fan\ panel} \times N \times 8760 \frac{h}{yr} \times 0.1627 \frac{\$}{kWh} \quad (equation\ 7.1.3.2)$$

The resulting air cooling cost parameters for each data center application are summarized in **Table 35**.

**Table 35:** Summary of air cooling data center preliminary calculations.

	10 kW <sub>th</sub> Data Center	1000 kW <sub>th</sub> Data Center
Required Air Flow (CFM)	1250	125,000
Number of fan panels	2	129
Power Demand (kW)	0.12	7.74
<b>Total Capital Cost</b>	<b>\$1,466.00</b>	<b>\$94,557.00</b>
<b>Annual Net Cost</b>	<b>\$171.03</b>	<b>\$11,031.45</b>

## 7.2 Annual Cost Analysis

Once all the preliminary cost parameters had been determined, an EAC analysis was conducted to compare the ORC/SHEC system with conventional air cooling for the two different data center scales.

The EAC cost parameters for the four scenarios are summarized in **Table 36**. The EAC equation was represented by,

$$EAC = A + P(A/P, i, n) \quad (\text{equation 7.2.1})$$

where  $A$  is the annual capital flow,  $P$  is the present value of the capital cost,  $i$  is the interest rate, and  $n$  is the lifetime of the system. (Note that the lifetime of the ORC/SHEC was the same as the data center, whereas the rack fan panel had a lifespan of approximately 6 years.) Compound interest tables were consulted for the  $(A/P, i, n)$  values corresponding to each system. For the ORC/SHEC,  $(A/P, 0.05, 20)$  corresponded to 0.0802 [95]. For air cooling,  $(A/P, 0.05, 6)$  corresponded to 0.1970 [95]. A summary of the input cost parameters and results for the EAC analysis is presented in **Table 36**.

**Table 36:** Equivalent Annual Cost (EAC) Summary.

	10 kW (ORC/SHEC)	10 kW (air cooling)	1000 kW (ORC/SHEC)	1000 kW (air cooling)	Parameter
<b>Capital Cost</b>	-\$2,079.23	-\$1,466.00	-\$207,922.89	-\$94,557.00	P
<b>Life (yrs)</b>	20	6	20	6	n
<b>Annual Capital Flow (+Revenue/-Cost)</b>	\$377.55	-\$171.03	\$54,056.96	-\$11,031.45	A
<b>Interest Rate</b>	5%	5%	5%	5%	i
<b>EAC</b>	\$210.80	-\$459.83	\$37,381.54	-\$29,659.18	

As shown by the results in **Table 36**, the ORC/SHEC system produces a positive EAC, whereas conventional air cooling results in negative EAC. With the ORC/SHEC system, the annual revenue produced by the generation of electricity not only offsets the capital and maintenance costs over its lifetime, but produces an annual surplus. Conversely, conventional air cooling does not have a source of revenue, and thus has a negative EAC. From the results, it can also be concluded that the ORC/SHEC system is more advantageous at larger scales (whereas conventional air cooling is more disadvantageous). The EAC for the 1000 kW data center with ORC/SHEC had over 180 times the EAC of the 10 kW system, even though the data center waste heat load only increased by a factor of 100. The EAC for the 1000 kW data center with air cooling had approximately 65 times the EAC of the 10 kW system. The results from the EAC serve to show why modern data centers seek efficient and cost effective alternatives to air cooling. The ORC/SHEC system detailed in this report is a proposed alternative that not only reduces the energy demand and costs related to cooling, but actually enables data centers to utilize the heat produced by the IT equipment to generate electricity and ultimately profit from the cooling system, where greater returns can be achieved at larger scales.

### 7.3 Payback Period

Another helpful metric used in evaluating economic feasibility is the payback period, which was used in the first-order economic analysis provided by Ebrahimi et al. The simple payback period can be determined by dividing the capital cost by the annual revenue. Since air cooling does not produce revenue, there is no payback period, and the system is only associated with annual costs.

**Table 37: Payback Period Summary.**

	<b>10 kW (ORC/SHEC)</b>	<b>10 kW (air cooling)</b>	<b>1000 kW (ORC/SHEC)</b>	<b>1000 kW (air cooling)</b>
<b>Simple Payback Period (yrs)</b>	5.51	--	3.85	--
<b>Discounted Payback Period (yrs)</b>	6.61	--	4.38	--

As shown in **Table 37**, the simple payback periods for the ORC/SHEC systems in 10 kW and 1000 kW data center applications were 5.51 years and 3.85 years, respectively. The 10 kW data center scenario had a larger payback period since the annual maintenance costs were fixed at \$247 per module. Since the modules were based on a 30 kW thermal load, there was one for the 10 kW data center, and 34 for the 1000 kW data center. Unlike the parameters for other costs, the maintenance cost did not increase by a factor of 100, thereby increasing the net annual capital flow for the ORC/SHEC in the 1000 kW data center and decreasing the simple payback period relative to the 10 kW system.

However, the simple payback period does not account for the time value of money. To more precisely quantify the payback period associated with the ORC/SHEC system at the two data center scales, the discounted payback period was determined. The discounted payback period accounts for the time value of money by iteratively calculating the present value of the annual revenue and subtracting it from the original (present value) capital cost until it is paid off [96]. The fractional component of the last year is determined by dividing the remaining amount of the (present value) capital cost by the next present value of annual revenue [96]. Additional details for calculating the discounted payback period can be found in **Appendix F**. The results for the discounted payback period are presented in **Table 37**, in the row below the simple payback period. As shown by the results, accounting for the time value of money increased the time required to pay off the initial capital cost of the ORC/SHEC system. Regardless, the discounted payback period for both data center scales was far less than the 20-year lifespan of the system and data center.

It is also important to note that the 1000 kW ORC/SHEC system may produce even greater profit margins due to the potential cost reductions associated with economies of scale. In the sample economic analysis provided by the EAC and discounted payback period, the capital cost of the ORC system was based on a flat rate of \$4,126 per kW of electricity produced, associated with a 30 kW<sub>th</sub> load ORC module. However, ORC pricing (\$/kW<sub>e</sub> produced) depends on the size of the system, where higher rates are associated with smaller systems and lower rates are associated with larger systems [3]. Based on a review of ORC pricing for a variety of systems, rates may vary from approximately \$1,250 to \$9,780 per kW<sub>e</sub> produced [3] (converted from € to USD and adjusted for inflation, then rounded). It can be reasonably assumed that larger data centers can take advantage of the lower rates associated with larger ORC systems, by replacing the numerous small ORC modules with a few larger ones. If this strategy was employed in larger data centers, the capital cost and payback period would decrease, enabling the data center to begin accumulating revenue from their IT waste heat even sooner.

## 8.0 Conclusions & Recommendations

In this project, a proposed solution for recovering waste heat produced by the IT equipment (i.e. CPUs) in a data center was researched, designed, and optimized. An ORC with an environmentally-conscious working fluid (R1234ze) was utilized for heat recovery, wherein waste heat from the data center was used to power the thermodynamic processes that drove R1234ze vapor through a turbine to generate electricity. The waste heat extracted and transferred to the ORC evaporator was not assumed, as it had been in prior studies [3], [20]. Rather, the design of a single-phase, liquid water microchannel heat sink was investigated, for the purposes of maintaining the IT equipment within safe operating temperatures while maximizing the temperature at the outlet of the heat sink. The higher waste heat temperatures were desirable for optimizing the ORC performance. Furthermore, adequate heat transfer between the water carrying the waste heat from the CPUs and the working fluid in the ORC was not assumed. Instead, a heat exchanger design analysis was conducted for the ORC evaporator to determine what configuration and additional design features would be required to enable the highest possible temperatures of the R1234ze vapor in the ORC, so as to optimize the ORC performance. Similarly, a heat exchanger design analysis was conducted for the ORC condenser to specify what configuration and additional design features would ensure adequate cooling and condensing of the R1234ze for optimal ORC conditions. Finally, a generalized SHEC piping schematic was also defined, which distributed water to each MCHS (to extract heat generated by the CPUs), directed the heated water to the ORC evaporator, and cycled the cooled water at the outlet of the evaporator back to the servers. The analyses of all the system components were represented in a comprehensive MATLAB program which generated a full-system, integrated analysis and allowed for efficient design iterations to be made.

The final design of the project encompassed all the relevant systems and components necessary for implementing an ORC at a data center for waste heat recovery. Furthermore, many aspects of the system were optimized, including the MCHS geometry, heat exchanger design (e.g. finned pipes), and ORC/SHEC pipe diameters. The additional considerations to optimize the design enabled greater temperature differentials, reduced pressure drops, decreased required HEX pipe lengths, and reduced pump power demands to advance the performance of the whole system. Ultimately, an economic analysis comparing the ORC/SHEC system (which utilizes server heat as an energy source) to conventional air cooling (where server heat is waste) showed that the ORC enabled data centers to produce revenue streams from IT cooling (in the form of offsetting electricity consumption), *instead of costs*. Not only has it been shown that the ORC/SHEC system can create its own power for cooling (significantly reducing the overall energy demand for the data center, since cooling accounts for as much as 50% of the data center electric power consumption [5]), but it has proven effective with a less-conventional, yet environmentally-conscious, working fluid. Furthermore, the ORC/SHEC system can produce greater profit margins for larger data centers (or higher density data centers) due to the potential cost reductions associated with economies of scale. The advantage of scaling the ORC/SHEC is crucial, since data centers are rapidly growing in size and density, and thus energy consumption.

Finally, it is important to note that although it was the aim of this project to consider all the mechanical aspects of the ORC system involved in extracting, transporting, and utilizing the waste heat produced

by IT equipment in data centers, (and although many aspects of the various sub-systems and components were optimized) it is highly recommended that future work further investigates and optimizes the different aspects of the system. The work on the design of the most effective MCHS may be expanded upon through deeper investigations of two-phase flow boiling and development of an optimized two-phase MCHS. Additionally, a range of CPUs with different TDPs and heat fluxes may be considered for various MCHS designs. Alternatively, investigations into the manufacturability of CPU MCHSs may also be pursued, potentially with the testing of an experimental prototype. Future work may also consider the utility of the waste heat produced by the other heat-generating components inside the server for the ORC waste heat recovery system. In terms of the evaporator and condenser in the ORC, extended efforts may include further specification and optimization of the heat exchanger designs, perhaps considering additional design elements such as baffles and/or tube spacing. Additionally, it is recommended that the pressure drop over the heat exchangers is also investigated, as the HEX tubes for smaller ORC systems may be associated with greater pressure gradients. (However, theoretical evaluation is complicated due to the phase transition regions.) The feasibility of the heat exchanger designs may also be investigated further, specifically regarding the flow phenomena between internal axial fins of the inner pipe and/or the mechanical integrity of the designs at the elevated pressures and temperatures, in both the short-term and long-term. Lastly, it should be noted that much of the piping analysis in this project may be considered ‘provisional’ as the system pipe lengths and configurations depend significantly on the specific layout of the data center, highly unique for each case.

Future work could include a robust specification of the physical integration of an ORC with a specific data center via the SHEC, given sufficient information about the unique thermal, physical, and technological characteristics of the data center. For example, the 10 kW server room in AK120b at WPI had several racks of scattered servers, hence the final design of four server racks with only a 2.5 kW heat load per rack. However, in typical US data centers, each rack has a load of approximately 16 kW [10], which would require the re-working of an optimal SHEC piping network. In the case that the exact specification of the piping and connections for an SHEC in a specific data center could be provided, a more robust fluid mechanics analysis could be pursued, accounting for minor losses associated with the various pipe features. Furthermore, if *all* the ORC/SHEC system components can be sized and specified for a specific data center application, a more robust economic analysis could also be conducted, accounting for individualized pricing for each component (e.g., evaporator, condenser, turbine, ORC pump, ORC piping/insulation/connections, CPU heat sinks, SHEC pump, SHEC piping/insulation/connections).

The highly encouraging results from this project ultimately warrant future extensions, investigations, and optimizations to eventually bring ORC data center waste heat recovery systems to commercial realization—for the benefit of the environment and data center proprietors.

## 9.0 References

- [1] Ebrahimi, K., Jones, G. F., & Fleischer, A. S. (2014). A review of data center cooling technology, operating conditions and the corresponding low-grade waste heat recovery opportunities. *Renewable and Sustainable Energy Reviews*, 31, 622-638. doi:<https://doi.org/10.1016/j.rser.2013.12.007>
- [2] Energy Innovation. (2020). How much energy do data centers really use? Retrieved from <https://energyinnovation.org/2020/03/17/how-much-energy-do-data-centers-really-use/>
- [3] Ebrahimi, K., Jones, G. F., & Fleischer, A. S. (2017). The viability of ultra low temperature waste heat recovery using organic rankine cycle in dual loop data center applications. *Applied Thermal Engineering*, 126, 393-406. doi:<https://doi.org/10.1016/j.applthermaleng.2017.07.001>
- [4] Brunschwiler, T., Smith, B., Ruetsche, E., & Michel, B. (2009). Toward zero-emission data centers through direct reuse of thermal energy. *IBM Journal of Research and Development*, 53(3), 11-1.
- [5] U.S. Department of Energy. (2014). 2014 renewable energy data book. Retrieved from <https://www.nrel.gov/docs/fy16osti/64720.pdf>
- [6] Synergy Research Group. (2019). Hyperscale data center count passed the 500 milestone in Q3. Retrieved from <https://www.srgresearch.com/articles/hyperscale-data-center-count-passed-500-milestone-q3>
- [7] Haranas, M. (2020). COVID-19 isn't slowing AWS and google's data center expansion plans. Retrieved from <https://www.crn.com/news/data-center/covid-19-isn-t-slowing-aws-and-google-s-data-center-expansion-plans?itc=refresh>
- [8] Synergy Research Group. (2020). *Hyperscale data center count reaches 541 in mid-2020; another 176 in the pipeline*. Retrieved from <https://www.globenewswire.com>
- [9] Cisco Systems, Inc. (2019). What is a data center. Retrieved from <https://www.cisco.com/c/en/us/solutions/data-center-virtualization/what-is-a-data-center.html>
- [10] West, B. (2018). Understanding the interplay between data center power consumption/data center energy consumption and power density. Retrieved from <https://www.datacenters.com/news>
- [11] Shehabi, A., Smith, S., Sartor, D., Brown, R., Herrlin, M., Koomey, J., & Lintner, W. (2016). *United states data center energy usage report*. (). United States: Retrieved from <https://www.osti.gov/biblio/1372902>
- [12] Sun, J., Fu, L., Zhang, S. (2012). A review of working fluids of absorption cycles. *Renewable and Sustainable Energy Reviews*, 16(4), 1899-1906. doi:<https://doi.org/10.1016/j.rser.2012.01.011>
- [13] The Engineering Mindset (Producer), & . (2017, August 12). *Absorption chiller, how it works - working principle hvac*. [Video/DVD]

- [14] Haywood, A., Sherbeck, J., Phelan, P., Varsamopoulos, G., & Gupta, S. K. (2012). Thermodynamic feasibility of harvesting data center waste heat to drive an absorption chiller. *Energy Conversion and Management*, 58, 26-34. doi:<https://doi.org/10.1016/j.enconman.2011.12.017>
- [15] Chiriac, F., & Chiriac, V. (2018). Energy recovery systems for the efficient cooling of data centers using absorption chillers and renewable energy resources. *Journal of Engineering Sciences and Innovation*, 3(4), 339-350.
- [16] Mahmoudi, A., Fazli, M., & Morad, M. R. (2018). A recent review of waste heat recovery by organic rankine cycle. *Applied Thermal Engineering*, 143, 660-675. doi:<https://doi.org/10.1016/j.applthermaleng.2018.07.136>
- [17] Access Energy. (2020). How It Works. Retrieved from <https://www.access-energy.com/tech-how.html>
- [18] Bianchi, M., Branchini, L., De Pascale, A., Melino, F., Ottaviano, S., Peretto, A., & Zampieri, G. (2018). Performance and operation of micro-ORC energy system using geothermal heat source. *Energy Procedia*, 148, 384-391.
- [19] Zhang, T., & Wang, E. N. (2012). Design of a microscale organic Rankine cycle for high-concentration photovoltaics waste thermal power generation. 13th InterSociety Conference on Thermal and Thermomechanical Phenomena in Electronic Systems, 993-1002.
- [20] Araya, S., Jones, G. F., & Fleischer, A. S. (2018). Organic rankine cycle as a waste heat recovery system for data centers: Design and construction of a prototype. Paper presented at the 2018 17th IEEE Intersociety Conference on Thermal and Thermomechanical Phenomena in Electronic Systems (ITherm), 850-858. doi:10.1109/ITHERM.2018.8419530
- [21] Chen, H., Goswami, D. Y., & Stefanakos, E. K. (2010). A review of thermodynamic cycles and working fluids for the conversion of low-grade heat. *Renewable and Sustainable Energy Reviews*, 14(9), 3059-3067. doi:<https://doi.org/10.1016/j.rser.2010.07.006>
- [22] Wang, E. H., Zhang, H. G., Fan, B. Y., Ouyang, M. G., Zhao, Y., & Mu, Q. H. (2011). Study of working fluid selection of organic rankine cycle (ORC) for engine waste heat recovery. *Energy*, 36(5), 3406-3418. doi:<https://doi.org/10.1016/j.energy.2011.03.041>
- [23] Sadeghi, M., Nemati, A., ghavimi, A., & Yari, M. (2016). Thermodynamic analysis and multi-objective optimization of various ORC (organic rankine cycle) configurations using zeotropic mixtures. *Energy*, 109, 791-802. doi:<https://doi.org/10.1016/j.energy.2016.05.022>
- [24] Intel. (2020). CPU Cooler: Liquid Cooling Vs Air Cooling. Retrieved October 12, 2020, from <https://www.intel.com/content/www/us/en/gaming/resources/cpu-cooler-liquid-cooling-vs-air-cooling.html>
- [25] CPU World. (2020, September). Intel Core i9-9900KS specifications. Retrieved October 16, 2020, from [https://www.cpu-world.com/CPUs/Core\\_i9/Intel-Core%20i9%20i9-9900KS.html](https://www.cpu-world.com/CPUs/Core_i9/Intel-Core%20i9%20i9-9900KS.html)

- [26] Mueller, S. (2006). Microprocessors Types and Specifications. In *Upgrading and Repairing PCs (17th Edition)* (p. 0-1582). United Kingdom: Que Publishing (Pearson).
- [27] Fox, Pamela. "CPU: Central Processing Unit | AP CSP (Article)." Khan Academy. Khan Academy, 2020.  
<https://www.khanacademy.org/computing/computers-and-internet/xcae6f4a7ff015e7d:computers/xcae6f4a7ff015e7d:computer-components/a/central-processing-unit-cpu/>
- [28] Gayde, W. (2020, April 06). Anatomy of a CPU. Retrieved October 25, 2020, from <https://www.techspot.com/article/2000-anatomy-cpu/>
- [29] CoolIT Systems. "Direct Liquid Cooling." CoolIT Systems, 2021, [www.coolitsystems.com/technology/#direct-liquid-cooling](http://www.coolitsystems.com/technology/#direct-liquid-cooling).
- [30] DV industrial computer ltd. Retrieved from <http://inpc.com.ua/data/d14.html>
- [31] How airflow works inside a server. (2020). Retrieved from <https://www.racksolutions.com/news/blog/airflow-in-a-server/>
- [32] Khalaj, A. H., & Halgamuge, S. K. (2017). A Review on efficient thermal management of air-and liquid-cooled data centers: From chip to the cooling system. *Applied energy*, 205, 1165-1188.
- [33] Gyarmathy, Kaylie. "What You Should Know About Data Center Cooling Technologies," January 17, 2020. <https://www.vxchnge.com/blog/data-center-cooling-technology>.
- [34] Chu, W., & Wang, C. (2019). A review on airflow management in data centers. *Applied Energy*, 240, 84-119. doi:<https://doi.org/10.1016/j.apenergy.2019.02.041>
- [35] Chayan, N., Hasna, L., & Stéphane, L. (2018). A review of thermal management and innovative cooling strategies for data center. *Sustainable Computing: Informatics and Systems*, 19, 14-28. doi:<https://doi.org/10.1016/j.suscom.2018.05.002>
- [36] Wilson, T. (2006, August 24). How Liquid-cooled PCs Work. Retrieved October 16, 2020, from <https://computer.howstuffworks.com/liquid-cooled-pc.htm>
- [37] Watts, D. (2020). Lenovo ThinkSystem SD650 server (xeon SP gen 2) product guide. Retrieved from <https://lenovopress.com/lp1042-thinksystem-sd650-server-xeon-sp-gen-2>
- [38] Branscombe, M. (2018, August 13). 5 Reasons Data Center Liquid Cooling Is on the Rise. October 16, 2020, from <https://www.datacenterknowledge.com/power-and-cooling/five-reasons-data-center-liquid-cooling-rise>
- [39] Quattro. "TWO-PHASE FLOW COOLING SYSTEMS." IN QUATTRO – Two-Phase Cooling, 2020. <https://www.in-quattro.com/two-phase-flow-cooling-systems/>.

- [40] Y. Madhour, J. Olivier, E. Costa-Patry, S. Paredes, B. Michel and J. R. Thome, "Flow Boiling of R134a in a Multi-Microchannel Heat Sink With Hotspot Heaters for Energy-Efficient Microelectronic CPU Cooling Applications," in *IEEE Transactions on Components, Packaging and Manufacturing Technology*, vol. 1, no. 6, pp. 873-883, June 2011, doi: 10.1109/TCPMT.2011.2123895.
- [41] Marcinichen, J. B., & Thome, J. R. (2010). *Refrigerated cooling of microprocessors with micro-evaporation New novel two-phase cooling cycles: A green steady-state simulation code*. Lausanne, Switzerland: ABCM. Retrieved from <https://abcm.org.br/anais/encit/2010/PDF/ENC10-0164.pdf>
- [42] Boiling crisis - critical heat flux. Retrieved from <https://www.nuclear-power.net/nuclear-engineering/heat-transfer/boiling-and-condensation/boiling-crisis-critical-heat-flux/>
- [43] Mudawar, I. (December 8, 2011). "Two-Phase Microchannel Heat Sinks: Theory, Applications, and Limitations." ASME. *J. Electron. Package*. December 2011; 133(4): 041002. <https://doi.org/10.1115/1.4005300>
- [44] Gigabyte. (2020). Two-Phase Liquid Immersion Cooling for servers: Solution - GIGABYTE Global. Retrieved October 12, 2020, from <https://www.gigabyte.com/Solutions/Cooling/immersion-cooling>
- [45] 3M. "3M Novec 7100 Engineered Fluid." 3m.com, 2009.
- [46] Coles, H. and Herrlin, M. "Immersion Cooling of Electronics in DoD Installations." *Ernest Orlando Lawrence Berkeley National Laboratory*, 2016. <https://doi.org/10.2172/1375005>.
- [47] Judge, Peter. "The Data Center Life Story." [Datacenterdynamics.com](http://Datacenterdynamics.com), 2017.
- [48] Nuclear Power. "Nucleate Boiling." Nuclear Power, 2020. <https://www.nuclear-power.net/nuclear-engineering/heat-transfer/boiling-and-condensation/nucleate-boiling/>.
- [49] Honeywell International Inc. (2020). Genetron refrigerants modeling software download. Retrieved from <https://www.fluorineproducts-honeywell.com/refrigerants/genetron-refrigerants-modeling-software-download/>
- [50] Jeong, J., & Kang, Y. T. (2004). Analysis of a refrigeration cycle driven by refrigerant steam turbine. *International Journal of Refrigeration*, 27(1), 33-41. doi:[https://doi.org/10.1016/S0140-7007\(03\)00101-4](https://doi.org/10.1016/S0140-7007(03)00101-4)
- [51] Boles, M., & Cengel, Y. (2006). *Thermodynamics: An engineering approach* (5th ed.) Tata McGraw-Hill.

- [52] eFunda.Copper. Retrieved from [https://www.efunda.com/formulae/fluids/roughness.cfm?search\\_string=roughness](https://www.efunda.com/formulae/fluids/roughness.cfm?search_string=roughness)
- [53] Lakeside Supply Company. Copper tubes. Retrieved from <https://www.lakesidesupply.com/lakesidesupply/catalog/pdfs/mueller.pdf>
- [54] Sakr, M., & Gooda, E. (2018). Economical velocity through pipeline networks “Case Studies of Several Different Markets.” *Science Direct*, 1–4. <https://doi.org/10.1016/j.aej.2018.05.001>
- [55] Investigating the thermal conductivity of batt insulation using the thermtest heat flow meter. Retrieved from <https://thermtest.com/applications/wall-insulation-thermal-conductivity-hfm>
- [56] JOHNS MANVILLE - duct insulation, wrap, fiberglass. Retrieved from <https://www.grainger.com/product/6ZKK3?gucid=N:N:FPL:Free:GGL:CSM-1946:tew63h3:20501231>
- [57] MUELLER INDUSTRIES - 50 ft. soft coil copper tubing. Retrieved from <https://www.grainger.com/product/3P670?gucid=N:N:FPL:Free:GGL:CSM-1946:tew63h3:20501231>
- [58] Reventos, F. (2017). *Thermal-hydraulics of water cooled nuclear reactors*. Woodhead Publishing.
- [59] Modest, M. F. (2003). *Radiative heat transfer* (2nd ed.). Elsevier Inc.
- [60] Rapp, B. E. (2017). *Microfluids: Modeling, mechanics, and mathematics*. Elsevier Inc.
- [61] Taler, D., & Taler, J. (2017). *Simple heat transfer correlations for turbulent tube flow*. (). Cracow, Poland: Retrieved from [https://www.e3s-conferences.org/articles/e3sconf/pdf/2017/01/e3sconf\\_wtue2017\\_02008.pdf](https://www.e3s-conferences.org/articles/e3sconf/pdf/2017/01/e3sconf_wtue2017_02008.pdf)
- [62] Kosky, P., Balmer, R., Keat, W., & Wise, G. (2013). *Exploring engineering* (Third ed.). Elsevier Inc.
- [63] Bergman, T. L., & Incropera, F. P. (2011). *Fundamentals of heat and mass transfer 7e: Heat transfer*. Hoboken, NJ: Wiley Custom Learning Solutions.
- [64] Kandlikar, S., Garimella, S., Li, D., Colin, S., & King, M. (2006). *Heat Transfer and Fluid Flow in Minichannels and Microchannels*. Elsevier.
- [65] Frei, Walter. “Which Turbulence Model Should I Choose for My CFD Application?” COMSOL, 2017.
- [66] Lyu, Peter. “Simulating Turbulent Flow in COMSOL Multiphysics.” COMSOL, 2016.
- [67] Szczukiewicz, S., Magnini, M., & Thome, J. R. (2014). Proposed models, ongoing experiments, and latest numerical simulations of microchannel two-phase flow boiling. *International Journal of Multiphase Flow*, 59, 84-101. doi:<https://doi.org/10.1016/j.ijmultiphaseflow.2013.10.014>

- [68] Intel® xeon® gold 6328H processor (22M cache, 2.80 GHz). Retrieved from <https://www.intel.com/content/www/us/en/products/sku/204088/intel-xeon-gold-6328h-processor-22m-cache-2-80-ghz/specifications.html>
- [69] Intel® xeon® platinum 8380HL processor (38.5M cache, 2.90 GHz). Retrieved from <https://www.intel.com/content/www/us/en/products/sku/205684/intel-xeon-platinum-8380hl-processor-38-5m-cache-2-90-ghz/specifications.html>
- [70] Sumitomo Precision Products - Heat Exchanger Division. High-performance CPU cooler. Retrieved from <https://www.spp.co.jp/netsu/en/products/cpu/>
- [71] Federal Energy Management Program. Cooling water efficiency opportunities for federal data centers. Retrieved from <https://www.energy.gov/eere/femp/cooling-water-efficiency-opportunities-federal-data-centers>
- [72] Mihai, Ioan. (2011). Heat Transfer in Minichannels and Microchannels CPU Cooling Systems. 10.1117/12.823670.
- [73] Heat exchanger. Retrieved from <https://www.real-world-physics-problems.com/heat-exchanger.html>
- [74] Ezgi, C. (2017). Basic design methods of heat exchanger. In S. M. S. Murshed, & M. M. Lopes (Eds.), *Heat exchangers - design, experiment and simulation*. Istanbul, Turkey: InTech Open.
- [75] Coker, A. K. (1995). *Fortran programs for chemical process design, analysis, and simulation Elsevier Inc.*
- [76] Qiu, J., Zhang, H., Yu, X., Qi, Y., Lou, J., & Wang, X. (2015). Experimental investigation of flow boiling heat transfer and pressure drops characteristic of R1234ze(E), R600a, and a mixture of R1234ze(E)/R32 in a horizontal smooth tube. *Advances in Mechanical Engineering*. <https://doi.org/10.1177/1687814015606311>
- [77] Kedzierski, M. & Park, K. (2013), Horizontal Convective Boiling of R134a, R1234yf/R134a, and R1234ze(E) within a Micro-Fin Tube with Extensive Measurement and Analysis Details, Technical Note (NIST TN), National Institute of Standards and Technology, Gaithersburg, MD, [online], <https://doi.org/10.6028/NIST.TN.1807>
- [78] Li, H., & Hrnjak, P. (2019). Heat transfer COEFFICIENT, pressure drop, and flow patterns of R1234ze(E) evaporating IN Microchannel tube. *International Journal of Heat and Mass Transfer*, 138, 1368-1386. doi:10.1016/j.ijheatmasstransfer.2019.05.036

- [79] eFunda.Copper. Retrieved from [https://www.efunda.com/materials/elements/TC\\_Table.cfm?Element\\_ID=Cu](https://www.efunda.com/materials/elements/TC_Table.cfm?Element_ID=Cu)
- [80] How a chilled water system works. (2018). Retrieved from <https://hvactrainingshop.com/how-a-chilled-water-system-works/>
- [81] *Solstice® ze refrigerant (HFO-1234ze)*. (2015). Honeywell. Retrieved from <https://www.honeywell-refrigerants.com/india/?document=solstice-ze-hfo-1234ze-brochure-2012&download=1>
- [82] Zhang, Xinxin, Zhang, Yin, Cao, Min, Wang, Jing-Fu, Wu, Yuting, & Ma, Chongfang. (2019). Working Fluid Selection for Organic Rankine Cycle Using Single-Screw Expander. *Energies*. 12. 3197. 10.3390/en12163197.
- [83] Li, M., Guo, Q., Lv, J., & Li, D. (2018). Research on condensation heat transfer characteristics of R447A, R1234ze, R134a and r32 In MULTI-PORT Micro-channel tubes. *International Journal of Heat and Mass Transfer*, 118, 637-650. doi:10.1016/j.ijheatmasstransfer.2017.10.101
- [84] Admin. (2021, February 05). Server rack sizes: Understanding the differences. Retrieved April 02, 2021, from <https://www.racksolutions.com/news/blog/server-rack-sizes/>
- [85] Uxcell Product-Line. (n.d.). Retrieved April 04, 2021, from <http://www.uxcell.com/aquarium-way-inline-manifold-air-flow-pump-tubing-splitter-lever-control-valve-p-734709.htm>
- [86] Kenton, W. (2020). Equivalent annual cost – EAC definition. Retrieved from <https://www.investopedia.com/terms/e/eac.asp>
- [87] US long-term interest rates. Retrieved from [https://ycharts.com/indicators/us\\_longterm\\_interest\\_rates](https://ycharts.com/indicators/us_longterm_interest_rates)
- [88] Electric power monthly. Retrieved from [https://www.eia.gov/electricity/monthly/epm\\_table\\_grapher.php?t=epmt\\_5\\_6\\_a](https://www.eia.gov/electricity/monthly/epm_table_grapher.php?t=epmt_5_6_a)
- [89] Gas Technology. (2015). Organic rankine cycle. Retrieved from <https://www.plantengineering.com/articles/organic-rankine-cycle/>
- [90] Quoilin, S., Broek, M. V. D., Declaye, S., Dewallef, P., & Lemort, V. (2013). Techno-economic survey of organic rankine cycle (ORC) systems. *Renewable and Sustainable Energy Reviews*, 22, 168-186. doi:<https://doi.org/10.1016/j.rser.2013.01.028>
- [91] Euro to US dollar spot exchange rates for 2017. Retrieved from [https://www.exchangerates.org.uk/EUR-USD-spot-exchange-rates-history-2017.html#:~:text=This%20is%20the%20Euro%20\(EUR,USD%20on%2003%20Jan%202017.](https://www.exchangerates.org.uk/EUR-USD-spot-exchange-rates-history-2017.html#:~:text=This%20is%20the%20Euro%20(EUR,USD%20on%2003%20Jan%202017.)

- [92] Inflation calculator. Retrieved from <https://smartasset.com/investing/inflation-calculator#mTsbAiR4kT%27>
- [93] *Cooling enclosures 101*. (n.d.). Retrieved from [https://www.accu-tech.com/hs-fs/hub/54495/file-17645763-pdf/docs/cooling\\_enclosures\\_101\\_4-16-12.pdf](https://www.accu-tech.com/hs-fs/hub/54495/file-17645763-pdf/docs/cooling_enclosures_101_4-16-12.pdf)
- [94] 972 CFM intelligent variable speed fan panel (master) - front inside / rear outside mount. Retrieved from <https://www.server-rack-online.com/mrf-33-9a.html>
- [95] *Compound interest tables*. (n.d.). Retrieved from [https://global.oup.com/us/companion.websites/9780199778126/pdf/Appendix\\_C\\_CITables.pdf](https://global.oup.com/us/companion.websites/9780199778126/pdf/Appendix_C_CITables.pdf)
- [96] Mukhopadhyay, S. (2021). Discounted payback period. Retrieved from <https://www.wallstreetmojo.com/discounted-payback-period-formula/>
- [97] Bell, I. H., Wronski, J., Quoilin, S., & Lemort, V. (2014). Pure and Pseudo-pure Fluid Thermophysical Property Evaluation and the Open-Source Thermophysical Property Library CoolProp. *Industrial & Engineering Chemistry Research*, 53(6), 2498-2508. doi:10.1021/ie4033999

# Appendices

## Appendix A: MATLAB Code for Initial Thermodynamics Calculations

```
clear;
%% Values
Th = 81.5; %C, hot temperature
Tc = 40; %C, cold temperature
P4 = 2075; %kPa, high pressure
P3 = py.CoolProp.CoolProp.PropsSI('P','T',Tc+273.15,'Q',1,'R1234ze(E)')/1000; %kPa, low
pressure
Q_server = 10; %kW
S2 = py.CoolProp.CoolProp.PropsSI('S','T',Tc+273.15,'Q',1,'R1234ze(E)')/1000; %kJ/kg-K
h1 = py.CoolProp.CoolProp.PropsSI('H','S',S2*1000,'P',P4*1000,'R1234ze(E)')/1000; %kJ/kg
h_2s = py.CoolProp.CoolProp.PropsSI('H','Q',1,'T',Tc+273.15,'R1234ze(E)')/1000; %kJ/kg
h3 = py.CoolProp.CoolProp.PropsSI('H','Q',0,'T',Tc+273.15,'R1234ze(E)')/1000; %kJ/kg
v3 = 1/py.CoolProp.CoolProp.PropsSI('D','T',Tc+273.15,'Q',0,'R1234ze(E)'); % (m^3)/kg
eta_t = 0.8; %Turbine efficiency
eta_p = 0.85; %Pump efficiency
%% T4 and v4 Calculation
S3 = py.CoolProp.CoolProp.PropsSI('S','T',Tc+273.15,'Q',0,'R1234ze(E)')/1000; %kJ/kg-K
S4 = S3;
T4 = py.CoolProp.CoolProp.PropsSI('T','S',S4*1000,'P',P4*1000,'R1234ze(E)'); %K
v4 = 1/py.CoolProp.CoolProp.PropsSI('D','S',S4*1000,'P',P4*1000,'R1234ze(E)'); % (m^3)/kg
%% Equations
syms h2 h_4s h4 mdot_R Wdot_t Qdot_coolant eta_th h4 eta_carnot eta_2 Wdot_p
eqn1 = h2 - h1 + eta_t*(h1-h_2s) == 0; %Actual enthalpy at point 2
eqn2 = h_4s - h3 - v3*(P4-P3) == 0; %Specific enthalpy at point 4
eqn3 = h4 - h3 - (h_4s - h3)/eta_p == 0; %Actual enthalpy at point 4
eqn4 = Q_server - mdot_R*(h1-h4) == 0; %Mass flow rate of R134a
eqn5 = Wdot_t - mdot_R*(h1-h2) == 0; %Turbine power
eqn6 = Qdot_coolant - mdot_R*(h2-h3) == 0; %Heat transfer rate in condenser
eqn7 = eta_th - (Wdot_t - Wdot_p)/Q_server == 0; %Thermal efficiency
eqn8 = eta_carnot - (1 - (Tc+273.15)/(Th+273.15)) == 0; %Carnot Efficiency
eqn9 = eta_2 - eta_th/eta_carnot == 0; %Second Law Efficiency
eqn10 = Wdot_p - mdot_R*(h4 - h3) == 0; %Pump power
sol = solve([eqn1, eqn2, eqn3, eqn4, eqn5, eqn6, eqn7, eqn8, eqn9, eqn10], [mdot_R, Wdot_t,
Qdot_coolant, eta_th, h4, eta_carnot, h2, h_4s, eta_2, Wdot_p]);
h2Sol = sol.h2;
h_4sSol = sol.h_4s;
h4Sol = sol.h4;
mdot_RSol = sol.mdot_R;
Wdot_tSol = sol.Wdot_t;
Qdot_coolantSol = sol.Qdot_coolant;
eta_thSol = sol.eta_th;
eta_carnotSol = sol.eta_carnot;
eta_2Sol = sol.eta_2;
Wdot_pSol = sol.Wdot_p;
%% Tabulate Results
h2 = double(vpa(h2Sol,6));
h_4s = double(vpa(h_4sSol,6));
h4 = double(vpa(h4Sol,6));
mdot_R = double(vpa(mdot_RSol,6));
Wdot_t = double(vpa(Wdot_tSol,6));
Wdot_p = double(vpa(Wdot_pSol,6));
Qdot_coolant = double(vpa(Qdot_coolantSol,6));
eta_th = double(vpa(eta_thSol,6)); %Thermal efficiency
eta_carnot = double(vpa(eta_carnotSol,6)); %Carnot efficiency
eta_2 = double(vpa(eta_2Sol,6)); %Second law efficiency
Results =
table(h2,h_4s,h4,mdot_R,Wdot_t,Wdot_p,Qdot_coolant,eta_th,eta_carnot,eta_2,P3,S2,h1,h_2s,h3,
v3,S3,S4,T4,v4)
```

[97]

## Appendix B: Thermodynamic Analysis Results from MATLAB Code

$$P3 = 766.35 \text{ kPa}$$

$$S2 = 1.6805 \text{ kJ/kg-K}$$

$$h1 = 427.72 \text{ kJ/kg}$$

$$h_{2s} = 409.81 \text{ kJ/kg}$$

$$h3 = 255.00 \text{ kJ/kg}$$

$$v3 = 0.00089966 \text{ (m}^3\text{)/kg}$$

$$S3 = 1.1861 \text{ kJ/kg-K}$$

$$S4 = 1.1861 \text{ kJ/kg-K}$$

$$T4 = 314.00 \text{ K}$$

$$v4 = 0.00089498 \text{ (m}^3\text{)/kg}$$

$$h2 = 413.39 \text{ kJ/kg}$$

$$h_{4s} = 256.18 \text{ kJ/kg}$$

$$h4 = 256.39 \text{ kJ/kg}$$

$$\dot{m}_R = 0.058367 \text{ kg/s}$$

$$\dot{W}_t = 0.8362 \text{ kW}$$

$$\dot{W}_p = 0.080844 \text{ kW}$$

$$\dot{Q}_{\text{coolant}} = 9.2446 \text{ kW}$$

$$\eta_{th} = 0.075535$$

$$\eta_{carnot} = 0.11702$$

$$\eta_2 = 0.64551$$

## Appendix C: Fluid Mechanics of Each ORC Connecting Pipe

**Table C.1:** Fluid mechanics calculation results for State 1 (saturated vapor) ORC connecting pipe.

Inner Diameter (m)	Velocity (m/s)	Reynolds Number	Friction Factor	Pressure Drop (kPa)	Power (W)
0.008	9.881	599700	0.015	10931.63	5.09137
0.010	5.688	454996	0.015	3179.53	1.48086
0.013	3.310	347075	0.015	970.89	0.45219
0.017	2.162	280534	0.015	387.59	0.18052
0.019	1.656	245515	0.016	219.22	0.10210
0.025	0.928	183828	0.016	64.41	0.03000
0.032	0.593	146914	0.017	25.18	0.01173
0.038	0.419	123503	0.017	12.22	0.00569
0.050	0.240	93368	0.018	3.84	0.00179
0.062	0.155	75116	0.019	1.57	0.00073
0.074	0.109	62920	0.020	0.76	0.00035

**Table C.2:** Fluid mechanics calculation results for State 2 (saturated vapor) ORC connecting pipe.

Inner Diameter (m)	Velocity (m/s)	Reynolds Number	Friction Factor	Pressure Drop (kPa)	Power (W)
0.008	30.486	742320	0.015	33478.81	48.10932
0.010	17.549	563203	0.015	9724.39	13.97402
0.013	10.211	429616	0.015	2967.21	4.26390
0.017	6.671	347251	0.015	1184.40	1.70199
0.019	5.110	303903	0.015	669.98	0.96276
0.025	2.865	227545	0.016	196.98	0.28306
0.032	1.830	181853	0.016	77.04	0.11071
0.038	1.293	152875	0.017	37.41	0.05376
0.050	0.739	115573	0.017	11.76	0.01691
0.062	0.478	92980	0.018	4.81	0.00691
0.074	0.336	77884	0.019	2.33	0.00334

**Table C.3:** Fluid mechanics calculation results for State 3 (saturated liquid) ORC connecting pipe.

<b>Inner Diameter (m)</b>	<b>Velocity (m/s)</b>	<b>Reynolds Number</b>	<b>Friction Factor</b>	<b>Pressure Drop (kPa)</b>	<b>Power (W)</b>
0.008	1.115	57474	0.021	1465.32	0.07699
0.010	0.642	43606	0.022	428.86	0.02253
0.013	0.373	33263	0.023	130.58	0.00686
0.017	0.244	26886	0.024	51.77	0.00272
0.019	0.187	23530	0.025	29.11	0.00153
0.025	0.105	17618	0.027	8.43	0.00044
0.032	0.067	14080	0.028	3.25	0.00017
0.038	0.047	11836	0.030	1.56	0.00008
0.050	0.027	8948	0.032	0.48	0.00003
0.062	0.017	7199	0.034	0.20	0.00001
0.074	0.012	6030	0.036	0.09	0.00000

**Table C.4:** Fluid mechanics calculation results for State 4 (subcooled liquid) ORC connecting pipe.

<b>Inner Diameter (m)</b>	<b>Velocity (m/s)</b>	<b>Reynolds Number</b>	<b>Friction Factor</b>	<b>Pressure Drop (kPa)</b>	<b>Power (W)</b>
0.008	1.109	60041	0.021	1450.47	0.07581
0.010	0.638	45554	0.022	424.55	0.02219
0.013	0.371	34749	0.023	129.30	0.00676
0.017	0.243	28087	0.024	51.27	0.00268
0.019	0.186	24581	0.025	28.84	0.00151
0.025	0.104	18405	0.026	8.35	0.00044
0.032	0.067	14709	0.028	3.23	0.00017
0.038	0.047	12365	0.029	1.55	0.00008
0.050	0.027	9348	0.031	0.48	0.00003
0.062	0.017	7521	0.033	0.19	0.00001
0.074	0.012	6299	0.035	0.09	0.00000

## Appendix D: Pre-Simulation Report (single-phase laminar flow through a single microchannel)

Before modeling the heat sink, it was important to have a theoretical understanding of the heat transfer and fluid mechanics of the component. The small scale dimensions of microchannels could not be described using basic heat transfer principles. Instead, the governing equations discussed in Kandlikar et al. were utilized to describe the heat sink. As shown in **Figure D.1**, the fluid is in contact with the heat sink on four sides: the bottom, two sides, and the top. The fluid absorbs heat from the heat sink from all four sides of the channel.

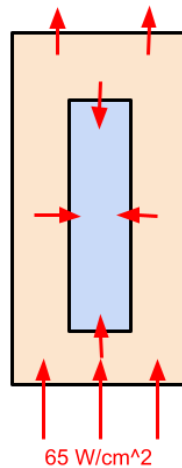


**Figure D.1:** Heat Flux in a Cross-section of the MCHS.

It is important to note that optimal heat transfer from the CPU to the heat sink is achieved with a fluid undergoing turbulent conditions [64]. However, the equations that describe turbulent conditions inside microchannels are difficult to compute by hand. Since the pre-simulation calculations are the first steps towards a theoretical understanding, laminar conditions from Kandlikar et al. will be used for our preliminary design. Future iterations will be simulated using COMSOL where turbulent conditions are used to ensure optimal heat transfer.

The dimensions of the heat sink are chosen based on the geometry of an average CPU. The calculations are done with an assumption that the CPU of the heat sink is  $1.58\text{cm} \times 1.58\text{cm}$  (an area of  $2.5\text{cm}^2$ ), and uniformly dissipates  $162.5\text{W}$  to the heat sink. The CPU is also assumed to have a surface temperature of  $85^\circ\text{C}$ . With these considerations, the design of the heat sink will have the same area as the CPU.

The next consideration is the microchannels themselves. Using Kandlikar et al. as a reference, and iterating for optimal laminar conditions, the following dimensions are chosen:

$a = 30\mu\text{m}$ ,  $b = 3500\mu\text{m}$ ,  $s = 30\mu\text{m}$ , where  $a$  is the width of each microchannel,  $b$  is the height of the

microchannel, and  $s$  is the spacing between each microchannel. **Figure D.2** shows the configuration of the microchannel heat sink.

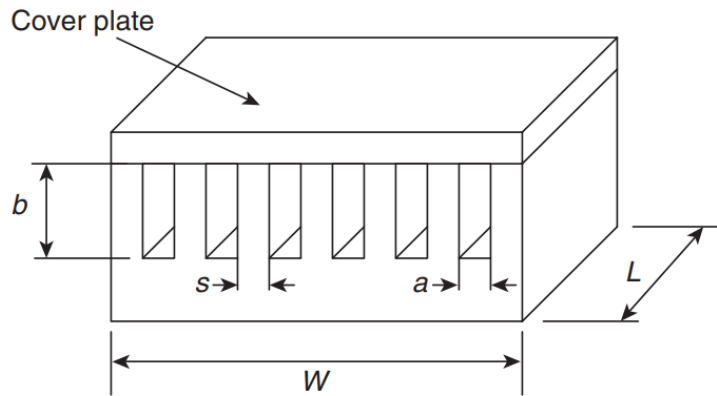


**Figure D.2:** Microchannel Dimensions [64].

With the microchannel dimensions known, the remaining width for  $n$  number of channels can be calculated. First, the width remaining for the channels is as follows:

$$\varpi = w - a = 15.8\text{mm} - 30\mu\text{m} = 0.01577\text{m}$$

And the pitch for the component is:

$$\rho = a + s = 30\mu\text{m} + 30\mu\text{m} = 60\mu\text{m} = 6.0 * 10^{-6}\text{m}$$

So, the number of channels can be obtained:

$$n = \frac{(\varpi - a)}{\rho} = \frac{(0.01577\text{m} - 30 * 10^{-6}\text{m})}{60 * 10^{-6}\text{m}} = 262 \text{ channels}$$

Adding the final channel not included at the edge of the component yields a total of 263 channels for the heat sink. **Figure D.3** shows a scaled model of the microchannel heat sink.

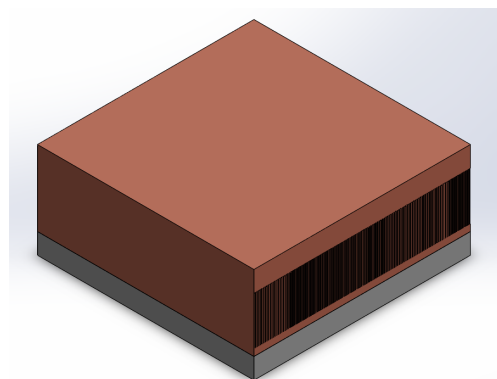


**Figure D.3:** Solidworks model of microchannel heat sink.

After calculating the optimal number of microchannels, the next detail to determine is the fluid mass flow rate. The boundary conditions for this design consist of an inlet temperature  $T_{in}=75^{\circ}\text{C}$  and an outlet temperature  $T_{out}=82^{\circ}\text{C}$  for the microchannels. The assumption that the CPU dissipates a uniform 162.5W is also made to simplify the calculation. Since the project is focusing on the behavior of

R-1234-ze as a working fluid, the fluid properties can be obtained using Honeywell's software detailing fluid properties:  $C_p \approx 1.765 \frac{kJ}{kg \cdot K}$  (obtained using the average temperature between  $T_{in}$  &  $T_{out}$ )

Then, it can be said that:

$$m_{dot} = \frac{q_{CPU}}{C_p \Delta T} = \frac{0.1625 kW}{(1.765 \frac{kJ}{kg \cdot K})(7^\circ K)} = 0.013 \frac{kg}{s}$$

Furthermore, the mass flow rate of each channel can be calculated by dividing  $m_{dot}$  with n-channels:

$$m_{dot(per\ channel)} = \frac{q_{CPU}}{nC_p \Delta T} = \frac{0.1625 kW}{263(1.765 \frac{kJ}{kg \cdot K})(7^\circ K)} = 5.0 * 10^{-5} \frac{kg}{s}$$

To continue investigating the fluid behavior, the Reynolds number of the fluid is required. Similar to Kandlikar et al., the definition of Reynolds number that will be used is

$$Re = \frac{m_{dot(per\ channel)} * D_h}{A_c * \mu}$$

Where  $D_h$  is the hydraulic diameter,  $A_c$  is the the cross sectional area of the microchannel, and  $\mu$  is the dynamic viscosity of R-1234-ze.

$$D_h = \frac{2ab}{(a+b)} = \frac{2(30\mu m)(3500\mu m)}{3530\mu m} = 59.5\mu m = 59.5 * 10^{-6} m$$

$$A_c = a * b = 30\mu m * 3500\mu m = 105,000\mu m^2 = 105 * 10^{-9} m^2$$

$$Viscosity\ (Dynamic) = \mu \approx 101.14 * 10^{-6} Pa * s$$

$$Re = \frac{m_{dot(per\ channel)} * D_h}{A_c * \mu} = \frac{(5.0 * 10^{-5} \frac{kg}{s})(59.5 * 10^{-6} m)}{(105 * 10^{-9} m^2)(101.14 * 10^{-6} Pa * s)} \approx 280 < laminar >$$

With the Reynolds number known, the thermal performance of the heat sink can be investigated by determining whether or not a fully developed flow assumption is valid.  $L_h$  is the hydrodynamic entrance length, and  $L_t$  is the thermal entrance length.

$$L_h = 0.05 Re D_h = 0.05(280)(59.5 * 10^{-6} m) = 0.00083 m \approx 0.83 mm$$

$$L_t = 0.1 Re P_r D_h = 0.1(280)(8.235)(59.5 * 10^{-6} m) = .0137 m \approx 13.7 mm$$

Note that in order for a fully developed flow assumption to be valid,  $(L_t - L_h) < (L=15.8mm)$ . The current configuration fulfills this requirement with  $12.87mm < 15.8mm$ , but it is important to realize that the microchannels are not thermally developed until the fluid is through 86% of the microchannel length. This is a design constraint that should be re-visited in the future in order to ensure a thermally developed flow closer to the entrance of the microchannel. Failure to do so would result in poor heat transfer from the CPU to the working fluid.

With the fully developed flow validated, and the fluid flow is laminar, the Nusselt relationships in Kandlikar et al. can be used to calculate the average heat transfer coefficient  $\bar{h}$ . Table 3.3 [64] in **Figure D.4** provides the Nusselt number given the ratio between the microchannel width and height,  $\alpha$ .

**Table 3.3**  
Fully developed laminar flow Nusselt numbers.

$\alpha_c = a/b$	$Nu_{fd,3}$	$Nu_{fd,4}$
0	<b>8.235</b>	8.235
0.10	6.939	6.700
0.20	6.072	5.704
0.30	5.393	4.969
0.40	4.885	4.457
0.50	4.505	4.111
0.70	3.991	3.740
1.00	3.556	3.599
1.43	3.195	3.740
2.00	3.146	4.111
2.50	3.169	4.457
3.33	3.306	4.969
5.00	3.636	5.704
10.00	4.252	6.700
>10.00	5.385	8.235

$a$  – unheated side in three-side heated case.

For intermediate values, use the curve-fit equations provided in Appendix A at the end of the chapter.

**Figure D.4:** Table 3.3 detailing Nusselt relationship between  $a$  &  $b$  [64].

$$\alpha = \frac{a}{b} = \frac{30\mu m}{3500\mu m} = 0.0086 \approx 0$$

Although  $N_u=8.235$  can be used, an interpolation of Table 3.3 will yield a more accurate Nusselt number.

$$y = y_1 + (x - x_1) \frac{(y_2 - y_1)}{(x_2 - x_1)}$$

$$N_u = 8.235 + (.0086 - 0) \frac{(6.939 - 8.235)}{(1 - 0)} = 8.124$$

Finally, using the software from Honeywell, the thermal conductivity of R-1234-ze can be determined using the average temperature of  $T_{in}$  and  $T_{out}$  - allowing the average heat transfer coefficient to be calculated:

$$k_{R-1234-ze} \approx 57.169 \frac{mW}{mk} = 5.7169 * 10^{-2} \frac{W}{mk}$$

$$\bar{h} = \frac{k N_u}{D_h} = \frac{(5.7169 * 10^{-2} \frac{W}{mk})(8.124)}{(59.5 * 10^{-6} m)} = 7805.7 \frac{W}{k}$$

The temperatures at the base of each fin at the inlet and outlet can be calculated from the heat flux over the surface of the chip. Assuming an adiabatic tip condition (negligible heat transfer at the tip of the fin), the fin efficiency equation is defined as:

$$\eta_f = \tanh(mb)/mb$$

For fins with a width ( $s = 30\mu m$ ) much smaller than its length ( $L = 15.8 * 10^3 \mu m$ ):

$$mb = \left(\frac{2\bar{h}}{k * s}\right)^{1/2} b$$

Using the thermal conductivity of copper,  $k = 385 \text{ W/m-K}$  :

$$mb = \left(\frac{2\bar{h}}{k\bar{s}}\right)^{1/2} b = \left(\frac{2 \cdot 7805.7 \frac{\text{W}}{\text{m}^2\text{K}}}{385 \text{ W/m-K} \cdot 30 \cdot 10^{-6} \text{ m}}\right)^{1/2} * 3500 * 10^{-6} \text{ m} = 4.07$$

The fin efficiency can now be calculated:

$$\eta_f = \tanh(mb)/mb = \frac{e^{2mb}-1}{e^{2mb}+1}/mb = \frac{e^{2 \cdot 4.07}-1}{e^{2 \cdot 4.07}+1}/4.07 = 0.246$$

Assuming the heat flux is constant over the surface of the chip, the surface heat flux considering fin efficiency is defined as:

$$q'' = q/(2b\eta_f + a)nL$$

$$q'' = 162.5 \text{ W}/[2(3500 * 10^{-6} \text{ m})(0.246) + 30 * 10^{-6} \text{ m}](263)(0.0158 \text{ m})$$

$$q'' = 22.32 * 10^3 \text{ W/m}^2$$

To calculate the surface temperatures at the base of the fins, the local heat transfer coefficients at the inlet and outlet of the microchannels are needed, and thus the Nusselt numbers at the inlet and outlet are also needed. The Nusselt number at the entrance for the three-side heating configuration, is given by the following equation if  $0.1 < \alpha_c < 10$  :

$$Nu_{x,3}(x^*, \alpha_c) = Nu_{x,4}(x^*, \alpha_c) \frac{Nu_{fd,3}(x^*=x^*_{fd}, \alpha_c)}{Nu_{fd,4}(x^*=x^*_{fd}, \alpha_c)}$$

If,  $\alpha_c \leq 0.1$  and  $\alpha_c \geq 10$ , the four-side heating table is used without any modification. Since  $\alpha_c = 0.0086 < 0.1$ , we use the four-side heating table from Table 3.3 without any modification. Using linear interpolation with Table 3.3:

$$Nu_{fd,4}(\alpha_c = 0.0086) = 8.235 + (0.0086 - 0) \frac{(6.700-8.235)}{(0.1-0)} = 8.103$$

Using the liquid thermal conductivity of R1234ze at the inlet temperature of  $75^\circ\text{C}$  as  $58.217 * 10^{-3} \text{ W/m-K}$ , obtained from Honeywell, the local heat transfer coefficient at the inlet:

$$h = \frac{k \cdot Nu}{D_h} = \frac{(58.217 * 10^{-3} \frac{\text{W}}{\text{mK}})(8.103)}{(59.5 * 10^{-6} \text{ m})} = 7928 \text{ W/m}^2 - \text{K}$$

Since the flow is fully developed at the outlet, the three-sided Nusselt number is used. Using linear interpolation with Table 3.3:

$$Nu_{fd,3}(\alpha_c = 0.0086) = 8.235 + (0.0086 - 0) \frac{(6.939-8.235)}{(0.1-0)} = 8.124$$

Using the liquid thermal conductivity of R1234ze at the outlet temperature of  $82^\circ\text{C}$  as  $56.13 * 10^{-3} \text{ W/m-K}$ , obtained from Honeywell, the local heat transfer coefficient at the outlet:

$$h = \frac{k \cdot Nu}{D_h} = \frac{(56.13 * 10^{-3} \frac{\text{W}}{\text{mK}})(8.124)}{(59.5 * 10^{-6} \text{ m})} = 7,664 \text{ W/m}^2 - \text{K}$$

The relationship between heat flux, heat transfer, and temperature difference is defined by:

$$q'' = h(T_s - T_f)$$

Subscripts  $s$  and  $f$  refer to the surface and fluid, respectively. The surface temperatures at the base of the fin at the fluid inlet and outlet:

$$T_s = \frac{q''}{h} + T_f$$

$$T_{s,i} = \frac{22.32 \cdot 10^3 \text{ W/m}^2}{7928 \text{ W/m}^2\text{-K}} + 75^\circ\text{C} = 77.8^\circ\text{C}$$

$$T_{s,o} = \frac{22.32 \cdot 10^3 \text{ W/m}^2}{7664 \text{ W/m}^2\text{-K}} + 82^\circ\text{C} = 84.9^\circ\text{C}$$

To calculate the pressure drop in the microchannel core, it is assumed that the pressure drop is impacted by frictional losses in the fully developed region and loss due to the developing region. The microchannel core is the section of the heat sink containing just the microchannels. The pressure drop is defined by the following equation:

$$\Delta p = \frac{2(f*Re)\mu*u_m*L}{D_h^2} + K(\infty)\frac{\rho u_m^2}{2}$$

The Hagenbach factor,  $K(\infty)$ , for rectangular channels is a function of the channel aspect ratio,  $\alpha_c$ :

$$K(\infty) = 0.6796 + 1.2197\alpha_c + 3.3089\alpha_c^2 - 9.5921\alpha_c^3 + 8.9089\alpha_c^4 - 2.9959\alpha_c^5$$

$$K(\infty) = 0.6796 + 1.2197(0.0086) + 3.3089(0.0086)^2 - 9.5921(0.0086)^3 + \dots$$

$$\dots + 8.9089(0.0086)^4 - 2.9959(0.0086)^5$$

$$K(\infty) = 0.6903$$

The  $f * Re$  term for rectangular channels is also a function of the channel aspect ratio,  $\alpha_c$ , and is defined as:

$$f * Re = 24(1 - 1.3553\alpha_c + 1.9467\alpha_c^2 - 1.7012\alpha_c^3 + 0.9564\alpha_c^4 - 0.2537\alpha_c^5)$$

$$f * Re = 24(1 - 1.3553(0.0086) + 1.9467(0.0086)^2 - 1.7012(0.0086)^3 + \dots$$

$$\dots + 0.9564(0.0086)^4 - 0.2537(0.0086)^5)$$

$$f * Re = 23.72$$

The mean flow velocity,  $u_m$ , can be calculated from the mass flow rate through a channel, the cross-section area of a channel, and the density of R1234ze at  $78.5^\circ\text{C}$ :

$$u_m = \frac{\dot{m}}{\rho * A_c} = \frac{5.0 \cdot 10^{-5} \frac{\text{kg}}{\text{s}}}{(941.3 \text{ kg/m}^3)(105 \cdot 10^{-9} \text{ m}^2)} = 0.507 \text{ m/s}$$

The pressure drop in the core of the microchannel:

$$\Delta p = \frac{2(23.72)(101.14 \cdot 10^{-6} \text{ Pa*s})(0.507 \text{ m/s})(15.8 \cdot 10^{-3} \text{ m})}{59.5 \cdot 10^{-6} \text{ m}^2} + (0.6903) \frac{(941.3 \text{ kg/m}^3)(0.507 \text{ m/s})^2}{2}$$

$$\Delta p = 10940 \text{ Pa} = 10.94 \text{ kPa}$$

The total pressure drop between the inlet and outlet manifolds is the pressure drop in the microchannel core plus minor losses at the inlet and outlet.  $K_c$  and  $K_e$  are the contraction and expansion loss coefficients, respectively. It is assumed that the areas of the reservoirs at the entrance and exits of the microchannels are much larger than the areas of the microchannels. From **Figure D.5**, since the area ratio is assumed to be 0,  $K_c = 0.8$  and  $K_e = 1.0$ .

$$\Delta p = \frac{2(f*Re)\mu*u_m*L}{D_h^2} + K(\infty)\frac{\rho u_m^2}{2} + K_c \frac{\rho u_m^2}{2} + K_e \frac{\rho u_m^2}{2}$$

$$\Delta p = \frac{2(23.72)(101.14*10^{-6} Pa*s)(0.507 m/s)(15.8*10^{-3} m)}{59.5*10^{-6} m^2} + (0.6903) \frac{(941.3 kg/m^3)(0.507 m/s)^2}{2} \dots$$

$$+ (0.8) \frac{(941.3 kg/m^3)(0.507 m/s)^2}{2} + (1.0) \frac{(941.3 kg/m^3)(0.507 m/s)^2}{2}$$

$$\Delta p = 11,158 Pa = 11.158 kPa$$

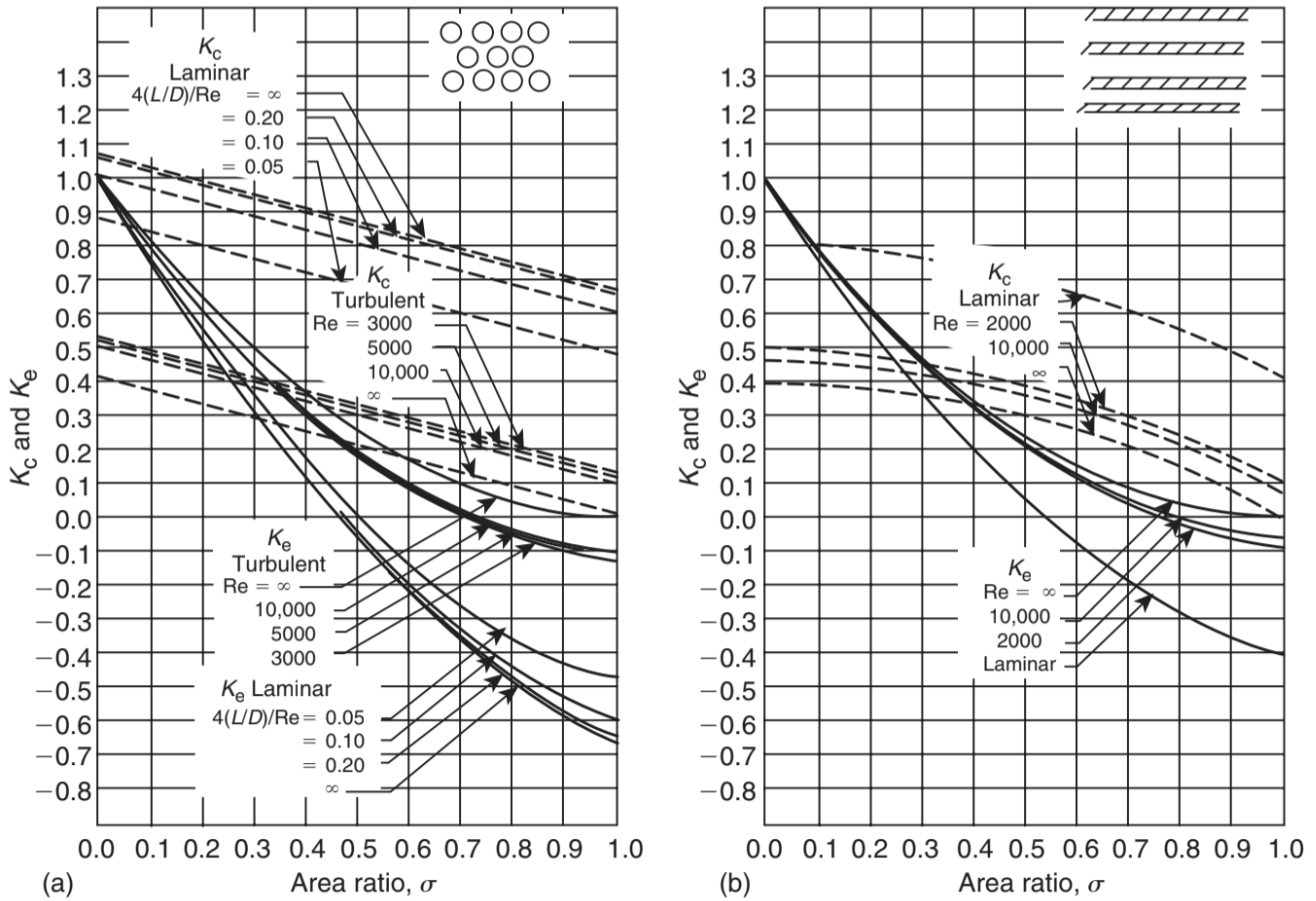


**Figure D.5:** Contraction and expansion loss coefficients for flow between inlet and outlet manifolds and the microchannels [64].

### Summary of Expected Results

The most important results from the pre-simulation calculations include the geometry of the heat sink, fluid flow rate, the heat transfer coefficient of the fluid, and the pressure drop. It was necessary to determine the width, height, and spacing of the microchannels to create a geometry for COMSOL simulations. The pressure drop is important because it will determine the size of the pump that is necessary for the server heat extraction loop.

## Appendix E: Example 5.2 from Kandlikar et al.

### Example 5.2

Microchannels are directly etched into the silicon chips to dissipate a heat flux of  $13,000 \text{ W/m}^2$  from a computer chip. The geometry may be assumed similar to Fig. 3.19. Each of the parallel microchannels has a width  $a = 200 \mu\text{m}$ , height  $b = 200 \mu\text{m}$ , and length  $L = 10 \text{ mm}$ . Refrigerant-123 flows through the horizontal microchannels at an inlet temperature of  $T_{B,i} = 293.15 \text{ K}$ . The heated perimeter  $P = b + a + b = 600 \times 10^{-6} \text{ m}$ , and the cross-sectional area  $A_c = a \times b = 40 \times 10^{-9} \text{ m}^2$ . Assume  $\theta_r$  from Fig. 5.1 is  $20^\circ$ , and  $\text{Re} = 100$ .

### Solution

Properties of R-123 at  $T_{\text{Sat}} = 300.9 \text{ K}$  and 1 atm:  $\mu_L = 404.2 \times 10^{-6} \text{ N-s/m}^2$ ,  $\mu_V = 10.8 \times 10^{-6} \text{ N-s/m}^2$ ,  $\rho_L = 1456.6 \text{ kg/m}^3$ ,  $\rho_V = 6.5 \text{ kg/m}^3$ ,  $c_{p,L} = 1023 \text{ J/kg K}$ ,  $k_L = 75.6 \times 10^{-3} \text{ W/m K}$ ,  $k_V = 9.35 \times 10^{-3} \text{ W/m K}$ ,  $\sigma_L = 14.8 \times 10^{-3} \text{ N/m}$ ,  $h_{LV} = 170.19 \times 10^3 \text{ J/kg}$ ,  $i_L = 228 \times 10^3 \text{ J/kg}$ ,  $i_V = 398 \times 10^3 \text{ J/kg}$ .

**(i) Calculate the incipient boiling location and cavity radius (Answers:  $z = 0.584 \times 10^{-3} \text{ m}$ , and  $r_{c,\text{crit}} = 2.23 \times 10^{-6} \text{ m}$ )**

From Eq. (5.18):

$$\begin{aligned}\Delta T_{\text{Sat,ONB}} &= \sqrt{8.8\sigma T_{\text{Sat}} q'' / (\rho_V h_{LV} k_L)} \\ &= \sqrt{8.8(14.8 \times 10^{-3})(300.9)(13,000) / (6.5)(170.19 \times 10^3)(75.6 \times 10^{-3})} \\ &= 2.47 \text{ K}\end{aligned}$$

Calculate the hydraulic diameter:

$$D_h = \frac{4A_c}{P_w} = a = b = 200 \times 10^{-6} \text{ m}$$

From Table 3.3,  $Nu_{fd,3} = 3.556$ , and note that:

$$h = \frac{Nu k_L}{D_h} = \frac{(3.556)(0.0756)}{(200 \times 10^{-6})} = 1344 \text{ W/m}^2 \text{ K}$$

From Eq. (5.19):

$$\Delta T_{\text{Sub,ONB}} = \frac{q''}{h} - \Delta T_{\text{Sat,ONB}} = \frac{13,000}{1344} - 2.47 = 7.2 \text{ K}$$

From Eq. (5.8),  $T_B$  at the onset of nucleate boiling is:

$$T_{B,ONB} = T_{\text{Sat}} - \Delta T_{\text{Sub,ONB}} = 300.9 - 7.2 = 293.7 \text{ K}$$

Calculate the flow velocity using the Reynolds number:

$$V = \frac{Re \mu_L}{\rho D_h} = \frac{(100)(404.2 \times 10^{-6})}{(1456.6)(200 \times 10^{-6})} = 0.139 \text{ m/s}$$

Calculate the mass flow rate:

$$\dot{m} = \rho V A_c = (1456.6)(0.139)(40 \times 10^{-9}) = 8.09 \times 10^{-6} \text{ kg/s}$$

Calculate the mass flux:

$$G = \frac{\dot{m}}{A_c} = \frac{8.09 \times 10^{-6}}{40 \times 10^{-9}} = 202 \text{ kg/m}^2 \text{ s}$$

The incipient boiling location can be calculated by rearranging Eq. (5.1):

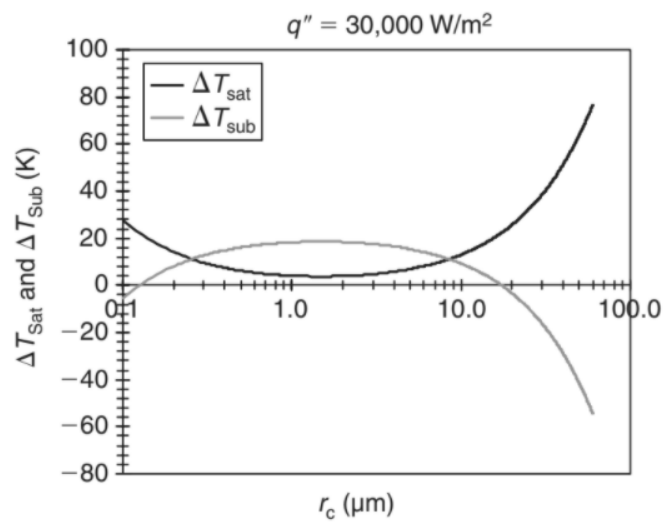
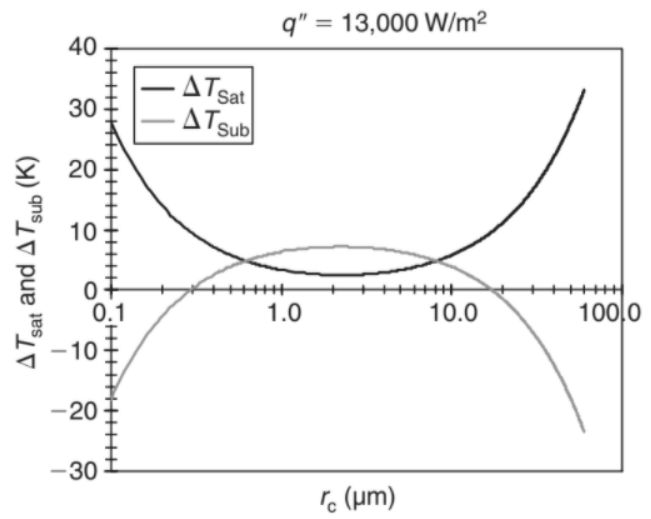
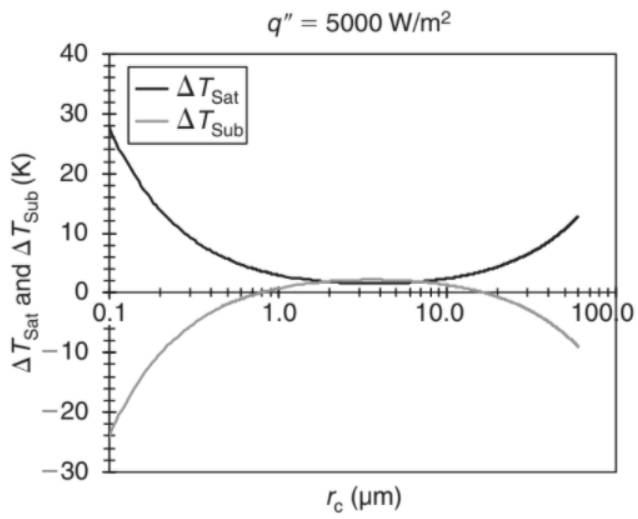
$$\begin{aligned} z &= (T_{B,ONB} - T_{B,i}) \left( \frac{\dot{m} c_{p,L}}{q'' P} \right) \\ &= (293.7 - 293.15) \left( \frac{(8.09 \times 10^{-6})(1023)}{(13,000)(600 \times 10^{-6})} \right) \\ &= 0.584 \times 10^{-3} \text{ m} \end{aligned}$$

To find the cavity radius, substitute Eqs. (5.3) and (5.19) into Eq. (5.17) we get

$$r_{c,crit} = \frac{k_L \sin \theta_r \Delta T_{\text{Sat,ONB}}}{2.2 q''} = \frac{(75.6 \times 10^{-3})(\sin 20^\circ)(2.47)}{2.2(13,000)} = 2.23 \times 10^{-6} \text{ m}$$

**(ii) Plot the wall superheat and liquid subcooling versus nucleating cavity radius for  $q'' = 5, 13, \text{ and } 30 \text{ kW/m}^2$ .**

Equations (5.19) and (5.20) are used to plot the following figures.



**(iii) Calculate the pressure drop in the test section (Answer: 426 Pa)**

For fully developed laminar flow, the hydrodynamic entry length may be obtained using Eq. (3.11):

$$L_h = 0.05\text{Re}D_h = 0.05(100)(0.200) = 1.0 \text{ mm}$$

Since  $L > L_h$ , the fully developed flow assumption is valid.

From Eq. (5.1):

$$\begin{aligned} z &= (T_{B,z} - T_{B,i}) \left( \frac{\dot{m}c_{p,L}}{q''P} \right) = (300.97 - 293.15) \left( \frac{(8.09 \times 10^{-6})(1023)}{(13,000)(600 \times 10^{-6})} \right) \\ &= 8.29 \times 10^{-3} \text{ m} \end{aligned}$$

Note that  $z$  is the location where two-phase boiling begins. So, we need to find the single-phase pressure drop until  $z$  and then add to that the value of the two-phase pressure drop from  $z$  to  $L$ .

The total pressure drop can be found using Eq. (5.28):

$$\Delta p = \Delta p_c + \Delta p_{f,1\text{-ph}} + \Delta p_{f,tp} + \Delta p_a + \Delta p_g + \Delta p_e$$

To find the single-phase pressure drop, the  $f$  Re term can be obtained using Eq. (3.10) and using an aspect ratio of one:

$$\alpha_c = a/b = 200/200 = 1$$

$$\begin{aligned} f \text{ Re} &= 24(1 - 1.3553\alpha_c + 1.9467\alpha_c^2 - 1.7012\alpha_c^3 + 0.9564\alpha_c^4 - 0.2537\alpha_c^5) \\ &= 24(1 - 1.3553 \times 1 + 1.9467 \times 1^2 - 1.7012 \times 1^3 + 0.9564 \times 1^4 \\ &\quad - 0.2537 \times 1^5) = 14.23 \end{aligned}$$

The single-phase core frictional pressure drop can be calculated using Eq. (3.14):

$$\Delta p_{f,1\text{-ph}} = \frac{2(f \text{ Re})\mu_L U_m z}{D_h^2} + K(\infty) \cdot \frac{\rho_L U_m^2}{2} \quad \text{where } K(\infty) \text{ is given by Eq. (3.18)}$$

$$\begin{aligned} K(\infty) &= (0.6796 + 1.2197\alpha_c + 3.3089\alpha_c^2 - 9.5921\alpha_c^3 \\ &\quad + 8.9089\alpha_c^4 - 2.9959\alpha_c^5) \\ &= 1.53 \end{aligned}$$

From Eq. (9.1-12):

$$i_{TP} = i_{IN} + \frac{q'' A_{h,tp}}{GA_c} = 228 \times 10^3 + \frac{(13,000)(1.026 \times 10^{-6})}{(8.09 \times 10^{-6})} = 229.6 \times 10^3 \text{ J/kg}$$

From Eq. (9.1-14):

$$x_e = \frac{i_{TP} - i_L}{h_{LV}} = \frac{(229.6 \times 10^3 - 228 \times 10^3)}{(170.19 \times 10^3)} = 0.0094$$

$$\begin{aligned} \Delta p_{f,1-ph} &= \frac{2(14.23)(0.404 \times 10^{-3})(0.139)(0.00829)}{(200 \times 10^{-6})^2} \\ &\quad + (1.53) \frac{(1456.6)(0.139)^2}{2} \\ &= 353 \text{ Pa} \end{aligned}$$

Note that  $\Delta p_c$ ,  $\Delta p_g$  and  $\Delta p_e$  can be neglected because we are calculating the core pressure drop in horizontal microchannels.

The following Eqs. (9.1-12, 14, 35, 36, 37, 39 and 40) are from Chapter 9 of Handbook of Phase Change (Kandlikar *et al.*, 1999). Assuming that the liquid pressure is 1 atm, then  $i_{IN} = 228 \times 10^3 \text{ J/kg}$ . The heated area in the two-phase region is:

$$\begin{aligned} A_{h,tp} &= (b + a + b)(L - z) = (200 \times 10^{-6} + 200 \times 10^{-6} + 200 \times 10^{-6}) \\ &\quad \times (10 \times 10^{-3} - 8.29 \times 10^{-3}) \\ &= 1.026 \times 10^{-6} \text{ m}^2 \end{aligned}$$

Use the average thermodynamic quality between 0 and  $x_e$ ,  $x_{avg} = 0.0047$ . From Eq. (9.1-39):

$$Re_V = \frac{Gx D_h}{\mu_V} = \frac{(202)(0.0047)(200 \times 10^{-6})}{(10.8 \times 10^{-6})} = 17.58$$

From earlier the vapor friction factor is:

$$f_V = \frac{14.23}{Re_V} = \frac{14.23}{17.58} = 0.809$$

From Eq. (9.1-35):

$$-\left(\frac{dp_F}{dz}\right)_V = \frac{2f_V G^2 x^2}{D_h \rho_V} = \frac{2(0.809)(202)^2(0.0047)^2}{(200 \times 10^{-6})(6.5)} = 1122 \text{ Pa/m}$$

From Eq. (9.1-40):

$$\text{Re}_L = \frac{G(1-x)D_h}{\mu_L} = \frac{(202)(1-0.0047)(200 \times 10^{-6})}{(0.4042 \times 10^{-3})} = 99.48$$

$$f_L = \frac{14.23}{\text{Re}_L} = \frac{14.23}{99.48} = 0.143$$

From Eq. (9.1-36):

$$-\left(\frac{dp_F}{dz}\right)_L = \frac{2f_L G^2 (1-x)^2}{D_h \rho_L} = \frac{2(0.143)(202)^2(1-0.0047)^2}{(200 \times 10^{-6})(1456.6)} = 39,683 \text{ Pa/m}$$

From Eq. (5.37):

$$X^2 = \left(\frac{dp_F}{dz}\right)_L / \left(\frac{dp_F}{dz}\right)_V = \frac{39,683}{1122} = 35.37$$

Assuming both phases are laminar, from Eq. (5.36d),  $C = 5$ .

Using Eq. (5.39):

$$\phi_L^2 = 1 + \frac{C(1 - e^{-319D_h})}{X} + \frac{1}{X^2} = 1 + \frac{5(1 - e^{-319(200 \times 10^{-6})})}{\sqrt{35.37}} + \frac{1}{35.37} = 1.08$$

From Eq. (5.34)  $\Delta p_{f,tp} = \left(\frac{dp_F}{dz}\right) = \left(\frac{dp_F}{dz}\right)_L \phi_L^2 = (39,683)(1.08) = 42,858 \text{ Pa/m}$

The acceleration pressure drop is calculated from Eq. (5.40):

$$\Delta p_a = G^2 v_{LV} x_e = (202)^2(0.00069)(0.0094) = 0.26 \text{ Pa}$$

The value of the acceleration pressure drop is negligible, and hence the total pressure drop is

$$\Delta p = \Delta p_{f,1-ph} + \Delta p_{f,tp} = (353) + (42,858)(0.01 - 0.00829) = 426 \text{ Pa}$$

**(iv) Plot the predicted heat transfer coefficient as a function of quality**

From Table 5.1, the Boiling number is:

$$Bo = \frac{q''}{Gh_{LV}} = \frac{(13,000)}{(202)(170.19 \times 10^3)} = 0.378 \times 10^{-3}$$

From Table 5.1, the convection number is:

$$\begin{aligned} Co &= [(1-x)/x]^{0.8} [\rho_V/\rho_L]^{0.5} = [(1-x)/x]^{0.8} (6.5/1456.6)^{0.5} \\ &= 0.0668[(1-x)/x]^{0.8} \end{aligned}$$

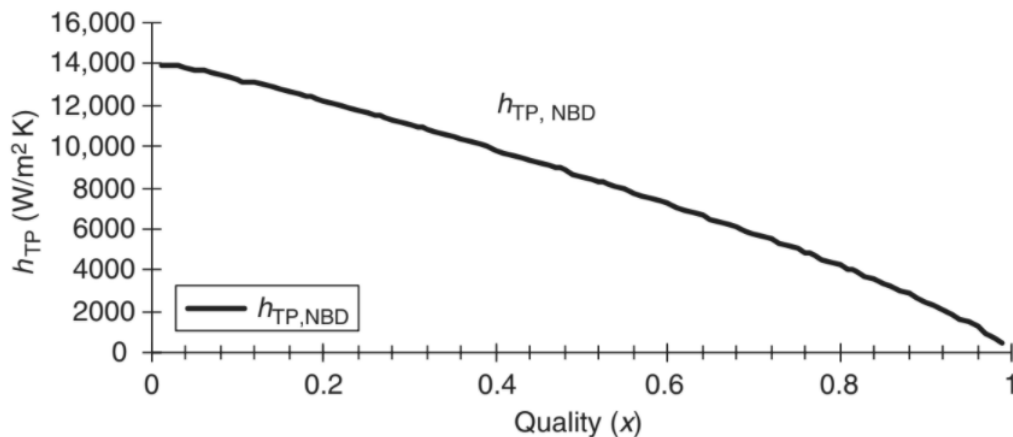
For  $Re_{LO} \leq 100$ , from Eqs. (5.26) and (5.27):

$$h_{LO} = \frac{Nuk_L}{D_h} = \frac{(3.556)(0.0756)}{(200 \times 10^{-6})} = 1344 \text{ W/m}^2 \text{ K}$$

From Table 3 in page 391 of Handbook of Phase Change (Kandlikar *et al.*, 1999), assume  $F_{FI} = 1.3$ .

For  $Re_{LO} \leq 100$ ,  $h_{TP} = h_{TP,NBD}$  and we can plot the predicted heat transfer coefficient as a function of quality using Eq. (5.27). This is very similar to the method followed in the previous example, but only the nucleate boiling dominant prediction is used from Eq. (5.27):

$$\begin{aligned} h_{TP} &= h_{TP,NBD} = h_{LO} \{ 0.6683 Co^{-0.2} (1-x)^{0.8} + 1058.0 Bo^{0.7} (1-x)^{0.8} F_{FI} \} \\ &= 1344 \{ 0.6683 (0.0668 [(1-x)/x]^{0.8})^{-0.2} (1-x)^{0.8} \\ &\quad + 1058.0 (0.378 \times 10^{-3})^{0.7} (1-x)^{0.8} F_{FI} \} \end{aligned}$$



The total frictional pressure drop has to consider the minor losses because the actual  $\Delta p$  is higher than the core frictional pressure drop. Due to the laminar conditions and the dominance of nucleate boiling effects, note the decreasing trend in  $h_{TP}$  as a function of quality.

## Appendix F: Discounted Payback Period (cont.)

The iterative calculations required for determining the discounted payback period were completed using a spreadsheet. For the ORC/SHEC system at the 10 kW data center scale, the annual revenue was \$377.55 and the total capital cost was \$2,079.23. Starting at year 1, the present value of the annual revenue decreases due to the time value of money. The present value of the annual revenue corresponding to each year was calculated using the following formula:

$$P = F/(1 + i)^n$$

where  $P$  is the present value of the annual cost,  $F$  is the future value (corresponding to the \$377.55 annual revenue),  $i$  is the interest rate (0.05), and  $n$  is the year. The discounted payback period was determined by iteratively subtracting the present values of the annual revenues (i.e. discounted cash flows) for each year from the original present value capital cost (see **Table F.1**).

**Table F.1:** Discounted Payback Period for 10 kW ORC/SHEC system.

year	revenue present value (discounted cash flow)	Initial cost left to reduce
0		\$2,079.23
1	\$359.57	\$1,719.66
2	\$342.45	\$1,377.21
3	\$326.14	\$1,051.07
4	\$310.61	\$740.46
5	\$295.82	\$444.64
6	\$281.73	\$162.90
7	\$268.32	-\$105.41

At year 6, there was only \$162.90 left to pay back and the next annual revenue of \$281.73 would exceed it. Thus the discounted payback period was represented by the expression,

$$\text{Year before recovery} + \frac{\text{cost left to pay back in year before recovery}}{\text{discounted cash flow in year after recovery}}$$

Thus, the discounted payback period for the 10 kW ORC/SHEC system was  $6 + (162.90 / 281.73)$ , or 6.61 years.

The same iterative process and calculation was conducted for the 1000 kW ORC/SHEC system, which had an annual revenue of \$54,056.96 and a total capital cost of \$207,922.89.

**Table F.2:** Discounted Payback Period for 1000 kW ORC/SHEC system.

year	revenue present value (discounted cash flow)	Initial cost left to reduce
0		\$207,922.89
1	\$51,482.82	\$156,440.08

2	\$49,031.25	\$107,408.83
3	\$46,696.43	\$60,712.40
4	\$44,472.79	\$16,239.60
5	\$42,355.04	-\$26,115.44

Using the same formula for the discounted payback period and values from **Table F.2**, the discounted payback period for the 1000 kW ORC/SHEC system was  $4 + (16,239.60 / 42,355.04)$ , or 4.38 years.

## Appendix G: MATLAB Code for Final Design of ORC/SHEC System

```
clear
clc
%% HEX Evaporator
%% Pre-defined parameters
Qdot_DC = 10; %[kW]
T_hi = 80.85; %[C]
T_ho = 74; %[C]
T_co = T_hi - 6; %[C]
ID_1 = 0.010211; %[m]
OD_1 = 0.012700; %[m]
ID_2 = 0.025273; %[m]
h_rvmax = 4200; %[W/m-K]
h_rvmin = 1000; %[W/m-K]
h_rvavg = 2600; %[W/m-K]
%% Calculated input parameters
% Thermodynamic Analysis
T_sat = T_co; %[C]
T1 = T_co; %[C]
P_sat = py.CoolProp.CoolProp.PropsSI('P','T',T_co+273.15,'Q',1,'R1234ze(E)')/1000; %[kPa]
P1 = P_sat; %[kPa]
s1 = py.CoolProp.CoolProp.PropsSI('S','T',T_co+273.15,'Q',1,'R1234ze(E)')/1000; %[kJ/kg-K]
s2 = s1; %[kJ/kg-K]
T_ci = 52.5; %[C]
P2 = py.CoolProp.CoolProp.PropsSI('P','T',T_ci+273.15,'Q',1,'R1234ze(E)')/1000; %[kPa]
% HEX Analysis
T_hio = (T_hi+T_ho)/2;
c_pwHEX = py.CoolProp.CoolProp.PropsSI('C','T',T_hio+273.15,'Q',0,'water')/1000; %[kJ/kg-K]
delT = T_hi - T_ho; %[K]
mdot_w = Qdot_DC/(c_pwHEX*delT); %[kg/s]
h_g = py.CoolProp.CoolProp.PropsSI('H','T',T1+273.15,'Q',1,'R1234ze(E)')/1000; %[kJ/kg]
h_f = py.CoolProp.CoolProp.PropsSI('H','T',T1+273.15,'Q',0,'R1234ze(E)')/1000; %[kJ/kg]
h_fg = h_g - h_f; %[kJ/kg]
c_p_r = py.CoolProp.CoolProp.PropsSI('C','T',(T_ci+T_co)/2+273.15,'Q',0,'R1234ze(E)')/1000;
%[kJ/kg-K]
mdot_r = Qdot_DC/(h_fg+(c_p_r*(T_co-T_ci))); %[kg/s]
q_c_vap = mdot_r*h_fg; %[kW]
T_mid = 75.5893; %[C] initial guess
c_pm = py.CoolProp.CoolProp.PropsSI('C','T',(T_mid+T_hi)/2+273.15,'Q',0,'water')/1000;
%[kJ/kg-K]
T_mid = T_hi-(q_c_vap/(mdot_w*c_pm)); %[C]
c_pmm = py.CoolProp.CoolProp.PropsSI('C','T',(T_mid+T_ho)/2+273.15,'Q',0,'water')/1000;
%[kJ/kg-K]
q_h_heat = mdot_w*c_pmm*(T_mid-T_ho); %[kW]
q_c_heat = mdot_r*c_p_r*(T_co-T_ci); %[kW]
%Pipe Analysis
A_c1 = pi*(ID_1/2)^2; %[m^2]
A_ca = pi*((ID_2/2)^2-(OD_1/2)^2); %[m^2]
D_h = 4*A_ca/(pi*ID_2+pi*OD_1); %[m]
%Fluid Property Context
T_wavgh = (T_mid+T_ho)/2; %[C]
T_ravgh = (T_ci+T_co)/2; %[C]
T_avgh = (T_wavgh+T_ravgh)/2; %[C]
T_wavgv = (T_mid+T_hi)/2; %[C]
T_ravgv = T_co; %[C]
T_vap_avg = (T_wavgv+T_ravgv)/2; %[C]
```

```

%% Summary of input parameters
q_heat = (q_h_heat+q_c_heat)/2; %[kW]
q_vap = q_c_vap; %[kW]
%% Summary of properties
k_p_heat = 397; %[W/m^2-k]
k_p_vap = 396; %[W/m^2-k]
mu_w_heat = py.CoolProp.CoolProp.PropsSI('V','T',T_wavgh+273.15,'Q',0,'water')*10^6;
%[microPa-s]
c_p_w_heat = py.CoolProp.CoolProp.PropsSI('C','T',T_wavgh+273.15,'Q',0,'water')/1000;
%[kJ/kg-K]
k_w_heat = py.CoolProp.CoolProp.PropsSI('L','T',T_wavgh+273.15,'Q',0,'water')*1000;
%[mW/m-K]
mu_r_heat = py.CoolProp.CoolProp.PropsSI('V','T',T_ravgh+273.15,'Q',0,'R1234ze(E)')*10^6;
%[microPa-s]
c_p_r_heat = py.CoolProp.CoolProp.PropsSI('C','T',T_ravgh+273.15,'Q',0,'R1234ze(E)')/1000;
%[kJ/kg-K]
k_r_heat = py.CoolProp.CoolProp.PropsSI('L','T',T_ravgh+273.15,'Q',0,'R1234ze(E)')*1000;
%[mW/m-K]
mu_w_vap = py.CoolProp.CoolProp.PropsSI('V','T',T_wavgv+273.15,'Q',0,'water')*10^6;
%[microPa-s]
c_p_w_vap = py.CoolProp.CoolProp.PropsSI('C','T',T_wavgv+273.15,'Q',0,'water')/1000;
%[kJ/kg-K]
k_w_vap = py.CoolProp.CoolProp.PropsSI('L','T',T_wavgv+273.15,'Q',0,'water')*1000; %[mW/-K]
%% HEX Design
P = (T_co - T_ci)/(T_hi - T_ci);
R = (T_hi - T_ho)/(T_mid - T_ci);
CF_hex = 0.8;
%% Inner Pipe (Cold Fluid, R1234ze) - Internal Axial Fins (Rectangular)
f_t = 0.00030; %[m]
D_fp = 0.4*ID_1; %[m]
C_fp = pi*D_fp; %[m]
Frac_fp = 0.5;
L_fp = C_fp*Frac_fp;
f_num = ceil(L_fp/f_t);
f_e = 0.3*ID_1; %[m]
C_i = pi*ID_1; %[m]
C_f = (f_num*f_t)/C_i;
C_iex = (1-C_f)*C_i; %[m]
L_c = f_e+(f_t/2); %[m]
A_1f = 2*L_c; %[m^2]
%% STAGE 1: Heating R1234ze(I) from T_ci to T_sat, T_co
% Find UA using LMTD Method
T_ho = T_ho + 273.15; %[K]
T_ci = T_ci + 273.15; %[K]
delT1_heat = T_ho - T_ci; %[K]
T_mid = T_mid + 273.15; %[K]
T_co = T_co + 273.15; %[K]
delT2_heat = T_mid - T_co; %[K]
delT_lm_heat = (delT1_heat - delT2_heat)/log(delT1_heat/delT2_heat);
q_heat = q_heat*1000; %[W]
UA_heat = q_heat/delT_lm_heat; %[W/K]
UA_heat_CF = q_heat/(CF_hex*delT_lm_heat); %[W/K]
% Determine Heat Transfer Coefficient for Hot Fluid (Water)
mu_w_heat = mu_w_heat*10^-6; %[Pa-s]
Re_h_heat = (mdot_w*D_h)/(A_ca*mu_w_heat);
c_p_w_heat = c_p_w_heat*1000; %[J/kg-K]
k_w_heat = k_w_heat/1000; %[W/m-K]
Pr_h_heat = mu_w_heat*c_p_w_heat/k_w_heat;

```

```

Nu_h_heat = (0.023*(Re_h_heat^0.8))*(Pr_h_heat^0.3);
h_h_heat = Nu_h_heat*k_w_heat/D_h;
% Determine Heat Transfer Coefficient for Cold Fluid (R1234ze)
mu_r_heat = mu_r_heat*10^-6; %[Pa-s]
Re_c_heat = (mdot_r*ID_1)/(A_c1*mu_r_heat);
c_p_r_heat = c_p_r_heat*1000; %[J/kg-K]
k_r_heat = k_r_heat/1000; %[W/m-K]
Pr_c_heat = mu_r_heat*c_p_r_heat/k_r_heat;
Nu_c_heat = (0.023*(Re_c_heat^0.8))*(Pr_c_heat^0.4);
h_c_heat = Nu_c_heat*k_r_heat/ID_1; %[W/m^2-K]
% Determine Required Length of HEX
L_heat =
UA_heat*((1/(h_c_heat*pi*ID_1))+(log(OD_1/ID_1)/(2*pi*k_p_heat))+(1/(h_h_heat*pi*OD_1)));
%[m]
L_heat_CF =
UA_heat_CF*((1/(h_c_heat*pi*ID_1))+(log(OD_1/ID_1)/(2*pi*k_p_heat))+(1/(h_h_heat*pi*OD_1)));
%[m]
% Required Length of Heating HEX with Internal Axial Fins on Inner Pipe
m = ((2*h_c_heat)/(k_p_heat*f_t))^(1/2);
eta_f = tanh(m*L_c)/(m*L_c); %[]
A_f = f_num*2*L_c; %[m^2]
A = C_iex + A_f; %[m^2]
A_eff = (A-(A_f*(1-eta_f))); %[m^2]
A_unf = ID_1 * pi; %[m^2]
FCF = A_eff/A_unf;
L_heat_fin =
UA_heat*((1/(h_c_heat*pi*ID_1*FCF))+(log(OD_1/ID_1)/(2*pi*k_p_heat))+(1/(h_h_heat*pi*OD_1)));
%[m]
L_heat_fin_CF =
UA_heat_CF*((1/(h_c_heat*pi*ID_1*FCF))+(log(OD_1/ID_1)/(2*pi*k_p_heat))+(1/(h_h_heat*pi*OD_1)));
%[m]
%% Stage 2: Vaporizing R1234ze from (l) to (v) at T_sat, T_co
% Find UA using LMTD Method
T_hi = T_hi + 273.15; %[K]
delT1_vap = T_hi - T_co; %[K]
delT2_vap = T_mid - T_co; %[K]
delT_lm_vap = (delT1_vap-delT2_vap)/log(delT1_vap/delT2_vap); %[K]
q_vap = q_vap*1000; %[W]
UA_vap = q_vap/delT_lm_vap; %[W/K]
% Determine Heat Transfer Coefficient for Hot Fluid (Water)
mu_w_vap = mu_w_vap*10^-6; %[Pa-s]
Re_h_vap = (mdot_w*D_h)/(A_ca*mu_w_vap);
c_p_w_vap = c_p_w_vap*1000; %[J/kg-K]
k_w_vap = k_w_vap/1000; %[W/m-K]
Pr_h_vap = (mu_w_vap*c_p_w_vap)/k_w_vap;
Nu_h_vap = (0.023*(Re_h_vap^0.8))*(Pr_h_vap^0.3);
h_h_vap = Nu_h_vap*k_w_vap/D_h; %[W/m^2-K]
% Heat Transfer Coefficient for Cold Fluid (R1234ze)
% Determine Required Length of HEX
h_c_vap_max = h_rvmax; %[W/m-K]
h_c_vap_min = h_rvmin; %[W/m-K]
h_c_vap_avg = h_rvavg; %[W/m-K]
L_r_vap_max =
UA_vap*((1/(h_c_vap_max*pi*ID_1))+(log(OD_1/ID_1)/(2*pi*k_p_vap))+(1/(h_h_vap*pi*OD_1)));
%[m]
L_r_vap_min =
UA_vap*((1/(h_c_vap_min*pi*ID_1))+(log(OD_1/ID_1)/(2*pi*k_p_vap))+(1/(h_h_vap*pi*OD_1)));
%[m]

```

```

L_r_vap_avg =
UA_vap*((1/(h_c_vap_avg*pi*ID_1))+(log(OD_1/ID_1)/(2*pi*k_p_vap))+(1/(h_h_vap*pi*OD_1)));
%[m]
% Required Length of Vaporizing HEX with Internal Axial Fins on Inner Pipe
m_fin_max = ((2*h_rvmax)/(k_p_vap*f_t))^(1/2);
m_fin_min = ((2*h_rvmin)/(k_p_vap*f_t))^(1/2);
m_fin_avg = ((2*h_rvavg)/(k_p_vap*f_t))^(1/2);
eta_f_max = tanh(m_fin_max*L_c)/(m_fin_max*L_c);
eta_f_min = tanh(m_fin_min*L_c)/(m_fin_min*L_c);
eta_f_avg = tanh(m_fin_avg*L_c)/(m_fin_avg*L_c);
A_eff_max = A-(A_f*(1-eta_f_max));
A_eff_min = A-(A_f*(1-eta_f_min));
A_eff_avg = A-(A_f*(1-eta_f_avg));
FCF_max = A_eff_max/A_unf;
FCF_min = A_eff_min/A_unf;
FCF_avg = A_eff_avg/A_unf;
L_r_vap_max_f =
UA_vap*((1/(h_c_vap_max*pi*ID_1*FCF_max))+(log(OD_1/ID_1)/(2*pi*k_p_vap))+(1/(h_h_vap*pi*OD_
1)))); %[m]
L_r_vap_min_f =
UA_vap*((1/(h_c_vap_min*pi*ID_1*FCF_min))+(log(OD_1/ID_1)/(2*pi*k_p_vap))+(1/(h_h_vap*pi*OD_
1)))); %[m]
L_r_vap_avg_f =
UA_vap*((1/(h_c_vap_avg*pi*ID_1*FCF_avg))+(log(OD_1/ID_1)/(2*pi*k_p_vap))+(1/(h_h_vap*pi*OD_
1)))); %[m]
%% HEX Condenser %%%%%%%%%%%%%%%%%%%%%%%%%%%%%%%%%%%%%%%%%%%%%%%%%%%%%%%%%%%%%%%%%%%%%%%%%
%% Pre-defined input parameters
% Temperatures
TI_hic = T_ci; %[K]
T_hoc = TI_hic; %[K]
T_cic = 280.37; %[K]
T_coc = T_cic + 20; %[K]
%Piping
ID_3 = 0.010211; %[m]
OD_3 = 0.012700; %[m]
ID_4 = 0.025273; %[m]
% Heat Transfer Coefficient - condensing R1234ze
h_r_cond_max = 4800; %[W/m-K]
h_r_cond_min = 900; %[W/m-K]
h_r_cond_avg = 2850; %[W/m-K]
%% Thermodynamic Analysis
h_2s = py.CoolProp.CoolProp.PropsSI('H','T',TI_hic,'Q',1,'R1234ze(E)')/1000; %[kJ/kg]
eff_t = 0.8;
h_1 = py.CoolProp.CoolProp.PropsSI('H','T',T_co,'Q',1,'R1234ze(E)')/1000; %[kJ/kg]
h_2 = h_1 - (0.8*(h_1-h_2s)); %[kJ/kg]
T_hic = py.CoolProp.CoolProp.PropsSI('T','H',h_2*1000,'P',P2*1000,'R1234ze(E)'); %[K]
h_3 = py.CoolProp.CoolProp.PropsSI('H','T',T_hoc,'Q',0,'R1234ze(E)')/1000; %[kJ/kg]
%% Calculated input parameters
% HEX Analysis
h_fg = h_2s - h_3;
c_p_rc =
((py.CoolProp.CoolProp.PropsSI('C','T',T_hic,'Q',1,'R1234ze(E)')/1000)+(py.CoolProp.CoolProp
.PropsSI('C','P',P2*1000,'Q',1,'R1234ze(E)')/1000))/2; %[kJ/kg-K]
q_totalc = mdot_r*(h_fg+(c_p_rc*(T_hic-TI_hic))); %[kW]
q_hcool = mdot_r*(c_p_rc*(T_hic-TI_hic)); %[kW]
q_hcond = mdot_r*h_fg; %[kW]
T_wavg = (T_cic+T_coc)/2; %[K]
c_pw = py.CoolProp.CoolProp.PropsSI('C','T',T_wavg,'Q',0,'water')/1000; %[kJ/kg-K]

```

```

delT = T_coc - T_cic; %[K]
mdot_wc = q_totalc/(c_pw*delT); %[kg/s]
T_midc = T_cic + (q_hcond/(mdot_wc*c_pw)); %[K]
%Pipe Analysis
A_c_3 = pi*(ID_3/2)^2; %[m^2]
A_c_4 = pi*((ID_4/2)^2-(OD_3/2)^2); %[m^2]
D_ha = 4*A_c_4/((pi*OD_3)+(pi*ID_4)); %[m^2]
%% Summary of actual condenser temperatures
T_pavg = (T_cic+T_hic)/2; %[K]
T_ravg = (T_hic+T_hoc)/2; %[K]
k_pcond = 401; %[W/m-K]
T_wcool = (T_coc+T_midc)/2; %[K]
mu_wcool = py.CoolProp.CoolProp.PropsSI('V','T',T_wcool,'Q',0,'water')*10^6; %[microPa-s]
c_pwcool = py.CoolProp.CoolProp.PropsSI('C','T',T_wcool,'Q',0,'water')/1000; %[kJ/kg-K]
k_wcool = py.CoolProp.CoolProp.PropsSI('L','T',T_wcool,'Q',0,'water')*1000; %[mW/m-K]
T_rcool = (T_hic+TI_hic)/2; %[K]
mu_rcool = py.CoolProp.CoolProp.PropsSI('V','T',T_rcool,'Q',1,'R1234ze(E)')*10^6;
[microPa-s]
c_prcool = py.CoolProp.CoolProp.PropsSI('C','T',T_rcool,'Q',1,'R1234ze(E)')/1000; %[kJ/kg-K]
k_rcool = py.CoolProp.CoolProp.PropsSI('L','T',T_rcool,'Q',1,'R1234ze(E)')*1000; %[mW/m-K]
T_wcond = (T_cic + T_midc)/2; %[K]
mu_wcond = py.CoolProp.CoolProp.PropsSI('V','T',T_wcond,'Q',0,'water')*10^6; %[microPa-s]
c_pwcond = py.CoolProp.CoolProp.PropsSI('C','T',T_wcond,'Q',0,'water')/1000; %[kJ/kg-K]
k_wcond = py.CoolProp.CoolProp.PropsSI('L','T',T_wcond,'Q',0,'water')*1000; %[mW/m-K]
T_rcond = (TI_hic + T_hoc)/2; %[K]
%% Condenser HEX Design
P_c = (T_hic - T_hoc)/(T_cic - T_hic);
R_c = (T_cic - T_coc)/(T_hic - T_hoc);
CF_hexc = 1;
%% Inner Pipe (Hot Fluid, R1234ze) Internal Axial Fins (Rectangular)
f_tc = 0.00030; %[m]
D_fpc = 0.4*ID_3; %[m]
C_fpc = pi*D_fpc; %[m]
Frac_fpc = 0.5;
L_fpc = C_fpc*Frac_fpc;
f_numc = ceil(L_fpc/f_tc);
f_ec = 0.3*ID_3; %[m]
C_ic = pi*ID_3; %[m]
C_fc = (f_numc*f_tc)/C_ic;
C_iexc = (1-C_fc)*C_ic; %[m]
L_cc = f_ec+(f_tc/2); %[m]
A_1fc = 2*L_cc; %[m^2]
%% Stage 1: Cooling R1234ze(v) from T_hic(SHv) to T_sat, TI_hic(v)
% Find UA using LMTD Method
delT1_cool = T_hic - T_coc; %[K]
delT2_cool = TI_hic - T_midc; %[K]
delT_lm_cool = (delT1_cool-delT2_cool)/log(delT1_cool/delT2_cool); %[K]
q_cool = q_hcool*1000; %[W]
UA_cool = q_cool/delT_lm_cool; %[W/K]
% Determine Heat Transfer Coefficient for Cold Fluid (water)
mu_wcool = mu_wcool*10^-6; %[Pa-s]
Re_c_cool = mdot_wc*D_ha/(A_c_4*mu_wcool);
c_pwcool = c_pwcool*1000; %[J/kg-K]
k_wcool = k_wcool/1000; %[W/m-K]
Pr_c_cool = mu_wcool*c_pwcool/k_wcool;
Nu_c_cool = (0.023*(Re_c_cool^0.8))*(Pr_c_cool^0.4);
h_c_cool = Nu_c_cool*k_wcool/D_ha; %[W/m^2-K]
% Determine Heat Transfer Coefficient for Hot Fluid (R1234ze)

```

```

mu_rcool = mu_rcool*10^-6; %[Pa-s]
Re_h_cool = mdot_r*ID_3/(A_c_3*mu_rcool);
c_prcool = c_prcool*1000; %[J/kg-K]
k_rcool = k_rcool/1000; %[W/m-K]
Pr_h_cool = mu_rcool*c_prcool/k_rcool;
Nu_h_cool = (0.023*(Re_h_cool^0.8))*(Pr_h_cool^0.4);
h_h_cool = Nu_h_cool*k_rcool/ID_3; %[W/m^2-K]
% Determine Required Length of HEX
L_cool =
UA_cool*((1/(h_c_cool*pi*ID_3))+(log(OD_3/ID_3)/(2*pi*k_pcond))+(1/(h_h_cool*pi*OD_3)));
%[m]
% Required Length of Cooling HEX with Internal Axial Fins on Inner Pipe
% (with R1234ze)
m_cool = ((2*h_h_cool)/(k_pcond*f_t))^(1/2);
eta_f_cool = tanh(m_cool*L_c)/(m_cool*L_c);
A_fc = f_numc*2*L_cc; %[m^2]
Ac = C_iexc + A_fc; %[m^2]
A_eff_cool = (Ac-(A_fc*(1-eta_f_cool))); %[m^2]
A_unf_cool = ID_3 * pi; %[m^2]
FCF_cool = A_eff_cool/A_unf_cool;
L_cool_f =
UA_cool*((1/(h_c_cool*pi*ID_3*FCF_cool))+(log(OD_3/ID_3)/(2*pi*k_pcond))+(1/(h_h_cool*pi*OD_3)));
%[m]
%% Stage 2: Condensing R1234ze from (v) to (l) at TI_hic/T_hoc
% Find UA using LMTD Method
delT1_cond = T_hoc - T_cic; %[K]
delT2_cond = T_hoc-T_coc; %[K]
delT_lm_cond = (delT1_cond-delT2_cond)/log(delT1_cond/delT2_cond); %[K]
q_cond = q_hcond*1000; %[W]
UA_cond = q_cond/delT_lm_cond; %[W/K]
% Determine Heat Transfer Coefficient for Cold Fluid (water)
mu_wcond = mu_wcond*10^-6; %[Pa-s]
Re_w_cond = mdot_wc*D_ha/(A_c_4*mu_wcond);
c_pwcond = c_pwcond*1000; %[J/kg-K]
k_wcond = k_wcond/1000; %[W/m-K]
Pr_w_cond = mu_wcond*c_pwcond/k_wcond;
Nu_w_cond = (0.023*(Re_w_cond^0.8))*(Pr_w_cond^0.4);
h_w_cond = Nu_w_cond*k_wcond/D_ha; %[W/m^2-K]
% Determine Required Length of HEX
Length_cmax =
UA_cond*((1/(h_r_cond_max*pi*ID_3))+(log(OD_3/ID_3)/(2*pi*k_pcond))+(1/(h_w_cond*pi*OD_3)));
%[m]
Length_cmin =
UA_cond*((1/(h_r_cond_min*pi*ID_3))+(log(OD_3/ID_3)/(2*pi*k_pcond))+(1/(h_w_cond*pi*OD_3)));
%[m]
Length_cavg =
UA_cond*((1/(h_r_cond_avg*pi*ID_3))+(log(OD_3/ID_3)/(2*pi*k_pcond))+(1/(h_w_cond*pi*OD_3)));
%[m]
% Required Length of Condensing HEX with Internal Axial Fins on Inner Pipe
% (with R1234ze)
m_cond_max = ((2*h_r_cond_max)/(k_pcond*f_tc))^(1/2);
m_cond_min = ((2*h_r_cond_min)/(k_pcond*f_tc))^(1/2);
m_cond_avg = ((2*h_r_cond_avg)/(k_pcond*f_tc))^(1/2);
eta_f_cond_max = tanh(m_cond_max*L_cc)/(m_cond_max*L_cc);
eta_f_cond_min = tanh(m_cond_min*L_cc)/(m_cond_min*L_cc);
eta_f_cond_avg = tanh(m_cond_avg*L_cc)/(m_cond_avg*L_cc);
A_eff_cond_max = Ac - (A_fc*(1-eta_f_cond_max)); %[m^2]
A_eff_cond_min = Ac - (A_fc*(1-eta_f_cond_min)); %[m^2]

```

```

A_eff_cond_avg = Ac - (A_fc*(1-eta_f_cond_avg)); %[m^2]
A_unf_cond = pi*ID_3;
FCF_cond_max = A_eff_cond_max/A_unf_cond;
FCF_cond_min = A_eff_cond_min/A_unf_cond;
FCF_cond_avg = A_eff_cond_avg/A_unf_cond;
L_fcond_max =
UA_cond*((1/(h_r_cond_max*pi*ID_3*FCF_cond_max)))+(log(OD_3/ID_3)/(2*pi*k_pcond))+(1/(h_w_con
d*pi*OD_3)); %[m]
L_fcond_min =
UA_cond*((1/(h_r_cond_min*pi*ID_3*FCF_cond_min)))+(log(OD_3/ID_3)/(2*pi*k_pcond))+(1/(h_w_con
d*pi*OD_3)); %[m]
L_fcond_avg =
UA_cond*((1/(h_r_cond_avg*pi*ID_3*FCF_cond_avg)))+(log(OD_3/ID_3)/(2*pi*k_pcond))+(1/(h_w_con
d*pi*OD_3)); %[m]
%% Thermodynamics %%%%%%%%%%%%%%%%%%%%%%%%%%%%%%%%%%%%%%%%%%%%%%%%%%%%%%%%%%%%%%%%%%%%%%%%%
% State 1
v1 = 1/py.CoolProp.CoolProp.PropsSI('D','T',T1+273.15,'Q',1,'R1234ze(E)'); %[m^3/kg]
% State 2
T_2SH = T_hic; %[K]
s_2SH = py.CoolProp.CoolProp.PropsSI('S','P',P2*1000,'T',T_2SH,'R1234ze(E)')/1000;
%[kJ/kg-K]
v_2SH = 1/py.CoolProp.CoolProp.PropsSI('D','P',P2*1000,'T',T_2SH,'R1234ze(E)'); %[m^3/kg]
% State 2'
T2 = TI_hic; %[K]
T_satc = T2; %[K]
v2 = 1/py.CoolProp.CoolProp.PropsSI('D','P',P2*1000,'Q',1,'R1234ze(E)'); %[m^3/kg]
% State 3
P3 = P2; %[kPa]
T3 = T2; %[K]
s3 = py.CoolProp.CoolProp.PropsSI('S','P',P3*1000,'Q',0,'R1234ze(E)')/1000; %[kJ/kg-K]
v3 = 1/py.CoolProp.CoolProp.PropsSI('D','P',P3*1000,'Q',0,'R1234ze(E)'); %[m^3/kg]
% State 4
P4 = P1; %[kPa]
h_4s = h_3 + (v3*(P4 - P3)); %[kJ/kg]
eff_p = 0.85;
h_4 = h_3 + ((h_4s - h_3)/eff_p); %[kJ/kg]
T_4SC = py.CoolProp.CoolProp.PropsSI('T','P',P4*1000,'H',h_4*1000,'R1234ze(E)'); %[K]
s_4SC = py.CoolProp.CoolProp.PropsSI('S','P',P4*1000,'H',h_4*1000,'R1234ze(E)')/1000;
%[kJ/kg-K]
v_4SC = 1/py.CoolProp.CoolProp.PropsSI('D','P',P4*1000,'H',h_4*1000,'R1234ze(E)'); %[m^3/kg]
% State 4'
h_4sat = h_f; %[kJ/kg]
s_4sat = py.CoolProp.CoolProp.PropsSI('S','P',P4*1000,'Q',0,'R1234ze(E)')/1000; %[kJ/kg-K]
v_4sat = 1/py.CoolProp.CoolProp.PropsSI('D','P',P4*1000,'Q',0,'R1234ze(E)'); %[m^3/kg]
% Final Thermodynamic Calculations
Wdot_turb = mdot_r*(h_1-h_2); %[kW]
Wdot_pump = mdot_r*(v3*(P4-P3)); %[kW]
Wdot_net = Wdot_turb-Wdot_pump; %[kW]
eff_th = Wdot_net/Qdot_DC;
eff_carnot = 1 - ((T3)/(T1 + 273.15));
eff_II = eff_th / eff_carnot;
% Cost Analysis
Price_e = 0.1373; %[$]
yrRevenue = Wdot_net * 24 * 365 * Price_e; %[$]
%% ORC Fluids %%%%%%%%%%%%%%%%%%%%%%%%%%%%%%%%%%%%%%%%%%%%%%%%%%%%%%%%%%%%%%%%%%%%%%%%%
rho_1 = py.CoolProp.CoolProp.PropsSI('D','T',T1+273.15,'Q',1,'R1234ze(E)'); %[kg/m^3]
rho_2 = py.CoolProp.CoolProp.PropsSI('D','P',P2*1000,'H',h_2*1000,'R1234ze(E)'); %[kg/m^3]
rho_3 = py.CoolProp.CoolProp.PropsSI('D','T',T3,'Q',0,'R1234ze(E)'); %[kg/m^3]

```

```

rho_4 = py.CoolProp.CoolProp.PropsSI('D','P',P4*1000,'H',h_4*1000,'R1234ze(E)'); %[kg/m^3]
mu_1 = py.CoolProp.CoolProp.PropsSI('V','T',T1+273.15,'Q',1,'R1234ze(E)'); %[Pa*s]
mu_2 = py.CoolProp.CoolProp.PropsSI('V','P',P2*1000,'H',h_2*1000,'R1234ze(E)'); %[Pa*s]
mu_3 = py.CoolProp.CoolProp.PropsSI('V','T',T3,'Q',0,'R1234ze(E)'); %[Pa*s]
mu_4 = py.CoolProp.CoolProp.PropsSI('V','P',P4*1000,'H',h_4*1000,'R1234ze(E)'); %[Pa*s]
E = 1.5*10^-5; %Absolute Roughness
L_ft = 1.5; %Length [ft]
L = L_ft*0.3048; %Length [m]
g = 9.806; %Gravity [m/s^2]
ID_5 = 0.0102; %[m]
%% State 1
V_1 = mdot_r/(rho_1*pi*(ID_5^2)/4);
Re_1 = rho_1*V_1*ID_5/mu_1;
f_1= (-1.8*log10((6.9/Re_1)+((E/(ID_5*3.7))^1.11)))^(-2);
h_L_1 =((V_1)^2/(2*g))*((f_1*(L/ID_5))+0.9); %head loss and accounting for minor loss
delP_1 = rho_1*g*h_L_1;
Q_1 = V_1*pi*(ID_5^2)/4;
Power_1 = delP_1*Q_1;
%% State 2
V_2 = mdot_r/(rho_2*pi*(ID_5^2)/4);
Re_2 = rho_2*V_2*ID_5/mu_2;
f_2= (-1.8*log10((6.9/Re_2)+((E/(ID_5*3.7))^1.11)))^(-2);
h_L_2 =((V_2)^2/(2*g))*((f_2*(L/ID_5))+0.9); %head loss and accounting for minor loss
delP_2 = rho_2*g*h_L_2;
Q_2 = V_2*pi*(ID_5^2)/4;
Power_2 = delP_2*Q_1;
%% State 3
V_3 = mdot_r/(rho_3*pi*(ID_5^2)/4);
Re_3 = rho_3*V_3*ID_5/mu_3;
f_3= (-1.8*log10((6.9/Re_3)+((E/(ID_5*3.7))^1.11)))^(-2);
h_L_3 =((V_3)^2/(2*g))*((f_3*(L/ID_5))+0.9); %head loss and accounting for minor loss
delP_3 = rho_3*g*h_L_3;
Q_3 = V_3*pi*(ID_5^2)/4;
Power_3 = delP_3*Q_3;
%% State 4
V_4 = mdot_r/(rho_4*pi*(ID_5^2)/4);
Re_4 = rho_4*V_4*ID_5/mu_4;
f_4= (-1.8*log10((6.9/Re_4)+((E/(ID_5*3.7))^1.11)))^(-2);
h_L_4 =((V_4)^2/(2*g))*((f_4*(L/ID_5))+0.9); %head loss and accounting for minor loss
delP_4 = rho_4*g*h_L_4;
Q_4 = V_4*pi*(ID_5^2)/4;
Power_4 = delP_4*Q_4;
delP_tot = delP_1 + delP_2 + delP_3 + delP_4; %[Pa]
Power_tot = Power_1 + Power_2 + Power_3 + Power_4; %[Watts]
%% SHEC Fluids %%%%%%%%%%%%%%%%%%%%%%%%%%%%%%%%%%%%%%%%%%%%%%%%%%%%%%%%%%%%%%%%%%%%%%%%%
T_in = T_ho; %[C] inlet of SHEC loop, outlet of evaporator
T_out = T_hi; %[C] outlet of SHEC loop, inlet of evaporator
rho_in = py.CoolProp.CoolProp.PropsSI('D','T',T_in,'P',101325,'Water'); %[kg/m^3] Density
rho_out = py.CoolProp.CoolProp.PropsSI('D','T',T_out,'P',101325,'Water'); %[kg/m^3] Density
mu_in = py.CoolProp.CoolProp.PropsSI('V','T',T_in,'P',101325,'Water'); %[Pa-s] Dynamic
viscosity
mu_out = py.CoolProp.CoolProp.PropsSI('V','T',T_out,'P',101325,'Water'); %[Pa-s] Dynamic
viscosity
E_shec = 1.5E-05; %[m] Absolute roughness
% mass flow rate (based on pre-simulation calculation process)through MCHS
T_shec = (T_in+T_out)/2; %[C]
rho_avg = py.CoolProp.CoolProp.PropsSI('D','T',T_shec,'P',101325,'Water'); %[kg/m^3] Density
c_p_shec = py.CoolProp.CoolProp.PropsSI('C','T',T_shec,'P',101325,'water')/1000; %[kJ/kg-K]

```

```

del_T = 7; %[C] temp change over CPU -- from pre-sim calculation process
q_CPU = 165; %[W] thermal design power of CPU
mdot_CPU = q_CPU/(1000*c_p_shec*del_T); %[kg/s] flow rate through MCHS over 1 CPU
num_CPUs = 64;
mdot_shec = num_CPUs*mdot_CPU; %[kg/s] flow rate through SHEC to all CPU
% Section 1-2
H_12 = 5; %[m] Height relative to ORC
L_12 = 6; %[m] Length of section
mdot_12 = mdot_shec; %[kg/s] Mass flow rate, based on mass flow through CPU and number of
CPUs (close to water mass flow through evaporator mdot_w)
loss_12 = 1.83; % Loss constants
ID_12 = 0.0253; %[m] Inner diameter
v_12 = (4*mdot_12)/(rho_in*pi*ID_12^2); %[m/s] Velocity
Re_12 = (rho_in*v_12*ID_12)/mu_in; % Reynolds number
f_12 = (1/(-1.8*log10((6.9/Re_12)+((E_shec/ID_12)/3.7)^(1.11))))^2; %Friction factor
dP_12 = (rho_in*g*H_12)+(rho_in*f_12*(L_12/ID_12)*((v_12)^2/2)); %[Pa] Pressure drop
Q_12 = v_12*pi*(ID_12^2)/4;
Power_12 = dP_12*Q_12; %[Watts]
% Section 2-Servers
H_2S = 0; %[m]
L_2S = 2; %[m]
mdot_2S = mdot_shec/4; %[kg/s]
loss_2S = 0.9;
ID_2S = 0.0102; %[m]
v_2S = (4*mdot_2S)/(rho_in*pi*ID_2S^2); %[m/s]
Re_2S = (rho_in*v_2S*ID_2S)/mu_in;
f_2S = (1/(-1.8*log10((6.9/Re_2S)+((E_shec/ID_2S)/3.7)^(1.11))))^2;
dP_2S = (rho_in*g*H_2S)+(rho_in*f_2S*(L_2S/ID_2S)*((v_2S)^2/2)); %[Pa]
Q_2S = v_2S*pi*(ID_2S^2)/4;
Power_2S = dP_2S*Q_2S; %[Watts]
% Section Servers-3
H_3S = 0; %[m]
L_3S = 2; %[m]
mdot_3S = mdot_shec/4; %[kg/s]
loss_3S = 0.9;
ID_3S = 0.0102; %[m]
v_3S = (4*mdot_3S)/(rho_out*pi*ID_3S^2); %[m/s]
Re_3S = (rho_out*v_3S*ID_3S)/mu_out;
f_3S = (1/(-1.8*log10((6.9/Re_3S)+((E_shec/ID_3S)/3.7)^(1.11))))^2;
dP_3S = (rho_out*g*H_3S)+(rho_out*f_3S*(L_3S/ID_3S)*((v_3S)^2/2)); %[Pa]
Q_3S = v_3S*pi*(ID_3S^2)/4;
Power_3S = dP_3S*Q_3S; %[Watts]
% Section 2-3 %% servers %%
H_server = 1.8796; % [m]
dP_HeatSink_23 = 994; %[Pa]
dP_Height_23 = rho_in*g*H_server; %[Pa]
dP_23 = dP_HeatSink_23 - dP_Height_23; %[Pa]
Q_23 = mdot_CPU/rho_avg;
Power_23 = dP_23*Q_23; %[Watts]
% Section 3-4
H_34 = 5-H_server; %[m]
HeadLoss_34 = 2; %[m]
L_34 = 4; %[m]
mdot_34 = mdot_shec; %[kg/s]
loss_34 = 1.83;
ID_34 = 0.0253; %[m]
v_34 = (4*mdot_34)/(rho_out*pi*ID_34^2); %[m/s]
Re_34 = (rho_out*v_34*ID_34)/mu_out;

```

```

f_34 = (1/(-1.8*log10((6.9/Re_34)+((E_shec/ID_34)/3.7)^(1.11))))^2;
dP_34 = -(rho_out*g*H_34)+(rho_out*f_34*(L_34/ID_34)*((v_34)^2/2)); %[Pa]
dP_Total = dP_12+dP_2S+dP_S3+dP_23+dP_34; %[Pa]
Q_34 = v_34*pi*(ID_34^2)/4;
Power_34 = dP_34*Q_34; %[Watts]
Power_SHEC_tot = Power_12 + Power_2S + Power_23 + Power_S3 + Power_34; %[Watts]
%% Tabulated Results
% ORC Fluids Results
State = {'State1';'State2';'State3';'State4'};
Velocity = [V_1;V_2;V_3;V_4];
ReynoldsNumber = [Re_1;Re_2;Re_3;Re_4];
FrictionFactor = [f_1;f_2;f_3;f_4];
PressureDrop = [delP_1;delP_2;delP_3;delP_4];
PumpPower = [Power_1;Power_2;Power_3;Power_4];
Results_ORC_Fluids = table(State, Velocity, ReynoldsNumber, FrictionFactor,PressureDrop,
PumpPower)
% SHEC Results
SHEC =
{'InnerDiameter';'FlowRate';'Velocity';'ReynoldsNumber';'VerticalPipe';'TotalPipe';'Friction
Factor';'PressureDrop';'PumpPower'};
SHEC_12 = [ID_12;mdot_12;v_12;Re_12;H_12;L_12;f_12;dP_12;Power_12];
SHEC_2S = [ID_2S;mdot_2S;v_2S;Re_2S;H_2S;L_2S;f_2S;dP_2S;Power_2S];
servers = {'na';mdot_CPU;'na';'na';H_server;'na';'na';dP_23;Power_23};
SHEC_S3 = [ID_S3;mdot_S3;v_S3;Re_S3;H_S3;L_S3;f_S3;dP_S3;Power_S3];
SHEC_34 = [ID_34;mdot_34;v_34;Re_34;H_34;L_34;f_34;dP_34;Power_34];
Results_SHEC = table(SHEC, SHEC_12, SHEC_2S, servers, SHEC_S3,SHEC_34)
% Thermo
State = {'1';'2';'2p';'3';'4';'4p'};
Pressures = [P1;P2;P2;P3;P4;P4];
Temperatures = [T1;T_2SH-273.15;T2-273.15;T3-273.15;T_4SC-273.15;T_sat];
Entropies = [s1;s_2SH;s1;s3;s_4SC;s_4sat];
Enthalpies = [h_1;h_2;h_2s;h_3;h_4;h_4sat];
SpecificVolumes = [v1;v_2SH;v2;v3;v_4SC;v_4sat];
Results_Thermo = table(State, Pressures, Temperatures, Entropies,Enthalpies,
SpecificVolumes)
% ORC Fluids
Table = {'Pressure Drop (Pa)';'Power (Watts)'};
State1 = [delP_1;Power_1];
State2 = [delP_2;Power_2];
State3 = [delP_3;Power_3];
State4 = [delP_4;Power_4];
Total = [delP_tot; Power_tot];
Results_ORC = table(Table, State1, State2, State3, State4, Total)
% Evaporator and Condenser
ORC_HEX =
{'Evaporator_heating';'Evaporator_evaporating';'Condenser_cooling';'Condenser_condensing'};
HotFluid_InletTemp = [T_mid-273.15;T_hi-273.15;T_hic-273.15;TI_hic-273.15];
HotFluid_OutletTemp = [T_ho-273.15;T_mid-273.15;TI_hic-273.15;T_hoc-273.15];
ColdFluid_InletTemp = [T_ci-273.15;T_co-273.15;T_midc-273.15;T_cic-273.15];
ColdFluid_OutletTemp = [T_co-273.15;T_co-273.15;T_coc-273.15;T_midc-273.15];
Results_EvapCond =
table(ORC_HEX,HotFluid_InletTemp,HotFluid_OutletTemp,ColdFluid_InletTemp,ColdFluid_OutletTem
p)
% Reynolds Number
Fluid =
{'Water_heating';'R1234ze_heating';'Water_evaporating';'R1234ze_cooling';'Water_cooling';'Wa
ter_condensing'};
Mass_Flow_Rate = [mdot_w;mdot_r;mdot_w;mdot_r;mdot_wc;mdot_wc];

```

```

Hydraulic_Diameter = [D_h;ID_1;D_h;ID_3;D_ha;D_ha];
CrossSectional_Area = [A_ca;A_cl;A_ca;A_c_3;A_c_4;A_c_4];
Dynamic_Viscosity = [mu_w_heat;mu_r_heat;mu_w_vap;mu_rcool;mu_wcool;mu_wcond];
Reynolds_Number = [Re_h_heat;Re_c_heat;Re_h_vap;Re_h_cool;Re_c_cool;Re_w_cond];
Results_Re =
table(Fluid,Mass_Flow_Rate,Hydraulic_Diameter,CrossSectional_Area,Dynamic_Viscosity,Reynolds
_Number)
% HTC
Fluid =
{'Water_heating';'R1234ze_heating';'Water_evaporating';'R1234ze_cooling';'Water_cooling';'Wa
ter_condensing'};
Reynolds_Number = [Re_h_heat;Re_c_heat;Re_h_vap;Re_h_cool;Re_c_cool;Re_w_cond];
Specific_Heat_Capacity = [c_p_w_heat;c_p_r_heat;c_p_w_vap;c_prcool;c_pwcool;c_pwcond];
Thermal_Conductivity = [k_w_heat;k_r_heat;k_w_vap;k_rcool;k_wcool;k_wcond];
Prandtl_Number = [Pr_h_heat;Pr_c_heat;Pr_h_vap;Pr_h_cool;Pr_c_cool;Pr_w_cond];
Nusselt_Number = [Nu_h_heat;Nu_c_heat;Nu_h_vap;Nu_h_cool;Nu_c_cool;Nu_w_cond];
HTC = [h_h_heat;h_c_heat;h_h_vap;h_h_cool;h_c_cool;h_w_cond];
Results_HTC =
table(Fluid,Reynolds_Number,Specific_Heat_Capacity,Thermal_Conductivity,Prandtl_Number,Nusse
lt_Number,HTC)
% HEX Table 1
ORC_HEX1 =
{'Evaporator_heating';'Evaporator_evaporating';'Condenser_cooling';'Condenser_condensing'};
InnerPipe_ID = [ID_1;ID_1;ID_3;ID_3];
Fin_Thickness = [f_t;f_t;f_tc;f_tc];
Number_of_Fins = [f_num;f_num;f_numc;f_numc];
InnerPipe_OD = [OD_1;OD_1;OD_3;OD_3];
OuterPipe_ID = [ID_2;ID_2;ID_4;ID_4];
Heat_Transfer_Rate = [q_heat;q_vap;q_cool;q_cond];
UA = [UA_heat;UA_vap;UA_cool;UA_cond];
Results_HEX1 =
table(ORC_HEX1,InnerPipe_ID,Fin_Thickness,Number_of_Fins,InnerPipe_OD,OuterPipe_ID,Heat_Tran
sfer_Rate,UA)
% HEX Table 2
ORC_HEX2 =
{'Evaporator_heating';'Evaporator_evaporating_MaxHTC';'Evaporator_evaporating_MinHTC';'Eva
porator_evaporating_AvgHTC';'Condenser_cooling';'Condenser_condensing_MaxHTC';'Condenser_conde
nsing_MinHTC';'Condenser_condensing_AvgHTC'};
Length_CounterFlow =
[L_heat;L_r_vap_max;L_r_vap_min;L_r_vap_avg;L_cool;Length_cmax;Length_cmin;Length_cavg];
Length_ShellTube = {L_heat_CF;'n/a';'n/a';'n/a';'n/a';'n/a';'n/a';'n/a'};
Fin_Efficiency =
[eta_f;eta_f_max;eta_f_min;eta_f_avg;eta_f_cool;eta_f_cond_max;eta_f_cond_min;eta_f_cond_avg
];
Fin_Correction_Factor =
double([FCF;FCF_max;FCF_min;FCF_avg;FCF_cool;FCF_cond_max;FCF_cond_min;FCF_cond_avg]);
Length_CounterFlow_fins =
double([L_heat_fin;L_r_vap_max_f;L_r_vap_min_f;L_r_vap_avg_f;L_cool_f;L_fcond_max;L_fcond_mi
n;L_fcond_avg]);
Length_ShellTube_fins = {double(L_heat_fin_CF);'n/a';'n/a';'n/a';'n/a';'n/a';'n/a';'n/a'};
Results_HEX2 =
table(ORC_HEX2,Length_CounterFlow,Length_ShellTube,Fin_Efficiency,Fin_Correction_Factor,Leng
th_CounterFlow_fins,Length_ShellTube_fins)

```